TESE DE DOUTORAMENTO

ULTRA-HIGH-ENERGY NEUTRINO SEARCH WITH THE PIERRE AUGER OBSERVATORY IN THE ERA OF GRAVITATIONAL WAVE ASTRONOMY

Francisco Pedreira Giralda

ESCOLA DE DOUTORAMENTO INTERNACIONAL DA UNIVERSIDADE DE SANTIAGO DE COMPOSTELA

PROGRAMA DE DOUTORAMENTO EN FÍSICA NUCLEAR E DE PARTÍCULAS

SANTIAGO DE COMPOSTELA

2020

USC
UNIVERSIDADE
DE SANTIAGO
DE COMPOSTELA

DECLARACIÓN DEL AUTOR/A DE LA TESIS

D./Dña. Francisco Pedreira Giralda

Título da tese: Ultra-high-energy neutrino search with the Pierre Auger Observatory in the era of Gravitational Wave astronomy

Presento mi tesis, siguiendo el procedimiento adecuado al Reglamento y declaro que:

1) La tesis abarca los resultados de la elaboración de mi trabajo.
2) De ser el caso, en la tesis se hace referencia a las colaboraciones que tuvo este trabajo.
3) Confirmo que la tesis no incurre en ningún tipo de plagio de otros autores ni de trabajos presentados por mí para la obtención de otros títulos.

Y me comprometo a presentar el Compromiso Documental de Supervisión en el caso que el original no esté depositado en la Escuela.

En Santiago de Compostela, 21 de diciembre de 2020.

Firma electrónica

USC
UNIVERSIDADE
DE SANTIAGO
DE COMPOSTELA

AUTORIZACIÓN DO DIRECTOR / TITOR DA TESE

ULTRA-HIGH-ENERGY NEUTRINO SEARCH WITH THE PIERRE AUGER OBSERVATORY IN THE ERA OF GRAVITATIONAL WAVE ASTRONOMY

D. Jaime Álvarez Muñiz
D. Enrique Zas Arregui

INFORMAN:

Que a presente tese, correspóndese co traballo realizado por D. Francisco Pedreira Giralda, baixo a miña dirección, e autorizo a súa presentación, considerando que reúne os requisitos esixidos no Regulamento de Estudos de Doutoramento da USC, e que como director desta non incorre nas causas de abstención establecidas na Lei 40/2015.

De acordo co indicado no Regulamento de Estudos de Doutoramento, declara tamén que a presente tese de doutoramento é idónea para ser defendida en base á modalidade de Monográfica con reproducción de publicaciones, nos que a participación do doutorando foi decisiva para a súa elaboración e as publicacións se axustan ao Plan de Investigación.

En Santiago, 16 de Marzo de 2021

USC
UNIVERSIDADE
DE SANTIAGO
DE COMPOSTELA

Publicacións con contidos incluídos nesta tese

Esta tese está baseada en parte nas seguintes publicacións da Colaboración Pierre Auger nas cales declaro que fixen significativas contribucións. Para todas as publicacións, o único contido empregado nesta tese é exclusivamente a miña contribución realizada en ditas publicacións.

- A. Aab *et al.* [Pierre Auger Collaboration],
  Ultrahigh-energy neutrino follow-up of gravitational wave events GW150914 and GW151226 with the Pierre Auger Observatory,
  Physical Review D **94** (2016) 122007.

  Factor de impacto en 2016: 4.804.
  Contido reproducido na Sección 4.4.1.
  DOI:10.1103/PhysRevD.94.122007.

- A. Albert *et al.* [ANTARES, IceCube, Pierre Auger and LIGO/Virgo Collaborations],
  Search for high-energy neutrinos from binary neutron star merger GW170817 with ANTARES, IceCube and the Pierre Auger Observatory,
  Astrophysical Journal Letters **850** (2017) L35.

  Factor de impacto en 2017: 6.452.
  Contido reproducido na Sección 4.4.2.
  DOI: 10.3847/2041-8213/aa9aed.

- A. Aab *et al.* [Pierre Auger Collaboration],
  Probing the origin of ultra-high-energy cosmic rays with neutrinos in the EeV energy range using the Pierre Auger Observatory,
  Journal of Cosmology and Astroparticle Physics **10** (2019) 022.

  Factor de impacto en 2019: 3.158.
  Contido reproducido nas Seccións 3.1, 3.2 e 3.3.
  DOI:10.1088/1475-7516/2019/10/022.

- A. Aab *et al.* [Pierre Auger Collaboration],
  Limits on point-like sources of ultra-high-energy neutrinos with the Pierre Auger Observatory,
  Journal of Cosmology and Astroparticle Physics **11** (2019) 004.

  Factor de impacto en 2019: 3.158.
  Contido reproducido na Sección 3.4.
  DOI: 10.1088/1475-7516/2019/11/004.

USC
UNIVERSIDADE
DE SANTIAGO
DE COMPOSTELA

Autorización das revistas

As tres revistas nas que publiquei artigos científicos autorizan a utilización dos contidos dos artigos publicados na tese dos autores. A continuación indico o texto íntegro onde indica iso, xunto co enlace onde se pode comprobar dita información.

- Physical Review D:

  (https://journals.aps.org/copyrightFAQ.html)

  As the author of an APS-published article, may I include my article or a portion of my article in my thesis or dissertation?

  Yes, the author has the right to use the article or a portion of the article in a thesis or dissertation without requesting permission from APS, provided the bibliographic citation and the APS copyright credit line are given on the appropriate pages.

- Astrophysical Journal Letters:

  (https://publishingsupport.iopscience.iop.org/permissions-faqs)

  Do I need to get permission to reuse original figure(s)/text from an article published under a CC BY licence?

  No. Anyone may reuse any original content, such as figures or text, from gold open access CC BY articles in any way they wish, so long as they include attribution to the author(s), the journal citation and notice of the CC BY licence. For full licence terms and attribution requirements, please refer to the CC BY licence on the Creative Commons website.

  Please note that you will need to obtain the permission of the copyright owner(s) to reuse any third party material included within the article as this may not be subject to the CC BY licence.

- Journal of Cosmology and Astroparticle Physics:

  (https://publishingsupport.iopscience.iop.org/permissions-faqs)

  May I include the Final Published Version of the article in my research thesis or dissertation?

  Upon transfer of copyright, IOP and/or the copyright owner grants back to authors a number of rights. These include the right to include the Final Published Version of the article in your research thesis or dissertation. Please include citation details and, for online use, a link to the Version of Record. IOP's permission will be required for commercial use of an article published as part of your thesis. IOP does not allow ProQuest to publish or sell the article as part of your dissertation.

USC
UNIVERSIDADE
DE SANTIAGO
DE COMPOSTELA

A mi familia y amigos

USC
UNIVERSIDADE
DE SANTIAGO
DE COMPOSTELA

Agradecimientos

La realización de esta tesis ha sido un largo recorrido, por lo que me gustaría agraceder a todas las personas que me han ayudado de una forma u otra a concluírla con éxito. En primer lugar me gustaría mostrar un profundo agradecimiento a mis directores de tesis, Jaime y Enrique, ya no solo por enseñarme tanto de física durante estos años, sino también por su apoyo y paciencia para que esta tesis llegase a buen puerto.

También quiero darle a gracias a toda la gente del Departamento de Física de Partículas y de la Facultad de Física que me ha facilitado y ayudado para cualquier problema que se me ha podido presentar durante la realización de esta tesis (profesores, secretarias, ...), sin olvidarme de mis compañeros tanto de mi despacho como de otros despachos.

I want to give thanks to all the members of the Pierre Auger Collaboration with whom I have worked at some point, specially the Wuppertal group. Thank you for the nice reception there and all the physics and computer knowledge that you teach me. Michael, it has been great working with you.

Por último, no me puedo olvidar de mi familia y amigos que han estado ahí apoyándome y seguirán ahí en el futuro, especialmente a mis padres ya que sin ellos todo esto no podría haber tenido lugar.

Muchas gracias a todos.

USC
UNIVERSIDADE
DE SANTIAGO
DE COMPOSTELA

Francisco Pedreira Giralda

Resumo

Esta tese está enfocada na busca de neutrinos de ultra alta enerxía (UHE neutrinos, polas súas iniciais en inglés) con enerxías por enriba de 10^{17} eV co Observatorio Pierre Auger. Este observatorio foi deseñado para detectar fervenzas de partículas producidas por raios cósmicos de ultra altas enerxías cando chegan á atmosfera. Buscando fervenzas moi inclinadas de certas características pode tamén detectar neutrinos. A tese ten varias partes, no Capítulo 2 detállase o procedemento empregado para seleccionar fervenzas de partículas inclinadas cos datos do Observatorio e buscar entre elas as producidas por neutrinos. A súa efectividade estúdase usando simulacións de fervenzas inclinadas producidas por neutrinos. O procedemento aplícase por vez primeira aos datos dende o 1 de Xaneiro do 2004 ata o 31 de Agosto do 2018 sen atopar ningún candidato a neutrino. No Capítulo 3 descríbese a área efectiva para fontes puntuais de UHE neutrinos para as principais canles de busca de neutrinos en función dos sabores de neutrinos e interaccións, das posicións das fontes e do instante e duración do fluxo de neutrinos. Tamén se describe o cálculo da exposición do detector para fontes difusas. Obtivéronse límites mellorados tanto para fontes difusas como para fontes puntuais con fluxos constantes no tempo. O Capítulo 4 trata da busca dos UHE neutrinos correlacionados cos eventos detectados por ondas gravitacionais cos interferómetros LIGO e Virgo, isto é, a busca de neutrinos en coincidencia con ditos eventos e o estudo das implicacións da ausencia de candidatos contribuíndo a un dos resultados máis relevantes do século: o nacemento da astronomía de multimensaxeiros grazas ao descubrimento da colisión de dúas estrelas de neutróns e ao estudo de todos os tipos de partículas e radiación xeradas pola explosión de raios gamma (GRB, polas súas iniciais en inglés) que se logrou identificar despois. Finalmente, faise un resumo das principais conclusións e resultados obtidos na tese.

A continuación imos detallar os contidos de cada capítulo. No primeiro capítulo poñemos en contexto esta tese, como nace a astronomía de multimensaxeiros grazas ao evento GW170817, no cal por primeira vez obsérvase o mesmo evento a través dunha gran parte do espectro electromagnético e como onda gravitacional. Tras isto, explicamos como se pode encadrar esta tese no marco do Observatorio Pierre Auger como detector de neutrinos. Tras unhas primeiras simulacións feitas a comezos de século, outras novas foron realizadas a comezos desta década. Aínda que estas últimas foron inicialmente analizadas, nesta tese completouse esta análise facendo un profundo estudo das mesmas, ademais dunha recompilación de toda a información da busca de UHE neutrinos que sirva como manual ao que poidan acudir futuros científicos onde estea toda a información detallada. Ademais de todo iso, na tese fíxose unha actualización dos límites de fluxos difusos e puntuais de UHE neutrinos, así como a busca de neutrinos en coincidencia con eventos astrofísicos transitorios.

A introdución continúa cunha sección sobre produción e detección de neutrinos e a súa conexión cos raios cósmicos, tanto dende o punto de vista da produción como da detección das fervenzas de neutrinos con detectores deseñados para detectar raios cósmicos. Faise unha explicación dos diferentes modelos e orixes de produción de UHE neutrinos e como

os raios cósmicos máis enerxéticos poden orixinalos, describindo cales son os factores que poden cambiar o resultado destes mecanismos. Por último, explícase concisamente a técnica grazas á que se poden detectar os neutrinos moi enerxéticos que chegan á Terra co Observatorio Pierre Auger. A idea básica é que cando un UHE neutrino ou un raio cósmico chega á Terra pode interactuar cun núcleo da atmosfera. Desta primeira interacción sae un chorro de partículas que inician unha reacción en cadea producindo unha fervenza de partículas. Serán estas partículas da fervenza as que cheguen á superficie terrestre para ser detectadas polas estacións do detector de superficie do Observatorio Pierre Auger. Unha análise posterior da información de varias estacións permitirá distinguir as fervenzas producidas por neutrinos das fervenzas de raios cósmicos.

No segundo capítulo comezamos describindo o detector de superficie do Observatorio Pierre Auger, este consta de 1660 estación con 12 toneladas de auga pura cada unha que emprega a radiación Cherenkov que emiten as partículas ao moverse dentro da auga para detectalas. Estas 1660 estacións están distribuídas nunha rede triangular cunha separación de 1500 m cubrindo unha área aproximada de 3000 km^2. A xigantesca cantidade de información obtida coas estacións fai imposible que se poida xestionar toda, polo tanto aplícanse unha serie de criterios para limitar a transmisión de información que só será gardada cando as estacións presentan un sinal moi grande ou moi prolongado no tempo. Ademais, vaise requirir que varias estacións relativamente próximas teñan sinal cunha diferenza de tempos consistentes coa velocidade da fervenza (practicamente a velocidade da luz).

Cabe destacar que o principal obxectivo do Observatorio Pierre Auger é a detección de raios cósmicos, polo que é destacable que tamén poidamos detectar UHE neutrinos que desenvolvan fervenzas de partículas na atmosfera empregando o detector de superficie. Para facer isto temos que ter claro como distinguir as fervenzas producidas por neutrinos das que producen os raios cósmicos. Cando un raio cósmico entra na atmosfera interactúa rapidamente cun núcleo da atmosfera, mentres que, dado que a probabilidade de interacción dos neutrinos é moitísimo menor, estes tenden a interactuar máis preto da superficie terrestre. Isto é clave, xa que se buscamos partículas que cheguen á Terra cun gran ángulo cenital hai unha clara diferenza. Para estes grandes ángulos a atmosfera é suficientemente grosa como para que a compoñente electromagnética das fervenzas producidas por raios cósmicos sexa completamente absorbida, chegando á Terra unicamente muóns. Pola contra, dado que os neutrinos de todos os sabores que veñen de enriba poden interactuar máis profundamente na atmosfera producindo as chamadas fervenzas "downward-going" (DG), esta compoñente electromagnética si que pode chegar á Terra e ser detectada polos detectores de superficie. Este método de busca de neutrinos está dividido na análise de datos en dúas diferentes canles en función do ángulo cenital coa finalidade de optimizar a análise: a denominada "downward-going high" (DGH) para ángulos entre $75^{\underline{o}}$ e $90^{\underline{o}}$ e a "downward-going low" (DGL) para ángulos entre $60^{\underline{o}}$ e $75^{\underline{o}}$. Ademais destas fervenzas, hai outra posible canle coa que se poden detectar neutrinos tau se consideramos un neutrino tau que pode interactuar producindo un leptón tau na cortiza da Terra que á súa vez saia á superficie e se desintegre na atmosfera, inducindo unha

fervenza "Earth-skimming" (ES) ascendente. Nesta tese estudaremos as canles DGH e ES.

Os datos son analizados e os eventos reconstrúense obtendo unha serie de variables, sobre as que se aplican unha serie de cortes en función da canle de estudo para seleccionar en primeiro lugar as fervenzas inclinadas e, tras isto, buscar mediante outras variables aquelas fervenzas nas que o sinal detectado nos tanques é parte da compoñente electromagnética das fervenzas, e polo tanto son fervenzas producidas preto da Terra e non nas capas altas da atmosfera. Na tese descríbense en detalle tanto todos estes cortes así como unhas condicións de calidade para que as estacións sexan aceptadas e asegurarnos así de que non hai detectores PMT que fallasen ou que o sinal dunha estación pertence efectivamente á fervenza e non ven dada por un muón accidental que coincidise en tempo coa mesma.

Tras a descrición de todo este procedemento analízanse as simulacións de neutrinos feitas previamente. O resultado de aplicar os diferentes cortes sobre estas simulacións arroxa resultados interesantes. Por un lado vese que a eficiencia dos cortes de neutrinos unha vez feita a selección de fervenzas inclinadas é moi boa. Por outra parte móstrase como os cortes feitos para obter estas fervenzas inclinadas non dan unha eficiencia máxima e polo tanto quizais poidan optimizarse no futuro para obter mellores límites. Ademais vese que a eficiencia dos cortes de selección depende da enerxía, aumentando coa enerxía para a canle ES, mentres que para a canle DGH a eficiencia é maior para enerxías máis baixas.

Na seguinte sección faise un estudo detallado do sinal que deixan tanto as fervenzas de neutrinos como as fervenzas producidas por raios cósmicos, ensinando varios gráficos. O obxectivo desta sección é profundar na comprensión das características diferenciais das fervenzas de neutrinos no detector de superficie do Observatorio Pierre Auger. Para iso desenvolvemos unha ferramenta gráfica que permite ver moi rápida e intuitivamente o sinal e o tempo no que chega dito sinal en cada estación así como o patrón das estacións no detector de superficie para distintos eventos de neutrinos. Ademais, e para entender mellor o comportamento das fervenzas de neutrinos, fanse unha serie de gráficos resumo onde se mostra a dependencia das variables que discriminan as fervenzas de neutrinos en función da profundidade onde se produce a fervenza ou o ángulo co que incide o neutrino. Para rematar o Capítulo 2, descríbese o resultado da análise de todos os datos dende o 1 de Xaneiro do 2004 ata o 31 de Agosto do 2018 segundo todos os cortes explícitos anteriormente sen obter ningún candidato a neutrino.

O Capítulo 3 comeza calculando o corresponde límite ao fluxo difuso de UHE neutrinos que se pode establecer ao non obter ningún candidato. Descríbese en detalle tanto a fórmula física para obter dito límite como o procedemento informático para procesar toda a información durante os 14 anos de toma de datos. Como paso intermedio para obter o límite a fluxos difusos de UHE neutrinos calcúlase a exposición do Observatorio Pierre Auger, que queda descrita en función da canle de estudo, sabor do neutrino incidente e da enerxía. Finalmente obtense que o límite do Observatorio Pierre Auger a un fluxo tipo lei de potencias inversamente proporcional ao cadrado da enerxía, incluíndo todas as canles

de estudo, ven dado por unha constante: $k_{90} < 4.4 \times 10^{-9}$ GeV cm^{-2} s^{-1} sr^{-1}.

Os límites obtidos para límites difusos impoñen grandes restricións, resultando moi desfavorecidos os modelos que supoñen a aceleración de protóns unicamente nas fontes que emiten UHE raios cósmicos, así como aqueles modelos cunha evolución co factor de corremento ao vermello máis forte que a taxa de formación estelar, quedando os fluxos difusos preditos por modelos que supoñen unha composición mixta fóra do alcance da sensibilidade do Observatorio Pierre Auger. Este traballo é recollido nunha publicación da Colaboración.

Ademais do límite a fluxos difusos, dado que no Observatorio Pierre Auger tamén podemos buscar neutrinos nas diferentes direccións do espazo, podemos obter un límite a fluxos puntuais de UHE neutrinos. Como paso intermedio obtemos a área efectiva (definida como a área que, multiplicada polo fluxo dunha fonte puntual, dá como resultado o espectro de enerxía da taxa instantánea de eventos detectados). Esta área efectiva instantánea é representada como función da enerxía para as diferentes canles e ángulos. Ademais, desenvolveuse unha ferramenta para saber se en cada instante de tempo unha fonte puntual está no campo de visión do Observatorio Pierre Auger en calquera das canles de estudo dos UHE neutrinos. Tamén se mostra como existen direccións privilexiadas nas que a área efectiva é superior á doutros detectores de neutrinos, aínda que durante un tempo limitado. Con isto pódese obter a exposición media por día en función da declinación ou da enerxía para as diferentes canles, sendo dominante a canle ES. Finalmente, obtense o límite para fontes puntuais en función da declinación, resultado que se recolle noutra publicación.

No que respecta aos límites de fluxos puntuais, móstrase como estes son complementarias aos que outros experimentos de neutrino de enerxías por debaixo do rango de EeV como ANTARES ou IceCube. Ademais, o Observatorio Pierre Auger pode cubrir unha gran rexión da esfera celeste, chegando dende case o polo sur celeste ata declinacións próximas a 60°, alcanzando as máximas sensibilidades en 55° e −53° (as declinacións que pasan máis tempo no campo de visión do Observatorio Pierre Auger).

No Capítulo 4 detallamos a busca de UHE neutrinos en coincidencia cos eventos detectados en ondas gravitacionais nos interferómetros LIGO e Virgo. O 14 de Setembro de 2015 o detector LIGO observou por primeira vez unha onda gravitacional, as cales foran preditas en 1916 por Albert Einstein. Esta primeira onda gravitacional foi causada pola colisión de dous buratos negros. Ao ser o primeiro caso non había nada previamente estudado sobre como proceder para o seguimento en UHE neutrinos das ondas gravitacionais no Observatorio Pierre Auger. Decidimos realizar un cálculo da área efectiva en intervalos de tempo prefixados seguindo o mesmo proceso que no estudo xeral de neutrinos, deixando aberta a posibilidade de optimización do procedemento no futuro. Desta forma definimos o proceso de busca de neutrinos tras a detección dun evento de coalescencia de dous buratos negros. Inicialmente este proceso facíase á man xa que tardábamos uns días en obter os datos do Observatorio Pierre Auger, pero a partir de Xullo do 2019 faise de xeito automático nos ordenadores de Auger en Malargüe (Arxentina) de modo que en menos de 15 minutos sabemos se hai algún candidato a UHE neutrino na fiestra de ±500 s ao redor

do intre de detección da onda gravitacional por LIGO e Virgo. Tras unha análise posterior obtense un límite ao fluxo de UHE neutrinos para cada onda gravitacional alertada por LIGO e Virgo.

Durante os tres períodos de busca de ondas gravitacionais de LIGO e Virgo (períodos O1, O2 e O3) detectáronse un total de 62 ondas gravitacionais. A maior parte delas foron colisións de dous buratos negros, pero tamén hai varias colisións de dúas estrelas de neutróns, candidatos á colisión dunha estrela de neutróns e un burato negro e uns poucos MassGap (os eventos así clasificados son aqueles nos que ao menos unha das masas é demasiado grande para ser unha estrela de neutróns e demasiado pequena como para ser un burato negro). O período de busca de UHE neutrinos en coincidencia coas ondas gravitacionais varía en función da súa orixe. Algúns modelos físicos internacionalmente aceptados indican que, ademais da posible emisión de UHE neutrinos producido no momento da colisión (a cal se busca no período $\pm$500 s), se coliden dúas estrelas de neutróns pode haber unha posible emisión posterior de UHE neutrinos, o cal fai que se analicen os datos ata 14 días despois da detección da onda gravitacional. Pola contra, se son dous buratos negros os que colisionan só se buscan UHE neutrinos ata un día despois da detección.

Neste capítulo amósanse os resultados da busca de UHE neutrinos co Observatorio Pierre Auger para unha serie de ondas gravitacionais detectadas por LIGO e Virgo. É bo sinalar que durante o período ao redor de case todas as detección de ondas gravitacionais o detector de superficie está moi estable o cal permite obter un bo límite para os fluxos de UHE neutrinos.

Un punto a parte merece o evento GW170817, esta onda gravitacional non só foi a primeira detectada con orixe na colisión de dúas estrelas de neutróns, senón que marcou o inicio da astronomía de multimensaxeiros. Ademais da detección da onda gravitacional por LIGO e Virgo, os satélites de raios gamma Fermi e INTEGRAL detectaron un curto GRB orixinado nunha dirección do espazo compatible co contorno de orixe da onda gravitacional menos de 2 segundos despois da detección da onda gravitacional. Isto non foi todo, nesa mesma dirección pouco despois detectouse emisión electromagnética en moitos rangos de lonxitude de onda (luz visible, infravermella, ultravioleta, radio, raios-X, ...). Loxicamente tamén se buscaron neutrinos en coincidencia con dito evento co Observatorio Pierre Auger e outros, máis non se atopou ningún candidato compatible con esa dirección.

Este evento puxo en relevancia o papel do Observatorio Pierre Auger como detector de UHE neutrinos. No intre da colisión das estrelas de neutróns, a dirección do evento estaba exactamente no campo de visión dos neutrinos ES, que é a canle máis eficiente para a busca de neutrinos. Grazas a iso, o límite obtido no período $\pm$500 s arredor da detección da onda gravitacional é realmente competitivo, sendo significativamente superior ao obtido por IceCube, o cal é un experimento dedicado á busca de neutrinos de alta enerxía. Tras o paso dos días, no límite a 14 días, nótase o efecto da gran direccionalidade do Observatorio para detectar neutrinos. A rexión do ceo que observa IceCube, a ve todo o tempo (24 h por día), mentres que a rexión accesible para o Observatorio Pierre Auger vai variando durante cada día a medida que a Terra rota. No límite a 14 días o resultado obtido

co Observatorio Pierre Auger pasa a ser comparable ao de IceCube. O Observatorio é competitivo, complementando perfectamente entre ANTARES, IceCube e o Observatorio Pierre Auger todo o rango de enerxías dende 10^{11} eV ata 10^{20} eV.

Finalmente, no último capítulo da tese preséntanse as conclusións. Hai dous tipos de conclusións, as relacionadas con aspectos técnicos da busca de UHE neutrinos no Observatorio Pierre Auger e as relativas a resultados físicos que se conclúen da análise dos datos realizada.

As primeiras delas pódense resumir basicamente en que se recompilou todo o traballo previo feito na busca de UHE neutrinos nas canles DGH e ES no Observatorio Pierre Auger, explicándose detalladamente todos os pasos realizados, e facendo unha análise profunda das simulacións feitas previamente. Todo este traballo fai que sexa moito máis sinxelo para futuros proxectos unha posible mellora e optimización do procedemento de selección coa intención de obter mellores límites aos fluxos de UHE neutrinos co Observatorio Pierre Auger. Ademais disto, durante o desenvolvemento desta tese tamén se logrou definir un protocolo para implementar de xeito automático nos ordenadores de Auger e facer o seguimento en UHE neutrinos de eventos astrofísicos singulares como os detectados con ondas gravitacionais.

Por outra banda, desta tese conclúense unha gran cantidade de resultados físicos relevantes. En primeiro lugar, analizáronse novos datos do Observatorio Pierre Auger, ata o 31 de Agosto do 2018, sen atopar candidatos a UHE neutrinos, obtendo novos límites a fluxos difusos e puntuais, resultando límites competitivos cos obtidos por experimentos dedicados a UHE neutrinos como IceCube a enerxías arredor de 10^{18} eV, e ademais, complementando os rangos de enerxías analizados perfectamente con outros experimentos. Os límites obtidos para límites difusos impoñen grandes restricións, resultando moi desfavorecidos os modelos que supoñen a aceleración de protóns unicamente nas fontes que emiten UHE raios cósmicos, así como aqueles modelos cunha evolución co factor de corremento ao vermello máis forte que a taxa de formación estelar. No que respecta aos límites de fluxos puntuais tamén cabe destacar que o Observatorio Pierre Auger pode cubrir unha gran rexión da esfera celeste, chegando dende case o polo sur celeste ata declinacións próximas a 60°. Ademais, o detector de superficie do Observatorio Pierre Auger presenta unha sensibilidade incomparable aos outros experimentos de neutrinos para potenciais fontes de EeV neutrinos cunha dirección que apunte ao hemisferio norte terrestre.

Con respecto a fontes transitorias de UHE neutrinos, a sensibilidade do Observatorio Pierre Auger é altamente dependente da posición da fonte no momento da emisión, o cal queda claramente exemplificado na GW170817. Se no momento da emisión a fonte se atopa xusto por debaixo do horizonte o límite obtido polo Observatorio Pierre Auger é excepcionalmente bo. Para declinacións de 55° e $-53°$ a eficiencia integrada nun tempo curto (da orde de 4 h) é máxima, moi superior a outros detectores de neutrinos.

Ademais, fixéronse por primeira vez seguimentos en UHE neutrinos de ondas gravitacionais, sen atopar candidatos, pero poñendo importantes límites para a enerxía emitida en neutrinos nos eventos producidos por colisións de dous buratos negros. Similares análises

tampouco deron ningún candidato nas colisións de dúas estrelas de neutróns, sendo no caso particular da GW170817 compatible coa observación dun GRB de curta duración fóra do eixo de emisión.

Finalmente, durante o desenvolvemento desta tese unha nova era da astronomía de multimensaxeiros comezou. Os resultados desenrolados nesta tese mostran que o Observatorio Pierre Auger é un experimento clave nesta nova maneira de facer astronomía, coas súas capacidades e sensibilidade para buscar neutrinos no rango EeV en correlación coa detección de fontes de neutrinos de enerxía TeV-PeV, de raios gamma de alta enerxía e/ou fontes de ondas gravitacionais.

USC
UNIVERSIDADE
DE SANTIAGO
DE COMPOSTELA

INDEX

1

Introduction

Astroparticle physics is nowadays experiencing an outstanding development. Since the discovery of gravitational waves in 2015, Astroparticle physics along with conventional Astronomy have merged to give birth to the so-called Multimessenger astronomy, which is rapidly developing and expanding. The aim is to observe astrophysical phenomena coordinating diverse experiments which detect different types of particles or radiation generically addressed as "cosmic messengers". The term now embraces: gravitational waves, electromagnetic radiation (from radio to γ-ray wavelength), neutrinos and cosmic rays.

Astronomy implies directionality, the messengers must travel straight to point to their sources. Charged cosmic rays are deflected by intervening magnetic fields and only the largest observed energies of order 10^{20} eV can be expected to allow the inference of the source position with limited precision due to small deviations. Gravitational waves provide a new means to observe the Universe but the technical challenge is huge and the source location is still limited to very large areas in the sky because of low angular resolution. Gamma rays are absorbed by intervening material or pair produce on photon backgrounds prevalent throughout the Universe. Neutrinos are neutral and only interact via the weak force. They travel through large matter depths and may be the only messenger that brings Ultra-High-Energy (UHE) particles from cosmological distances. The counterpoint of neutrinos is that they only interact weakly with matter and are extremely difficult to detect, being necessary vast extensions of interacting material to build neutrino detectors.

In this thesis we focus on the search of UHE neutrinos with energies above 10^{17} eV with the Pierre Auger Observatory, most efficiently close to $\sim 10^{18}$ eV. This observatory was conceived the largest and most precise installation to measure cosmic rays above

$\sim 10^{16}$ eV. In this first Chapter we give a brief introduction to the beginning of multimessenger astronomy and we also review neutrino production and their interactions paying special attention to their relation to cosmic ray both at production and detection level. In Chapter 2 we present an overview of the Pierre Auger Observatory with particular emphasis on its Surface Detector (SD), the neutrino selection criteria and the expected characteristics of neutrino-induced showers in the SD. In Chapter 3 we present the results of the search for diffuse and point-like fluxes of UHE neutrinos and present upper limits to these fluxes. Finally, Chapter 4 is dedicated to the follow-up in UHEν of the gravitational-wave events detected by LIGO and Virgo.

1.1 The birth of Multimessenger Astronomy

Until the second half of the twentieth century, our knowledge of the Universe was only based on observations of the electromagnetic radiation, using optical photons extended to the near infrared through photography. Tecnological improvements gave us access to other wavelengths. For example, after the Second World War the development of the radar techniques allowed the opening of the radio window, achieving the discovery of the Cosmic Microwave Background, quasars and pulsars. In the 1960s and 1970s most of the electromagnetic spectrum (full infrared, ultraviolet, X-ray and γ photons) was studied with the detectors that were sent above the atmosphere. The combined information obtained about astrophysical objects, covering a large fraction of the electromagnetic spectrum, is denoted as multiwavelength astronomy and has brought along many complementary discoveries to astronomy and astrophysics [1].

This was only the beginning. In the last decades new detectors have greatly enhanced the sensitivity in all bands from radio to gamma rays, with more precise instruments such as the FERMI LAT telescope for γ-rays up to the TeV regime. Moreover, the techniques developed for the study of cosmic rays made it possible in the 90's to detect γ-rays from the ground at the TeV scale, a technique that is now routine, with arcminute resolution from 50 GeV into the PeV band. Cosmic rays are measured with precision at energies in excess of 100 EeV. The detection of the first astrophysical neutrinos, born with the solar neutrino experiments in the 60's and stimulated with the detection of neutrinos from the supernova 1987A, have led to the recent discovery of neutrinos in TeV to 10 PeV range in 2013 with the IceCube detector in the South Pole [2]. An alternative telescope in the Mediterranean Sea, ANTARES, is being developed to complement IceCube. Cosmic rays with GeV energy were measured in 1910s, but we have to wait until 1960s to the construction of large detectors that could measure cosmic rays with higher energy, of extragalactic origin at UHE. Only in the last decade the investigation of the spectrum, arrival directions and composition of UHECR in the 10^{18}-10^{20} eV energy range has reached enough precision to allow the study of anisotropies [3], while the detection of UHEν and UHEγ-rays awaits discovery.

Finally, in 2015 the first gravitational waves (GW) were detected by LIGO [4]. This

was a break through after many decades of fabulous technological advances. It led to the discovery of Black Hole binary sistems that merge into a single one. We can now observe and study the Universe using the four fundamental forces in Nature (electromagnetic force - photons, gravitational force - GW, weak nuclear force - neutrinos and strong nuclear force - cosmic rays).

All this converged at the most impressive episode that gave birth multimessenger astronomy on August 17, 2017. At 12:41:20 UTC the Fermi γ-ray satellite sent a trigger alert through a GCN notice[1]. A total of 3 automatic messages were sent by Fermi with the detailed information of the trigger alert, which was detected at 12:41:06 UTC. After receiving this GCN message, LIGO checked their data and they realised that just 2 seconds before the Fermi trigger, at 12:41:04 UTC a signal was detected in both Livingston and Hanford detectors. The reason why LIGO did not sent the automatic trigger alert was that one of their detectors (Livingston) suffered a short instrumental noise transient 1.1 s before the coalescence time, making the automatic analysis discard the data. At 13:21:42 UTC, after a manual analysis, LIGO sent a GCN circular where they noticed that a binary neutron star merger candidate had been identificated and it is associated with the time of the Fermi trigger. Finally, at 13:47:37 UTC, LIGO sent another GNC circular where they reported that the trigger time of Fermi is approximately 2 seconds after the LIGO trigger.

This joint detection of a gravitational wave (named GW170817) and GRB (named GRB170817A) was followed up by the most extensive observation operation ever performed up to date, employing space- and ground-based telescopes (also neutrino detectors) to scan the region of the sky where the event was detected. Less than 12 h after the GW/GRB event, a new point-like optical source was detected by optical telescopes in the galaxy NGC 4993 at a distance of ~ 40 Mpc from Earth. The official designation of the optical counterpart in the International Astronomical Union (IAU) was AT 2017gfo. That source was exhaustively analyzed in the following weeks by all traditional telescopes from radio to X-rays. As a summary, a very relevant joint paper was published on October 20, 2017. The paper describes the multimessenger observations, which was co-authored by almost 4000 physicists from more than 900 institutions, using 70 different observatories on all continents and in space, marking the birth of multimessenger astronomy [6]. It has reached more than 1700 citations.

Fig. 1.1 shows the combined information obtained with each messenger. The solid circles represent the observations in each band, while the solid horizontal lines show when the source was visible by at least one telescope after the LIGO trigger. On the other hand, the vertical dashes show the time when information was reported in a circular of the GCN.

This multimessenger event was also followed up by the dedicated high-energy and ultra-high-energy neutrino detectors, ANTARES and IceCube. Notably the Pierre Auger Observatory can also search for neutrinos in the UHE range. No candidate was found to be

[1]Gamma-Ray Coordinate Network [5].

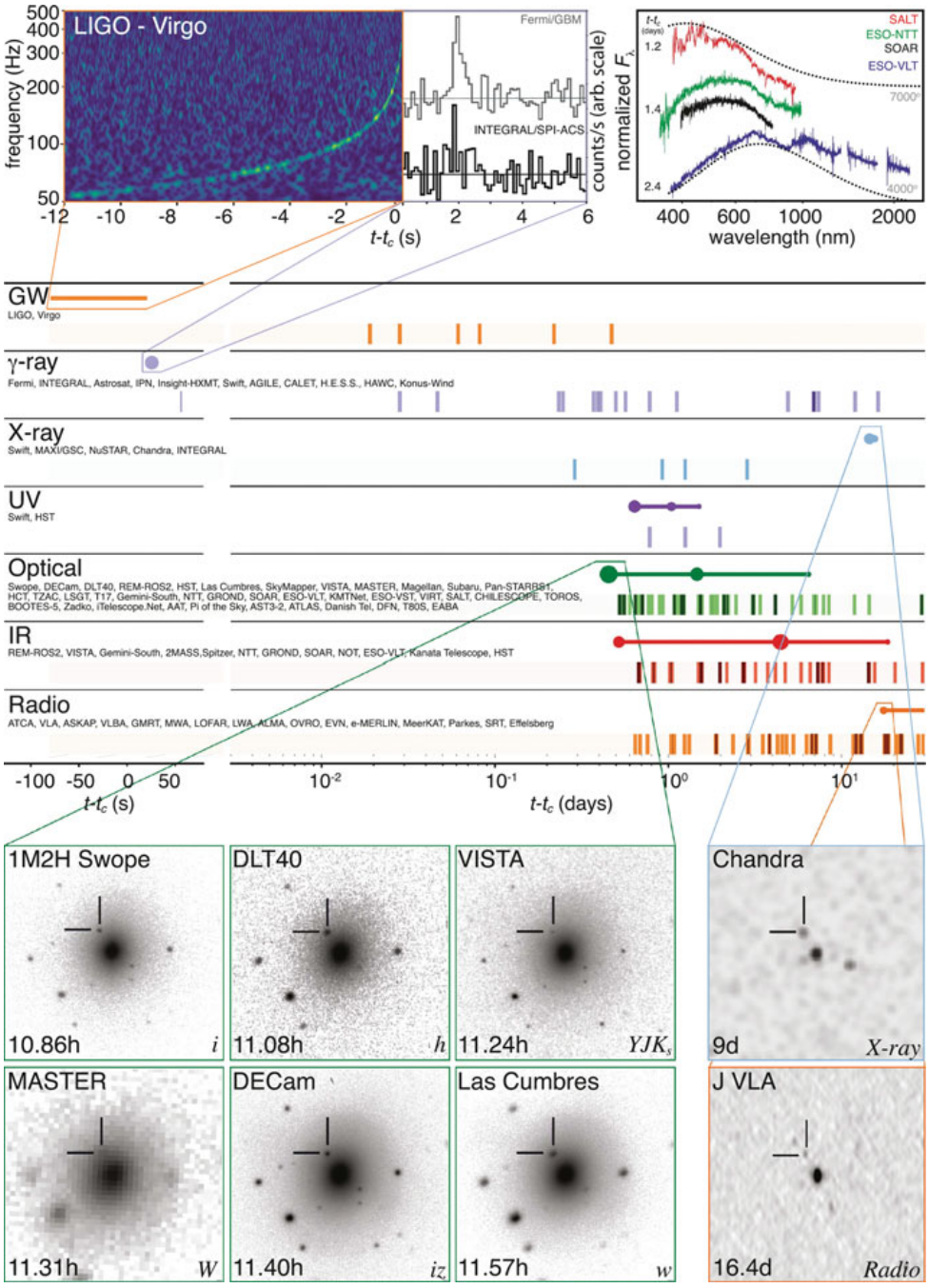

Figure 1.1: Timeline of the discovery of GW170817, GRB 170817A, AT 2017gfo. All the follow-up observations are shown by messenger and wavelength relative to the time t_c of the gravitational-wave event. The name of the more relevant experiments are at the beginning of each row. The solid circles represent the observations in each messenger, while the solid horizontal lines show when the source was visible by at least one telescope. The vertical dashes show the time when information was reported in a circular of the GCN [6].

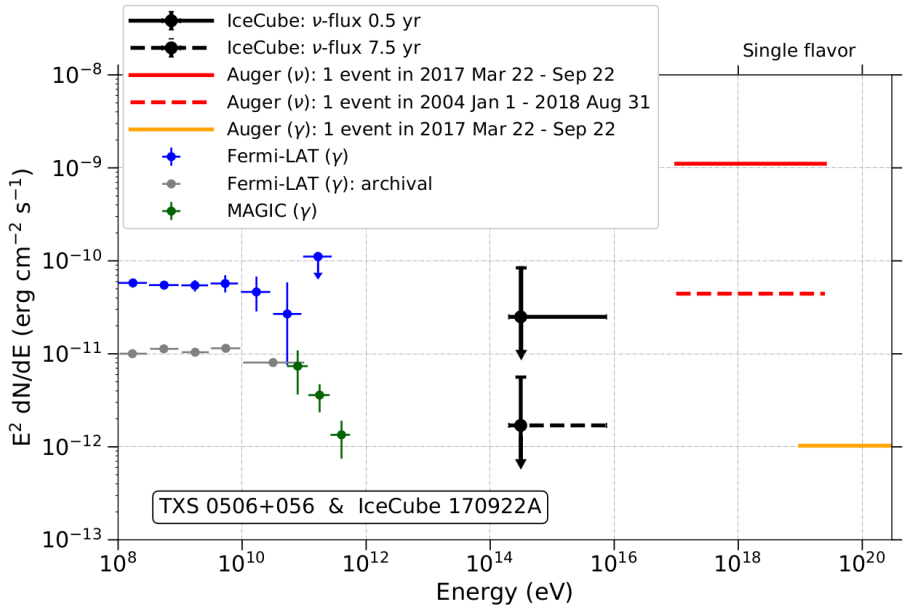

Figure 1.2: Solid red and black lines: UHE flux reference that would give one expected neutrino event at the Pierre Auger Observatory (red line) [8] over a period of six months for a spectrum $dN/dE \propto E^{-2}$ in comparison to the flux that would produce on average one detection like the IceCube-170922A event over the same period (black line). Dashed red and black lines: Flux references for the Pierre Auger Observatory for a period of 15 years (red line) and for a period of 7.5 years for IceCube (black line) [7]. Yellow line and dots: UHE photon flux from the direction of the blazar that would give one expected photon event in six months at the Pierre Auger Observatory (yellow line) in comparison with the average photon fluxes measured with Fermi, and MAGIC during a period of two weeks [7], and the archival photon measurement from Fermi [9].

directionally coincident with the source with any of these three neutrino telescopes. The results of the analysis of the Pierre Auger data are detailed in Chapter 4. They illustrate the enormous potential and complementarity that the Pierre Auger Observatory has to measure UHE neutrinos. This topic will be addressed throughout this thesis.

The example of GW170817/GRB170817A/AT2017gfo demonstrated that observation in different multimessengers may not just be regarded as a mere advantage; it should be considered as a priority, a necessary appreach required to address some of the most outstanding and challenging issues in astrophysics.

Indeed, other multimessenger events have been analyzed since GW170817. A recent example is that of the blazar TXS 0506+056, which was detected in high-energy neutrinos and gamma rays with IceCube, Fermi-LAT, MAGIC and other detectors of electromagnetic radiation in several bands [7]. This source was also followed-up in UHE neutrinos with the Pierre Auger Observatory, without finding any UHE neutrino candidate [8].

Fig. 1.2 shows the UHE neutrino flux reference that would give one expected neutrino event at the Pierre Auger Observatory over different periods for a spectrum $dN/dE \propto E^{-2}$ in comparison with IceCube. These results rely on the results described in this thesis but are not addressed further in this work[2].

The Pierre Auger Observatory has a prominent role in Multimessenger Astronomy [10], especially due to its sensitivity to UHE neutrinos. This thesis represents a contribution to the development of this fascinating and emerging field.

1.2 The Pierre Auger Observatory as a neutrino detector

In 1975 Berezinskii and Smirnov proposed that UHE neutrinos could be detected by the extensive air showers produced by the interaction of a neutrino with an nucleus of the atmosphere at large zenith angle [11]. This idea was picked up by the group of the University of Santiago de Compostela in the 90's and they proposed the search for neutrinos using inclined showers in the Pierre Auger Observatory before the construction of the observatory had begun [12].

It was in the beginning of the next decade when the Paris' group proposed the search of tau neutrinos via Earth-skimming interactions, which proved to be potentially more efficient than searching for downward-going inclined showers [13]. In these years, when IceCube was under construction, scientists thought that the discovery of UHE neutrinos was really close. Under this context it is understandable that the priority for the simulations and results was speed but not perfection, especially considering that the $\overline{\text{Off}}\underline{\text{line}}$ (the official simulation and reconstruction software of the Pierre Auger Collaboration) was not completely developed when simulations were done. This work finished with the publication of two papers with the first limit on the diffuse flux of UHE tau neutrinos from the Pierre Auger Observatory in 2008 and 2009 [14, 15].

After this speed run, the first simulations with the $\overline{\text{Off}}\underline{\text{line}}$ were performed, including also the analysis of downward-going inclined showers. The work was mainly done by four PhD students [16–19], two of them directed in Santiago de Compostela, that finished their thesis between 2011 and 2015. Several papers were published during these years about downward-going neutrinos, the search for point-like sources and, finally, a limit to the diffuse flux combining downward-going and Earth-skimming neutrinos [20–22].

My thesis fits within all this background. My work was to analyze in detail the simulations made in the last years to gain insight into the characteristics of neutrino-induced showers in the Surface Detector of the Pierre Auger Observatory, and also to compile and systematize the unblinding neutrino search process to make it possible to improve both the simulations and data analysis in the future. Moreover, updates to the

[2]The UHE γ-ray flux that would give 1 event in Auger is also plotted along with γ-ray fluxes at energies $\lesssim$ TeV detected by Fermi and MAGIC is also shown for completitude.

limits to the diffuse and point-like fluxes of neutrinos with new data were performed [23–25], and also neutrinos were searched in coincidence with transient astrophysical events [8, 26, 27].

An important result that will be detailed along this thesis is that the Pierre Auger Observatory is as good as IceCube for detecting neutrino energies larger than $\sim 10^{18}$ eV, so if in the future it is possible to improve the efficiency with better selection criteria it would be possible to overtake IceCube at these energies.

1.3 Cosmic rays

Cosmic rays (CRs) are very energetic particles (mostly charged) that reach the Earth from Galactic and extragalactic sources. CRs are mainly protons, but also heavier nuclei. When a CR arrive at the top of Earth's atmosphere, it interacts with an atmospheric nucleus and a particle shower develops in the atmosphere. Cosmic rays with energies larger than $\sim 10^{18}$ eV are known as ultra-high-energy cosmic rays (UHECRs) and the Pierre Auger Observatory is the biggest and most precise experiment designed to detect them (see Chapter 2).

Fig. 1.3 shows the all-particle cosmic rays energy spectrum using Pierre Auger Observatory data from $E \sim 10^{17.5}$ eV to $E \sim 10^{20}$ eV. The flux decreases following a series of power law ($E^{-\alpha}$):

$$\frac{dN}{dE} \propto E^{-\alpha}, \tag{1.1}$$

with the spectral index α suffering some changes among the several orders of magnitude in energy (see Fig. 1.3), presumably due to the different CR sources (Galactic or extragalactic origin) and propagation effects [28].

A cutoff was predicted in 1966 by Greisen [29] in the United States, and Zatsepin and Kuzmin in Russia [30] (GZK mechanism) after the discovery of the Cosmic Microwave Background (CMB). They calculated the energy lost by CR due to the interactions with the CMB and they realised that the amount of energy dissipated increases with the energy of the CR and it is so extreme that it imposes an upper limit to the energy of the cosmic rays when they come from very large distances exceeding ~ 100 Mpc.

The main reactions responsible for the loss of energy are:

1. Pair production:

$$p + \gamma_{\text{CMB}} \rightarrow p + e^+ + e^- \tag{1.2}$$

2. Photo-pion production:

$$\begin{aligned} p + \gamma_{\text{CMB}} &\rightarrow \Delta^+ \rightarrow p + \pi^0 \\ p + \gamma_{\text{CMB}} &\rightarrow \Delta^+ \rightarrow n + \pi^+ \end{aligned} \tag{1.3}$$

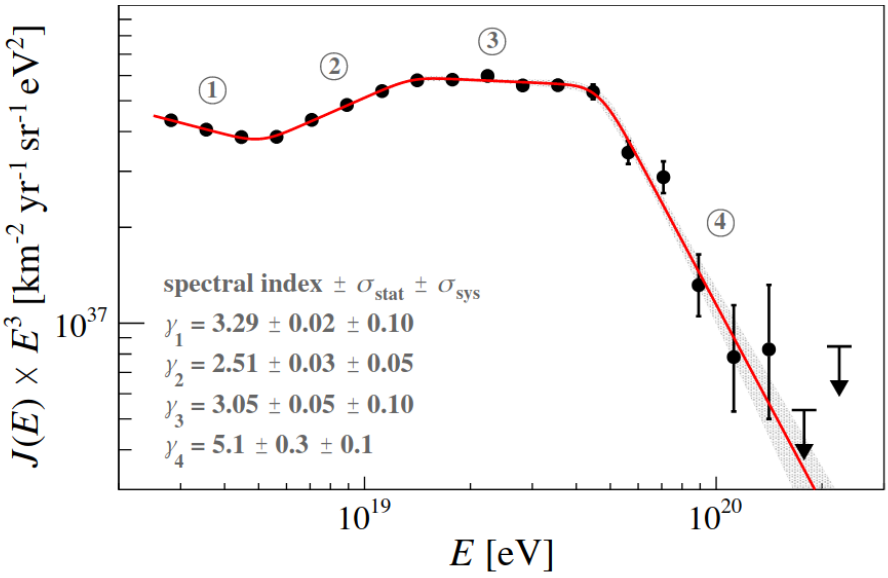

Figure 1.3: Combined energy spectrum measured at the Pierre Auger Observatory, with the flux multiplied by E^3, fitted with a sequence of four power laws (red line). The numbers ($i = 1, 2, 3, 4$) enclosed in the circles identify the energy intervals where the spectrum is described by a power law with spectral index γ_i without cutoff. Upper limits for higher energies are at the 90% confidence level [31, 32].

3. Photo-disintegration reaction:

$$\begin{aligned}(A, Z) + \gamma_{\text{CMB}} &\rightarrow (A-1, Z-1) + p \\ (A, Z) + \gamma_{\text{CMB}} &\rightarrow (A-1, Z) + n\end{aligned} \tag{1.4}$$

The GZK cutoff implies that if we observe nucleons with energy greater than $5{\cdot}10^{19}$ eV, they should be coming from extragalactic sources not farther than distances of order a hundred Mpc. The mechanism at the same time give us confidence that the observation of UHECRs must imply the production of UHE neutrinos through the desintegration of pions and neutrons. These reactions can also happen in the sources that produce the cosmic rays which are not yet identified. In summary the existence of cosmic rays in the 10^{20} eV energy range, a confirmed fact, makes us expect fluxes of UHE neutrinos.

1.4 Overview of neutrino flux expectations: Neutrino models

Neutrinos are very relevant in cosmology and astrophysics because they are very efficient in cooling of dense regions. They take part in many processes like the Big Bang, neutron star cooling, core-collapse supernovae, stellar reactions chains and are expected

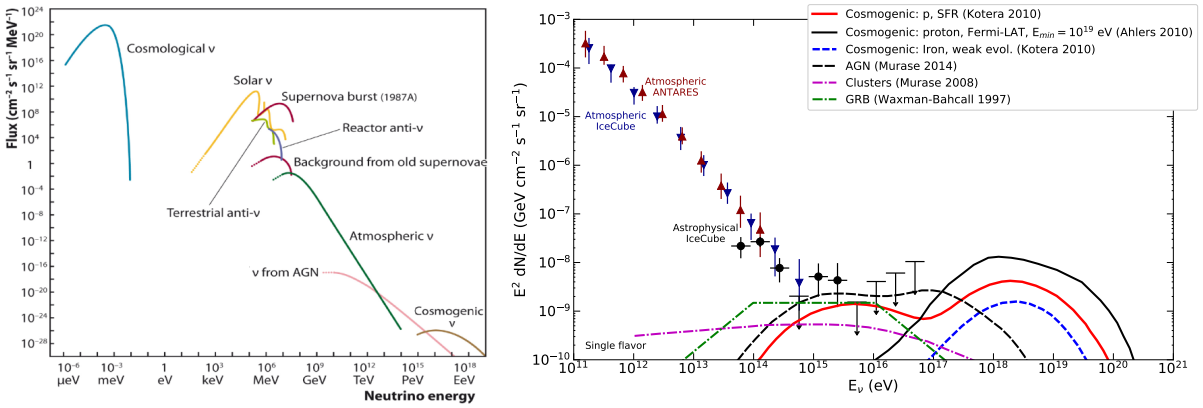

(a) All neutrino fluxes.

(b) HE and UHE neutrino fluxes.

Figure 1.4: Left: Neutrino fluxes of different sources, both of terrestial and cosmic origin [34]. Right: Fluxes of atmospheric, cosmogenic and astrophysical neutrinos. Fluxes are obtained from several experiments or different models.

to be produced along with the UHECRs in their sources [33]. Each one of these processes produces different neutrino spectra. Fig. 1.4a shows a compilation of neutrino spectra for different scenarios. The most abundant are cosmological neutrinos, a relic blackbody spectrum that originated in the Big Bang. The neutrino flux becomes smaller as the energy increases, falling by $\sim$ 50 orders of magnitude in $\sim$ 25 orders of magnitude in energy. An overall picture of the expected and measured neutrino flux with energy higher than 10^{11} eV is also shown in Fig. 1.4b. It displays the astmospheric neutrino flux measured by ANTARES and IceCube due to CR interactions in the atmosphere, and the first astrophysical fluxes in the 100 TeV to 10 PeV measured by IceCube. Several astrophysical fluxes obtained in different astrophysical scenarios are also shown for comparison.

1.4.1 Cosmogenic neutrinos

Cosmogenic neutrinos are produced by the GZK mechanism explained previously. The UHE charged pions produced through reactions such as Eq. (1.3) decay into UHE neutrinos:

$$\pi^+ \rightarrow \mu^+ + \nu_\mu \rightarrow e^+ + \nu_e + \overline{\nu}_\mu + \nu_\mu, \tag{1.5}$$

while neutrons produced in reactions such as Eqs. (1.3) and (1.4) produce also UHE neutrinos.

Proton-photon cross-section

The neutrino yield from the decay of the charged pion obtained in the photo-pion production of the GZK mechanism is determined by the proton-photon cross-section, $\sigma_{p\gamma}$.

The fraction of energy going into neutrinos is estimated from accelerator data [35]. The fraction of energy going into the charged pion from the primary proton is on average $x_{p\to\pi} \approx 0.2$ and after the pion decays, its energy is distributed equally between the four leptons, so on average each neutrino energy is about $\sim 0.05E_p$. In the photo-pion production as well as in the photo-desintegration processes the resulting neutron can decay producing electron neutrinos, but its energy is only about $\sim 4 \times 10^{-4}E_n$.

Neutrino oscillations

In the charged pion decay there are two muon neutrinos (either ν_μ or $\overline{\nu}_\mu$) for each neutrino electron in the final state. Due to neutrino oscillations over cosmological distances, the original cosmic neutrino fluxes with a $\nu_e : \nu_\mu : \nu_\tau$ ratio at the source of $1 : 2 : 0$ change to a ratio of $1 : 1 : 1$ at the Earth [36].

The exact flux of the cosmogenic neutrinos depends on many aspects so there are many different models assuming different conditions. The cosmogenic neutrino fluxes predicted by the models depend on the assumed:

1. UHECR composition.
2. Cosmological evolution of the sources with redshift.
3. UHECR energy spectrum and the maximum energy reached.
4. Cosmological model.

UHECR composition

The first predictions of the cosmogenic neutrino flux assumed pure protons for UHECR primaries. Pure ^{56}Fe, ^{4}He or ^{16}O and mixtures of these nuclei with protons as the primaries were taken into account in other cosmogenic neutrino fluxes calculations [37, 38]. Heavier nuclei lose energy due to photo-disintegration and secondary nucleons are produced. The energy of the secondary nucleons is smaller than the primary energy by a factor $1/A$ (this happens because the Lorentz factor is the same for the nucleon and for the nucleus). Photopion production of the secondary nucleons produce UHE neutrinos (Eq. (1.5)) as long as the energy of these secondary nucleons is not too low to interact through the GZK mechanism and neutron decay produces neutrinos too, at much lower energies though. For a non-pure proton composition, the neutrino flux is smaller than the one expected from a pure proton component: For example, for ^{4}He, the cosmonegic neutrino flux is reduced by about $\sim 50\%$, but for heavy nuclei like ^{56}Fe, the suppression is around one order of magnitude [38]. Taking all this in consideration, changing the mass of primary UHECR produces an uncertainty in the neutrino fluxes of more than an order of magnitude.

Recent experimental results by Auger [39] indicate that the flux of UHECRs has a fraction of nuclei heavier than protons that steadily increases as the energy rises above $3{\cdot}10^{18}$ eV. On the other hand, limits to the diffuse flux of EeV neutrinos from IceCube [40] and the Pierre Auger Observatory [23] are disfavouring many models of neutrino production due to GZK interactions, as long as the primary cosmic rays are protons and their sources evolve rather strongly with redshift (see Chapter 3). These results are compatible with the experimental observation of the composition of UHECR getting heavier as energy increases [41], and thus producing a reduced flux of cosmological neutrinos as explained above.

Cosmological evolution of the sources with redshift

The cosmological evolution of the potential UHECRs sources is a very important factor that affects predictions of neutrino fluxes. To describe it, a source evolution term $\mathcal{H}$ is employed, defined as the ratio of the mass density ρ of sources within a comoving volume between redshift z and now ($z = 0$):

$$\rho(z) = \mathcal{H}(z) \times \rho(0). \tag{1.6}$$

The most popular evolution models are:

- **No evolution:** In this model it is assumed that there is no evolution with redshift ($\mathcal{H} = 1$) and the predicted cosmogenic neutrino flux is typically the lowest one.
- **Star Formation Rate (SFR):** This model uses data from different experiments that measure the number of sources as a function of redshift. The model assumes that the density of CR sources follows the SFR and hence first increases with z, then remains constant (or almost constant with a small decrease) and, finally, there is a cutoff. An example of the SFR evolution is [42, 43]:

$$\mathcal{H}(z) \propto \begin{cases} (1+z)^{3.4} & \text{for } z < 1 \\ (1+z)^{-0.3} & \text{for } 1 < z < 4.5 \\ (1+z)^{-8} & \text{for } z > 4.5 \end{cases} \tag{1.7}$$

- **Active Galactic Nuclei (FRII):** Radio galaxies are a kind of active galaxies very luminous at radio frecuency. These galaxies can be divided in two types following the Fanaroff-Riley classification: FRI galaxies (with bright jets in the center) and FRII galaxies (with faint jets in the center but bright hotspots at the ends of the lobes). This second kind of radio galaxies, FRII, are able to accelerate particles to UHE according to models. A simple approximation to the distribution is [44]:

$$\mathcal{H}(z) \propto \begin{cases} (1+z)^4 & \text{for } z < 2 \\ e^{\frac{2-z}{1.5}} & \text{for } z > 2 \end{cases} \tag{1.8}$$

This kind of sources produce an enhancement of the cosmogenic neutrino flux of a factor 7 with respect to SFR [45].

- **Strong Gamma Ray Burst (GRB):** This model is similar to SFR, but taking into account GRBs. The presence of GRB increases the $\mathcal{H}$ function for $z > 4$, however, the difference between GRB and SFR is very small because the contribution of sources at high redshift ($z > 4$) is less than 1% of the total flux [43].

UHECR energy spectrum and the maximum energy reached

The injection spectrum of UHECR at the sources can be inferred from experimental results of cosmic-ray detectors on Earth. Eq. (1.1) shows the dependence of the UHECR spectrum with the energy. For the prediction of cosmogenic neutrino fluxes it is typically assumed that there is a cutoff energy at the source between 10^{20} eV and 10^{23} eV. Once the cutoff energy and the spectral index are set, the normalization is chosen so that the propagated CRs that arrive at Earth fit the observed CR spectrum. The smaller the cutoff energy, the smaller neutrino fluxes at $10^{18} - 10^{19}$ eV due to the smaller number of protons and nuclei at high energies that would produce secondary neutrinos.

Cosmological model

The cosmological model of the Universe is another factor that influences the cosmogenic neutrino flux. Experimental observations nowadays point to the Λ Cold Dark Matter (ΛCDM). According to this model, the Universe has a cosmological constant, Λ, associated with dark energy and cold dark matter. The updated cosmological best-fit parameters ($\Omega_\Lambda = 0.692$ and $\Omega_M = 0.315$) reveals that dark energy is about the 70% of the total mass-energy of the Universe [46]. A comparison between two different cosmological models was performed in [47] and the result was that the $\Omega_\Lambda = 0.7$ model increases the neutrino flux by 60% for a moderate redshift evolution of the sources with respect to the Einstein-de Sitter Universe (model with $\Omega_\Lambda = 0$).

Taking into account all these dependences, the flux of the cosmogenic neutrinos spans over four orders of magnitude [48].

1.4.2 Astrophysical neutrinos

These neutrinos are produced in Galactic and extragalactic sources. The process of neutrino creation is similar to the cosmogenic neutrinos but, instead of a UHECR interacting with a CMB photon to produce a charged pion that decays producing neutrinos, the charged pion is produced inside the source or in the collision of protons with gas, dust or radiation surrounding the source. There are two main kind of sources that can produce UHE neutrinos: Active Galactic Nuclei (AGN) and Gamma Ray Bursts (GRB).

AGNs are galaxies with a central compact region with a very high luminosity in all the electromagnetic spectrum. Their emission is powered by an active supermassive black hole accreting matter. Depending on where the neutrinos are produced, there are two main types of neutrino models in AGNs: AGN core models or AGN jet models. In the first models, protons are accelerated and interact with the photon field inside the cores of AGNs [49]. In the second one, two relativistic jets are emitted perpendicular to the accretion disk in opposite directions [50]. Protons are accelerated at shock waves in the jets and then interact with photons radiated from the accretion disk, producing neutrinos.

GRBs are brief (a few tens of seconds or less) flashes of γ-ray emitted by sources at cosmological distances [51]. They are the most energetic explosions in the Universe, being their luminosity in this short period of time comparable to the entire host galaxy. GRBs are classified in two classes depending on their duration: short GRBs (if the gamma emission lasts less than $\sim$ 2 s) and long GRBs (if the gamma emission lasts more than $\sim$ 2 s). The first class can be explained with the merger of two compact objects in a binary system such as two neutron star, while the long GRBs can be explained as the result of the collapse of massive stars.

The photons ejected in the GRB can interact with accelerated protons or protons in the supernova remnant shell to produce pions that decay into neutrinos. Moreover, there are two different ways to produce UHE neutrinos due to the jets: The so-called *burst* or *prompt* neutrinos are the neutrinos generated in the jet by the collision of accelerated protons with gamma rays of the jet (prompt γ rays), while the *afterglow* neutrinos are produced by the accelerated protons colliding with the photons produced by the collision of jetted material with the external medium (afterglow photons) [52].

1.5 Detection of neutrinos: Neutrino showers

When an UHE neutrino arrives at the Earth, it can interact through the weak force with a nucleus of the atmosphere in the case of downward-going neutrinos or with the Earth crust in the case of Earth-skimming νs. This primary interaction is a deep inelastic scattering (DIS) as shown in Fig. 1.5.

In all cases at UHE and on average around $\sim$ 20% of the energy of the primary neutrino is transferred to the hadronic jet that results from the fragments of the nucleus, while the remaining 80% is transferred to the energy of the lepton in the lepton vertex.

The hadronic jet starts a chain reaction that produces a hadronic shower. In this shower at the beginning most of the particles ($\sim$ 80%) are hadrons (pions, kaons, other mesons mainly) but with the evolution of the shower and soon after the first interaction, the unstable particles with low energy typically decay (for example the neutral pions decay into two photons) and transfer their energy to the electromagnetic and muonic components of the shower. At the end, around 90% of the energy of the shower goes into the electromagnetic component [53].

If the weak interaction is a neutral current interaction (NC), the outgoing lepton is a

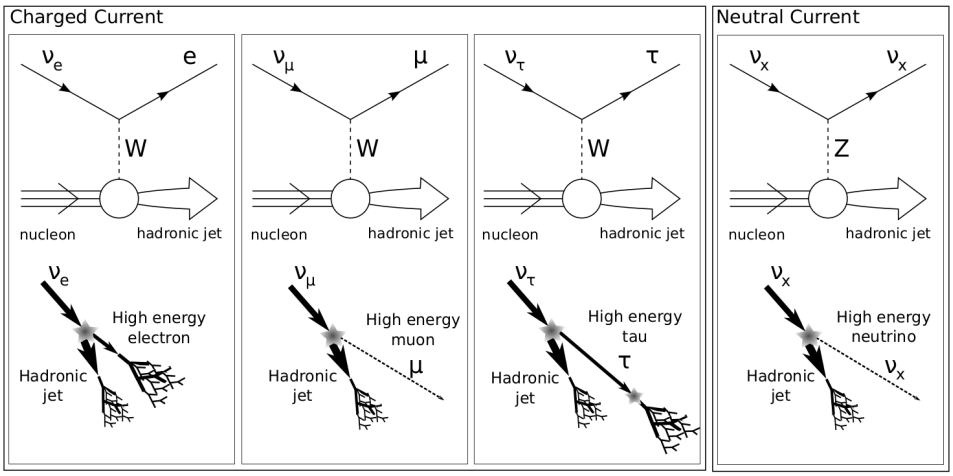

Figure 1.5: Neutrino interaction channels according to the Standard Model. In every case the Feynman diagram is shown at the lowest order.

neutrino, which escapes undetected. As a consequence $\sim 80\%$ of the energy of the primary neutrino will be lost, and the shower will only have $\sim 20\%$ of the primary neutrino energy. On the other hand, for charged current interactions (CC) the resulting lepton depends on the flavor of the primary neutrino. If it is an electronic neutrino, the outgoing lepton is an electron, that produces an electromagnetic shower, that is explained with the well-known Heitler model [54]. So in this case $\sim 100\%$ of the energy of the primary neutrino will be invested in the atmospheric shower. For showers initiated by muonic neutrinos the outgoing lepton is a muon, that is very unlikely to decay again or interact in the atmosphere, so again, as in the case of NC interactions, the atmospheric shower only contains $\sim 20\%$ of the energy of the primary neutrino.

Finally, for tau neutrinos CC, the tau lepton produced has a relatively short lifetime ($\sim 2.9 \cdot 10^{-13}$ s), so it can decay before reaching the surface producing a secondary shower. This type of showers are known as "Double-Bang". A sketch of DIS ν interactions at UHE for different ν flavors and channels (CC, NC) is shown in Fig. 1.5.

1.5.1 Neutrino cross-section

To describe in a more quantitative way the neutrino interactions at UHE, it is necessary to estimate their cross sections for CC and NC interactions using Quantum Chromodynamics (QCD) predictions and experimental measurements at lower energies. For energies in the range $10^{16} - 10^{21}$ eV a possible parametrization for the CC cross-section is [55]:

$$\ln\left(\frac{\sigma_{CC}}{\text{pb}}\right) = \ln(10^{36}) - 98.8\left(\ln\frac{E}{\text{GeV}}\right)^{-0.0964}. \tag{1.9}$$

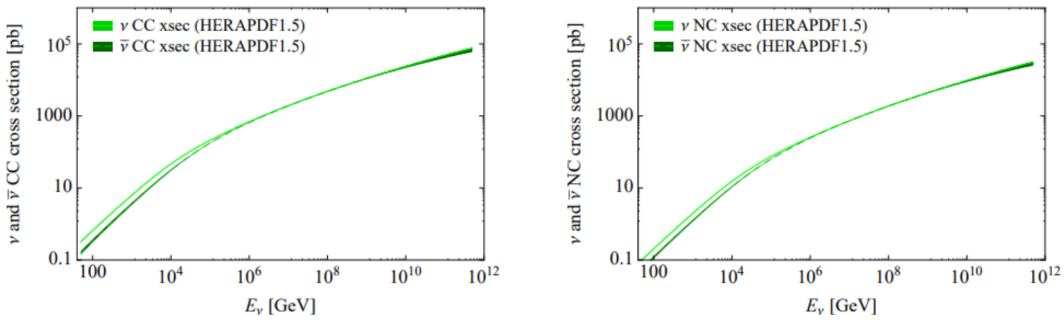

Figure 1.6: Neutrino and anti-neutrino cross-sections for CC and NC scattering according to HERA-PDF1.5, a recent parameterization of the parton distribution functions of the nucleon [35].

The interaction cross section for NC interactions at UHE is ~ 2.5 times lower than in the CC case (see Fig. 1.6). At these energies neutrino and anti-neutrino cross-sections can be considered equal. UHE neutrinos probe the sea quarks and gluons (partons) in the nucleon with which they collide, at very low fractions of momentum $x \lesssim 10^{-6}$ carried by the partons in the nucleon (see [56]).

At the energies of interest for this thesis $E_\nu = 1$ EeV, $\sigma_{\text{tot}} = \sigma_{\text{CC}} + \sigma_{\text{CC}} \simeq 1.3 \cdot 10^4$ pb. This corresponds to a mean free path $\lambda_\nu \simeq 1.3 \cdot 10^8$ g/cm^2 equivalent to 1300 km of water.

USC
UNIVERSIDADE
DE SANTIAGO
DE COMPOSTELA

2

Search for UHE neutrinos with the SD of Auger

The Pierre Auger Observatory is a hybrid UHECR detector located close to Malargüe, in Mendoza (Argentina). It is able to detect UHECR combining two independent detectors: the surface detector (SD) and the fluorescence detector (FD). In this thesis only data collected with the SD was used and a description of the SD is given in the next section. A detailed description of the Pierre Auger Observatory can be found in [57].

2.1 The SD of the Pierre Auger Observatory

The surface detector array is composed by 1600 water-Cherenkov stations in the form of cylinders of 3.6 m diameter and 1.2 m height, containing 12 tonnes of purified water each. The stations are set in a triangular grid with a separation of 1500 m (see Fig. 2.1), covering an area of ~ 3000 km^2.

The interior walls of each station are covered with a material (Tyvek) that diffusively reflects the Cherenkov light with very high efficiency. The multiple reflections reduce the dependence of the signal with the direction of the incoming particles. Cherenkov light is collected in three photomultipliers, whose signal is digitized by a 40 MHz 10-bit Flash Analog to Digital Converter (FADC), with a 25 ns time bin. Moreover, each station is equipped with a GPS that allows to synchronize the clocks between stations with a precision of 8 ns, and with a communication antenna which is used to send the signal acquired by the phototubes and the timing to the Central Data Acquisition System (CDAS) (Fig. 2.2).

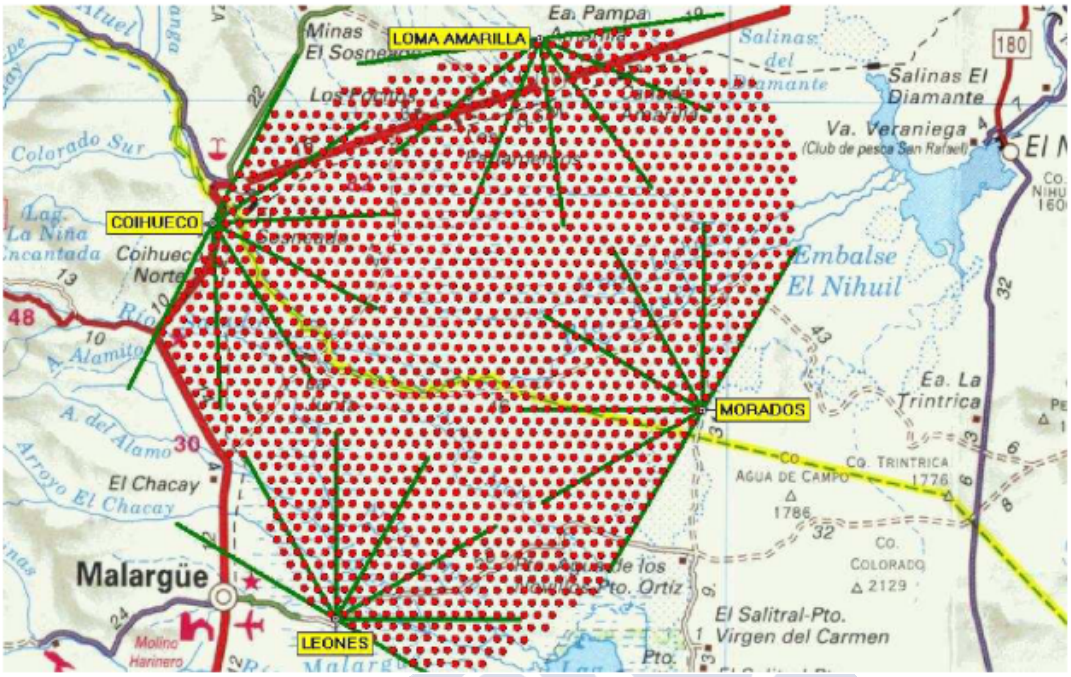

Figure 2.1: Schematic map of the Pierre Auger Observatory. Each red dot represents a water-Cherenkov station of the surface detector (SD).

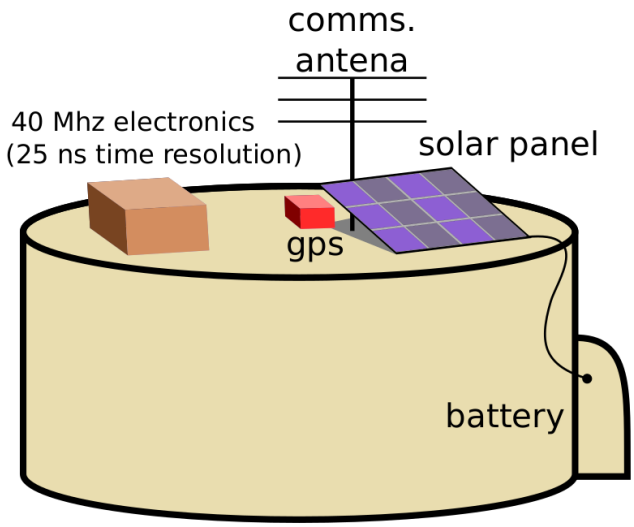

Figure 2.2: Schematic drawing of a water-Cherenkov station of the surface detector, with a solar panel, a battery, a GPS and a communication antenna.

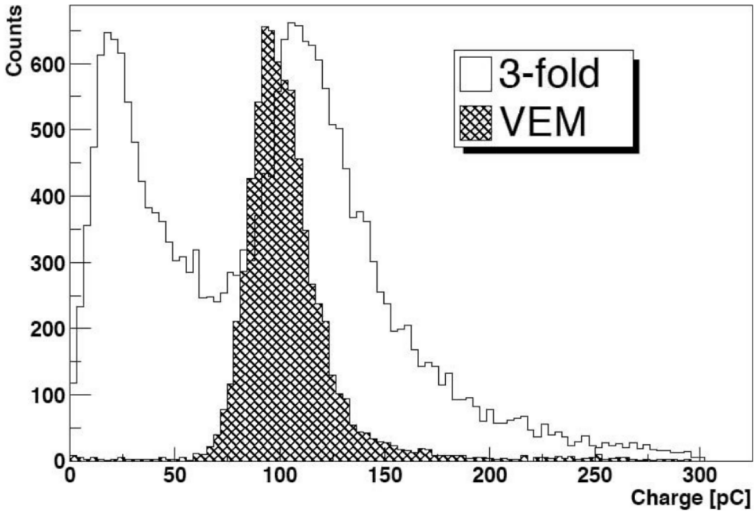

Figure 2.3: Distribution of charge in a typical SD station produced by the Cherenkov light induced by atmospheric muons used for calibration. The open histogram is the charge spectrum, summed for the three PMTs, obtained when an SD station is triggered by a threefold coincidence between the three PMTs. The first peak is due to low energy particles and corner-clipping muons and the second one is due to atmospheric muons. The hatched histogram shows the spectrum of the vertical and central muons. The atmospheric muon peak in the open histogram is a slightly larger value because here we are considering also inclined muons, which go through more distance inside the station and produce more Cherenkov light.

2.1.1 Surface detector calibration

The large amount of stations, the limitations on the quantity of data that they can save, the difficulty of accessing them and the restricted bandwidth available for data transmission from the stations to the CDAS, that is 1200 bits per second, make it necessary that the calibration is done autonomously in each station. This is achieved using atmospheric muons.

Fig. 2.3 displays the distribution of the Cherenkov light induced by atmospheric muons in a typical station of the SD. We define a VEM (Vertical Equivalent Muon) as the average charge collected by a PMT from the Cherenkov light produced by a vertical and central through-going muon, this VEM is the unit to measure the signals obtained by the SD that the Collaboration has adopted. It has been determined that the peak in the charge distribution of atmospheric muons corresponds to 1.09 VEM for the sum of the three PMTs, so searching for this peak allows us to obtain the VEM calibration for each station. The calibration is performed systematically every minute[1] with 2% accuracy [57].

[1]The atmospheric muon flux at sea level is approximately 1 $\mu/\mathrm{cm}^2/\mathrm{min}$.

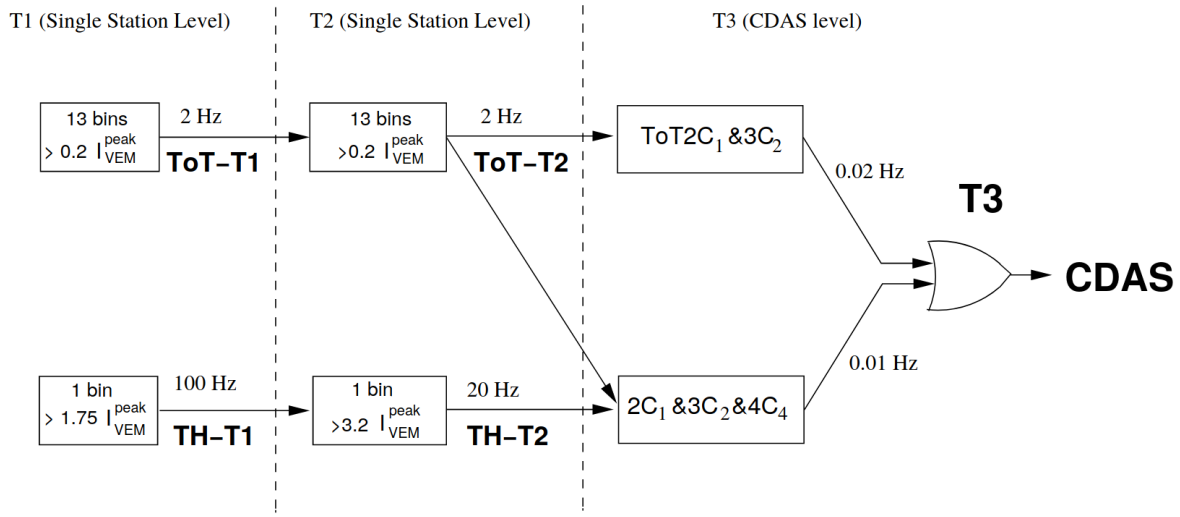

Figure 2.4: Trigger hierachy scheme in the Pierre Auger Observatory SD array, see text for details [58].

2.1.2 Trigger system and data acquisition

The huge amount of information involved makes it impossible to save all the data of the stations, so the Pierre Auger Collaboration has adopted a three hierarchical trigger levels for the SD: the first and second levels, called T1 and T2 respectively, apply at a local level selecting data in each station, while the third level designed to select cosmic-shower events, called T3, involves several stations searching for temporal and spatial coincidence between them [58]. The trigger hierarchy scheme is shown in Fig. 2.4.

There are two kinds of T1 trigger criteria that have been implemented sensitive in a complementary way to the electromagnetic and muonic components of the shower. The first one the "Time-over-Threshold" trigger (ToT) requires 13 time bins of 25 ns above a threshold of 0.2 VEM in coincidence in 2 out of 3 PMT. The second T1 mode is a threshold trigger (TH) that requires the coincidence of the three PMTs each with a peak signal over 1.75 VEM.

The ToT criteria is implemented to separate long signals in time produced by the electromagnetic component (electrons and photons) from short signals produced by muons. It has a trigger frequency of 1-5 Hz, that is expected for the random coincidence of two atmospheric muons within the 3 μs window. On the other hand, the threshold criteria has a trigger frequency of 100 Hz and it was included to increase the sensitivity to the muonic component of the showers.

The T2 trigger is applied in each station to reduce the trigger rate to about 20 Hz per detector, so the communication between stations and the CDAS is possible. All the ToT-T1 triggers are promoted automatically to T2, while the TH-T1 triggers are required to exceed the threshold of 3.2 VEM in coincidence among the three PMTs.

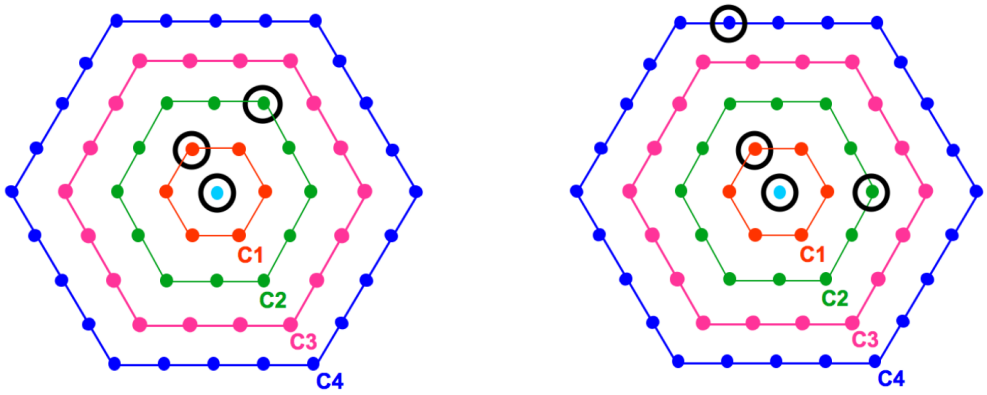

Figure 2.5: Example of T3 configurations. T2 triggered stations are surrounded by black circles. In the left side we show an example of a configuration satisfying $ToT2C1\&3C2$, that is: at least 2 T2 trigger of ToT type within the first ring (or crown) and 3 T2 triggers within the second ring. On the right side a configuration satisfying the condition $2C1\&3C2\&4C4$. In cyan color we show the central station with the surroundings crowns, see text for details [58].

The third level trigger, T3, initiates the central data acquisition from the array. Once the T2 trigger is fulfilled, the station sends the information (identifier number of the station, recorded time and kind of trigger) to CDAS. With this infomation the central trigger tests several configurations in space and time looking for coincidences. The spatial configuration is based on "crowns" of stations around one first station. The first crown (C1) is associated with the six nearest stations composing a hexagon around the given station. The second crown (C2) corresponds to the greater hexagon and so on, as shown in Fig. 2.5.

There are two main modes of the T3 trigger. The first one requires the coincidence of at least three stations that have passed the ToT condition and which have the requirement of a minimum of compactness, specifically, one of the three stations must be within in the first crown and a second one within the second crown. It is called "$ToT2C1\&3C2$". Where mCn indicates that at least m detectors with a T2 trigger are to be found within the nth ring around the central station. The second T3 mode is less restrictive, it requires a four-fold coincidence of any T2 with a moderate compactness. Specifically, among the four triggered stations, at least one must be in first crown, another one must be in the second crown and the last one can be as far as the fourth crown. This trigger is called "$2C1\&3C2\&4C4$". In both cases there is a temporal coincidence required: each station must be within $(6 + 5\ n)$ μs of the first one.

There is also a third T3 trigger mode for hybrid data acquisition. In this one, an event observed by the FD also triggers at least one SD detector. The position and time of the impact are evaluated and the CDAS looks for such event in the network.

If any of the three previous conditions is fulfilled, the central system emits a T3. Once a T3 triggers, every candidate station (T2 and T1 trigger) sends its identifier number (station ID), position, GPS time, calibration histograms, signal traces and trigger information to the CDAS.

2.2 Neutrino selection

The main objective of the Pierre Auger Observatory is the detection of cosmic rays, but UHE neutrinos that develop air showers can also be detected using the surface detector. In this section we are going to explain the way to distinguish the showers produced by a neutrino from the showers produced by a cosmic ray.

2.2.1 Neutrino showers vs cosmic-ray showers: generalities

Protons, heavier nuclei, and photons interact shortly after entering the atmosphere, while neutrinos typically initiate showers deep in the atmosphere. In Fig. 2.6 we show a sketch of the shower produced by a cosmic ray arriving at the Earth with an inclined direction with respect to the vertical to ground. At large zenith angles, the atmosphere is thick enough so that the electromagnetic component of nucleonic cosmic ray-induced showers gets absorbed, and the shower front at ground level is mainly composed of muons ("old" shower front). On the other hand, in Fig. 2.7 we show the shower produced by an inclined neutrino. Showers induced by neutrinos that start deep in the atmosphere can have a considerable electromagnetic component at the ground ("young" shower front).

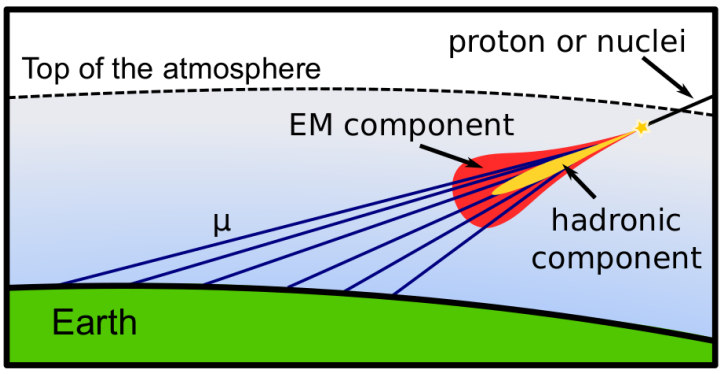

Figure 2.6: Schematic representation of an inclined shower induced by a cosmic ray. These showers start on the top of the atmosphere. The hadronic and electromagnetic components are absorbed in the atmosphere and as a first approximation only muons arrive to the ground.

Neutrinos of all flavors can interact in the atmosphere through charged (CC) or neutral current (NC) interactions as we explained in the previous lines and induce a

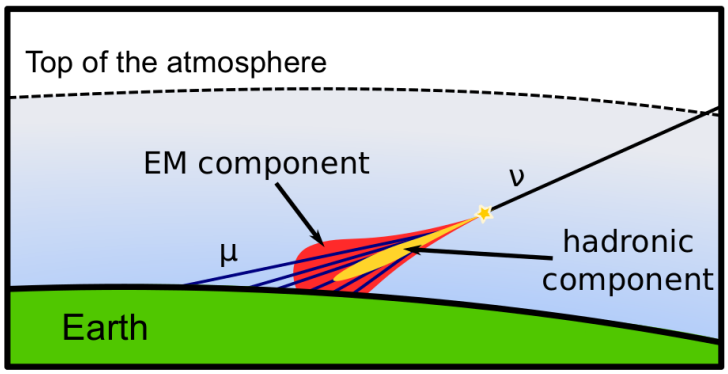

Figure 2.7: Schematic representation of an inclined shower induced by a neutrino. These showers can start deep in the atmosphere. Both electromagnetic component and muons can arrive to the ground.

"downward-going" (DG) shower that can be detected [12]. In addition, we can consider a tau neutrino that can interact through CC interactions and produce a tau lepton in the Earth crust that exits the Earth surface and decays in the atmosphere (this is shown in Fig. 2.8), inducing an "Earth-skimming" (ES) upward-going shower [59,60]. Tau neutrinos are not expected to be abundantly produced at the astrophysical sources, but thanks to neutrino oscillations over cosmological distances, approximately equal fluxes for each neutrino flavor should reach the Earth [36, 61, 62].

Neutrino-induced showers must be identified in Auger data in the large background of showers initiated by UHECRs (protons and/or nuclei). The different showers explained in the previous lines allow identification based on the search for inclined DG (zenith angle $\theta > 60°$) and ES (zenith angle $\theta > 90°$) neutrino-induced showers initiated deep in the atmosphere close to the ground. Thanks to the fast sampling rate (25 ns) of the SD digital electronics, we can distinguish the electromagnetic signal from the muon signal produced by inclined showers initiated by UHECRs. These young inclined showers have a significant electromagnetic component when they reach the SD array, producing signals in the triggered SD stations that spread over several hundreds of ns in time. The signals due to muons from older showers induced by cosmic rays at the top of the atmosphere have signals that spread less in time. Auger data are searched for UHE neutrino candidates in two separate analyses, DG and ES, respectively targeting the zenith angle ranges $60° < \theta < 90°$ and $90° < \theta < 95°$ [23]. To optimize the study, the DG analysis is splitted into two different channels: the downward-going high (DGH), from 75° to 90°, and the downward-going low (DGL), from 60° to 75°. In this thesis we are going to concentrate only on the DGH and ES channels. The other channel DGL has been studied in detail elsewhere [17, 63].

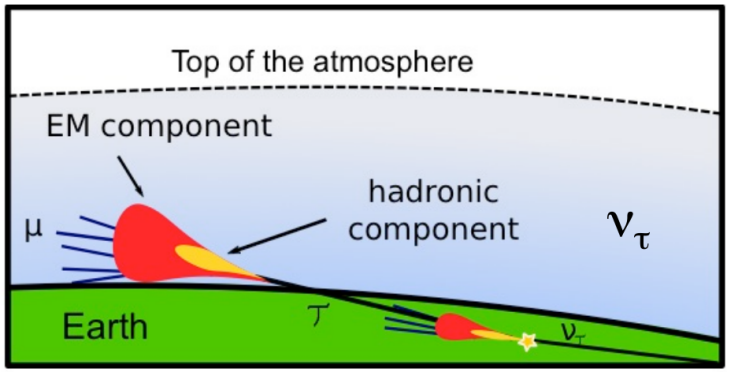

Figure 2.8: Schematic representation of an ES shower induced by a ν_τ. Despite the produced shower, induced by τ decay, is up-going, the electromagnetic component can be detected by the stations of the surface detector when the zenith angle is between 90° and 95°

2.2.2 Event reconstruction

As we explained in the previous section, the search strategy consists in selecting inclined showers and identifying those with a broad time structure in the signals induced in the SD stations. To establish the selection algorithms of neutrino-induced showers and optimize the numerical values of the cuts of selection we follow a blind analysis procedure. A fraction of $\sim$ 15 % of the data sample analyzed (from 1 January 2004 up to 31 August 2018), along with Monte Carlo simulations of UHE neutrinos, is used to define the selection algorithms and the value of the cuts. We assume that this "training" data set is constituted of background UHECR-induced showers only once the selection procedure is defined the remaining fraction of data ("search data") is "unblinded" to look for neutrino candidates.

The selection algorithms are optimized for each channel depending on the zenith angle ranges: DGL, DGH and ES. Due to the larger uncertainties of the standard angular reconstruction techniques for nearly horizontal events [16, 64], we apply another strategy to select these nearly horizontal showers. For geometrical reasons, the pattern of the triggered SD stations in inclined events generally displays an elliptical shape on the ground with the major axis of the ellipse along the azimuthal arrival direction (see Fig. 2.9). These patterns can be characterized by a length L (major axis) and a width W (minor axis) that are calculated analogously to the moment of inertia in a rigid body:

$$\begin{aligned} L^2 &= \frac{I_{xx} + I_{yy} + \sqrt{(I_{xx} - I_{yy})^2 + I_{xy}^2}}{2\ S} \\ W^2 &= \frac{I_{xx} + I_{yy} - \sqrt{(I_{xx} - I_{yy})^2 + I_{xy}^2}}{2\ S}, \end{aligned} \tag{2.1}$$

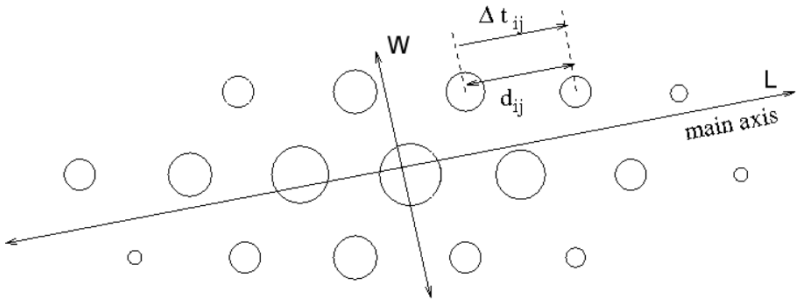

Figure 2.9: Schematic representation of footprint of an inclined event. Each circle is a station and the size is related to the signal detected in each one. The length L (major axis) and the width W (minor axis) of the ellipse are shown, as well as the distance between stations (d_{ij}) projected along the direction L and the difference of trigger time between stations (Δt_{ij}).

where:

$$\begin{aligned} S &= \sum_i s_i, \qquad \langle X\rangle = \sum_i s_i\ x_i/S, \qquad \langle Y\rangle = \sum_i s_i\ y_i/S \\ I_{xx} &= \sum_i s_i(x_i - \langle X\rangle)^2/S, \qquad I_{yy} = \sum_i s_i(y_i - \langle Y\rangle)^2/S \\ I_{xy} &= I_{yx} = \sum_i s_i(x_i - \langle X\rangle)(y_i - \langle Y\rangle)/S, \end{aligned} \tag{2.2}$$

being s_i the signal in the i-station and x_i and y_i the coordinates of that station.

Inclined events frequently exhibit large values of L/W, so an appropriate cut in L/W is an efficient selector of inclined events [14, 15, 20]. The average (apparent) speed $\langle V\rangle$ of the trigger time from one station to another is another indicator of the arrival direction of the event. This is calculated from the projected distance between pairs of stations along the major axis of the ellipse and the trigger times of the two stations, and it is averaged over all pairs of stations in each event. In very inclined events $\langle V\rangle$ is close to the speed of light, while in vertical showers $\langle V\rangle$ exceeds the speed of light because all triggers happen approximately at the same time. Additionaly, the Root-Mean-Square (RMS(V)) of the apparent speed, that is obtained from the values of V using different pairs of stations, is typically below $\sim$ 25% of $\langle V\rangle$ [14, 15, 20].

For the purpose of identifying those inclined events that interact deep in the atmosphere, we have to choose an observable that contains information on the spread in time in the SD stations and that can be extracted from the time traces. In Ref. [22] it has been shown that the Area-over-Peak[2] (AoP) serves as an efficient observable to discriminate

[2]The Area-over-Peak is defined as the ratio of the integral of the time trace to its peak value normalized to the average signal produced by a single vertical muon.

neutrinos from cosmic-ray showers. Inclined background showers of hadronic origin have mainly muons detected in the station, inducing a peaked signal with AoP value close to one. On the other hand, in neutrino-induced showers the values of AoP are typically larger. In Fig. 2.10 we show examples of traces of stations belonging to an inclined and a vertical event detected with the SD of Auger, as well as the trace of a station in a neutrino-induced simulated event.

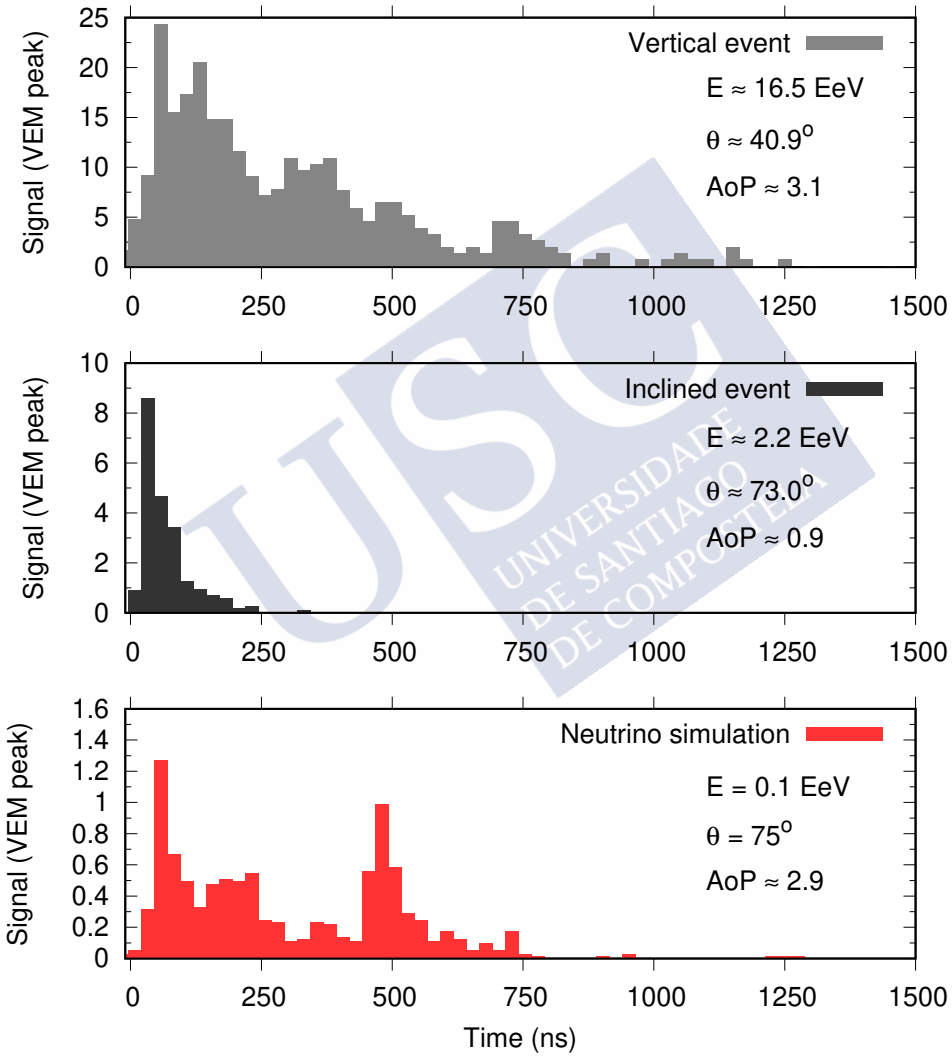

Figure 2.10: FADC traces of stations at a distance of approximately 1 km to the shower core. In the top panel for a vertical cosmic ray event, in the middle one for an inclined event also induced by a cosmic ray, and in the bottom one for a neutrino-simulated event. The labels in each panel indicate the reconstructed energy (E) and zenith angle (θ) for the sample events, or the simulated E and θ for the neutrino-induced shower. The value of the Area-over-Peak (AoP) of each trace is also given.

2.2.3 Selection criteria

The selection criteria have three different levels: quality selection, inclined selection and young selection. The quality criteria is used both for ES and DGH channels, but the following two selections are specific for each channel.

Quality selection

The central data acquisition system registers events that fulfilled the T3 trigger conditions. These constitute the data set that we have for the analysis. The first step we have performed is to reject the events collected when the detector is unstable (Bad Periods) [65]. After that, we apply to each event the following procedures:

- PMT selection.
- Station selection.
- Preliminary Reconstruction.
- Additional cuts.

PMT selection

The neutrino search aims at finding extremely rare events, so that if a candidate appears it is important to be sure that the PMTs work properly. In particular, it is essential to identify PMT pathologies that can induce a signal extended in time, since, as we explain in Section 2.2.1, the time spread of the signal is crucial for identifying neutrinos. There are two kinds of cuts employed to discard a PMT: criteria based on the area of the signal and criteria based on the shape of the signal.

The criteria based on the area of the signal is the result of studies performed with the monitoring data (see Section 2.1.2) [65]. A list of unstable PMTs is elaborated on a daily basis using that data. The parameters employed to assign this label to a given PMT are the anode and dynode baselines and the dynode/anode ratio. In the case of the baselines, a limit to the fluctuations is imposed with a cut on their RMS, while in the case of the dynode/anode ratio the maximum and minimum values are limited in addition to a limit to the fluctuations. This criteria excludes, for instance, saturated PMTs.

The criteria based on the shape of the signal allows us to detect other kind of "pathologies", most of them consisting on an excess of signal in the PMT trace after the signal induced by the shower. The first step to find these pathologies is to calculate the sum of the dynode signals corresponding to the second half of the PMT trace (denoted as $\sum_i$, where i stands for each PMT). After that, the content of the maximum bin, as well as the bin before and the bin after, are substracted from each sum $\sum_i$ (doing this we eliminate posible peaks that could be produced by accidental single muons). Finally, we check if the station has at least 2 active PMTs and if the maximum $\sum_i$ is larger than 4 VEM and

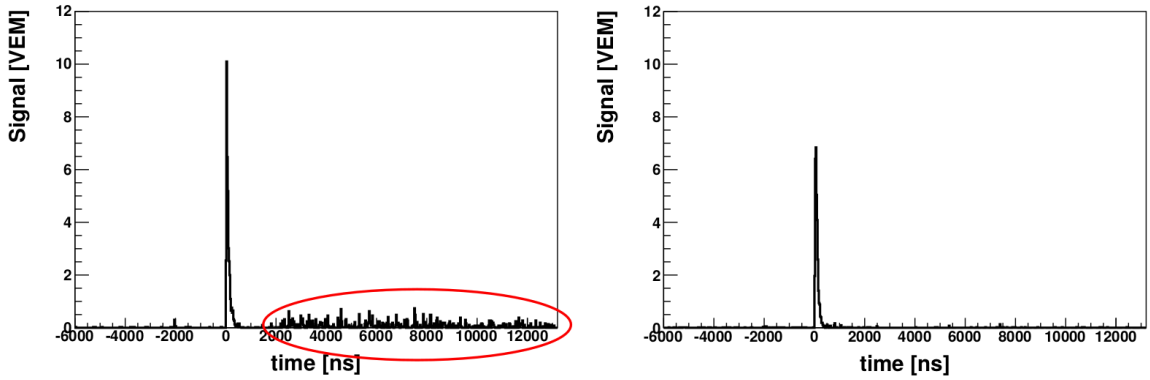

Figure 2.11: Example of a discarded PMT (left) after applying the criteria based on the shape of the signal and comparison with an accepted PMT (right) in the same station (station 1440 from event 3995196). The signal that makes that the PMT is discarded is marked with a red ellipse.

at least 7 times larger than the others. If a certain PMT verify these conditions systematically over a period of time it is removed from the analysis. In Fig. 2.11 an example of this behaviour is shown.

Station selection

There are several reasons to discard a station. For instance, if there is only one active PMT for a period of time, if a certain event is registered during a storm or if an accidental muon triggers the station. In the next paragraphs we summarize them.

Stations with only one active PMT

Despite each station has 3 PMT, some of them can have permanent or temporary fails, and can be tagged as seen earlier. If a neutrino candidate appears we need to compare the signal of the station at least between two PMTs. In this case the cross-checking is not possible and we have to discard this station.

Stations with signal caused by lightning

Lightning strikes generate an electromagnetic pulse, that can cause oscillating signals in the SD detector (see Fig. 2.12). The oscillations in the signal trace are used to detect this kind of situations and if an event contains one or more stations classified as lightning then it is discarded.

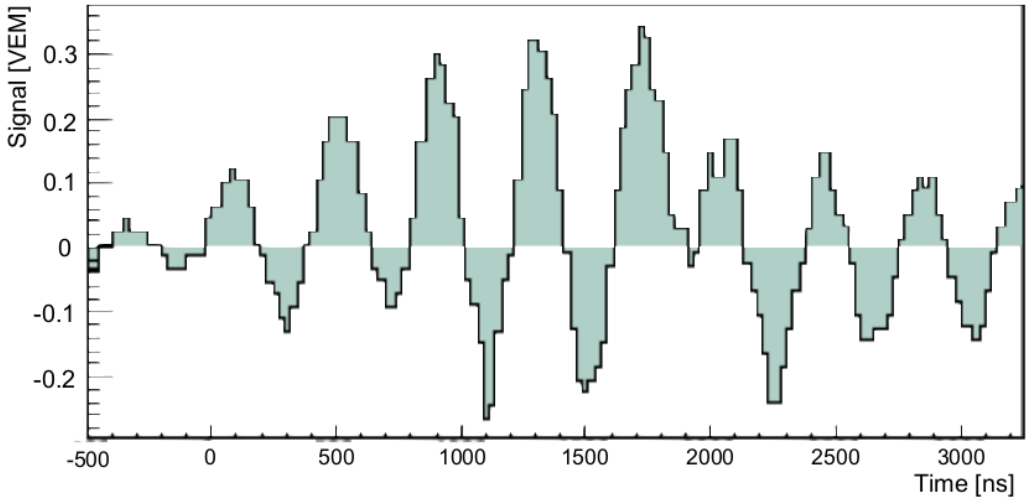

Figure 2.12: Example of a signal generated by a lightning. The signal corresponds to the PMT 3 of the station 506 in the event 3995197 (26 January 2005).

Accidental stations: effects of muon background

The detector is exposed to a constant flux of atmospheric muons and low energy particles which are more frequent than the showers produced by UHECR. At the height of the SD (1400 m above sea level) the muons have thpical energies in the 1-10 GeV range [66]. These muons can affect the reconstruction in two different ways:

- **Produce a T2 trigger in a SD station that is not part of the event:** the additional particles that trigger the station do not belong to the shower, so their T2 trigger time will have a uniform distribution within the time window of the T3 trigger. The inclined selection procedure is based on the position and timing of the triggered stations, so that a spurious station can give a wrong estimation of the geometry of the shower, especially for low multiplicity events. We will explain how these stations are removed later in this section.

- **Add a spurious signal to one of the stations belonging to the event:** if the accidental signal occurs a few μs before or after the particles of the shower reach the stations both signals are merged in the same trace. When the spurious signal comes first it alters the T2 trigger time (see Fig. 2.13) and affects the reconstruction of the event, and when the spurious signal comes after it does not affect the trigger, but it changes many of the trace observables, most importantly for the neutrino searches, the AoP.

To minimize the impact of spurious signals produced by atmospheric muons in stations belonging to the event, a trace cleaning algorithm is used. The purpose of this algorithm is to identify and remove the fractions of the trace produced by accidental muons.

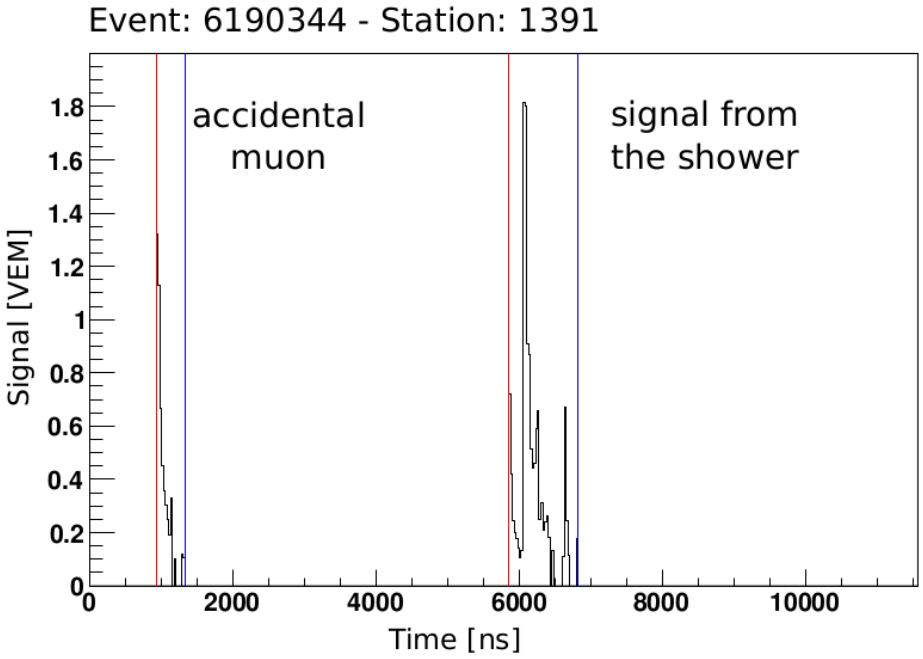

Figure 2.13: Example of the signal when an accidental muon triggers the station a few μs before the shower reaches the station.

This algorithm is based on the idea that the amount of energy produced by a muon is, to first order, proportional to its path length in the water inside the station. As the SD stations are much wider (3.6 m diameter) than taller (1.2 m height), inclined muons induce on average a higher signal than the vertical ones.

Given that accidental muons are mainly vertical [67], the signals deposited will be smaller than the ones produced by muons in inclined showers. Based on this simple idea, the algorithm separates the signal into segments and keeps the one with largest integrated signal. For instance, in Fig. 2.13 we have two different segments, being the second segment the one with largest integrated signal.

In case the integrated signal is similar for several segments, the algorithm obtains a score for each segment defined by $s = nBoT \times Q_T$, where $nBoT$ is the number of bins with signal higher than 0.02 VEM and Q_T is the sum of the signal over the bins with signal higher than 0.02 VEM. The signal of the segments induced by the bulk of the atmospheric muons tends to be smaller than the one induced by inclined muons or by the electromagnetic component. If there is more than one segment fullfilling that $s > 0.15\ s_{max}$, where s_{max} is the maximum score, the station is rejected because it cannot be unambiguously decided which of the segments is due to an atmospheric muon. If only one segment satisfies that $s > 0.15\ s_{max}$, and all segments except that one are rejected, the station is kept. All the details of the trace cleaning algorithm are given in [68].

Preliminary reconstruction

After the procedure explained in the previous section is applied, the events are composed only by stations with well-defined trigger times. Nevertheless, accidental stations produced by accidental muons or by an independent low-energy shower can still be present. A selection of stations based on temporal and spatial compatibility is performed to identify and reject those accidental stations. The procedure consists of two steps: Isolated Station removal and Top-Down Selection.

Isolated Station removal

In the first step isolated stations are removed. Stations are kept only when they verify the two following conditions:

- Standard Isolated: For a station to be classified this way it must satisfy the following two conditions:
  - There is at least one station in its third crown (at a distance closer than $d_1 = 4700$ m allowing for some tolerance) and the trigger times difference between both stations is compatible with the speed of light $\left(t_1 < \frac{d_1}{c} \approx 15700 \text{ ns}\right)$.
  - There is a second station in its fourth crown (at a distance closer than $d_2 = 6200$ m allowing for some tolerance) and the trigger times difference between both stations is compatible with the speed of light $\left(t_2 < \frac{d_2}{c} \approx 20700 \text{ ns}\right)$.
- Muonic signal: if a station has AoP < 1.4 (indicative of a signal induced by a single muon) at least one neighbour station at a distance closer than $d = 2700$ m is required.

Top-Down Selection

The second step consists in selecting stations with space and time compatibility. The algorithm employed for this purpose is the Top-Down Selection [69]. The idea of this method is based on, starting with a set of N stations, reconstructing the zenith angle of the event, θ_{rec}, assuming a plane shower front. Using this reconstruction a temporal and spatial compability is required and, if any of the conditions is not satisfied we discard stations in the set of N stations successively until a compatible configuration is found. The detailed algorithm of the Top-Down Selection is explained in Appendix A.

Additional cuts

Once the stations with spurious signals are discarded we perform two additional quality cuts to improve the ES selection. The events to be kept for the analysis must satisfy:

1. **isContained:** The triggered station closest to the barycenter of the event, which is calculated weighting the stations with their signals, is identified. If the event has less than 6 stations we check if that station has less than 5 active stations around it. When this happens the event is rejected. The purpose is to avoid small multiplicity events close to the borders of the array that could be part of a higher multiplicity event where a large fraction of the event is missing because the core fell outside the array.

2. **hottestHasNeighbour:** We require that the station with the highest signal has at least one T2 station in the first crown of stations around it. The purpose of this cut is to avoid small multiplicity events with "holes".

Moreover, other "soft" cuts on the inclination of the events are applied to reduce the amount of data to analyze in the search for inclined shower in ES and DGH:

- $\theta_{rec} > 58°$.
- $\langle V \rangle < 0.35$ m ns^{-1}.

Finally, in DGH analysis at least 4 stations after the station selection and preliminary reconstruction are required to constitute a candidate event. For ES analysis the minimum number of stations is 3.

Inclined selection

Once the quality cuts have been applied, the next step is to select the inclined events. The selection criteria is different for Earth-skimming and downward-going high channels. In this section we are going to detail each set of criteria.

Earth-skimming inclined selection

Analyzing Monte Carlo simulations of UHE ν_τ propagating inside the Earth, it has been determined that τ leptons above the energy threshold of the SD are efficiently produced only at zenith angles between 90° and 95° [22]. Therefore, in the Earth-skimming analysis we establish very restrictive cuts to select quasi-horizontal showers with largely elongated footprints:

- $L/W > 5$.
- $\langle V \rangle \in [0.29, 0.31]$ m ns^{-1}.
- $RMS(V) < 0.08$ m ns^{-1}.

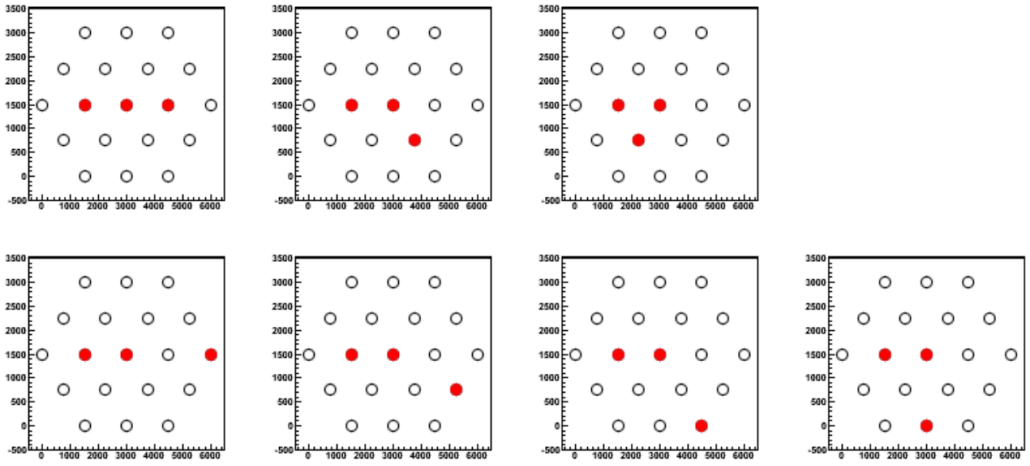

Figure 2.14: Sketches of the 7 possible T3 configurations for 3-station events. Red circles indicate the triggered stations. Top: Configurations number 1 to 3 from left to right. Bottom: Configurations number 4 to 7 from left to right.

The details on how these values were obtained are explained in [18, 19].

In addition, events with only 3 stations were analyzed independently. The number of 3-station configurations that can satisfy a T3 trigger is only 7. In Fig. 2.14 a sketch of these 7 configurations is shown. An analysis of these 7 configurations with the data performed in [18, 19] throws that the geometrical configuration 1 contributes $\sim 70\%$ to the efficiency in the selection of 3-station events, while configurations 2, 3, 4, 6 and 7 contribute in total less than 4%. The remaining 26% is contributed by configuration number 5 that was neglected since background events are more prone to produce this type of configuration.

An analysis of the efficiency of these cuts will be performed later Section 2.2.4.

Downward-going high inclined selection

Analyzing Monte Carlo simulations of very inclined UHE ν interacting in the atmosphere close to the Earth, it has been determined that neutrinos above the energy threshold of the SD are more efficiently identified at zenith angles between 75° and 90°. Therefore, in the downward-going high analysis we establish again restrictive cuts to select very inclined showers with elongated footprints:

- $L/W > 3$.
- $\theta_{rec} > 75°$.
- $\langle V \rangle < 0.313$ m ns^{-1}.
- $RMS(V)/\langle V \rangle < 0.08$.

- "Well-conditioned" spatial configuration.

The details on how the values of these cuts are obtained are explained in [16]. An analysis of the efficiency of these cuts is performed in Section 2.2.4.

We defined an event as "spatially bad conditioned" when it is formed by an aligned set of SD stations plus one station not aligned. The reason why these kind of events are prone to constitute a dangerous background can be ilustrated with the following extreme example: a completely vertical event that triggers three aligned stations. In this case, all three stations have the same time so the reconstruction would throw a zenith angle compatible with a vertical event. However, in case that an accidental station is produced in coincidence, for instance by an atmospheric muon, and that the station is not aligned with the vertical event, the reconstructed angle would be determined just by the time of the extra station.

To avoid this problem, we apply to the events with this bad-conditioned spatial configuration an extra cut. We ignore the station that is not aligned, we reconstruct the aligned event, and we require this event to be also inclined, with $\theta_{rec} > 75°$.

Neutrino selection

Finally, once we have selected the inclined events, we can apply the cuts to search for neutrinos. The main idea is the same in both the ES and DGH channels, namely looking for electromagnetic signal that reflects itself on the spread of the time traces of the events, but optimization leads to different selection criteria for Earth-skimming and downward-going high.

Earth-skimming neutrino selection

The inclined events produced by Monte Carlo simulations of UHE ν_τ propagating inside the Earth [18, 19] have been analyzed. It was deduced that a simple variable, the average Area-over-Peak ($\langle$AoP$\rangle$) over all triggered stations in the event, is enough to efficiently distinguish ES neutrino from hadronic showers. The value of the cut was obtained using the tail of the distribution of $\langle$AoP$\rangle$ in real data. The tail of the training data was fitted and extrapolated to find the $\langle$AoP$\rangle$ corresponding to less than 1 expected background event per 50 years on the full SD array.

Taking this into account, the optimal cuts obtained were:

- $\langle \text{AoP} \rangle > 1.83$.
- $\text{AoP}_{\text{min}} > 1.4$ if $N_{st} = 3$.

Where the second cut was established to reduce the larger background expected from events with only 3 SD stations and requires that the minimum value of AoP in the 3 stations is >1.4 [22].

Downward-going high neutrino selection

For DGH showers, the algorithm employed is a multivariate analysis (Fisher method [70]) combining several observables that carry information on the time spread of the signals in the SD stations. The analysis, which is optimized with Monte Carlo simulations of UHE ν and the training sample of real data, shows us that the discrimination is better if we divide the DGH category of events into three sets depending on the number of triggered stations: $4 \leqslant N_{st} \leqslant 6$ (DGH low), $7 \leqslant N_{st} \leqslant 11$ (DGH medium) and $N_{st} \geqslant 12$ (DGH high). A different Fisher discriminant is constructed in each set and the cut value is independently optimized.

The linear Fisher discriminants are constructed with ten variables based on the AoP of each station, and taking into account that, due to the large inclination of the shower, the electromagnetic component is larger in the stations that are first hit by a deep inclined shower than in those that are hit last [16, 20]. Based on this, a good discrimination was found when constructing the Fisher discriminant with the AoP and $(\text{AoP})^2$ of the four stations that trigger first in each event, the product of the four AoPs, and a global parameter of the event that is sensitive to the asymmetry between the average AoP of the early stations and those triggering last in the event (see [22] for further details).

An analysis of the efficiency of the cuts is performed in Section 2.2.4, the value of the optimized cuts are:

- Fisher value > 2.17 for DGH low.
- Fisher value > 3.28 for DGH medium.
- Fisher value > 2.91 for DGH high.

The values of the cuts were again obtained using the tails of the distributions of the Fisher values in the real (training) data. The tail was fitted and extrapolated and the Fisher value was obtained using the same criterion as for Earth-skimming neutrinos, corresponding to less than 1 expected background event per 50 years on the full SD array for each multiplicity [22].

2.2.4 Efficiencies of the cuts on simulated neutrino-induced showers

In this section we study the efficiency of the cuts defined as the fraction of simulated events that are kept after each cut in the inclined and neutrino selection. These simulations are detailed in [18,19] and here we only explain them briefly. The simulation process is divided into three steps:

1. First ν interaction and τ decay: This step includes the simulation of the interaction neutrino-nucleon (made with Herwig) and the τ decay when appropriate (made with Tauola).

2. Atmospheric evolution of the shower: The result of the first step is fed as the input of Aires to simulate the shower and propagate it to the surface of the Earth.

3. Surface detector signal: Finally, we can simulate the signal registered by the surface detector stations from the particles on surface using Offline .

In the ES simulations, 150 showers were simulated for each combination of τ energy E_τ, zenith angle θ and decay height h detailed in Table 2.1. For several energies there are two different steps in the simulated decay lengths, on the one hand there is a short step (50 m) for the closest distances (between 0 m to 300 m) and on the other hand there is a large step (100 m) for larger distances, being also simulated a larger angular range in θ for these large step simulations. While in the DGH simulations, 150 showers were simulated for each combination of ν energy E_ν, zenith angle θ and depth interaction X detailed in Table 2.2. In this case instead of use a step in depth interaction X, the simulations are performed considering a determined number of equidistant points.

In Table 2.3, we give the fraction of events passing the inclined cuts over the total number of ES events after the quality cuts, and the resulting fraction when we take into account a weight ω_i for each event as given by the following equation:

$$\omega_i = \cos\theta_i \ \sin\theta_i \ E_i^{-1}, \tag{2.3}$$

with θ_i and E_i the zenith angle and energy of each event. Monte Carlo events have been prepared for an energy distribution with $\mathrm{d}N/\mathrm{dlog}(E) = \text{constant}$, or equivalently $\mathrm{d}N/\mathrm{d}E = \text{constant}/E$, and for fixed zenith angles, but the "real" distribution of neutrino events is assumed to be isotropic and to follow a $\mathrm{d}N/\mathrm{d}E = E^{-2}$ spectrum. The factor $\cos\theta$ is due to the projection of the detector area in the direction perpendicular to the observing direction and factor $\sin\theta$ comes from the solid angle distribution, $\mathrm{d}\varphi\ \mathrm{d}(\cos\theta)$, isotropical in spherical coordinates. In addition, we also give these fractions for the neutrino cuts over the number of events after the inclined cuts.

An important point is that the total efficiency, around 76% obtained from the events after quality cuts, is very dependent on neutrino energy. In Table 2.4 it is shown that the lower the neutrino energy, the lower the efficiency obtained.

In Table 2.5 we give the corresponding efficiencies for the DGH events for each multiplicity (N_{st}) for CC interaction (which is the most efficient channel).

In Table 2.6 we show the efficiency of the cuts for the different interactions CC, NC, TAU for DGH simulations. The result is that the cuts select more efficiently CC interactions (80.04 %) while for NC (71.43 %) and TAU (73.05 %) the efficiency is a bit lower.

Again, the efficiency of DGH selection is dependent on neutrino energy. In Table 2.7 we show that, contrary to the ES channel, the efficiency decreases with neutrino energy.

E_τ [eV]	θ min-max [°]	Step [°]	h min-max [m]	Step [m]
$3.16 \cdot 10^{16}$	$95.884 - 90.111$	0.573	$0 - 600$	100
	$93.549 - 90.111$	0.573	$0 - 300$	50
$5.62 \cdot 10^{16}$	$93.549 - 90.111$	0.573	$0 - 300$	50
10^{17}	$95.884 - 90.111$	0.573	$0 - 700$	100
	$93.549 - 90.111$	0.573	$0 - 300$	50
$1.78 \cdot 10^{17}$	$93.549 - 90.111$	0.573	$0 - 300$	50
$3.16 \cdot 10^{17}$	$95.884 - 90.111$	0.573	$0 - 1000$	100
	$93.549 - 90.111$	0.573	$0 - 300$	50
$5.62 \cdot 10^{17}$	$93.549 - 90.111$	0.573	$0 - 300$	50
10^{18}	$95.884 - 90.111$	0.573	$0 - 1400$	100
	$93.549 - 90.111$	0.573	$0 - 300$	50
$3.16 \cdot 10^{18}$	$95.884 - 90.111$	0.573	$0 - 1300$	100
10^{19}	$95.884 - 90.111$	0.573	$0 - 1300$	100
$3.16 \cdot 10^{19}$	$95.884 - 90.111$	0.573	$0 - 2500$	100

Table 2.1: Parameters (τ energy E_τ, zenith angle θ and decay height h) employed to obtain the ES library.

ν_e CC & ν_x NC			ν_τ CC		
θ [°]	# points	X min-max [g cm^{-2}]	θ [°]	# points	X min-max [g cm^{-2}]
75	30	$0 - 2993$	75	33	$0 - 3325$
80	30	$0 - 3066$	80	48	$0 - 4866$
85	30	$0 - 3540$	85	84	$0 - 8803$
87	30	$0 - 4469$	87	123	$0 - 12968$
88	30	$0 - 5683$	88	165	$0 - 16570$
89	30	$0 - 8599$	89	218	$0 - 22085$
$E_\nu = [5.62 \cdot 10^{16}, 10^{17}, 3.16 \cdot 10^{17}, 10^{18}, 3.16 \cdot 10^{18}, 10^{19}, 3.16 \cdot 10^{19}]$ eV					

Table 2.2: Parameters (ν energy E_ν, zenith angle θ and depth interaction X) employed to obtain the DGH library. The parameters, with the exception of energy, are different depending on the presence or absence of the τ after the first interaction.

	Criteria	Fraction	Fraction in weight
After QC	Total	100 %	100 %
Inclined cuts	$L/W > 5$	92.90 %	96.21 %
	$\langle V \rangle \in [0.29, 0.31]$ m ns^{-1}	91.54 %	95.12 %
	RMS$(V) < 0.08$ m ns^{-1}	91.54 %	95.12 %
	Config. 1 if $N_{st} = 3$	84.94 %	80.58 %
Neutrino cuts	$\langle \text{AoP} \rangle > 1.83$	80.95 %	76.13 %
	$\text{AoP}_{\text{min}} > 1.4$ if $N_{st} = 3$	(95.31) %	(94.48) %

Table 2.3: Statistics of Monte Carlo ES ν_τ applying the inclined and neutrino cuts sequentially. We give the fraction of events over the total after the quality cuts (QC), and the fraction taking into account the weight ω_i of the events with ω_i given in Eq. (2.3). The numbers in brackets in the last row indicate the fractions over the events that have passed the inclined cuts.

$\log E_\tau$ (eV)	17.0	17.5	18.0	18.5
Total after QC	100 %	100 %	100 %	100 %
Cut in L/W	97.95 %	96.16 %	94.56 %	91.07 %
Cut in $\langle V \rangle$	97.44 %	94.49 %	93.27 %	89.51 %
Cut in RMS(V)	97.44 %	94.49 %	93.27 %	89.51 %
Cut in Config. 1	69.31 %	79.73 %	83.21 %	82.83 %
Neutrino Cuts	56.38 %	78.27 %	82.42 %	81.91 %
	(81.34 %)	(98.17 %)	(99.06 %)	(98.90 %)

Table 2.4: Statistics of Monte Carlo ES ν_τ applying the inclined and neutrino cuts sequentially for different E_τ. We give the fraction of events over the total after the quality cuts (QC) taking into account the weight ω_i of the events with ω_i given in Eq. (2.3). The numbers in brackets in the last row indicate the fractions over the events that have passed the inclined cuts.

	Criteria	Fraction	Fraction in weight
After QC	Total	100 %	100 %
Inclined cuts	$L/W > 3$	91.55 %	94.81 %
	$\theta_{rec} > 75°$	80.11 %	86.57 %
	$\langle V \rangle < 0.313$ m ns^{-1}	78.61 %	85.48 %
	RMS$(V)/\langle V \rangle < 0.08$	78.39 %	85.41 %
	BadSpConf=0	73.33 %	80.85 %
Neutrino cuts	Fisher cut	48.48 % (66.11 %)	65.40 % (80.90 %)

(a) Statistics for DGH low multiplicity ($N_{st} \leq 6$).

	Criteria	Fraction	Fraction in weight
After QC	Total	100 %	100 %
Inclined cuts	$L/W > 3$	93.73 %	95.50 %
	$\theta_{rec} > 75°$	81.17 %	84.84 %
	$\langle V \rangle < 0.313$ m ns^{-1}	79.17 %	83.39 %
	RMS$(V)/\langle V \rangle < 0.08$	78.43 %	82.95 %
	BadSpConf=0	77.76 %	82.52 %
Neutrino cuts	Fisher cut	56.44 % (72.58 %)	69.98 % (84.80 %)

(b) Statistics for DGH medium multiplicity ($7 \leq N_{st} \leq 11$).

	Criteria	Fraction	Fraction in weight
After QC	Total	100 %	100 %
Inclined cuts	$L/W > 3$	98.68 %	97.95 %
	$\theta_{rec} > 75°$	90.28 %	86.03 %
	$\langle V \rangle < 0.313$ m ns^{-1}	88.79 %	84.31 %
	RMS$(V)/\langle V \rangle < 0.08$	87.65 %	83.31 %
	BadSpConf=0	87.64 %	83.29 %
Neutrino cuts	Fisher cut	72.20 % (82.38 %)	70.35 % (84.46 %)

(c) Statistics for DGH high multiplicity ($N_{st} \geq 12$).

Table 2.5: Statistics of Monte Carlo DGH ν for CC interaction applying the inclined and neutrino cuts sequentially for each multiplicity. We give the fraction of events over the total after the quality cuts (QC), and the fraction taking into account the weight ω_i of the events with ω_i given in Eq. (2.3). The numbers in brackets in the last row indicate the fractions over the events that have passed the inclined cuts.

	Criteria	CC	NC	TAU
After QC	Total	100 %	100 %	100 %
Inclined cuts	$L/W > 3$	95.38 %	94.86 %	95.63 %
	$\theta_{rec} > 75°$	85.40 %	81.91 %	86.18 %
	$\langle V \rangle < 0.313$ m ns^{-1}	84.14 %	80.51 %	84.97 %
	RMS$(V)/\langle V \rangle < 0.08$	83.96 %	80.30 %	84.79 %
	BadSpConf=0	81.02 %	77.56 %	81.96 %
Neutrino cuts	Fisher cut	64.85 % (80.04 %)	55.40 % (71.43 %)	59.88 % (73.05 %)

Table 2.6: Statistics of Monte Carlo DGH ν applying the inclined and neutrino cuts for all multiplicities sequentially for different channel interactions. We give the fraction of events over the total after the quality cuts (QC) taking into account the weight ω_i of the events with ω_i given in Eq. (2.3). The numbers in brackets in the last row indicate the fractions over the events that have passed the inclined cuts.

$\log E_\nu$ (eV)	17.0	17.5	18.0	18.5
Total after QC	100 %	100 %	100 %	100 %
Cut in L/W	98.77 %	96.56 %	92.74 %	92.17 %
Cut in θ	98.77 %	91.00 %	76.61 %	68.52 %
Cut in $\langle V \rangle$	98.77 %	89.92 %	75.17 %	65.92 %
Cut in RMS(V)	98.77 %	89.92 %	74.94 %	65.57 %
Cut in BadSpConf	97.55 %	86.26 %	70.80 %	63.74 %
Neutrino Cuts	80.30 % (82.32 %)	75.75 % (87.82 %)	54.72 % (77.29 %)	45.08 % (70.72 %)

Table 2.7: Statistics of Monte Carlo DGH ν for CC interaction applying the inclined and neutrino cuts for all multiplicities sequentially for different E_τ. We give the fraction of events over the total after the quality cuts (QC) taking into account the weight ω_i of the events with ω_i given in Eq. (2.3). The numbers in brackets in the last row indicate the fractions over the events that have passed the inclined cuts.

2.3 Characteristics of UHE neutrino-induced showers in the SD

In this section we give a closer look at neutrino simulations with the goal of obtaining a deeper understanding of the relation between the global neutrino properties (energy, zenith angle, decay height h of the τ lepton in the case of Earth-skimming (ES) ν_τ interactions and interaction depth in the case of downward-going (DG) events, etc.), and their characteristics in the SD of Auger (multiplicity, signal and AoP values of the triggered stations, etc.). For this purpose we have analyzed simulations of ES and DG neutrino-induced showers performed with Aires and the $\overline{\text{Off}}\underline{\text{line}}$ framework. In the following we show two different sets of plots taking into account all the simulated neutrino events that trigger the SD, even if they do not pass the inclined or neutrino selection:

- Examples of individual representative neutrino-induced showers in the SD of Auger.
- "Summary plots" in which we group together neutrino-simulated events binned in energy and/or zenith angle.

2.3.1 Earth-skimming neutrino-induced shower simulations

Individual events

In Figs. 2.15 and 2.16 we show several examples of representative neutrino-induced showers.

In each panel of each figure, we show the position of the triggered stations on the ground (i.e. the footprint of the event). Each circle represents one SD station and they are colored from red to violet following the trigger time sequence (red for the earliest trigger time and violet for the latest). Next to each station we give the value of AoP and the fraction of electromagnetic signal in the station as obtained in the simulation.

We also plot the AoP of each station as a function of the trigger time. Information of the simulated event is also given in each plot, namely energy, zenith and azimuth angles, height h of τ decay and mean value of AoP $\langle \text{AoP} \rangle$. All events shown in the figures pass the inclined and neutrino selection cuts, the latter corresponding to $\langle \text{AoP} \rangle > 1.83$.

Inspecting Fig. 2.15 the first thing to note is that the events are highly elongated in the azimuthal direction of arrival, almost aligned in some cases, as expected for almost horizontal events with $\theta = 90.1°$. The AoP of the stations in the event evolves with trigger time with typically larger values in the stations that trigger earlier, indicative of the presence of electromagnetic component arriving spread in time, and smaller values in the stations triggering later indicative of the presence of muons. This interpretation is confirmed by the fraction of electromagnetic signal of the stations also given in the figure, that is typically smaller at later trigger times. In the event produced by a τ decaying

at height $h = 1400$ m (i.e. at the ground level), the values of AoP are typically smaller than those in the events produced by τ decays at larger heights. The reason for this is mainly geometrical, a shower induced closer to the ground evolves less in the lateral direction (perpendicular to the shower axis) in the smaller amount of atmosphere that needs to traverse before reaching ground. As a consequence, the particles spread less in time inducing smaller values of AoP. It is also interesting to note that showers starting at a relatively large height $h = 2000$ m above the ground can still be identified as being induced by a neutrino because due to their large inclination, almost parallel to ground, the electromagnetic component still reaches the stations. All three events depicted in Fig. 2.15 would have been identified as neutrino candidates with high significance given the large values of the discriminating variable $\langle \mathrm{AoP} \rangle$, well above the value of the cut $\langle \mathrm{AoP} \rangle_{\mathrm{cut}} = 1.83$.

The trends are similar in the events depicted in Fig. 2.16. In this case their direction is slightly less horizontal ($\theta = 91.3°$) than those shown in Fig. 2.15. As a consequence the showers starting at ground level $h = 1400$ m have more atmosphere to evolve in the lateral direction before reaching ground inducing larger values of AoP. On the other hand, showers starting high in the atmosphere $h > 2000$ m and being more upward-going, have smaller multiplicities (compare the bottom panels of Figs. 2.15 and 2.16) and smaller probability to trigger the array and to be identified as neutrino candidates.

These trends will become more clear in the following when analyzing the summary plots.

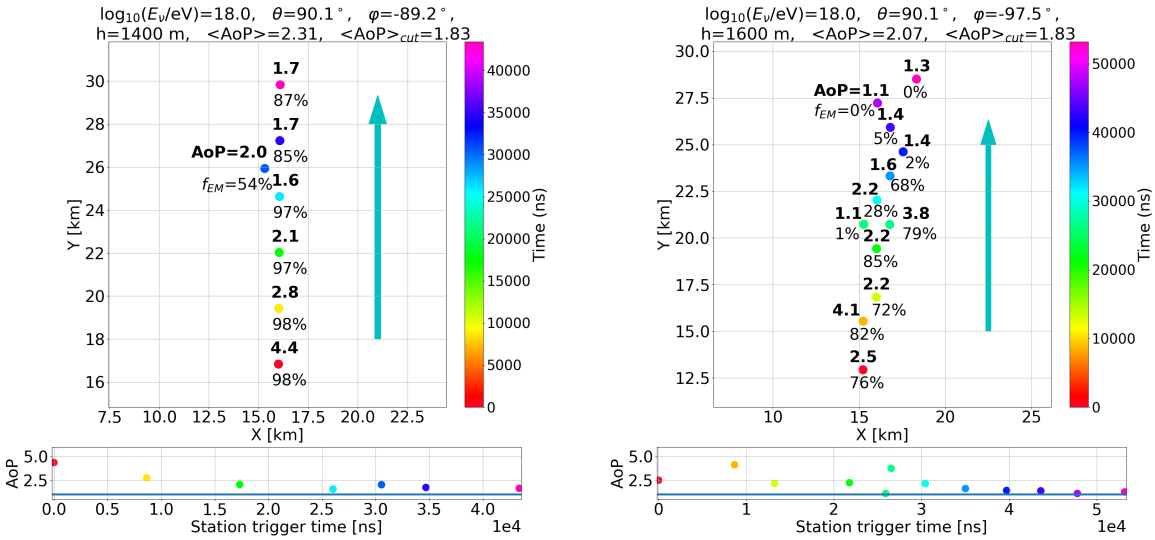

(a) $h = 1400$ m. (b) $h = 1600$ m.

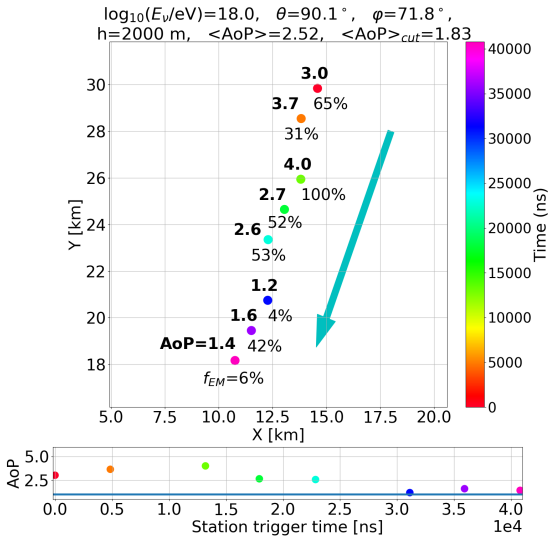

(c) $h = 2000$ m.

Figure 2.15: Examples of Earth-skimming τ-decay induced simulated showers. In each of the three panels (a), (b) and (c) the upper part shows the position of the triggered tanks on the ground, with the numbers on top of each tank indicating the AoP, and the numbers under each tank indicating the fraction of electromagnetic signal detected over the total signal. In the bottom part we show the AoP vs trigger time. The color-coding follows the trigger time sequence from red (earliest) to violet (latest). Information on the events is also given in each panel: $\log_{10}(E_\tau/\text{eV}) = 18$, $\theta = 90.1°$, φ, h of τ decay and $\langle\text{AoP}\rangle$. Panel (a) $h = 1400$ m (τ decay at ground); (b) $h = 1600$ m and (c) $h = 2000$ m.

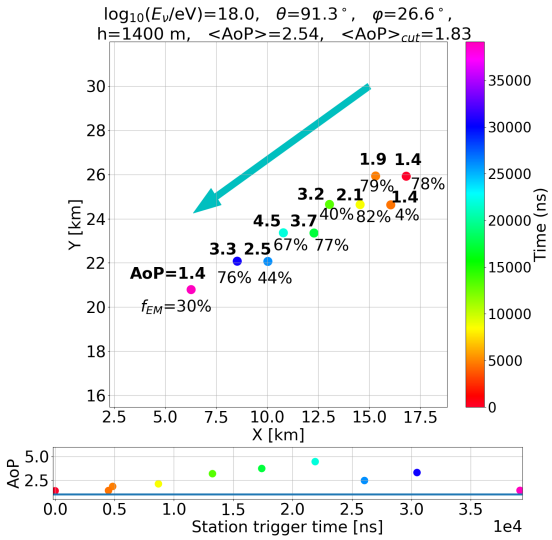

(a) $h = 1400$ m.

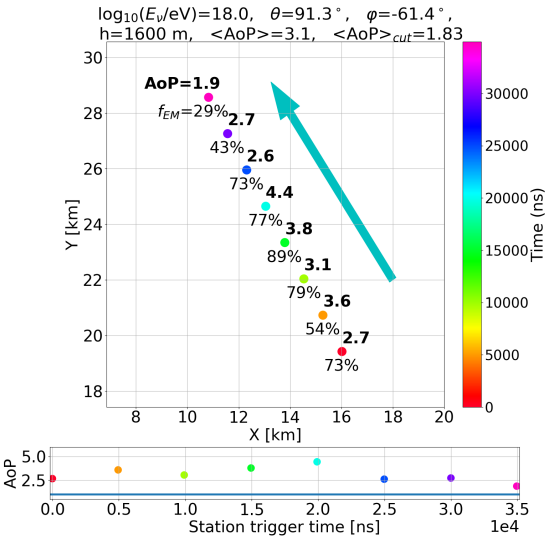

(b) $h = 1600$ m.

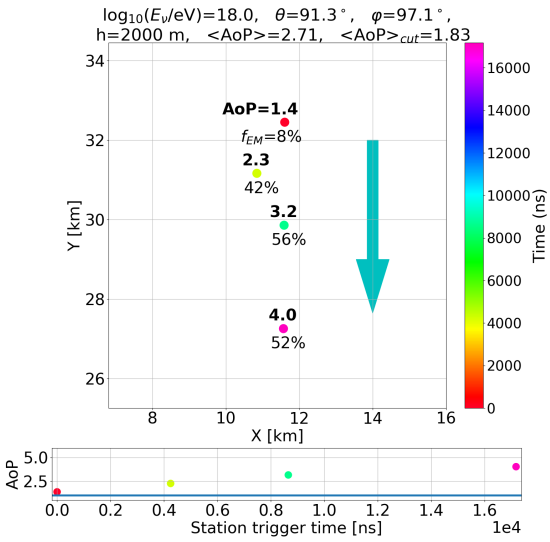

(c) $h = 2000$ m.

Figure 2.16: Same as Fig. 2.15 for $\log_{10}(E_\tau/\text{eV}) = 18$, $\theta = 91.3°$. Panel (a) $h = 1400$ m (τ decay at ground); (b) $h = 1600$ m and (c) $h = 2000$ m.

Summary plots

In addition to inspecting individual events, we have also made an analysis based on "summary plots" that help understading the dependence of the neutrino trigger and identification efficiencies on height of τ decay, zenith angle θ and τ energy E_τ.

In Fig. 2.17 we plot the area defined as:

$$A(E_{\tau \text{ or } \nu}, \theta, h \text{ or } X) = \frac{N_{\text{pass}}(E_{\tau \text{ or } \nu}, \theta, h \text{ or } X)}{N_{\text{tot}}} A_{\text{extended}}, \tag{2.4}$$

with $\frac{N_{\text{pass}}}{N_{\text{tot}}}$ the fraction of simulated events that trigger the surface detector and are identified as neutrino candidates, and A_{extended} the area where the simulations are thrown (more details in Section 3.1.2). The effective area is plotted as a function of height and zenith angle for different energies of the τ. The main result is that in general the closer to ground and more energetic the showers are, the more probable is to trigger the SD of Auger and as consequence the larger the effective area is. At a given height, the range in zenith angle where the effective area is sizeable increases as the shower energy increases for the reasons explained before. Showers of lower energy have a sizeable trigger probability only when their direction is rather close to the horizontal, while at higher energies the tendency is for more upward-going showers to be more likely to trigger.

We have also studied the dependence of the neutrino discriminating variable, namely $\langle \text{AoP} \rangle$ on the height h of τ decay, zenith angle θ and energy E_τ. This is shown in Fig. 2.18. The trends are the same in the three panels: $\langle \text{AoP} \rangle$ increases with h up to a maximum value achieved at a height that is zenith angle and energy dependent, and decreases after that. This behavior can be understood mainly on geometrical grounds. Showers starting higher above sea level have more atmosphere to evolve in the lateral dimension r (perpendicular distance to the shower axis) before reaching ground. As a consequence the particles arriving at the SD stations are more spread in time and induce larger values of $\langle \text{AoP} \rangle$.

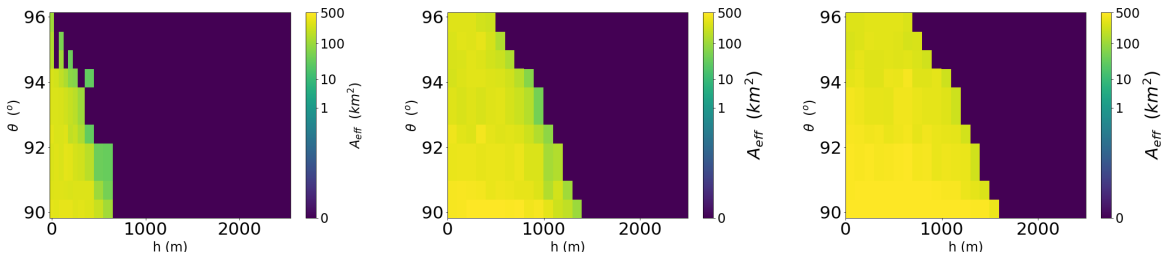

(a) $E_\tau = 10^{17.5}$ eV. (b) $E_\tau = 10^{18.5}$ eV. (c) $E_\tau = 10^{19}$ eV.

Figure 2.17: Color scale: Effective area in km^2 (defined in Eq. (2.4)) for simulated ES neutrinos as a function of height h of τ decay and zenith angle θ for τ leptons with energy: Panel (a) $E_\tau = 10^{17.5}$ eV; (b) $E_\tau = 10^{18.5}$ eV and (c) $E_\tau = 10^{19}$ eV.

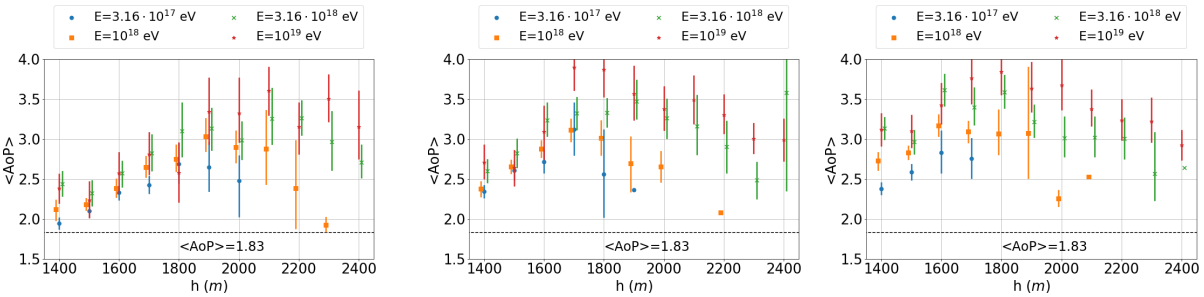

(a) $\theta \sim 90°$. (b) $\theta \sim 91°$. (c) $\theta \sim 92°$.

Figure 2.18: $\langle \text{AoP} \rangle$ vs height h of τ decay for several τ energies and zenith angles θ: Panel (a) $\theta \sim 90°$; (b) $\theta \sim 91°$ and (c) $\theta \sim 92°$. For reference the value of the discriminating variable $\langle \text{AoP} \rangle$ above which an event would be regarded as a neutrino candidate $\langle \text{AoP} \rangle_{\text{cut}} = 1.83$ is indicated as a dashed horizontal black line.

However, above a certain height the larger amount of atmosphere between shower axis and ground (larger r) attenuates the electromagnetic component to the extent that only muons reach the SD stations. Since muons follow straighter paths than the electromagnetic component their spread in time is smaller and as a consequence $\langle \text{AoP} \rangle$ decreases. This also explains why the decline of $\langle \text{AoP} \rangle$ starts at an increasingly larger value of h as energy increases: for a given height, the higher the shower energy the larger the thickness of atmosphere the electromagnetic component can traverse before reaching ground. On the contrary, as can be clearly seen in Fig. 2.18 as the zenith angle increases $\langle \text{AoP} \rangle$ reaches a maximum value at smaller values of h. This is due to the attenuation of the electromagnetic component because, for a given height, showers develop farther from ground as the zenith angle increases.

Finally it is important to remark that Fig. 2.18 only informs about the ranges of decay height h of the τ, zenith angle θ and energy E_τ in which the discriminating variable $\langle \text{AoP} \rangle$ achieves the largest values, and hence the significance of a neutrino detection would be larger, but they do not inform about the range in h, θ and E_τ where most of the events are expected to be identified. These depend on the effective area (proportional to the trigger probability) shown in Fig. 2.17 as well as on the energy spectrum assumed.

2.3.2 Downward-going neutrino-induced shower simulations

We now repeat the study for the case of downward-going neutrinos interacting in the atmosphere at a depth X measured in the slanted direction from ground.

Individual events

In Figs. 2.19 and 2.20 we show several examples of representative DG neutrino-induced showers. We show again the position of the triggered stations on the ground, with each circle representing one SD station colored from red to violet following the trigger time sequence (red for the earliest trigger time and violet for the latest). Although the values of AoP of all stations are not directly used in the identification of DG neutrinos, but instead functions of AoP are combined in a more complex Fisher discriminant variable (see Section 2.2.3), we also show the AoP of each station as a function of trigger time for comparison with ES events. Information on the simulated event is also given in each plot, namely energy, zenith and azimuth angles, depth X of ν interaction (measured in the slanted direction from ground) and value of the Fisher discriminant. All events shown in the figures pass the inclined and neutrino selection cuts, with the value of the cut in the Fisher variable also indicated in the plots.

Inspecting Fig. 2.19 and as in the case of ES events, the events are highly elongated in the azimuthal arrival direction. The AoP of the stations evolves with trigger time and the asymmetry between the early and late parts of the showers, one of the variables that enter in the Fisher discriminant is apparent. The AoP is larger in the stations that trigger earlier compared to those in the stations triggering later. This behaviour follows the evolution of the electromagnetic component along the arrival direction of the event, that suffers less attenuation in the early part of the shower compared to the later one. This is confirmed by the fraction of electromagnetic signal of the stations also given in the figure, that is typically smaller at later trigger times. In the event shown in Fig. 2.19 corresponding to the neutrino that interacts closest to ground at depth $X = 761$ g/cm^2 (measured from the ground in the slanted direction so that $X = 0$ g/cm^2 would correspond to showers injected at ground), the values of AoP in the earlier stations are smaller than those in the events produced by interactions farther from the ground. The reason for this is also geometrical: a shower induced closer to the ground evolves less in the smaller amount of atmosphere that crosses before reaching ground and as a consequence, the particles spread less in time inducing smaller values of AoP. The AoP increases with depth up to a value $\tilde{X}(E_\nu, \theta)$. As will become clear in the following when inspecting the summary plots, if the shower is sufficiently far away from ground the electromagnetic component is attenuated so that only muons reach ground and, as a consequence, the values of AoP are typically small (close to 1) in all the stations. The three events depicted in Fig. 2.19 would have been identified as neutrino candidates with high significance given the large values of the discriminating Fisher variable, well above the value of the corresponding Fisher cuts that depend on the multiplicity of the considered event.

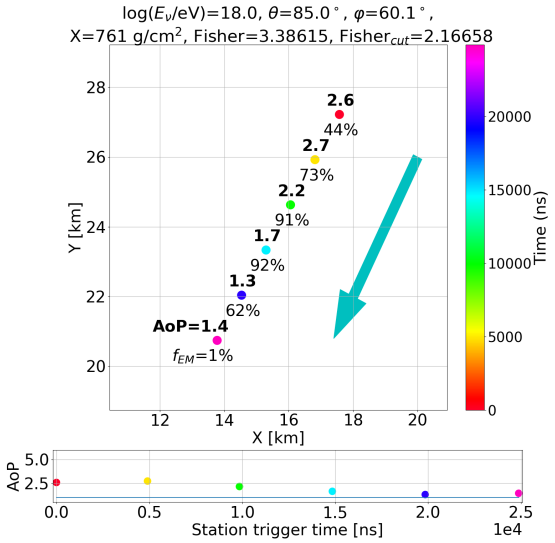

(a) $X = 761$ g/cm^2.

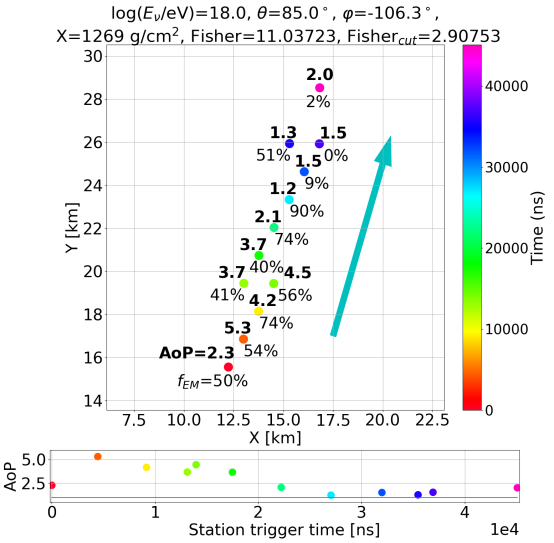

(b) $X = 1269$ g/cm^2.

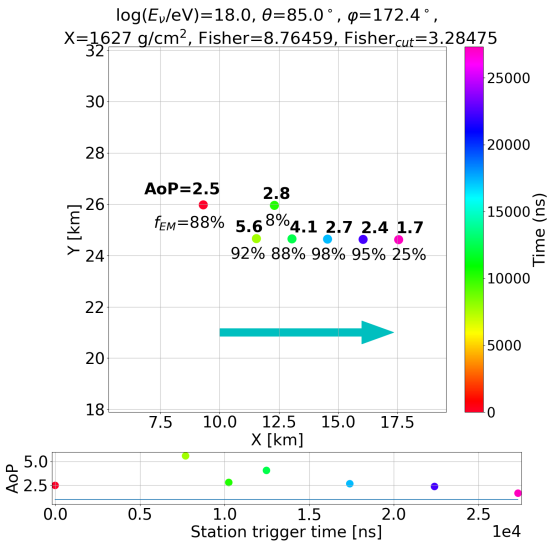

(c) $X = 1627$ g/cm^2.

Figure 2.19: Examples of downward-going high CC simulated showers. In each of the panels (a), (b) and (c) the upper part shows the position of the triggered tanks on the ground, with the numbers on top indicating the AoP, and the numbers under indicating the fraction of electromagnetic signal over the total signal. In the bottom part we show AoP vs trigger time. The color-coding follows the trigger time sequence from red (earliest) to violet (latest). Information on the events is also given in each panel: $\log_{10}(E_\nu/\text{eV}) = 18$, $\theta = 85°$, φ angle, depth X of neutrino interaction (measured in the slanted direction from ground) and Fisher value. Panel (a) $X = 761$ g/cm^2 ($X = 0$ g/cm^2 corresponds to showers injected at ground); (b) $X = 1269$ g/cm^2 and (c) $X = 1627$ g/cm^2.

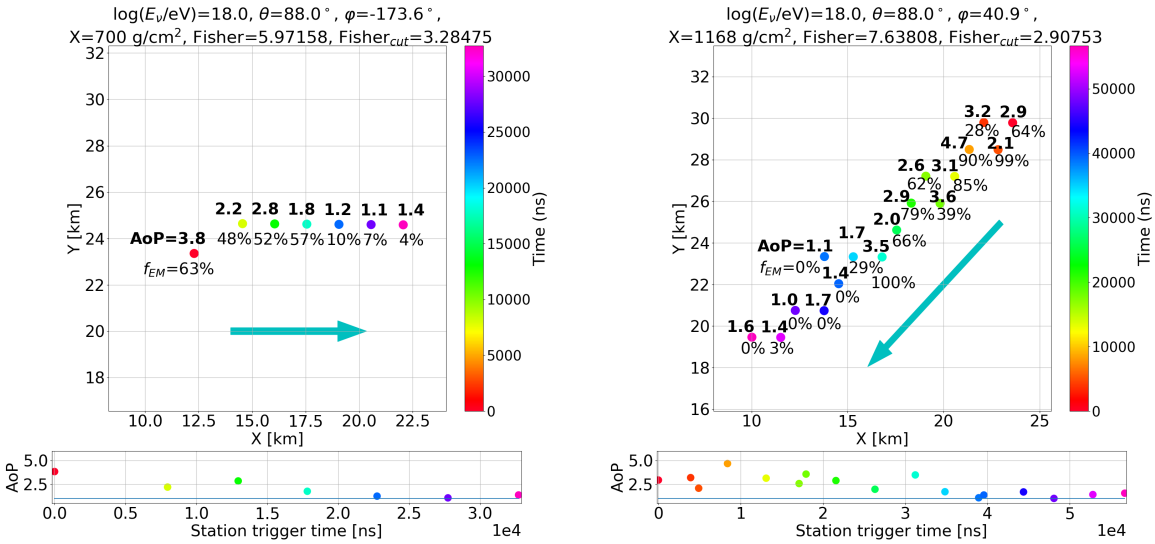

(a) $X = 700$ g/cm^2. (b) $X = 1168$ g/cm^2.

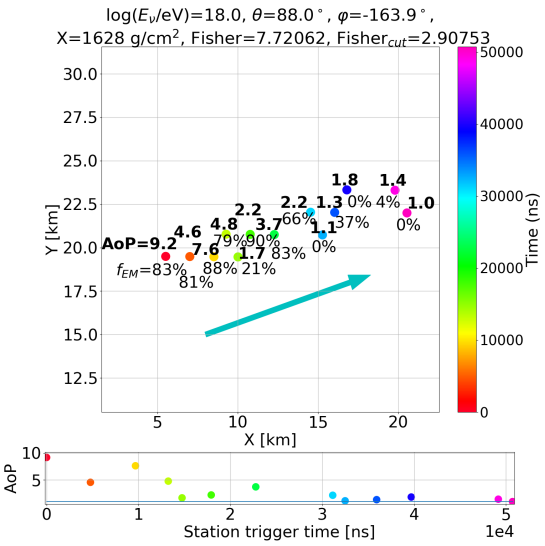

(c) $X = 1628$ g/cm^2.

Figure 2.20: Same as Fig. 2.19 for $\log_{10}(E_\nu/\text{eV}) = 18$, $\theta = 88°$. Panel (a) $X = 700$ g/cm^2; (b) $X = 1168$ g/cm^2 and (c) $X = 1628$ g/cm^2.

The trends are similar in the events depicted in Fig. 2.20. In this case their direction is more horizontal ($\theta = 88°$) than those shown in Fig. 2.19 ($\theta = 85°$). As a consequence the showers are even more aligned and elongated, and trigger on average a larger number of stations. Also the asymmetry of AoP and of the electromagnetic component between the early and late parts of the shower is stronger than in the events shown in Fig. 2.19. The electromagnetic component almost completely attenuates in the large amount of atmosphere to cross before reaching ground at $\theta = 88°$ and only muons survive as reflected in the small values of the fraction of electromagnetic component in some of the latest stations.

These trends will become more clear in the following when analyzing the summary plots.

Summary plots

In addition to inspecting individual DG neutrino events, we also made an analysis based on "summary plots" that help understading the dependence of the trigger efficiencies on the depth of neutrino interaction X, the zenith angle θ and the neutrino energy E_ν. The plots shown are all for the DGH high channel (event multiplicities above 11). Equivalent plots for events with medium and low multiplicities show similar trends.

In Fig. 2.21 we plot the effective area (defined in Eq. (2.4)) as a function of depth and zenith angle for different neutrino energies. The range in depth where the effective area is sizeable increases with energy and zenith angle. For fixed energy and zenith angle, the effective area is small for neutrino-induced showers initiated very close to ground, because these showers have not evolved enough in the amount of atmosphere available before reaching ground and then they either do not trigger a minimum of 3 stations to be considered a T3 event, or their electromagnetic component does not arrive sufficiently scattered and spread in time to produce values of AoP above 1. The effective area is also small for neutrinos interacting far from the ground, because in this case the electromagnetic component is absorbed before reaching ground and only muons survive inducing small values of AoP in the stations (and hence small values of the Fisher discriminant).

We have also studied the behavior of the neutrino discriminating variable, namely the Fisher value, on neutrino interaction depth, X, zenith angle, θ, and energy, E_ν. This is depicted in Fig. 2.22 where in the top panel we show the average Fisher value as a function of neutrino interaction depth for several neutrino energies and a fixed angle of $\theta = 85°$, while in the bottom panel we fixed instead the energy to $E_\nu = 10^{19}$ eV and show the average Fisher value for several zenith angles.

In both panels the Fisher value increases with depth reaching a maximum value at $\tilde{X} \in (1000, 1500)\mathrm{g/cm^2}$, and decreases after that. The explanation of this behaviour is similar to the one given for the effective area. Showers induced by neutrinos interacting close to ground have not yet evolved enough in the atmospheric depth available before reaching ground, and then their electromagnetic component of the shower is not sufficiently developed to produce values of AoP above 1 and hence to lead to large Fisher

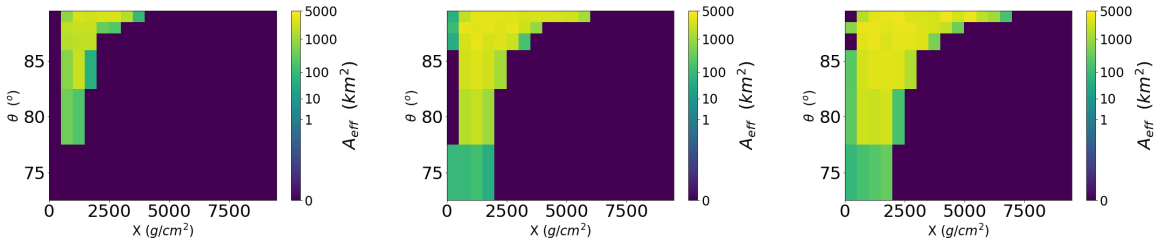

(a) $E_\nu = 10^{17.5}$ eV. (b) $E_\nu = 10^{18.5}$ eV. (c) $E_\nu = 10^{19}$ eV.

Figure 2.21: Color scale: Effective area in km^2 (defined in Eq. (2.4)) for simulated DGH CC electron neutrinos as a function of depth X of neutrino interaction (measured in the slant direction from ground) and zenith angle θ for neutrinos with energy: Panel (a) $E_\nu = 10^{17.5}$ eV; (b) $E_\nu = 10^{18.5}$ eV and (c) $E_\nu = 10^{19}$ eV.

values. Also for neutrinos interacting far from the ground, the electromagnetic component can be partially absorbed before reaching ground, the surviving muons, inducing small values of AoP at the stations, dominate the shower front and lead to smaller values of the Fisher discriminant. One can see that there is an optimal region in depth depending on the zenith angle of the shower and on the energy, where the Fisher values are largest and hence neutrinos are identified with the largest significance. The decline of Fisher value starts at an increasingly larger value of X as energy increases because for a given depth, the higher the shower energy the more penetrating the electromagnetic component is. A decline can also be seen with decreasing zenith angle. For a given neutrino interaction depth X, the smaller the zenith angle, the higher above ground the shower starts in the atmosphere and the more attenuated the electromagnetic component is, inducing smaller values of the Fisher discriminant.

Finally, as in the case of the ES showers, it is important to note that Fig. 2.22 only informs about the ranges of ν-interaction depth, zenith angle and energy E_ν in which the Fisher discriminating variable achieves the largest values, and hence the significance of a neutrino detection would be highest, but they do not inform about the ranges where most of the events are expected to be identified. These depend also on the trigger efficiency (proportional to the effective area shown in Fig. 2.21), as well as on the energy spectrum assumed for the neutrinos.

The same analysis for other multiplicities (DGH medium and DGH low) and other interactions (NC and CC interactions of ν_τ) was also performed, but it is not shown here because the trends are very similar to the DGH high and ν_e CC case. There are some differences in the case of the ν_τ CC channel, in the effective area for the different interactions, but this is going to be further explained in Section 3.1.2.

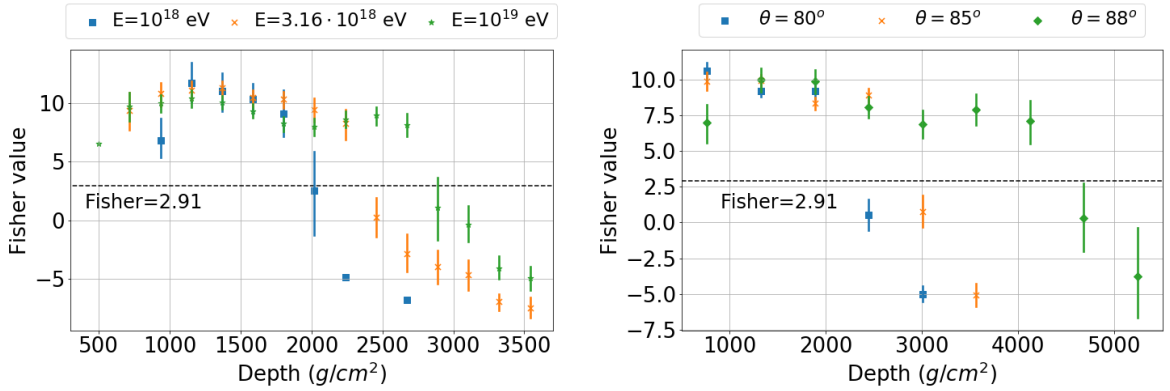

(a) Plot for different E_ν with $\theta = 85°$.

(b) Plot for different θ with $E_\nu = 10^{19}$ eV.

Figure 2.22: Fisher value vs depth X for DGH ν_e CC interaction (that triggers 12 or more SD stations - DGH high channel): Panel (a) Plot for different E_ν with $\theta = 85°$ and (b) Plot for different θ with $E_\nu = 10^{19}$ eV. For reference the value of the discriminating variable (Fisher value) for the DGH high channel above which an event would be regarded as a neutrino candidate $\text{Fisher}_{\text{cut}} = 2.91$ is indicated as a dashed horizontal black line.

2.3.3 Real (background) events

Individual events

In Fig. 2.23 we show several representative examples of real events induced by cosmic rays.

In each panel of each figure, we show again the position of the triggered stations on the ground (i.e. the footprint of the event), as well as the AoP as a function of the trigger time of each station. Each circle represents one SD station and they are colored from red to violet following the trigger time sequence (red for the earliest trigger time and violet for the latest). Information on the real event is also given in each plot, namely event ID, UTC time, and mean value of AoP $\langle \text{AoP} \rangle$ or the Fisher value (depending on which is the relevant variable), as well as the cut value for this variable. All events shown in the figures pass the inclined selection cuts, but not neutrino cuts since no neutrino has been detected.

Inspecting Fig. 2.23 the main difference with the neutrino-induced events in Figs. 2.19, 2.20 and Figs. 2.15, 2.16 is that the AoP of almost all the stations is close to 1. This fact makes that the $\langle \text{AoP} \rangle$ for the ES selection or the Fisher value for the DGH selection is below the cut value and as a consequence all real events passing the inclined cuts are classified as background.

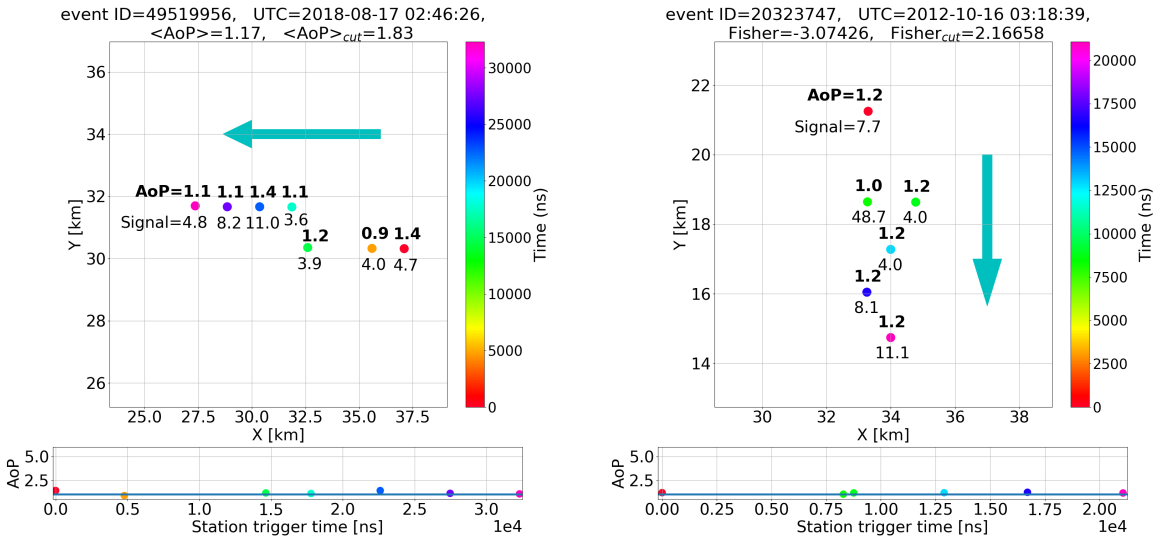

(a) ES. (b) DGH low.

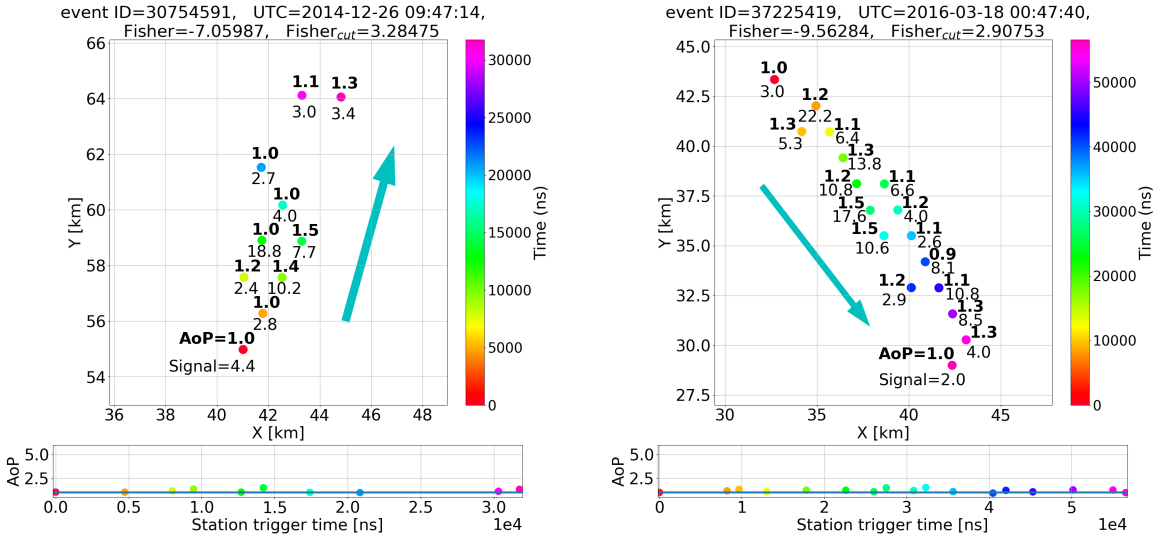

(c) DGH medium. (d) DGH high.

Figure 2.23: Examples of real events detected with the SD. In each of the panels (a), (b), (c) and (d) the upper panel shows the position of the triggered tanks on the ground, with the numbers on top indicating the AoP, and the numbers under indicating the signal detected. In the bottom part we show the AoP vs trigger time. The color-coding follows the trigger time sequence from red (earliest) to violet (latest). Information on the events is also given in each panel: event ID, UTC time and $\langle \text{AoP} \rangle$ for the ES event or Fisher value for the DGH events. Panel (a) event passing the ES: inclined cuts; (b) DGH low inclined cuts; (c) DGH medium inclined cuts and (d) DGH high inclined cuts.

2.4 Search for UHE neutrinos

The search strategy is detailed in Section 2.2.3. It consists on selecting showers that arrive in the inclined directions at the SD array and identifying those that show a broad time structure in the signals induced in the SD stations. Such signals are the signature of a shower developing close to the ground characteristic of ν-induced events. To define the selection algorithms and optimize the numerical values of the cuts employed to identify neutrino-induced showers we performed a blind analysis. A fraction of $\sim$ 15 % of the whole data sample (from 1 January 2004 up to 31 August 2018), along with Monte Carlo simulations of UHE neutrinos, is dedicated to obtain the selection algorithms, the most efficient observables for neutrino identification, and the value of the cuts. This "training" data set is assumed to be constituted of background UHECR-induced showers, while the remaining fraction of data ("search data") is only "unblinded" to search for neutrino candidates after the selection procedure is established.

The only difference with the strategy explained in Section 2.2.3 is that we have to take into account that the Surface Detector is not always working properly. The intervals when this occurs are classified as "Bad Periods" by the Pierre Auger Collaboration [71], and we discard all the events that trigger in them.

In Fig. 2.24 we show the Bad Periods as a function of time. They correspond to 8.7% of the total lifetime of Auger at the 31 August 2018.

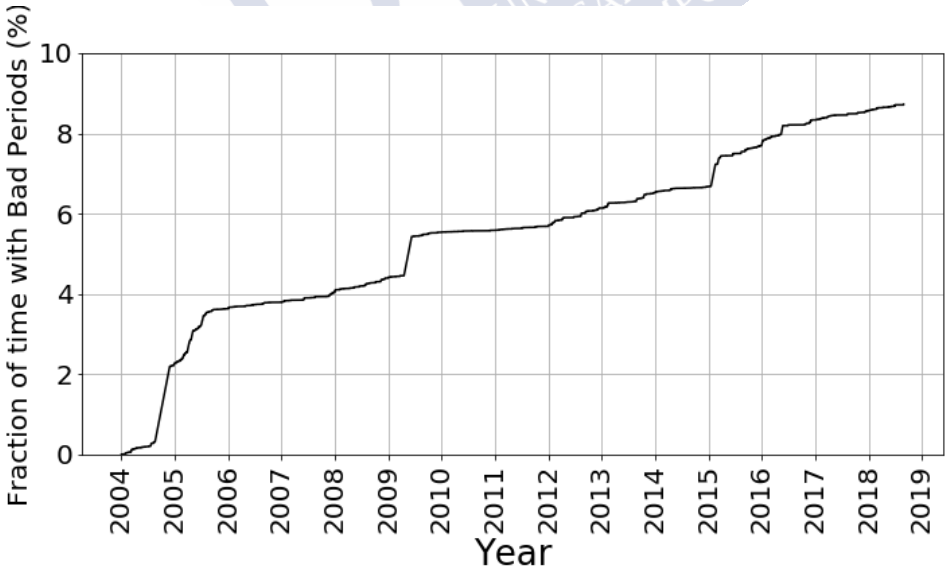

Figure 2.24: Fraction of Bad Periods time over the total lifetime of Auger versus the year.

	Criteria	Fraction
After QC	Total	100 %
Inclined cuts	$L/W > 5$	15.18 %
	$\langle V \rangle \in [0.29, 0.31]$ m ns^{-1}	6.64 %
	RMS$(V) < 0.08$ m ns^{-1}	6.63 %
	Config. 1 if $N_{st} = 3$	6.54 %
Neutrino cuts	$\langle \text{AoP} \rangle > 1.83$	0 %
	$\text{AoP}_{\text{min}} > 1.4$ if $N_{st} = 3$	

Table 2.8: Statistics of real events applying the ES inclined and neutrino cuts sequentially. We give the fraction of events over the total events after the quality cuts (QC).

2.4.1 Efficiencies of the cuts on real showers

In this section we perform a study of the efficiency of the cuts to reject background events, analogous to the one in Section 2.2.4. In Table 2.8, we give the fraction of events that are kept after each cut in the inclined and neutrino selection over the total after the quality cuts (see Section 2.2.3) for the Earth-skimming selection. Only $\sim 6.5\%$ of the preselected events pass the ES inclined (almost horizontal) cuts[3] with no events passing the final neutrino cuts.

The same study is performed for the downward-going high selection. In Table 2.9 we give the fractions of events that are kept after each cut for the DGH selection for the different subsets depending on multiplicity in which the selection is divided.

2.4.2 Distributions of inclined events

In this section we show the distribution of the $\langle \text{AoP} \rangle$ (Fisher value) for Earth-skimming (downward-going high) inclined selections.

For data previous to 31 May 2010, the neutrino ES identification included the condition that the fraction of stations with Time-over-Threshold (ToT) trigger and having AoP > 1.4 [58] was above 60 % of the triggered stations in the event. For data after 1 June 2010, an improved selection is employed using the average value of AoP ($\langle \text{AoP} \rangle$) over all the triggered stations in the event to distinguish between hadronic showers and ES neutrinos. The value of the cut on $\langle \text{AoP} \rangle$ is fixed using the tail of the distribution of $\langle \text{AoP} \rangle$ in real data, which is consistent with an exponential function. Following the chosen criteria for backgroundt its tail is fitted and extrapolated to find the value of $\langle \text{AoP} \rangle$ corresponding to less than 1 expected background event per 50 yr on the full SD array (more details in [22]).

[3]One should keep in mind that preselected events include all events with $\theta \gtrsim 58^\circ$ while events selected with the ES cuts are almost horizontal.

	Criteria	Fraction
After QC	Total	100 %
Inclined cuts	$L/W > 3$	53.46 %
	$\theta_{rec} > 75°$	19.84 %
	$\langle V \rangle < 0.313$ m ns^{-1}	16.70 %
	RMS$(V)/\langle V \rangle < 0.08$	16.37 %
	BadSpConf=0	14.21 %
Neutrino cuts	Fisher cut	0 %

(a) Statistics for DGH low multiplicity ($N_{st} \leq 6$).

	Criteria	Fraction
After QC	Total	100 %
Inclined cuts	$L/W > 3$	55.40 %
	$\theta_{rec} > 75°$	29.10 %
	$\langle V \rangle < 0.313$ m ns^{-1}	25.38 %
	RMS$(V)/\langle V \rangle < 0.08$	24.51 %
	BadSpConf=0	24.32 %
Neutrino cuts	Fisher cut	0 %

(b) Statistics for DGH medium multiplicity ($7 \leq N_{st} \leq 11$).

	Criteria	Fraction
After QC	Total	100 %
Inclined cuts	$L/W > 3$	61.12 %
	$\theta_{rec} > 75°$	42.94 %
	$\langle V \rangle < 0.313$ m ns^{-1}	39.90 %
	RMS$(V)/\langle V \rangle < 0.08$	37.09 %
	BadSpConf=0	37.09 %
Neutrino cuts	Fisher cut	0 %

(c) Statistics for DGH high multiplicity ($N_{st} \geq 12$).

Table 2.9: Statistics of real events applying the DGH inclined and neutrino cuts sequentially. We give the fraction of events over the total events after the quality cuts (QC).

Applying these criteria, a search for ES neutrino-induced showers is performed in the Observatory data from 1 January 2004, when data taking started, up to 31 August 2018. No neutrino candidates are identified. In Fig. 2.25a we show the distribution of $\langle$AoP$\rangle$ for the whole data period compared to that expected in Monte Carlo simulations of ν_τ-induced ES showers, along with the optimized value of the cut ($\langle$AoP$\rangle = 1.83$) above which an event would be regarded a neutrino candidate. After the inclined selection and

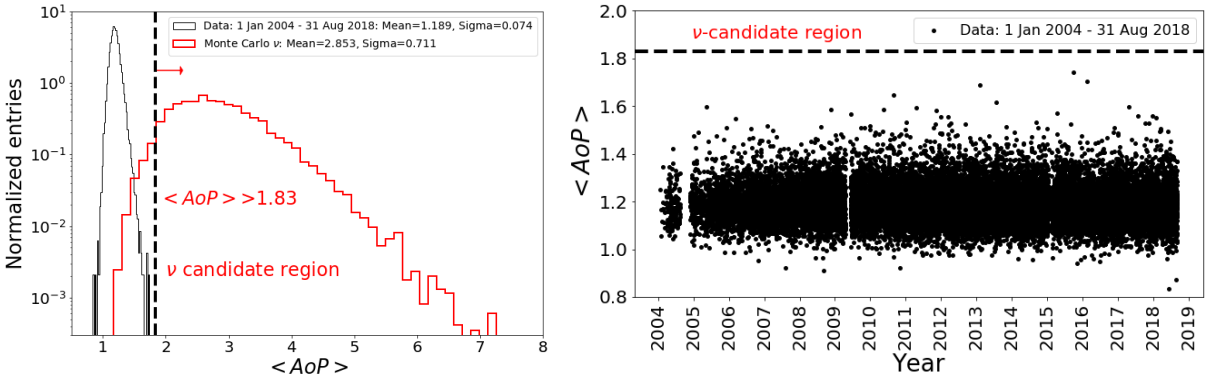

(a) ⟨AoP⟩ for ES.

(b) ⟨AoP⟩ vs time for ES.

Figure 2.25: (a) Distribution of ⟨AoP⟩ after the Earth-skimming inclined selection. Black histogram: full data set up to 31 August 2018 containing 26120 events. Red histogram: Monte Carlo simulated ES ν_τ events. (b)⟨AoP⟩ vs time after the Earth-skimming inclined selection.

the neutrino identification criteria, $\sim$ 95% of the simulated neutrinos that induce triggers are kept, as it is detailed in Section 2.2.4. This proves that the Pierre Auger Observatory is highly efficient as a neutrino detector, with its sensitivity mostly governed by its lifetime and the available target matter for neutrino interactions along the Earth's chord. The neutrino search is not limited by the background due to UHECR-induced showers since this can be very efficiently reduced as shown in Fig. 2.25a.

In Fig. 2.25b we show the ⟨AoP⟩ as a function of the time. The distribution is the same as in Fig. 2.25a with a large amount of data around ⟨AoP⟩ =1.2. Some large Bad Periods can be seen like the one from August to November in 2004 or the one from April to June in 2009.

In the DGH channel, the linear Fisher discriminants are constructed with ten variables that exploit the fact that the electromagnetic component is less attenuated in the stations that are first hit by a deep inclined shower than in those that are hit last due to the large inclination of the shower [16, 20]. These variables are: the AoP and $(\text{AoP})^2$ of the four stations that trigger first in each event, the product of the four AoPs, and a global parameter of the event that is sensitive to the asymmetry between the average AoP of the early stations and those triggering last in the event

Once the Fisher discriminant $\mathcal{F}$ is defined (more details in Section 2.2.4), an optimized value for the cut is selected to efficiently distinguish neutrino candidates from regular hadronic showers for the three DGH multiplicy sets. Each value is chosen performing an exponential fit to the corresponding Fisher distribution of the training data, extrapolating it, and requiring less than 1 event per 50 yr on the full SD array [22].

Applying these criteria, a search for DGH neutrino-induced showers is performed in the Observatory data since 1 January 2004 up to 31 August 2018. No neutrino candidates

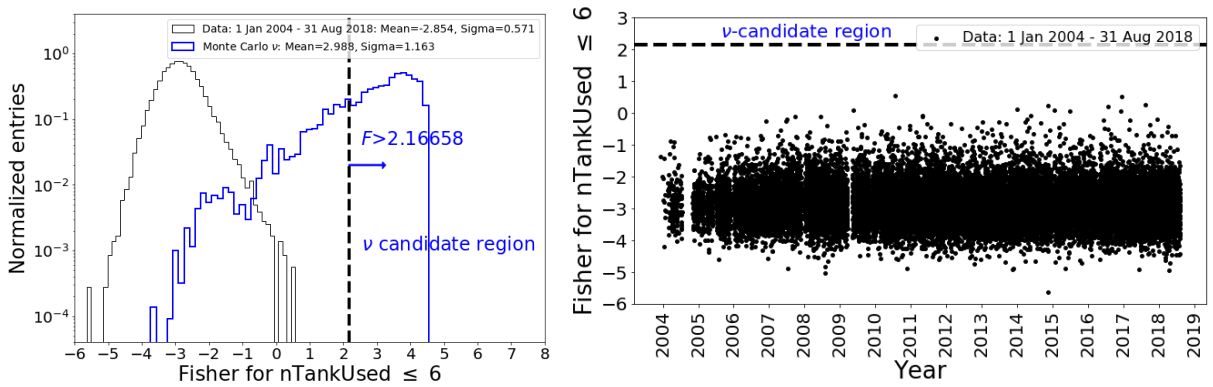

(a) Fisher for DGH low.

(b) Fisher vs time for DGH low.

Figure 2.26: (a) Distribution of the Fisher variable after the downward-going inclined event selection for events with number of triggered stations 6 or less (DGH low). Black histogram: full data set up to 31 August 2018 containing 29768 events. Blue histogram: Monte Carlo simulated charged-current ν DGH events. (b): Fisher value vs time after the DGH low inclined event selection.

are identified in any of the three subcategories of DGH.

In Figs. 2.26a, 2.27a and 2.28a, we show the distribution of the Fisher variable in DGH for the three subsamples for the whole data period compared to that expected in Monte Carlo simulations of CC ν-induced DGH showers, as well as the optimized value of the respective cut above which an event would be regarded a neutrino candidate. Of all the simulated inclined ν events that trigger the Observatory, a weighted fraction between $\sim$ 81 % and $\sim$ 85 % (depending on multiplicity N_{stat}) are kept after the cuts on the Fisher variable in the DGH analysis (more details in Section 2.2.4).

In Figs. 2.26b, 2.27b and 2.28b we show the Fisher variable in DGH for the three subsamples as a function of the time. The distribution is the same as in Figs. 2.26a, 2.27a and 2.28a, being a large amount of data around Fisher $= -3, -6$ and -9, respectively. Some large Bad Periods can be seen like the one from August to November in 2004 or the one from April to June in 2009.

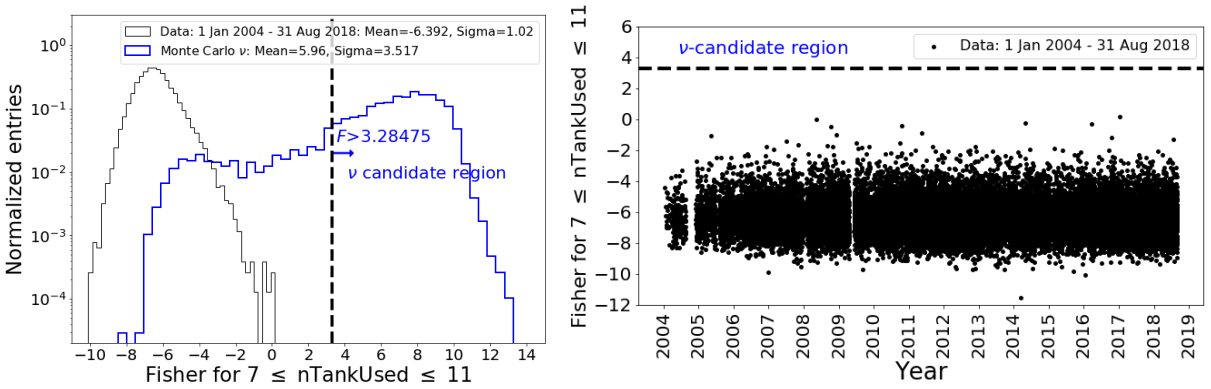

(a) Fisher for DGH medium.

(b) Fisher vs time for DGH med.

Figure 2.27: (a) Distribution of the Fisher variable after the downward-going inclined event selection for events with number of triggered stations between 7 and 11 (DGH medium). Black histogram: full data set up to 31 August 2018 containing 33997 events. Blue histogram: Monte Carlo simulated charged-current ν DGH events. (b): Fisher value vs time after the DGH medium inclined event selection.

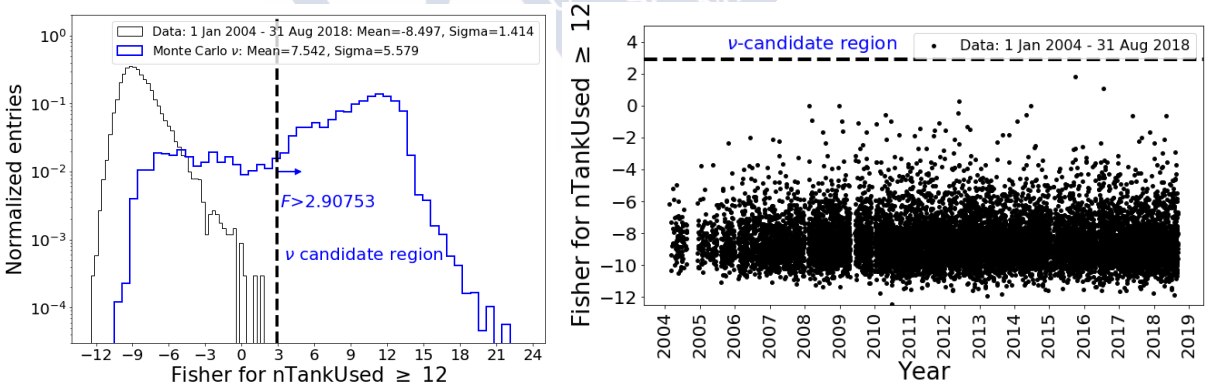

(a) Fisher for DGH high.

(b) Fisher vs time for DGH high.

Figure 2.28: (a) Distribution of the Fisher variable after the downward-going inclined event selection for events with number of triggered stations 12 or higher (DGH high). Black histogram: full data set up to 31 August 2018 containing 12199 events. Blue histogram: Monte Carlo simulated charged-current ν DGH events. (b): Fisher value vs time after the DGH high inclined event selection.

USC
UNIVERSIDADE
DE SANTIAGO
DE COMPOSTELA

3

Limits to diffuse and point-like fluxes of UHE neutrinos

3.1 Diffuse fluxes

In the previous chapter we reported that no neutrino candidates were found so an upper limit to the diffuse flux of UHE neutrinos can be established. To obtain the limit it is necessary to calculate the exposure of the SD of Auger for the period of data taking. This is done with Monte Carlo simulations of neutrino-induced showers to which we applied the same selection and identification criteria that we applied to the data. The identification efficiencies, ε, for each channel were obtained as the fraction of simulated events that trigger the Observatory and pass the inclined selection and identification cuts [20].

In the following we explain the calculation of the exposure of the SD of Auger to a diffuse flux of UHE neutrinos for the different channels separately.

For **downward-going neutrinos**, the identification efficiency, $\varepsilon_{i,c}$, depends on neutrino flavor $i = \nu_e, \nu_\mu, \nu_\tau$, the type of interaction (c = CC, NC), zenith θ and azimuth φ angles, neutrino energy E_ν, the point of impact of the shower core on the ground, and the depth in the atmosphere X measured along the shower axis at which the neutrino is forced to interact in the simulations [20, 22]. Moreover, the identification efficiency has some dependence on time because the SD array grew continuously from 2004 up to its completion in 2008, and, to a lesser degree, because the number of working stations fluctuates constantly with time (the fraction of working stations is generally above 95%). For downward-going neutrinos the computation of the exposure involves folding the detection

efficiencies with the area of the SD projected onto the direction perpendicular to the arrival direction of the neutrino, and with the ν interaction probability for a neutrino energy E_ν at a depth X that also depends on the type of interaction (CC or NC). So for each flavor i and channel c we obtain the exposure integrating the detection efficiency $\varepsilon_{i,c}$ over the parameter space ($\theta,\ \varphi,\ X$), detector area, and time over the search period [20, 22],

$$\mathcal{E}_{i,c,\mathrm{DG}}(E_\nu) = \int_A \int_\theta \int_\varphi \int_X \int_t \cos\theta \sin\theta\ \varepsilon_{i,c}\ \sigma_\nu^c\ m_\mathrm{p}^{-1}\ \mathrm{d}A\ \mathrm{d}\theta\ \mathrm{d}\varphi\ \mathrm{d}X\ \mathrm{d}t, \tag{3.1}$$

where $\varepsilon_{i,c}$ is the detection efficiency for a neutrino flavor i and type of interaction c. The efficiency is calculated using simulations of extensive air showers. It includes an average over the fraction of energy y transferred to the nucleus in the collision, and it depends on both energy and zenith angle of the neutrino. As a function of neutrino interaction depth X, the efficiency is maximized when X is such that the shower maximum is approximately reached at ground level. Additionally, it also depends on the impact point of the shower at the ground and on the instantaneous configuration of the SD (which changed substantially until deployment was completed in May 2008). σ_ν^c is the neutrino-nucleon cross-section [35] and m_p is the proton mass.

The term $\sigma_\nu^c\ m_p^{-1}\ \mathrm{d}X$ represents the probability of neutrino-nucleon interactions along a depth $\mathrm{d}X$ (in $\mathrm{g\,cm^{-2}}$) with $\sigma_\nu^c\ m_p^{-1}$ representing the ν-nucleon interaction length. Summing over channels (CC and NC) and neutrino flavors, weighting each with the relative flavor ratios (for instance weight 1 for each flavor corresponding to a 1:1:1 flavor ratio at the Earth) gives us an effective total exposure.

In the ν_τ **Earth-skimming channel**, the calculation of the exposure is similar but more elaborate. The identification efficiency ε_ES depends on the energy of the emerging τ leptons E_τ, the position of the signal pattern on the ground, on the zenith θ and azimuth φ angles, and on the altitude h_c of the decay point of the τ above ground [15]. The detection efficiency ε_ES is averaged over the decay channels of the τ with their corresponding branching ratios, that determine the amount of energy fed into the shower. The efficiency ε_ES is folded with the projected area of the SD, with the differential probability $p_\mathrm{exit}(E_\nu, \theta, E_\tau) = \mathrm{d}p_\mathrm{exit}/\mathrm{d}E_\tau$ of a τ emerging from the Earth with energy E_τ (given a neutrino with energy E_ν crossing an amount of Earth determined by the zenith angle θ), as well as with the differential probability $p_\mathrm{dec}(E_\tau, \theta, h_\mathrm{dec}) = \mathrm{d}p_\mathrm{dec}/\mathrm{d}h_\mathrm{dec}$ that the τ decays at an altitude h_dec [15]. An integration over the whole parameter space ($E_\tau,\ \theta,\ \varphi,\ h_\mathrm{dec}$), area and time yields the exposure [15, 22]:

$$\mathcal{E}_\mathrm{ES}(E_\nu) = \int_A \int_\theta \int_\varphi \int_{E_\tau} \int_{h_\mathrm{dec}} \int_t |\cos\theta|\ \sin\theta\ p_\mathrm{exit}\ p_\mathrm{dec}\ \varepsilon_\mathrm{ES}\ \mathrm{d}A\ \mathrm{d}\theta\ \mathrm{d}\varphi\ \mathrm{d}E_\tau\ \mathrm{d}h_\mathrm{dec}\ \mathrm{d}t. \tag{3.2}$$

The probability $p_\mathrm{exit}(E_\nu, E_\tau, \theta)$ is obtained using a dedicated Monte Carlo simulation of ν_τ propagation inside the Earth [72] that includes ν_τ interaction through CC (NC) channels and sampling of the resulting τ (ν_τ) energy, τ energy loss, and τ decay inside the Earth before emerging with ν_τ regeneration following the decay [72, 73]. The probability of τ decay after traveling a distance $l = h_c/|\cos\theta|$ can be obtained analytically

$p_{\rm dec}(E_\tau, \theta, h_{\rm dec}) = (\lambda_{\rm dec}|\cos\theta|)^{-1} \exp(-l/\lambda_{\rm dec})$ where $\lambda_{\rm dec} = \gamma_\tau c\tau_0 = E_\tau c\tau_0/m_\tau$ is the average τ decay length with $m_\tau \simeq 1.777$ GeV the mass of the τ lepton, and $c\tau_0 \simeq 86.93\times10^{-6}$ m the lifetime of the τ multiplied by the speed of light c.

3.1.1 Time evolution of the SD

One of the hardest points in the calculation of the exposure calculation is the time integration. This is because the SD was in construction up to 2008 and also the number of active stations is continuously changing due to diverse reasons like maintenance periods or hardware failures.

The state of the detector is monitored every second and the information of which stations are working correctly is saved in a text file (T2File). Ideally, the exposure would have to be evaluated over every single configuration of the T2File, but this is not convenient due to the huge number of configurations over the 14 years of operation of the SD considered in this thesis.

The chosen solution is to divide all the data-taking period from January 2004 to August 2018 in sub-periods of 3 days and select a representative configuration for each one of them. The representative configuration is selected choosing one with N active stations, where N is chosen so that the product $N \times T$ is maximum, where T is the time during which the detector has equal or more active stations than N [74]. The time while the number of stations is lower than the chosen N will be added to the deadtime of the period. If there are several configurations satisfying the criteria, the earliest one is chosen because for large values of N there is not much difference, on average, between using the first one or any other one. This representative configuration is neither the best (largest number of active stations) nor the worse in the sub-period of 3 days, but it is a intermediate configuration that can be understood as the most likely of all the configurations over the 3 days.

With this method the exposure is underestimated because the real number of active stations in T will be always larger than the chosen N for the representative configuration, so using it we obtain a lower limit to the exposure of the detector. The systematic uncertainty of this approach was studied by analyzing the discrepancies produced when choosing a representative configuration for different number of days. The result is that the effect is around 1%, much lower than other uncertainties due to neutrino cros-section or τ-energy loss models.

Fig. 3.1 shows the evolution of the number of active stations from 2004 to 2018. The increase of the number of active stations due to the construction of the detector is clearly visible before 2008 and after that a stabilization at around 1600 active stations.

3.1.2 Effective area of the real array

In the previous subsection we discussed how we can account for the temporal evolution of the SD. In this subsection we describe how to obtain the effective area of the SD as a

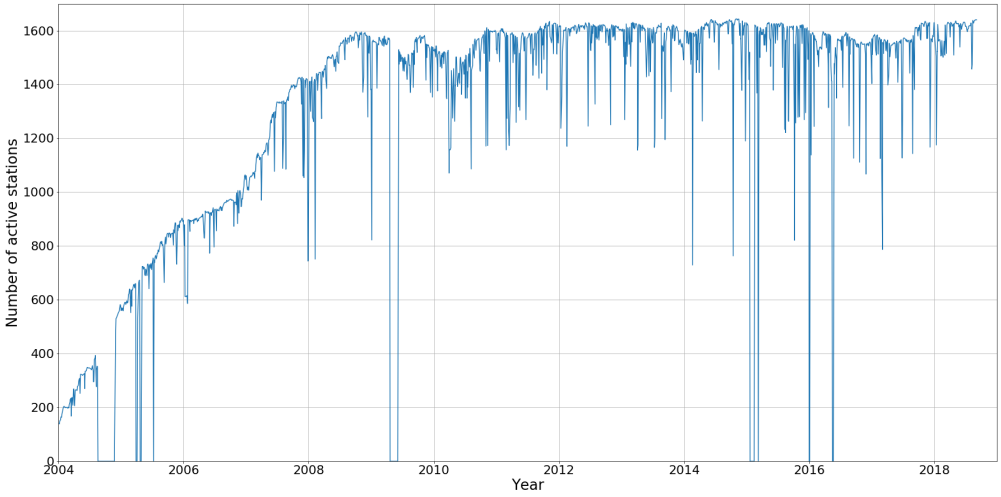

Figure 3.1: Time evolution of the number of active stations from January 2004 up to August 2018. The number of active stations for the representative configuration of each 3-day period is plotted.

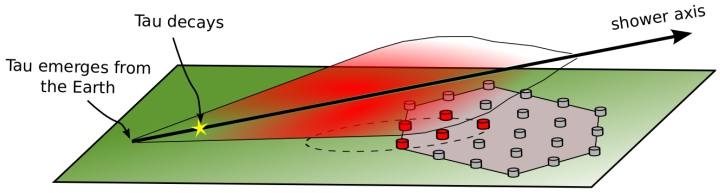

Figure 3.2: Sketch of a very inclined event where the interaction is produced outside the instrumented area but can still trigger the SD.

function of neutrino energy, zenith angle, interaction depth and time.

As we explained previously, inclined showers are characterized by having an elongated footprint. They can trigger the SD and be identified even if only a fraction of the footprint is contained in the SD area (this is represented in Fig. 3.2 for an ES event, but a similar diagram could be shown for DGH events).

As a consequence, we define an extended circular area, A_{extended}, fully containing the SD array and large enough so that showers whose core falls outside the SD still have the possibility of triggering the detector (see Fig. 3.3). For this purpose the radius of the extended circular area is chosen as an energy-dependent quantity obtained as the sum of the length L of the longest simulated shower at each energy, and the radius R_{SD} of the SD array, with R_{SD} obtained as the distance of the station that is farthest from the barycenter of the array.

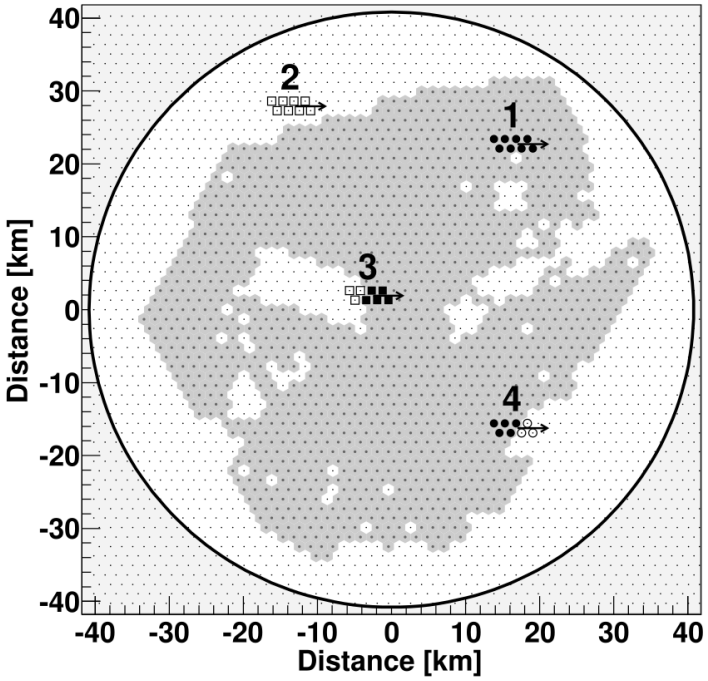

Figure 3.3: Examples of simulated neutrino showers, initiated by the decay of a τ, in four positions over the SD, shadowed area (corresponding to 1 November 2007). The arrows point to the azimuthal direction of the shower, the small dots represent an ideal and infinite array of stations and the circumference delimits the extended area, A_{extended}, where the simulated neutrino events are "thrown". Solid (open) symbols correspond to the stations of the simulated shower which have (would have) a T2 local trigger and which are active (non existing or non active) in the actual reference configuration. Circle symbols indicate showers which are correctly identified as neutrinos and square symbols those which are not. In case 1 the shower is fully contained and identified as a neutrino. In case 2 the shower is completely outside the SD array and cannot trigger the detector. In case 3 the shower is partially contained and triggers the SD, nevertheless it is not identified as a neutrino because the most relevant stations, with higher AoP, fall outside the real detector, i.e. are non existing. On the other hand, in case 4 the shower is also partially contained and triggers the SD, but it is correctly identified as a neutrino because the stations with higher AoP fall inside the real detector.

For each 3-day period of time, we throw 3 times each of the 50 simulations for each depth/height (for DGH/ES), angle and energy in different positions in the extended circle. We count how many of them (N_{pass}) trigger and pass the inclined and neutrino identification cuts in the representative configuration of the array. An effective geometrical area

is then obtained as:

$$A(E_\nu, \theta, h \text{ or } X) = \frac{N_{\text{pass}}(E_\nu, \theta, h \text{ or } X)}{N_{\text{tot}}} A_{\text{extended}}, \tag{3.3}$$

with $N_{\text{tot}} = 150$ in our calculation.

It is good to point that the geometrical area is not the same as the *effective area* $\mathcal{A}$ for neutrino detection defined such the area multiplied by the flux gives the event rate and that involves the probability of neutrino interaction in the atmosphere or the Earth (details in Section 3.4.1). The area that we refer here is just the result of the integral of the detection efficiency ε over the extended area that appears in Eqs. (3.1) and (3.2). The dependence of $\mathcal{A}$ with the $\cos\theta$ is not taken into account to obtain the area in Eq. 3.3.

An analysis of the dependence of A with E_ν, θ and h or X can be done. To do this we average $A(E_\nu, \theta, h \text{ or } X)$ over 2 years. Specifically, for each angle, energy and depth/height we average A over all the 3-days periods since the beginning of 2012 to the end of 2013 (244 periods). The selection of this 2-year period is due to the stability of the array over this time, with around 1600 active stations and few very short drops down to 1200 active stations.

In Fig. 3.4a we plot the effective geometrical area A vs depth for ν_e charged-current interactions of $E_\nu = 10^{18}$ eV and several zenith angles in the DGH case. For all zenith angles the area first increases with depth (as measured from the ground), then reaches a plateau and then decreases again. Showers injected close to the ground do not spread sufficiently in the lateral direction to trigger the SD, while showers injected far from the ground are rather similar to cosmic ray-induced showers and are not identified with the current criteria. The effective area is clearly dominated by the largest angles and the range of depths where it is sizeable is increasing with θ. The effective geometrical area can be even larger than the actual geometrical area of the SD.

In Fig. 3.4b we also plot A vs depth for ν_e interactions of different energies and a fixed zenith angle $\theta = 85°$. In this case it is clear that the larger the neutrino energy, the larger the effective area and also the width of the plateau, or the range of injection depths in which the effective area is non-zero. Finally, in Fig. 3.5 we plot the effective geometrical area vs depth for $E = 10^{18}$ eV and $\theta = 85°$ and different neutrino flavors and interaction channels. The effective geometrical area is typically largest for ν_e CC interactions. In this case essentially all the energy of the neutrino goes into the shower, and $\sim 80\%$ of it feeds a purely electromagnetic shower initiated by the secondary electron produced in the weak interaction vertex, what makes it simpler to distinguish this shower from that induced by CRs because it has fewer muons. This enhances the trigger and neutrino identification probabilities with respect to NC interactions. For ν_τ CC interactions we include the possibility of observing either the hadonic shower induced in the ν_τ CC interactions or the τ-decay shower that follows. This can be seen in Fig. 3.5, which has a long tail due to τ decays. The lifetime of the τ ($\sim 2.9 \cdot 10^{-13}$ s) combined with a large Lorentz factor is such that it can decay close to the surface when the neutrino interaction is produced high in the atmosphere, this is the reason why a long tail towards large depths as measured

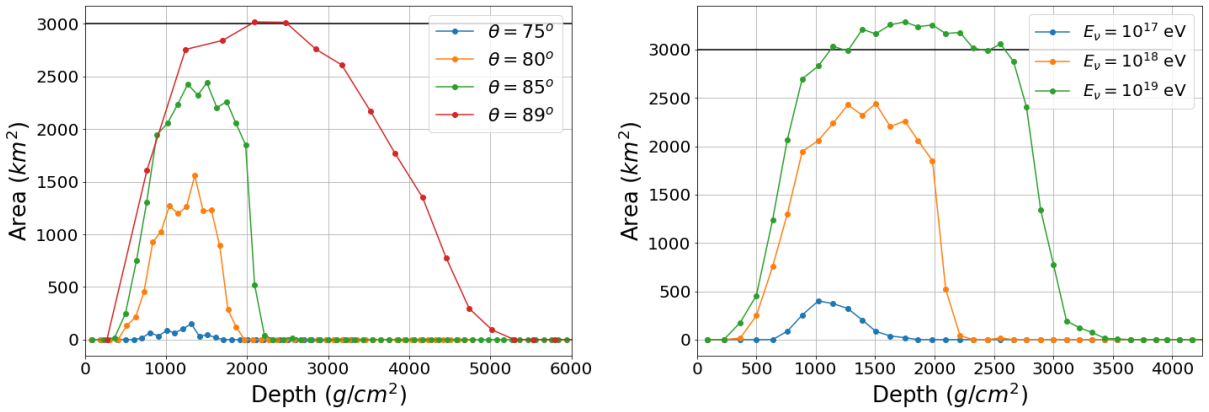

(a) Different θ.

(b) Different E_ν.

Figure 3.4: Left panel: Effective geometrical area A (as defined in Eq. (3.3)) vs slant injection depth measured from the ground for DGH ν_e CC interactions of $E_\nu = 10^{18}$ eV and different angles. Right panel: A vs slanted injection depth measured from the ground for DGH ν_e CC interactions of $\theta = 85°$ and different neutrino energies. Note that 0 g/cm^2 corresponds to showers injected at ground level. The black solid line indicates the approximate actual geometrical area of the SD.

from the ground is seen in the geometrical effective area of ν_τ CC interactions.

Summing up the DGH channels: the effective area is the largest for ν_e CC interacting at relatively short distances. However, for larger depths the area for ν_e CC falls to zero quickly, while for ν_τ it is greater than zero even for very large distances to the ground for the reasons explained before. Finally, A increases with neutrino energy and with zenith angle.

In the case of ES (upcoming ν_τ CC neutrinos) the effective geometrical area is shown in Fig. 3.6a vs the height of tau decay (where $h = 0$ m corresponds to the altitude of Auger). Several curves are shown for selected angles, keeping $E_\tau = 10^{18}$ eV. In Fig. 3.6b we also fix $\theta = 91°$ and each curve corresponds to a fixed energy of the τ. The behavior of the effective area with the height of τ decay is similar in both plots. The area is typically largest for showers initiated at $h = 0$ and decreases as the shower develops higher in the atmosphere, until it reaches a height above which it does no longer trigger the SD. The greater the energy of the τ, the larger the shower dimensions and the effective area that is obtained. Similarly, as the neutrino arrival direction gets more horizontal, the height at which the tau decays and the shower develops is closer to the ground.

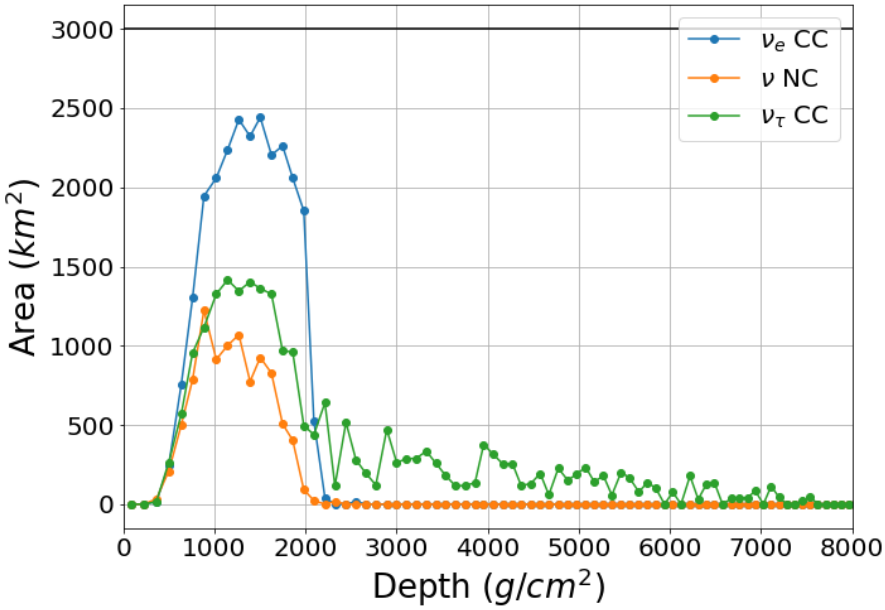

Figure 3.5: Effective geometrical area (as defined in Eq. (3.3)) vs slanted injection depth measured from the ground for interactions of $\theta = 85°$, $E_\nu = 10^{18}$ eV and different neutrino flavors and interaction channels. Note that 0 g/cm^2 corresponds to showers injected at ground level. The black solid line indicates the approximate geometrical area of the SD.

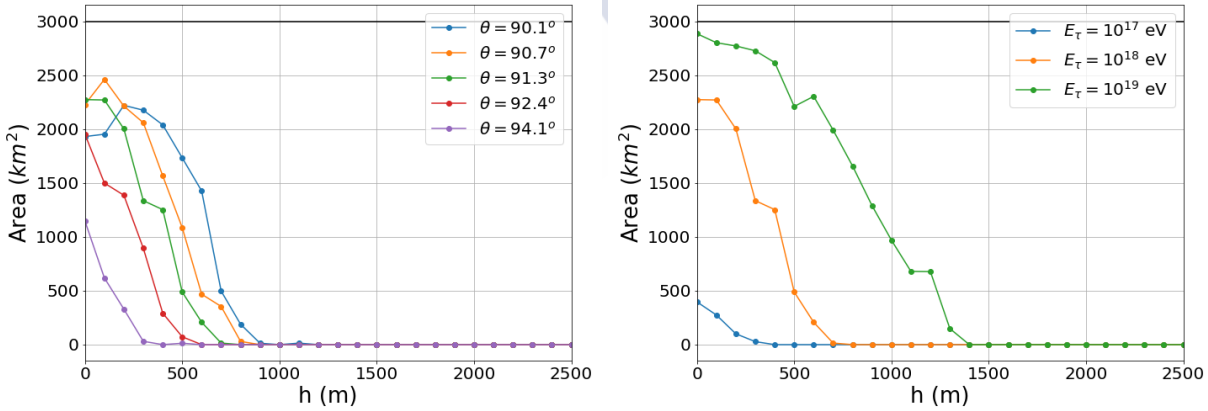

(a) Different θ.

(b) Different E_τ.

Figure 3.6: Left panel: Effective geometrical area A vs height of τ decay ($h = 0$ m corresponds to the altitude of Auger) for τ decay-induced showers with $E_\tau = 10^{18}$ eV produced by ES ν_τ CC interactions and different angles. Right panel: A vs height of τ decay for τ decay-induced showers with $\theta = 91°$ produced by ES ν_τ CC interactions and different τ energies. The black solid line indicates the approximate geometrical area of the SD.

3.1.3 Exposure

In the previous subsections we explained the procedure to calculate the two most delicate complex integrals in the formulas for the exposure (Eqs. (3.1) and (3.2)): the integrals over time and over area. The remaining integrals are simpler to deal with. The angular integral could be a problem, but with the typical assumption of isotropic fluxes it turns into a trivial integral.

If fluxes of each flavor are equal at Earth, as approximately expected in standard production mechanisms with vacuum oscillations over scales of hundreds of Mpc [36, 61], it is possible to combine the two exposures in a total, simply summing the two exposures. To obtain the event rate one only has to multiply the combined exposure with the *single-flavor* neutrino flux [23].

The resulting exposure from combining Earth-skimming and downward-going high channels, $\mathcal{E}_{\mathrm{ES-DGH}}$, is plotted in Fig. 3.7a. The exposures due to Earth-skimming ν_τ alone and the sum of all the exposures due to the three flavors and two channels (CC & NC) contributing to the downward-going neutrino category are also shown.

In addition, in Fig. 3.7b the combined exposure $\mathcal{E}_{\mathrm{ES-DGH}}$ is represented again, but in this case curves for each neutrino flavor $\mathcal{E}_i$ with $i = \nu_e, \nu_\mu, \nu_\tau$ are also plotted. When we compare the different neutrino flavors, the ν_τ dominates the contribution to the total exposure essentially due to the higher sensitivity of the Earth-skimming channel because of the denser target provided by the Earth's crust for the ES ν_τ to interact, and the large range of τ leptons at EeV energies ($\sim$ 10 km at 1 EeV in rock [75]). The contribution to the ν_τ-flavor exposure $\mathcal{E}_{\nu_\tau}$ because of downward-going ν_τ is typically small, but increases as the energy rises reaching a fraction of $\sim$ 30 % of $\mathcal{E}_{\mathrm{ES}}$ at $E_\nu = 10^{20}$ eV. This can be seen in Fig. 3.7 by comparing $\mathcal{E}_{\nu_\tau}$ and $\mathcal{E}_{\mathrm{ES}}$. The next in importance is the exposure due to electron neutrinos $\mathcal{E}_{\nu_e}$ (CC and NC interactions together) dominating over muon neutrinos $\mathcal{E}_{\nu_\mu}$. This is in part because in ν_e CC interactions the total neutrino energy goes into the shower compared to for instance $\sim 20\%$ in CC ν_μ interactions, and in part because of the larger electromagnetic content of the shower induced by the electron produced in the ν_e CC interaction. When we compare the exposure for ES ν_τ with the sum of all flavors that contribute to the downward-going high exposure, it can be seen in Fig. 3.7b that the latter overtakes ES exposure only for the most energetic neutrinos $\sim 2 \times 10^{20}$ eV. This happens because above $\sim 3 \times 10^{19}$ eV the exposure to ES ν_τ starts to decrease with energy due to absorption of ν_τ in the Earth and to the growing decay length of the emerging τ leptons in air at increasing energies, favouring decays at higher altitude above the detector and reducing the probability that the τ-induced shower triggers the SD array.

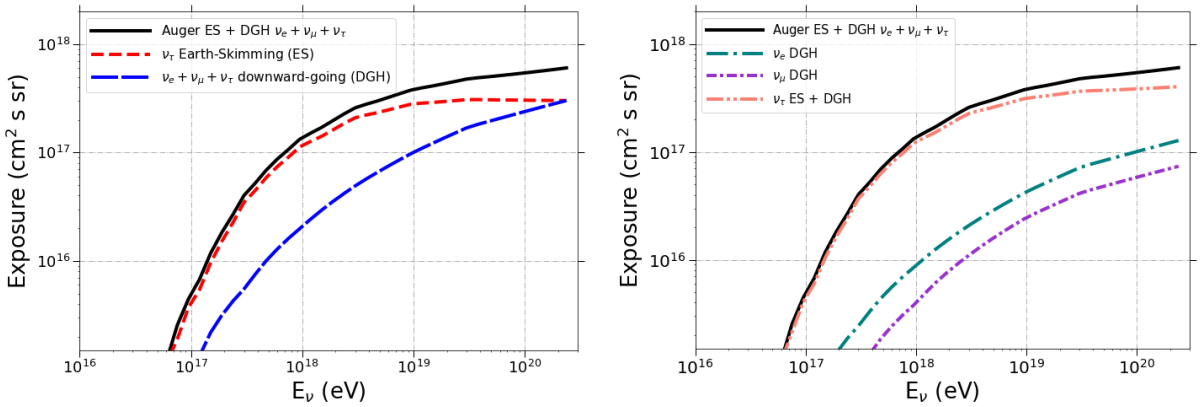

(a) Different channels.

(b) Different flavors.

Figure 3.7: Left panel: Combined exposure of the SD of the Pierre Auger Observatory (1 January 2004 - 31 August 2018) to UHE neutrinos as a function of neutrino energy for upward-going Earth-skimming ν_τ only, and for downward-goinghigh neutrinos of all flavors including CC and NC interactions and assuming a flavor mixture of $\nu_e : \nu_\mu : \nu_\tau = 1 : 1 : 1$. The combined ES+DGH exposure is also shown. Right panel: Same plot that left panel but spliting in neutrino flavors combining ES and DGH cases. The exposures are obtained taking the exposure sums for all flavors (assuming a flavor mixture of $\nu_e : \nu_\mu : \nu_\tau = 1 : 1 : 1$).

3.2 Limits to diffuse fluxes

Assuming equal fluxes of neutrino flavors at Earth, we can then fold the single flavor neutrino flux with the combined exposure of the Observatory obtained taking the simple sum of exposures for each flavor. The total exposure $\mathcal{E}_{\rm tot}(E)$ folded with a single-flavor flux of UHE neutrinos per unit energy, area A, solid angle Ω and time, $\phi(E_\nu) = {\rm d}^6 N_\nu/({\rm d}E_\nu\ {\rm d}\Omega\ {\rm d}A\ {\rm d}t)$ and integrated in energy gives the expected number of events for that flux:

$$N_{\rm evt} = \int_{E_\nu} \mathcal{E}_{\rm tot}(E_\nu)\ \phi(E_\nu)\ {\rm d}E_\nu. \tag{3.4}$$

Assuming a differential neutrino flux $\phi = k \cdot E_\nu^{-2}$, an upper limit to the value of k at 90% C.L. is obtained as

$$k_{90} = \frac{2.39}{\int_{E_\nu} E_\nu^{-2}\ \mathcal{E}_{\rm tot}(E_\nu)\ {\rm d}E_\nu}, \tag{3.5}$$

where 2.39 is the Feldman-Cousins factor [76] for non-observation of events in the absence of expected background accounting for systematic uncertainties, i.e. under the conditions of non-observation of events in the absence of expected background, the 90% C.L. due to statistical fluctuations is 2.39 [22, 77]. The integrated limit represents the value of the normalization of a E_ν^{-2} differential neutrino flux needed to observe a total of 2.39 events.

There are several sources of systematic uncertainty that were taken in account in the calculation of the exposure and limit [14,15]. The uncertainty attributed to simulations is estimated looking at differences when using several neutrino interaction generators, shower simulations, cross sections, hadronic interaction models and thinning levels. In the case of DGH these would modify the event rate for a $\phi(E_\nu) \propto E_\nu^{-2}$ flux in Eq. (3.4) between -3% and 4% with respect to the calculation of the exposure shown in Fig. 3.7a. The ES channel is the one with largest uncertainty mostly attributed to the ν_τ cross-section and particularly to the tau energy loss that plays a crucial role. The corresponding range of variation of the event rate is estimated between -28% and 34%. The topography around the Observatory is not accounted for explicitly in the calculation of the exposure, but it is taken as a systematic uncertainty that would increase the event rate by an estimated $\sim$ 20 % [14, 15]. The total uncertainty, obtained by adding these bands in quadrature, ranges from -28% to 39%, and is incorporated in the value of the limit itself through a semi-Bayesian extension [77] of the Feldman-Cousins approach [76].

The single-flavor 90% C.L. integrated limit taking into account only the ES and DGH channels is:

$$k_{90} \;<\; 4.5 \;\times\; 10^{-9}\ \mathrm{GeV\ cm^{-2}\ s^{-1}\ sr^{-1}},\ \mathrm{ES + DGH\ only}, \tag{3.6}$$

or equivalently 1.4 EeV $\mathrm{km^{-2}\ yr^{-1}\ sr^{-1}}$. It applies in the energy interval 10^{17} eV $- 2.5 \times 10^{19}$ eV for which $\sim$ 90 % of the total event rate is expected in the case of a E_ν^{-2} spectral flux.

Flavor	Relative contribution
ν_e	0.10
ν_μ	0.04
ν_τ	0.86
Channel	**Relative contribution**
Earth-skimming ν_τ	0.79
Downward-going $\nu_e + \nu_\mu + \nu_\tau$	0.21

Table 3.1: Top of table: Relative contribution of the three neutrino flavors to the event rate in Auger due to a neutrino flux $\phi_\nu \propto E_\nu^{-2}$. Bottom: Relative contribution to the rate in the Earth-skimming (ES) and downward-going (DG) channels including DGH and DGL (see Ref. [23]).

Including the downward-goinglow (DGL) angle channel as in Ref. [23] the limit improves to:

$$k_{90} \;<\; 4.4 \;\times\; 10^{-9}\ \mathrm{GeV\ cm^{-2}\ s^{-1}\ sr^{-1}},\ \mathrm{all\ channels}. \tag{3.7}$$

In Table 3.1 we first show the relative contributions to the expected rate of events for a E_ν^{-2} flux for each neutrino flavor and below the relative contribution of the ES and DG channels. For such a spectral shape τ neutrinos contribute to $\sim$ 86 % of the total event rate, and in particular ES neutrinos dominate the rate of ν_τ events over the downward-going ν_τ. The contribution of ν_e and ν_μ together is smaller than 15%. Only at the highest energies DG and ES are roughly similar.

The denominator of Eq. (3.5) can also be integrated in bins of neutrino energy of width ΔE_ν, and a limit $\hat{k}_{90}$ can be obtained in each energy bin. This is shown in

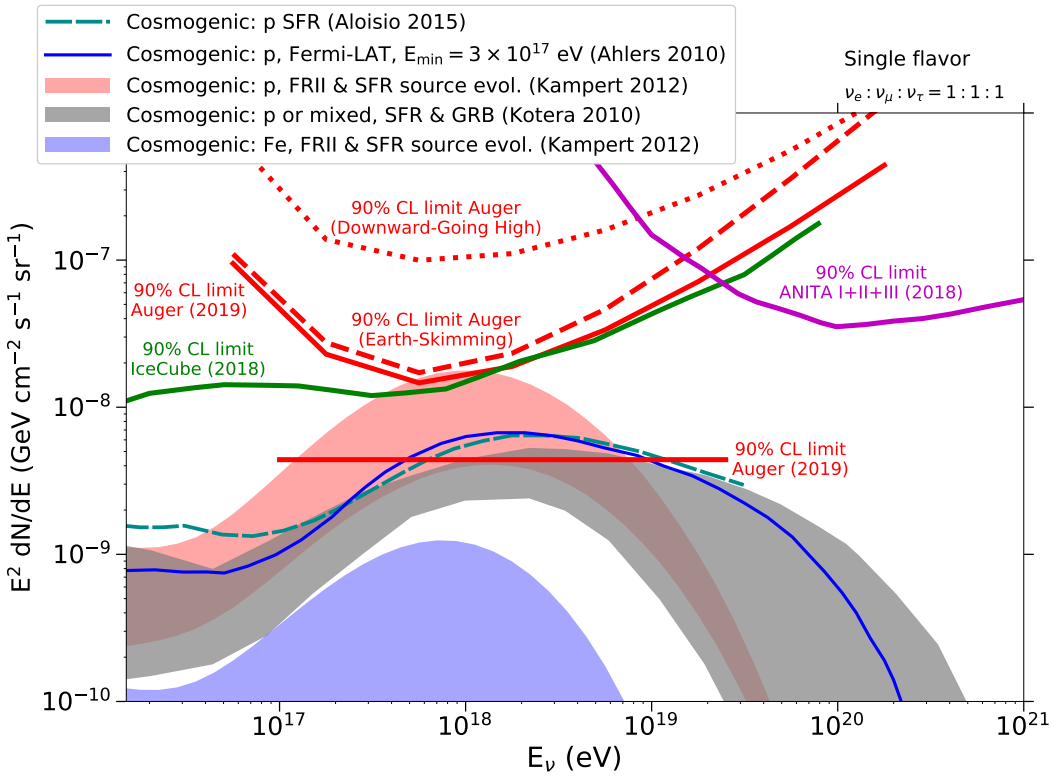

Figure 3.8: Pierre Auger Observatory upper limit (90% C.L.) to the normalization k of the diffuse flux of UHE neutrinos assuming a flux $\phi_\nu = k\ E_\nu^{-2}$, as given in Eqs. (3.5) and (3.7) (straight solid red line). The upper limits to the normalization of the diffuse flux when integrating the denominator of Eq. (3.5) in bins of width 0.5 in $\log_{10} E_\nu$ (differential limits) are also plotted. Solid red line: All channels (ES+DGH+DGL) and flavors. Dashed red line: Earth-skimming channel, only relevant for ν_τ. Dotted red line: Downward-going high (DGH) channel designed to select neutrinos with $\theta \in [75°, 90°]$. The differential limits obtained with IceCube [40] (solid green) and ANITA data I+II+III [78] (solid dark magenta) are also shown together with the expected neutrino fluxes for several cosmogenic neutrino models [48, 79–81]. All limits and fluxes are converted to single flavor.

Fig. 3.8 and Fig. 3.9 for logarithmic energy intervals $\Delta \log_{10} E_\nu = 0.5$ for all channels (ES+DGH+DGL) and for the ES and DGH channel separately. The differential limit is an effective way of characterizing the energy dependence of the sensitivity of a neutrino experiment. Otherwise it is a conservative limit because it applies independently for each bin, i.e. it would work for a flux that has a spectrum which is concentrated in half a decade of energy which is unrealistic. For the case of Auger it can be seen that the best sensitivity is achieved for energies around 1 EeV.

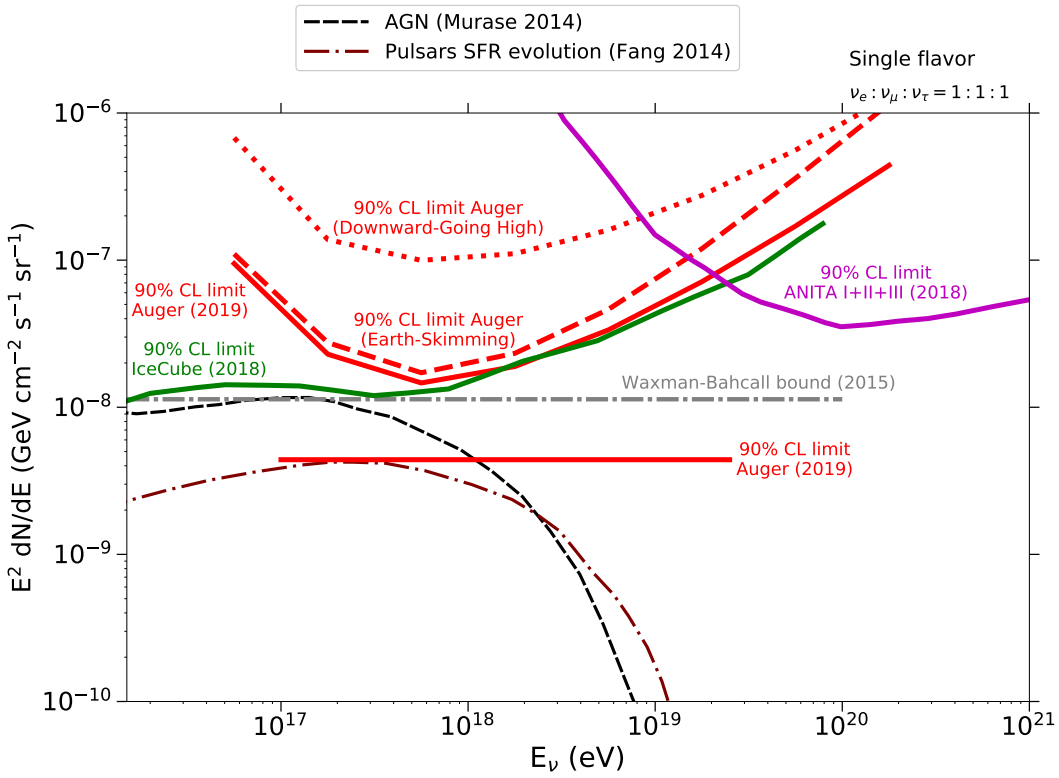

Figure 3.9: Pierre Auger Observatory upper limit (90% C.L.) to the normalization k of the diffuse flux of UHE neutrinos $\phi_\nu = k\ E_\nu^{-2}$ as given in Eqs. (3.5) and (3.7) (solid straight red line). The upper limits to the normalization of the diffuse flux when integrating the denominator of Eq. (3.5) in bins of width 0.5 in $\log_{10} E_\nu$ (differential limits) are also plotted. Solid red line: All channels (ES+DGH+DGL) and flavors. Dashed red line: Earth-skimming channel, only relevant for ν_τ. Dotted red line: downward-goinghigh (DGH) channel designed to select neutrinos with $\theta \in [75°, 90°]$. The differential limits obtained with IceCube [40] (solid green) and ANITA data I+II+III [78] (solid dark magenta) are also shown. The expected neutrino fluxes for several astrophysical models of neutrino production, as well as the Waxman-Bahcall bound [82], are also plotted. All limits and fluxes are converted to single flavor.

3.3 Constraints on the origin of UHECR

3.3.1 Cosmogenic neutrino models

Once we have obtained the upper limit with the Observatory, we can constrain several classes of models of neutrino production in interactions of UHECR with the Cosmic Microwave Background (CMB) and Extragalactic-Background Light (EBL), generally referred to as cosmogenic neutrino models. The expected event rate in the Auger Observatory due to cosmogenic neutrinos depends strongly on the redshift evolution of the UHECR sources, on the nature of the primaries, namely whether they are protons or heavier nuclei, on the maximal redshift at which UHECR are produced, $z_{\max}$, and on the maximum energy acquired in the CR acceleration process, $E_{\max}$. Frequently, cosmogenic neutrino models assume that the observed UHECR flux-suppression [31, 32, 83] is based completely on the GZK effect, i.e. on energy losses of protons or nuclei in the background radiation fields. The highest fluxes of cosmogenic neutrinos are then expected for injection of protons, while those expected for injection of iron nuclei are down typically by about an order of magnitude [37,38,48] (c.f. Fig. 3.8)[1]. A simple astrophysical model fitting the energy spectrum and the mass composition suggests that the observed flux suppression could be dominated by the maximum rigidity of the sources of UHECR, rather than being only the effect of energy losses in the CMB and EBL [88, 89]. Accordingly, cosmogenic neutrino fluxes would be reduced much further and may escape detection for the foreseeable future [90–92]. Thus, fluxes of cosmogenic neutrinos provide an independent probe of source properties and of the origin of the UHECR flux suppression at the highest energies.

In Table 3.2, the expected number of events in the lifetime of the Observatory up to 31 August 2018 is shown for several cosmogenic neutrino models, together with the associated Poisson probability of observing no events. Several important conclusions can be extracted after inspecting Table 3.2:

- Scenarios assuming sources that accelerate only protons and that have a strong evolution with z, similar to Fanaroff-Riley type II (FRII) radio-loud AGN [80], are strongly constrained by the Auger results at more than 90 % C.L. [22].

- If instead of protons the primaries are heavier nuclei, photodisintegration is more likely than pion production, and the flux of cosmogenic neutrinos is suppressed [37,38,48]. For models assuming mixed (Galactic) composition of the UHECR such as those in [48], the constraints placed by the Observatory limits are weaker, below the 90 % C.L. threshold of exclusion, as can be seen in Table 3.2. An about threefold increase in the current exposure will be needed to constrain at 90 % C.L. the lower edge of the gray band in Fig. 3.8 for a mixed composition.

[1]The possibility of pure proton (or iron) primaries in the energy range of interest is disfavored by recent results on the composition of UHECR [41, 84–87]. Instead, a progressively increasing fraction of heavier primaries is observed with increasing energy up to at least $E \sim 5 \times 10^{19}$ eV [86] with some hints of the UHECR composition becoming lighter at the highest energies [41].

- The constraints are much weaker if pure iron would be produced at the sources. Dismissing at 90 % C.L. the most optimistic predictions of cosmogenic neutrino flux at $10^{18} - 10^{19}$ eV in such a scenario [80], would require at least a sixfold increase in exposure. This is out of the range of sensitivity of the current configuration of the Pierre Auger Observatory.

- In other class of cosmogenic neutrino models for pure protons [79] the fluxes are normalized in such a way that the associated UHE photons produced along with the neutrinos, after cascading in the Universe and being converted into GeV photons, saturate the measurements of the diffuse extragalactic γ-ray background performed by *Fermi*-LAT [93]. Such models are in tension with the limits on cosmogenic neutrinos obtained with the Auger Observatory.

As shown in Fig. 3.8, the upper bounds of cosmogenic neutrinos start to constrain astrophysical models that describe the UHECR flux suppression above 4×10^{19} eV by energy losses of protons in the CMB. To analyze the excluded parameter space of such proton models in more detail, we performed a scan on the m parameter of a standard function used to describe the redshift evolution of sources, $\Psi(z) \propto (1+z)^m$, as well as on the value of $z_{\max}$. The spatial distribution of sources is assumed to be homogeneous, with all the sources assumed to have the same UHECR luminosity. The simulations predicting the associated cosmogenic neutrino fluxes were performed with the CRPropa package [94] for a fixed spectral index of the UHECR proton spectrum $E^{-\alpha}$ at the sources (with $\alpha = 2.5$), and a maximum energy of the protons $E_{\max} = 6 \times 10^{20}$ eV. In the energy range $\sim 3 \times 10^{17}$ to $\sim 3 \times 10^{18}$ eV, where the sensitivity of Auger peaks, the cosmogenic neutrino flux is weakly dependent on α and $E_{\max}$ as long as the latter is not below 10^{20} eV (see Fig. 1 in [95]). The proton flux at Earth is normalized to the Auger spectrum at $E = 7 \times 10^{18}$ eV. For each pair of m and $z_{\max}$, the cosmogenic flux was obtained, and the expected number of neutrino events in Auger was calculated using Eq. (3.4). Models predicting more than 2.39 neutrinos are disfavored at $> 90\,\%$ C.L. The resultant exclusion plot is shown in Fig. 3.10a with the contours representing the 68 % and 90 % C.L. exclusion limits. The non-observation of neutrino candidates in the Observatory data allows us to disfavor a significant region of the parameter space $(m, z_{\max})$.

In Fig. 3.10 we have also explored the possibility of a proton component above $E \gtrsim 50\,\mathrm{EeV}$ [96], i.e. in the energy range above $\sim 10^{19.5}$ eV presently not covered by the measurements of the depth of shower maximum of Auger [86]. Such a subdominant proton component would have a limited effect on the observed spectrum and composition, but would strongly alter the expected cosmogenic neutrino flux [95], because protons produce significantly more neutrinos when propagating through the Universe than heavier nuclei of the same total energy. Assuming conservatively that the cosmogenic neutrinos result only from the proton component, neglecting the contribution to neutrino flux produced by heavier nuclei, the rejection power depends on the relative contribution of protons normalized to the fixed all-particle flux denoted as f_p [95]. The exclusion plot is shown in Fig. 3.10b. Proton flux normalizations down to $f_p \simeq 0.2$ can be discarded with the present

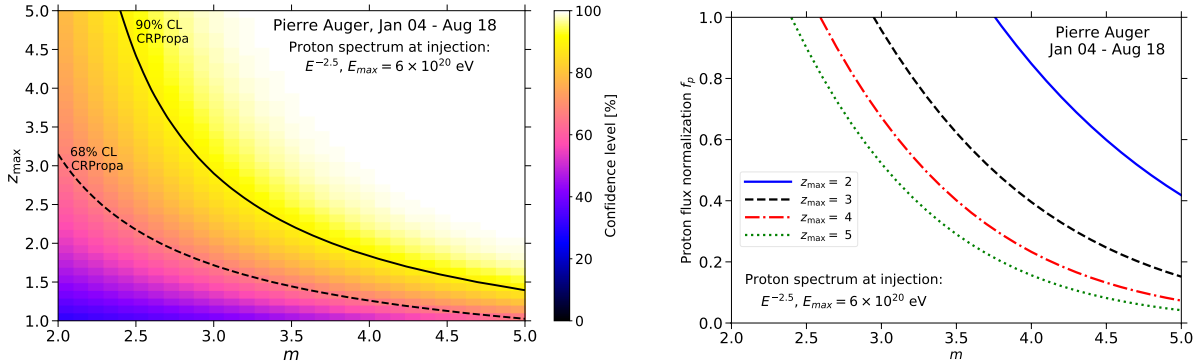

(a) For m and $z_{\max}$ when $f_p = 1$.

(b) For m and variable $f_p \leq 1$.

Figure 3.10: Constraints on UHECR source evolution models parameterized as $\psi(z) \propto (1+z)^m$ for sources distributed homogeneously up to a maximum redshift $z_{\max}$ and emitting protons following a power-law $\mathrm{d}N/\mathrm{d}E \propto E^{-2.5}$ up to $E = 6 \times 10^{20}$ eV. A proton-only flux is matched to the Auger spectrum at 7×10^{18} eV (benchmark calculation for $f_p = 1$, where f_p is the fraction of protons of the UHECR spectrum at $7 \cdot 10^{18}$ eV, see text). The cosmogenic neutrino fluxes for each combination of m and $z_{\max}$ were obtained with the Monte Carlo (MC) propagation code CRPropa [94]. Left panel: Exclusion plot for source evolution parameters m and $z_{\max}$ when $f_p = 1$. The colored areas represent confidence levels (C.L.) for the exclusion. The solid and dashed lines represent the contours of 90% and 68% C.L. exclusion, respectively. Right panel: Exclusion plot for source evolution model parameter m and variable $f_p \leq 1$. The regions above the four colored lines corresponding to fixed values of $z_{\max}$, are excluded at 90 % C.L. using the non existence of neutrino candidates in Auger data [23].

data for sources following a cosmological evolution of $m \simeq 3.8$ up to redshift $z_{\max} = 5$. The constraint on the value of m for a fixed $f_p \simeq 0.2$ is weaker if the sources are closer, for instance $m \simeq 4.7$ if $z_{\max} = 3$.

3.3.2 Astrophysical models

After inspecting Table 3.2 and Fig. 3.9 we can extract several conclusions regarding UHEν production in astrophysical sources:

- As shown in Table 3.2 some astrophysical models are excluded at 90 % C.L. such as those assuming UHECR acceleration to trans-GZK energies in radio-loud AGN [97].
- Other models predicting UHEν production in pulsars with the sources following a moderate evolution with z [98] are not strongly constrained by Auger results.
- The IceCube Neutrino Observatory detected a flux of astrophysical neutrinos including a $\sim$ 6.3 PeV event compatible with being produced by the Glashow res-

onance [99, 100]. Extrapolating the detected flux normalized at the energy of the Glashow event to Auger energies, using a power-law in energy $dN_\nu/dE_\nu \propto E^{-2.3}$, would give ~ 0.4 events in Auger, with an uncertainty of the flux of a factor of ~ 3. This suggests that, in an optimistic scenario, if the measured IceCube flux extends into the EeV energy range, it could be within reach of Auger in the next decade.

Neutrino Model (Diffuse flux)	Expected number of ν events	Probability of observing 0
Cosmogenic		
(Kampert *et al.* [80])		
proton, FRII	~ 5.9	$\sim 2.7 \times 10^{-3}$
proton, SFR	~ 1.4	~ 0.25
iron, FRII	~ 0.4	~ 0.67
(Aloisio *et al.* [81])		
proton, SFR	~ 2.3	~ 0.10
(Ahlers *et al.* [79])		
proton, $E_{\rm min} = 10^{19}$ eV	~ 4.6	$\sim 1.0 \times 10^{-2}$
proton, $E_{\rm min} = 10^{17.5}$ eV	~ 2.4	$\sim 9.0 \times 10^{-2}$
(Kotera *et al.* [48])		
p or mixed, SFR & GRB	$\sim 0.8 - 2.0$	$\sim 0.45 - 0.13$
Astrophysical		
(Murase *et al.* [97])		
Radio-loud AGN	~ 2.9	$\sim 5.5 \times 10^{-2}$
(Fang *et al.* [98])		
Pulsars - SFR	~ 1.5	~ 0.22
IceCube astrophysical		
ν flux (extrapolated)	$\sim 0.4 - 1.2$	$\sim 0.67 - 0.30$

Table 3.2: Number of expected neutrino events $N_{\rm evt}$ in the period 1 Jan 2004 - 31 August 2018 for several models of UHE neutrino production (see Figs. 3.8 and 3.9), given the exposure of the Surface Detector Array of the Pierre Auger Observatory shown in Fig. 3.7. The last column gives the Poisson probability $\exp(-N_{\rm evt})$ of observing 0 events when the number of expected events is $N_{\rm evt}$.

3.4 Point-like neutrino fluxes

With the Pierre Auger Observatory it is also possible to look for neutrinos in different directions in the sky and search for point sources of neutrinos. The absence of neutrino candidates can be converted to an upper limit to the point-like flux of UHE neutrinos. To obtain this limit it is necessary to calculate the directional exposure of the SD of Auger i.e. fixing the observing direction in the sky. To do this, the main procedure is similar to that in the previous section. Eqs. (3.1) and (3.2) must be integrated but restricting the angular and time integrals to fixed direction in Equatorial coordinates without performing the angular integral [24].

3.4.1 Sensitivity of the Pierre Auger Observatory to point-like neutrino sources

Each neutrino search category, ES, DGH and DGL, corresponds to a given range of zenith angles, and the three categories combined cover the range between $\theta = 60°$ and $\theta = 95°$. As explained above, the neutrino identification efficiency is different in each category, making the sensitivity of the Observatory highly dependent on the direction in the sky where the search is done and also on observation time. This thesis is focused on ES and DGH, with DGL just included in the final results for completeness.

Effective Area

The sensitivity in each direction can be evaluated in terms of the effective area $\mathcal{A}_i(E_\nu)$, to neutrinos of flavor $i = \nu_e,\ \nu_\mu,\ \nu_\tau$ and energy E_ν, defined such that $\mathcal{A}_i$ multiplied by the spectral flux of flavor i from a point source, $\phi_i(E_\nu) = \mathrm{d}^4N/(\mathrm{d}E_\nu\ \mathrm{d}A\ \mathrm{d}t)$, gives the energy spectrum of the instantaneous rate of detected events. The rate of detected events is obtained by integrating it over energy:

$$\frac{\mathrm{d}N_i}{\mathrm{d}t} = \int_{E_\nu} \mathrm{d}E_\nu\ \phi_i(E_\nu)\ \mathcal{A}_i(E_\nu). \tag{3.8}$$

Each neutrino flavor must be considered separately because the showers they initiate through charged-current (CC) interactions are substantially different in the fraction of energy that they carry relative to the incident neutrino [17, 20]. For DG showers, the effective area is obtained by integrating the neutrino identification efficiency, $\varepsilon_{i,c}$, and the interaction probability per unit depth $\lambda_c^{-1} = \sigma_c\ m_p^{-1}$, where m_p is the mass of a proton, and σ_c the neutrino-nucleon cross-section, over the array area A, (transverse to the neutrino direction) and over the atmospheric matter depth of the neutrino trajectory X:

$$\mathcal{A}_{i,c}^{\mathrm{DG}} = \int_X \int_A \mathrm{d}X\ \mathrm{d}A\ \cos\theta\ \varepsilon_{i,c}\ \sigma_c\ m_p^{-1}. \tag{3.9}$$

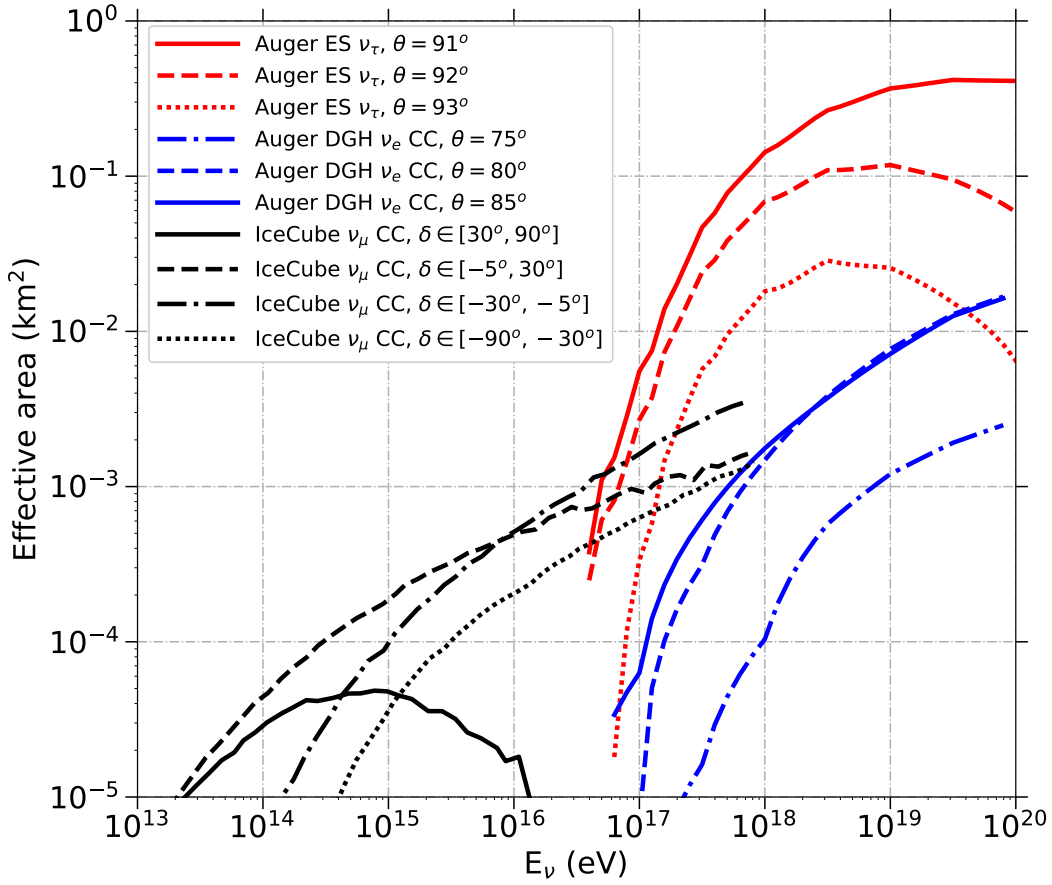

Figure 3.11: Instantaneous effective areas for ES (red lines) and DGH (blue) channels as a function of neutrino energy for selected zenith angles (θ) as labelled, compared to those of IceCube [101] (black). The DGH and ES effective areas are respectively obtained with Eqs. (3.9) and (3.10). Numerical values of the effective areas for ES and DGH analyses as a function of energy and zenith angle are available at [102]. For IceCube at a latitude $\lambda = -90°$, the zenith angle θ and the declination δ are related by $\theta = 90° + \delta$.

Both $\varepsilon_{i,c}$, and σ_c are different for neutral- (NC) and charged-current (CC) interactions, but at EeV energies of interest, the change in the cross sections for different flavors is negligible. Nevertheless there are instantaneous effective areas $\mathcal{A}^{\rm DG}_{i,c}$ for DG showers for each flavor i and interaction type c. The effective areas also depend on neutrino energy and on zenith angle (see Figs. 3.11 and 3.12) due to the strong dependence of $\varepsilon_{i,c}$ on these parameters.

For the ES channel, the calculation of the effective area is much more involved, as we explained in the previous section. The differential probability that a tau neutrino of energy E_ν undergoes a CC interaction along the Earth's chord, and that the resulting tau lepton exits to the atmosphere with energy E_τ, denoted as $p_{\rm exit}(E_\nu, E_\tau, \theta)$, has a strong

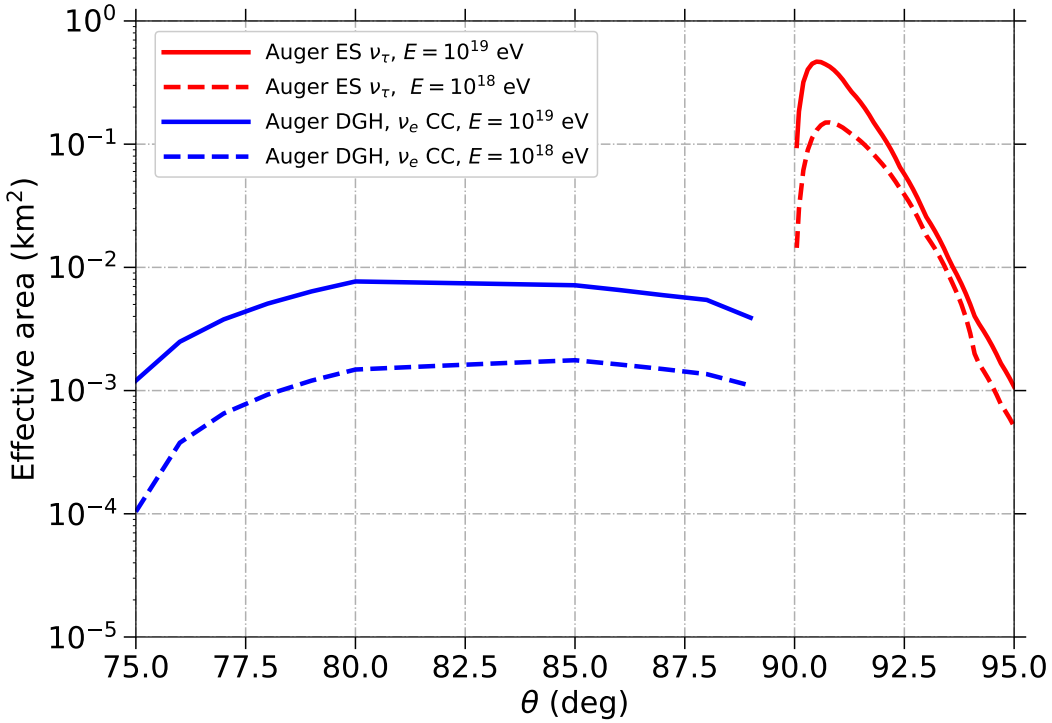

Figure 3.12: Instantaneous effective areas for ES (red lines) and DGH (blue) neutrinos as a function of zenith angle for selected neutrino energies. The DGH and ES effective areas are respectively obtained with Eqs. (3.9) and (3.10).

dependence of $p_{\rm exit}$ on θ within a small range from $\theta = 90°$ to $\theta \simeq 95°$, which is caused by the rapid rise of the Earth's chord as the zenith angle increases below the horizon and its absorptive effect for high-energy neutrinos [13, 72, 73, 103]. This probability, folded with the selection and identification efficiency $\varepsilon_{\rm ES}$ and the tau decay probability per unit length, must be integrated over tau energy E_τ and decay length l to obtain the effective area:

$$\mathcal{A}^{\rm ES} = \int_{E_\tau}\int_{A}\int_{l} {\rm d}A\ {\rm d}E_\tau\ \frac{{\rm d}l}{\lambda}\exp\left[-\frac{l}{\gamma_\tau\lambda}\right]\cos\theta\ p_{\rm exit}\ \varepsilon_{\rm ES}, \tag{3.10}$$

where $\lambda = c\beta_\tau\tau_\tau \simeq 86.93\times10^{-6}$ m is the decay length of the τ, β_τ and $\gamma_\tau = E_\tau/(m_\tau c^2)$ are the speed and Lorentz factor of the tau lepton, with $m_\tau \simeq 1.777$ GeV the mass of the τ, assumed to be ultra-relativistic.

The instantaneous effective area for the ES and DGH neutrinos as a function of neutrino energy is shown in Fig. 3.11 for different zenith angles and is compared to that of IceCube [101]. The Pierre Auger Observatory has optimal effective area at EeV energies and, for favourable source positions as seen from the SD, the effective area of the Pierre Auger Observatory is significantly larger than the published effective area of IceCube.

The dependence of the effective area on the zenith angle is displayed in Fig. 3.12, for DGH charged-current electron neutrinos and different neutrino energies in the zenith angle range from $\theta = 75°$ to $\theta = 90°$, and for ES events from $\theta = 90°$ to $\theta = 95°$. A strong dependence on θ can be clearly seen in the ES range and at $\theta = 90°$, the transition from DGH to ES. At 10^{18} eV the ES effective area at $\theta = 91°$ is around two orders of magnitude higher than for DGH electron neutrinos with CC interactions at $\theta \sim 80°$. The ES search is remarkably more sensitive than the DGH searches due to several reasons. The matter depth for neutrino interactions along the Earth's chord is much larger than the available depth of the atmosphere for DGH showers and, at zenith angles very close to the horizontal, the conversion probability is maximized for energies just below the EeV for specific arrival directions that roughly match the neutrino interaction depth to the matter depth of the neutrino trajectory along the Earth's chord [13, 72, 73, 103]. Moreover, the ES search takes into account events with just three stations making this channel more efficient to detect lower-energy showers than in DGH which requires four or more.

It is worth mentioning that for two different instants of time, the position of a source in the sky is different, having different zenith angles as seen from Auger. The relation between zenith angle and time is explained in the following.

Sky Coverage

The neutrino search at the Pierre Auger Observatory is limited to showers with zenith angle θ between 90° and 95° in the ES analysis, and between 60° and 90° in the DG analysis, so at each instant neutrinos can be detected only from the specific region of the sky corresponding to this range. A point-like source at a declination δ and right ascension α (in equatorial coordinates) is seen from the latitude of the Observatory ($\lambda = -35.2°$) with a time-dependent zenith angle $\theta(t)$ given by:

$$\cos\theta(t) = \sin\lambda\,\sin\delta + \cos\lambda\,\cos\delta\,\cos\left(2\pi\frac{t}{T} - \alpha\right), \tag{3.11}$$

where t is the local sidereal time, T is the duration of the sidereal day, and the angle in brackets $(2\pi\frac{t}{T} - \alpha)$ is the so-called hour-angle. At any given instant, the field of view (FoV) of the Observatory for neutrino search is limited by the defined zenith angle range where the three searches ES, DGH and DGL are performed, each corresponding to different fields of view. This can be seen in Fig. 3.13a, where the corresponding FoV bands are plotted in equatorial coordinates as a function of $\alpha - t_{\rm GS}$, where $t_{\rm GS}$ is the Greenwich Sidereal Time (GST) converted to angle and is given by $t_{\rm GS} = 2\pi\ t/T + \ell$ with ℓ the mean longitude of the Observatory. For a source at a given α and observed from the position of Auger exactly at time 00:00 GST ($t_{\rm GS} = 0$), the instantaneous declination range where the source needs to be so that is seen in the FoV of ES, DGH or DGL can be directly read from the plot at a value α of the abscissa. At any other $t_{\rm GS}$, the corresponding declination range is simply read from Fig. 3.13a at $\alpha - t_{\rm GS}$. Using Fig. 3.13a it is easy to find out if a given source is going to be visible from the position of Auger along the day. Taking the position

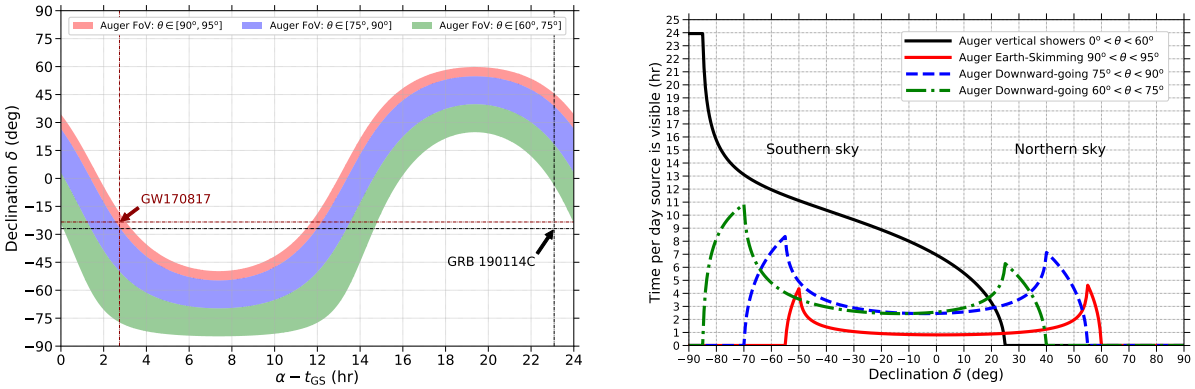

(a) FoV vs hour angle.

(b) Time in FoV vs declination.

Figure 3.13: Left panel: Instantaneous field of view (FoV) of the Pierre Auger Observatory for ES, DGH and DGL neutrinos as a function of the hour angle. The declination range for a given location in right ascension, α, at a given Greenwich Sidereal Time (converted to angle), $t_{\rm GS}$, is directly read at the corresponding hour angle: $\alpha - t_{\rm GS}$ (see text). Two source examples are shown: the source of GW170817 visible in Auger in the ES at the time of emission [26], and GRB 190114C (the first Gamma-Ray Burst detected by the MAGIC Cherenkov telescope) [104] not visible in Auger in the inclined directions at the time of the burst. Right panel: Time per sidereal day that a source at declination δ is visible in the field-of-view of the Earth-skimming (red line), downward-going channels (blue line: $75^\circ < \theta < 90^\circ$, green line: $60^\circ < \theta < 75^\circ$), and also for vertical directions ($\theta < 60^\circ$) for comparison [24].

of the source of GW170817 as an example at coordinates δ(J2000.0) $= -23^\circ 22' 53''.343$ and α(J2000.0) $= 13^{\rm h}09^{\rm m}48^{\rm s}.085$. At the time of emission this source was in the ES FoV and as times goes by, the position of the source is moving to the left over the horizontal red line in Fig. 3.13a, so in the following hours the source would be seen in the DGH FoV first, and in the DGL FoV later.

As can be seen in Fig. 3.13a, the SD of the Pierre Auger Observatory is sensitive to point-like sources of neutrinos over a broad declination range between $\delta \sim -85^\circ$ and $\delta \sim 60^\circ$. The search for ES showers is limited to a narrower band between $\delta \sim -55^\circ$ and $\delta \sim 60^\circ$ (red band), for DGH showers between $\delta \sim -70^\circ$ and $\delta \sim 55^\circ$ (blue band), and for DGL showers between $\delta \sim -85^\circ$ and $\delta \sim 40^\circ$ (green band) - see also Fig. 3.13b.

Eq. (3.11) also reveals that the detector location has a large impact on the sensitivity to point-like sources of neutrinos. In particular, for a detector such as IceCube located at the South Pole at a latitude $\lambda = -90^\circ$, Eq. (3.11) reads $\cos\theta = -\sin\delta$, and this implies that, a source at a given declination is seen at all times with the same zenith angle. But in the Pierre Auger Observatory a given point source in the sky has a zenith angle that is moving with a period of one sidereal day and only visible in the inclined directions for a limited amount of time per sidereal day. Figure 3.13a shows the duration

of the time interval over which a source is in each of the zenith angle ranges during a sidereal day, obtained with Eq. (3.11). The preferred declination values are located near the extreme values of declination in the field of view for the ES, DGH or DGL channels. This is because the sources are in the field of view for a maximal period of time as can be read from the y axis of Fig. 3.13a. These preferred directions appear as marked peaks in Fig. 3.13b, a consequence of the oscillatory nature of the observing zenith angle with time. As the zenith reaches its extreme value it changes with time with a relatively slower rate for declination values that can be read in Fig. 3.13a. The point source sensitivity of the Pierre Auger Observatory is, therefore, a direct result of the long-term averaging of its periodically changing field of view.

Exposure

In the case of a steady flux, the exposure $\mathcal{E}$ to a point-like source of UHE neutrinos multiplied by the spectral flux gives the expected energy distribution of the detected events. The exposure depends on neutrino energy and on the declination δ of the source and it is obtained integrating the θ-dependent effective area $\mathcal{A}$ (see Fig. 3.12) over a given time interval:

$$\mathcal{E}(E_\nu, \delta) = \int_{t_1}^{t_2} \mathrm{d}t \; \mathcal{A}(E_\nu, \theta(t), t). \tag{3.12}$$

For a given source position δ, the effective area $\mathcal{A}$ depends on θ (Fig. 3.12) which changes with time as given by Eq. (3.11). In addition there is an extra dependence on time through explicit variations of the effective area with time because of the changing size of the SD of Pierre Auger. Between 2004 and 2008, as the SD was being constructed, the size increased steadily. Variations have been relatively small after 2008, since they are due to temporary failures of stations and the fraction of working stations is typically above 95%, as obtained from the continuous monitoring of the SD (see Fig. 3.1) [57]. The time evolution of the effective area (averaged over intervals of three days) is displayed in Fig. 3.14 during the data-taking period of the Observatory until 31 Aug 2018 for selected values of zenigh angle and energy. The rise during detector deployment is visible before May 2008. The effective area is quite stable after 2008 except for fluctuations lasting of the order of days or less. The plot also displays a few periods excluded in the following years: 2004, 2005, 2008, 2009, 2014, 2015 and 2016, in which the array was not running stably mainly due to communication problems (see also Fig. 2.24). These periods are removed from the searches.

The time integral for the exposure in Eq. (3.12) is done with simulations, sampling the array configuration at regular time intervals which are adjusted depending on the total observation period (see also Section 3.1.1). If the duration of the search interval is of order a day or shorter, the start time of the search interval and its duration take particular relevance for the effective exposure, because of the dependence of effective area with zenith angle, and due to the limited fraction of the sidereal day during which a source at a given declination δ is within each of the zenith-angle ranges for ES, DGH and DGL

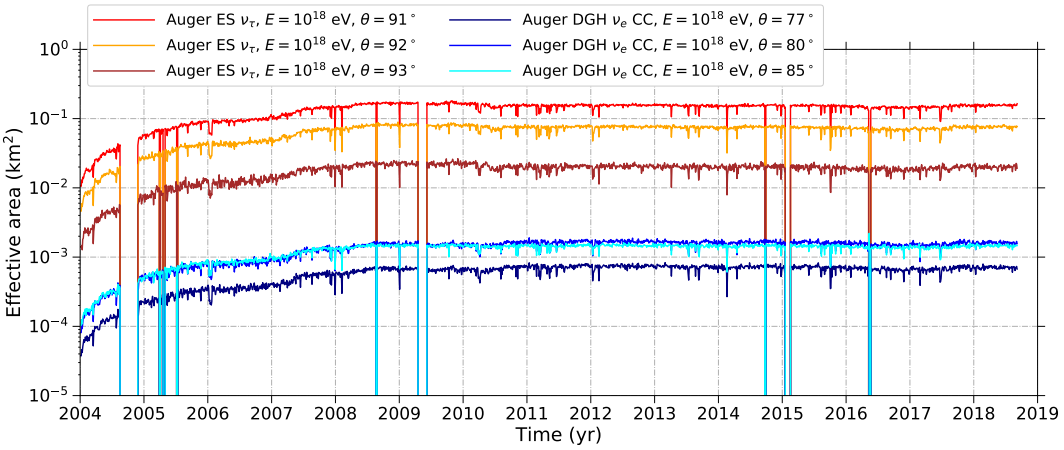

Figure 3.14: Average effective area calculated in three-day intervals for the ES and DGH channels as a function of time for the data taking period of the Observatory from 1 Jan 2004 to 31 Aug 2018. See also Fig. 3.1.

neutrino searches (see Fig. 3.13b).

The directional exposure obtained daily for the ES and DGH selections at fixed energies, averaged in the period between 1 May 2008 and 31 August 2018 (excluding the intervals over which the array was unstable) is shown in Fig. 3.15a as a function of source declination. Complementary, in Fig. 3.15b we also show the average exposure as a function of energy for a few declinations. When the search interval is much larger than a day, the dependence of the exposure on declination is well approximated by the daily average. Each of the average exposures obtained for each channel displays two peaks in declination, close to those that have maximal observation times in Fig. 3.13b. In the ES search, the maximal values are obtained for declination values $\delta \sim -53^\circ$ and $\delta \sim 55^\circ$, while in the DGH channel the exposure peaks at $\delta \sim -55^\circ$ and $\delta \sim 45^\circ$. As the effective area for ES neutrinos is larger than that for DGH (Figs. 3.11 and 3.12), the overall largest exposures are obtained for declination values that are close to the peaks in observation time of the ES band alone. This translates into average differences of about an order of magnitude in the exposure for ES relative to DGH at 10^{18} eV energies despite the transit time per day of a given source being typically shorter for ES. However, at higher energies ($\sim 3 \times 10^{19}$ eV), both searches have comparable exposures. The behaviour of the Pierre Auger Observatory in the search for point sources of neutrinos is thus dependent on the exact energy range of the flux to measure and its spectral features.

In the case of searches in short time intervals, in addition to this general behaviour of the exposures with declination and energy for each selection group, the position of the source relative to the Observatory at the start point of the search period plays a decisive role. When the source lies at a zenith angle between $\theta \sim 91^\circ$ and $\theta \sim 93^\circ$ degrees, just below the horizon, the effective area is maximal (see Figs. 3.11 and 3.12). An example

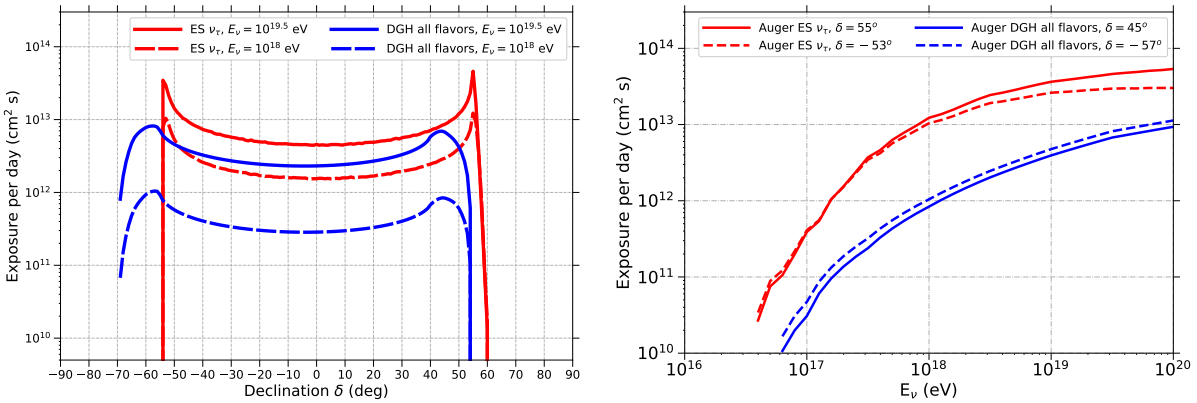

(a) Exposure vs declination.

(b) Exposure vs neutrino energy.

Figure 3.15: Left panel: Average exposure per day at $E_\nu = 10^{18}$ eV and 3×10^{19} eV as a function of declination δ, calculated for the period from 1 May 2008 when the SD array was completed up to 31 Aug 2018 for the ES and DGH channels. Right panel: Average exposure per day as a function of energy, calculated in the same period for the pair of declinations at which the exposure in each of the ES and DGH channels peaks [24].

is shown in Fig. 3.13a. The event GW170817 corresponding to the collapse of a binary neutron star was at the instant of merging in the FoV of the ES channel, the most sensitive channel in Auger, with the largest effective area and hence highest sensitivity, exceeding that of IceCube above 0.1 EeV by one order of magnitude [26].

3.4.2 Limits for steady sources of UHE neutrinos

The expected number of neutrino events in an energy range $[E_{\rm min}, E_{\rm max}]$ from a point-like source located at a declination δ is given by[2]:

$$N_{\rm expected}(\delta) = \int_{E_{\rm min}}^{E_{\rm max}} \int_{t_1}^{t_2} {\rm d}E_\nu \, {\rm d}t \, \phi(E_\nu, t) \, \mathcal{A}(E_\nu, \delta, t). \tag{3.13}$$

To calculate a flux bound for a point source, the time dependence of the neutrino flux of each flavor should be known. In the absence of reliable predictions it is customary to assume that the flux is independent of time during a given time interval, and that it follows a generic power law $\phi = k_{\rm PS} \, E_\nu^{-\alpha}$ with $\alpha = 2$, where $k_{\rm PS}$ is the normalization, and that the fluxes of the three neutrino flavors are equal, as quite accurately expected from vacuum flavor oscillations. If the flux is independent of time, the exposure integral:

$$\mathcal{E}(E_\nu, \delta) = \int_{t_1}^{t_2} {\rm d}t \mathcal{A}(E_\nu, \delta, t), \tag{3.14}$$

[2]For simplicity we have dropped the flavor sub-index i; a similar equation can be assumed for each flavor.

can be factored out and the equation for the number of events simplifies to:

$$N_{\text{expected}}(\delta) = \int_{E_{\text{min}}}^{E_{\text{max}}} \mathrm{d}E_\nu \, \phi(E_\nu) \, \mathcal{E}(E_\nu, \delta). \tag{3.15}$$

For steady fluxes, the time interval is the active period between 1 Jan 2004 and 31 Aug 2018, excluding the unstable periods. The lower limit of the energy integral can be taken as zero because the exposure, $\mathcal{E}$, becomes practically negligible for energies below $\sim 5 \times 10^{16}$ eV. Also, under the assumption made for a spectral index of $\alpha = 2$, the bulk of the neutrino triggers is not much dependent on the upper limit of the integral. As in the case of diffuse fluxes the expected ES events are between 1.6×10^{17} eV to 2×10^{19} eV while the DG events are $\sim 90\%$ between 10^{17} and 10^{20} eV. There is little dependence of these energy intervals on δ or E_{max} provided that $E_{\text{max}} \gtrsim 10^{20}$ eV.

As stated in Section 3.2 a blind search for UHE neutrinos in the data period up to 31 Aug 2018 has yielded no candidate neutrino events in the ES, DGH, and DGL analyses [23]. Under the conservative assumption of zero background, a 90% C.L. upper limit on the neutrino flux from point-like sources is derived assuming $\phi = k_{\text{PS}} \cdot E_\nu^{-2}$. The bound on $k_{\text{PS}}(\delta)$ is the value that gives a total of 2.39 expected events according again to Feldman-Cousins [76] with systematic uncertainties on the exposure calculated using the semi-Bayesian approach described in [22]. A bound on $k_{\text{PS}}(\delta)$ can be obtained separately for the ES, DGH, and DGL channels. The dependence of the neutrino detection efficiency on the zenith angle and its variation with time as the source transits in the field of view of the Pierre Auger Observatory are taken into account in the calculation of the limits. The data period corresponds to almost 14 years, so the exposure can be assumed uniform in right ascension within $\pm 0.6\%$ [105]. As a consequence and as a good approximation the limits on point-like sources depend only on the declination.

The limits are shown in Fig. 3.16 as a function of declination in comparison to those obtained by IceCube [101] and ANTARES neutrino telescopes [106]. The limits reported by ANTARES and IceCube apply to energies just below the energy range of the search for neutrinos with the Pierre Auger Observatory that starts at $\sim 10^{17}$ eV, in this sense, the Auger limits are complementary to those of IceCube and ANTARES. The different energy ranges are completely dependent of each detector features, for example, in IceCube UHE neutrinos coming from the northern sky have to go through the Earth, and at those energies the neutrinos will interact inside the Earth (Earth absorption). This is the reason why the energy range of the IceCube limit in the northern sky finishes at 10^{15} eV, while for the sourthern sky it finishes at 10^{17} eV.

The complementarity between the limits of ANTARES, IceCube and Auger are apparent for the particular case of the active galaxy Centaurus A, a potential source of UHECRs, shown in Fig. 3.17. CenA at $\delta \sim -43°$ is observed $\sim 7\%$ ($\sim 29\%$) of one sidereal day in the range of zenith angles corresponding to ES (DG) events (see Fig. 3.13b). The predicted fluxes for two theoretical models of UHE ν-production – in the jets [107] and close to the core of Centaurus A [108] – are also shown. We expect ~ 0.7 events from Cen A for the flux model in [107] and ~ 0.025 events for the model in [108]. How-

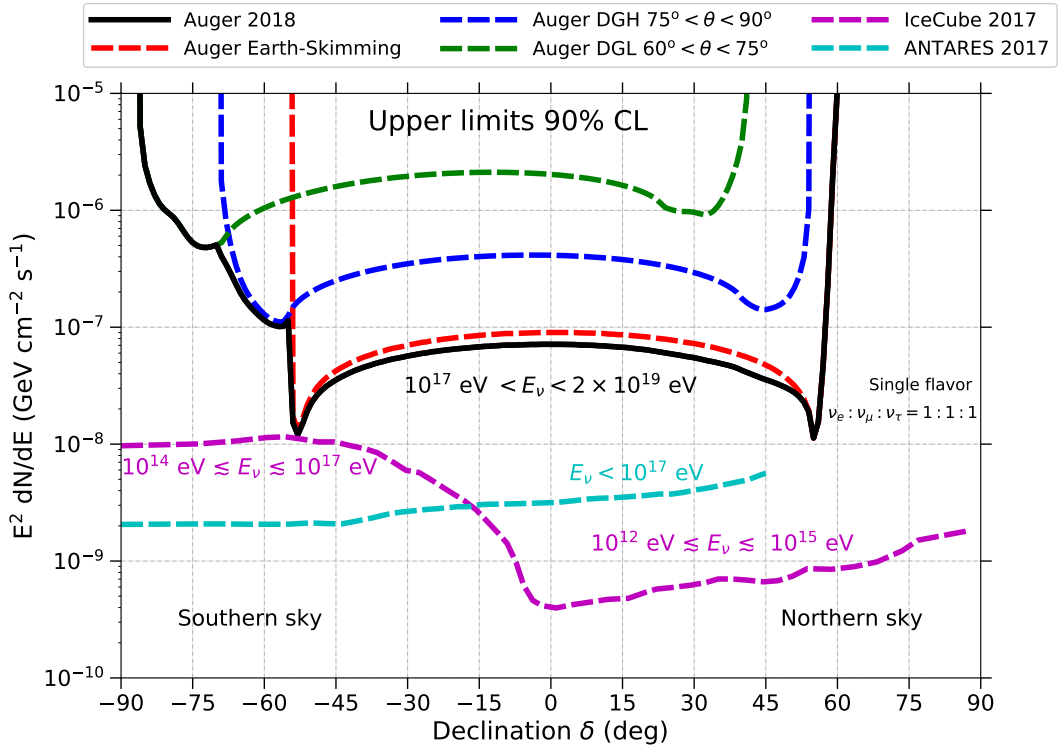

Figure 3.16: Pierre Auger Observatory upper limits (1 Jan 2004 - 31 Aug 2018) at 90% C.L. on the normalization k^{PS} of a single flavor point-like flux of UHE neutrinos $\mathrm{d}N/\mathrm{d}E_\nu = k^{\mathrm{PS}} E_\nu^{-2}$ as a function of the source declination δ [24]. Also shown are the limits for IceCube (2008 - 2015) [101] and ANTARES (2007 - 2015) [106]. Note the different energy ranges where the limits of each observatory apply.

ever, there are significant uncertainties in these models that stem from the fact that the neutrino flux is normalized to the UHECR proton flux assumed to originate from CenA, which is highly uncertain.

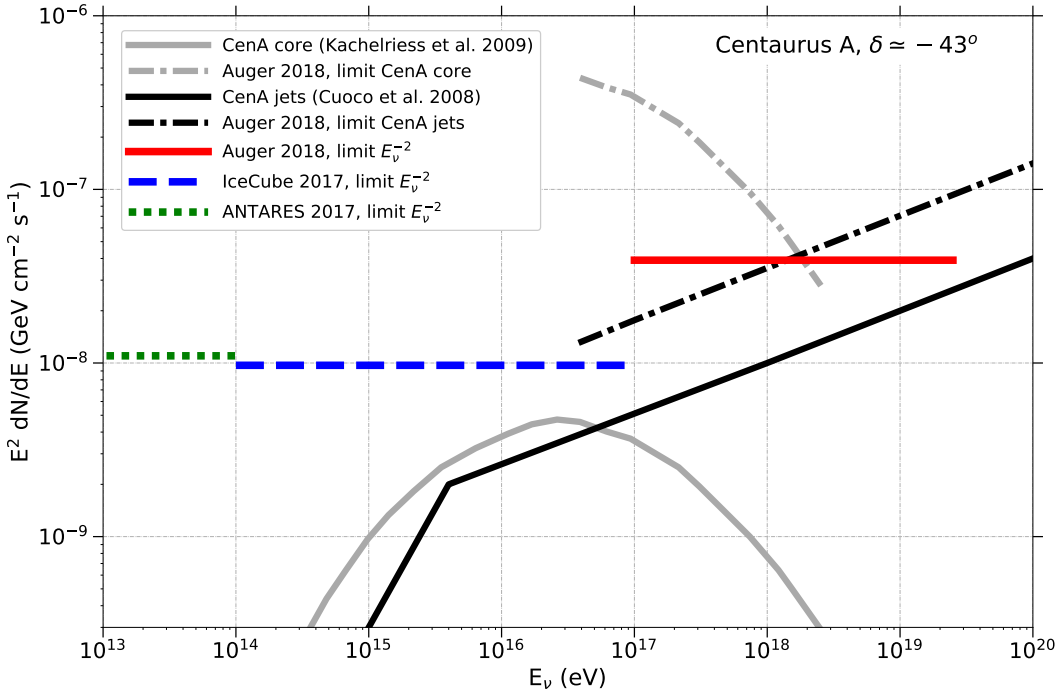

Figure 3.17: Upper limits at 90% C.L. from the Pierre Auger Observatory on a single flavor E^{-2} neutrino flux from the active galaxy Centaurus A, together with limits from IceCube [101] and ANTARES [106]. We again show the upper limits to the normalization of the fluxes following the same spectral shape as the models needed to produce 2.39 events in Auger (dash-dotted lines). We also ilustrate the predictions of two models of UHE neutrino production in the jets [107], and close to the core of Centaurus A [108], along with 90% C.L. upper limits to these specific models with the Pierre Auger Observatory [24].

3.5 Future prospects

In June 2013 two new types of triggers started to be implemented in the water-Cherenkov stations: Time over Threshold deconvolved (ToTd) and Multiplicity of Positive Steps (MoPs) [109, 110]. The objective of these triggers is to select smaller and broader signals and to lower the energy threshold.

To remove signals compatible with isolated muons the ToTd algorithm applies a deconvolution of FADC traces by a decreasing exponential of characteristic time of 60 ns, and then requires at least 10 slots above 0.2 VEM in deconvoluted trace within a time window of 3 μs, for at least 2 working PMTs.

On the other hand, the MoPs algorithm is based on counting *positive steps*, being a step the difference between successive slots in FADC trace. If more than 4 positive steps are counted during 3 μs in at least 2 PMT, the station triggers as MoPs.

A preliminar study about the impact of ToTd and MoPs triggers on the trigger

efficiency in the search of neutrinos with the surface detector has been done showing enhancements of the trigger efficiency much higher than 100% for neutrinos of energy up to 10^{18} eV [111].

Furthermore the currently ongoing upgrade of the Surface Detector of the Pierre Auger Observatory, AugerPrime, will add a plastic scintillation detector [112] and a radio antenna [113] to each Water-Cherenkov Detector. Thanks to the data collected simultaneously with the Water-Cherenkov and the scintillation detectors for a high statistics sample of ultra-high-energy events, additional measurements of composition-sensitive observables will be possible, and these measurements are not affected by the low duty cycle of the Fluorescence Detector. This will improve the potential to identify the primary masses to the highest energies and will further add discrimination power for the primary mass on an event-by-event basis. It has been calculated that the upgrade will enable us to directly identify a possible proton component at the highest energies as small as $f_p = 0.1$ [112, 114]. This will be essential for determining the role of cosmic-ray observations in UHE astronomy, and for establishing the potential of present and future detectors to the detection of the cosmogenic neutrino flux [115].

USC
UNIVERSIDADE
DE SANTIAGO
DE COMPOSTELA

4

Search for UHE neutrinos in coincidence with GW events

4.1 Introduction to Gravitational Waves

In 1915 Albert Einstein published the General theory of Relativity. One year later he predicted the existence of gravitational waves (GW) as a consequence of his theory: when a massive object is accelerated (for example, a black hole or neutron star orbiting another one) it would disrupt space-time creating 'waves' that would propagate at the speed of light in all directions away from the source [116].

Gravitational waves were detected by LIGO on September 2015 for first time with the LIGO Interferometric detectors [4]. Given the fact that they are produced (among other sources) in energetic sources such as the merging of binary compact objects (black-holes and neutron stars), the question naturally arises on the possibility that these mergers are also a source of UHECR and UHEν. This is addressed in this chapter, reporting on the search for UHEν in coincidence with GW events using data collected with the SD of the Pierre Auger Observatory.

4.2 Summary of LIGO observations

On September 14, 2015 at 09:50:45 universal time (UTC) the Advanced LIGO detectors observed the first gravitational wave generated by two colliding black holes (BH-BH merger or BBH). LIGO ("Laser Interferometer Gravitational-wave Observatory") is the

world's largest gravitational-wave observatory. It is composed of two laser interferometers located in Livingston and Hanford in the USA (3000 km between them), consisting each LIGO detector of two 4 km-long arms that is capable of measuring a distance on the order of 10^{-19} m [116]. The next day, on September 15, 2015 the following GCN Circular[1] was sent:

```
TITLE: GCN CIRCULAR
NUMBER: 18330
SUBJECT: LIGO/Virgo G184098:  Burst candidate in LIGO engineering run data
DATE: 15/09/20 00:53:16 GMT
FROM: Leo Singer at NASA/GSFC <leo.p.singer@nasa.gov>

Dear colleagues,

We would like to bring to your attention a trigger identified by the
online Burst analysis during the ongoing Engineering Run 8 (ER8).
Normally, we would send this in the form of a private GCN Circular, but
the LIGO/Virgo GCN Circular list is not ready yet.

The LIGO Scientific Collaboration and Virgo report that the cWB unmodeled
burst analysis identified candidate G184098 during real-time processing of
data from LIGO Hanford Observatory (H1) and LIGO Livingston Observatory
(L1) at 2015-09-14 09:50:45 UTC (GPS time:  1126259462.3910).  Alerts were
not sent in real-time because the candidate occurred in ER8 data; however,
we have now sent GCN notices through our normal channel.

G184098 is an unvetted event of interest, as the false alarm rate (FAR)
determined by the online analysis would have passed our stated alert
threshold of ~ 1/month.  The event's properties can be found at this URL:

https://gracedb.ligo.org/events/G184098

There are important caveats associated to this event:
* It occurred before the initiation of the planned observing run;
* The detectors were not in their final O1 configuration;
* Calibration is not finalized.
In particular, calibration uncertainties may imply systematic errors in
sky localization.

Nevertheless, the trigger is of sufficient interest to present an
```

[1] Gamma-Ray Coordinate Network [5].

important opportunity to exercise the EM follow-up process, and we invite you to make use of the information in the above link.

Two sky maps are available at the moment: the rapid localization from cWB itself, and a refined localization from LALInference Burst (LIB). They are in good qualitative agreement with each other. The 50% credible region spans about 200 deg^2 and the 90% region about 750 deg^2.

Updates on our analysis of this event will be sent as they become available.

PLEASE REMEMBER that this message is being sent only to groups that have signed MOUs with LIGO and Virgo and have observing capabilities during O1, and that this event and the LIGO/Virgo data related to it remain confidential at this time.

We are looking forward to learn what you will see, and to an exciting time in the Advanced LIGO/Virgo era.

Best wishes,
Leo, Marica, Peter

[GCN OPS NOTE(19sep15): This Circular was originally published on 05:39 16-Sep-2015 UT.]

Posterior refined analyses confirmed that the event had indeed originated in the collision of two black-holes with estimated masses $m_1 \simeq 36^{+5}_{-4}$ M$_\odot$ and $m_2 \simeq 29^{+4}_{-4}$ M$_\odot$, at a luminosity distance $D_s = 410^{+160}_{-180}$ Mpc.

In Fig. 4.1 we reproduce the so called strain $h = \frac{\Delta L}{L}$ with ΔL the variation of the length ($L = 4$ km) of the arms of the LIGO Interferometers as a function of time [117]. The signal lasted $\simeq$ 200 ms. The measured strain is compared to the predictions of General Relativity with a high-degree of consistency between them. This event marked the beginning of GW Astronomy.

Over the years LIGO and Virgo have been taken data in three different periods:

- Run O1: 12 September 2015 - 19 January 2016.
- Run O2: 30 November 2016 - 25 August 2017.
- Run O3: 1 April 2019 - 27 March 2020 (it has been planned to end on April 30, but due to COVID-19 the run was suspended).

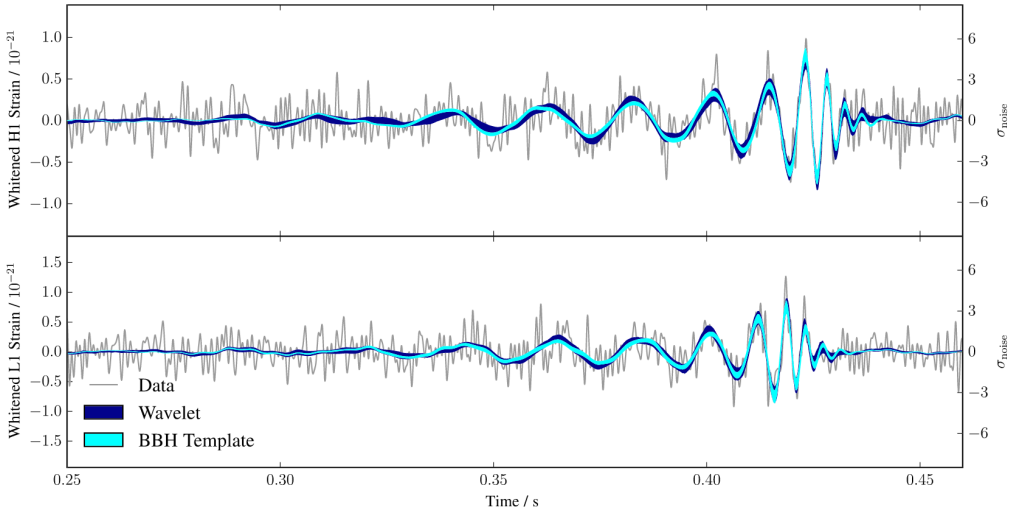

Figure 4.1: Time-domain data and reconstructed waveforms of GW150914 whitened by the noise power spectral density, for the Hanford (top) and Livingston (bottom) detectors. Times are shown relative to September 14, 2015 at 09:50:45 UTC. The ordinate axes on the right are in standard deviations units and on the left are normalized. The grey lines are the data and the two different waveforms (blue bands) are plotted as bands representing the uncertainty in the reconstruction and they correspond to two different models. More details in [117].

4.3 Searches for UHE neutrinos from GW events

In this section the neutrino identification criteria is applied to data collected with the Pierre Auger Observatory as described in Chapter 2. Firstly, inclined showers are selected in the different angular ranges of the ES and DGH channels. Secondly, deeply penetrating showers are identified in the inclined-event sample through the broad time structure of the signals expected to be induced in the water-Cherenkov SD stations indicative of the presence of a significant fraction of electromagnetic component.

The sensitivity to UHE neutrinos in Auger is limited to large zenith angles $\theta \gtrsim 60°$. As a consequence at each instant in time, neutrinos can be detected efficiently only from a specific portion of the sky: the one visible from the Auger site with $\theta \in (90°, 95°)$ for ES and with $\theta \in (60°, 90°)$ for downward-going[2]. As explained in Section 3.4.1, a point-like source at a declination δ and right ascension α (in equatorial coordinates) is seen from the latitude of Auger ($\lambda = -35.2°$) with a time-dependent zenith angle $\theta(t)$ given by:

$$\cos\theta(t) = \sin\lambda\sin\delta + \cos\lambda\cos\delta\cos\left(2\pi\frac{t}{T} - \alpha\right),$$

[2]In this Section we will only consider the downward-going events with $\theta \in (75°, 90°)$, the so-called DGH channel.

where T is the duration of one sidereal day. The time interval for the neutrino search is crucial in the case of transient sources such as BBH and BNS mergers. For searches over short periods of time (of the order of minutes or less), the SD of Auger is sensitive to UHEν only if the zenith angle of the source is in the range of the ES or DG channels. This is the case of BBH or BNS when considering the interval of time during which GW are detected, lasting only a few seconds at most. For longer search intervals (of order a day or more) a source is seen in the angular range of ES or DG for a fraction of time that depends on its declination as shown in Fig. 3.13b.

Follow-up of GW events with Auger

Every time a GW trigger above a certain threshold is observed, LIGO/Virgo communicate it with a latency of less than a minute for follow-up observations in electromagnetic wavelengths and neutrinos [118]. When the Pierre Auger Collaboration receives a Gravitational Wave alert the first step is to analyze the data looking for UHE neutrinos in the ES and DGH channels.

The data is analyzed in two time windows:

- $\pm$500 s around the trigger time of the GW event. This interval is motivated by the duration of the prompt emission of long Gamma-Ray Burst (GRB) and accounts for the possibility of emission prior to the merger of the binary compact system (more details about the selection of the time window in [119]).
- 1 day after the first trigger time of the event to account for possible afterglow emission.

The cuts applied for this search are detailed in Section 2.2.3 and summarized in Tables 2.3 and 2.5. A possible change of the applied cuts was thought about, and it is an interesting study for the future.

Once the 1 day-unblinding is performed in Auger, a response email is sent through GCN notices to inform other collaborations if a neutrino candidate is detected or (up to now) that no neutrinos have been detected. Here is an example of the response GCN sent corresponding to the binary neutron star merger GW190425:

```
TITLE: GCN CIRCULAR
NUMBER: 24240
SUBJECT: LIGO/Virgo S190425z:  Pierre Auger Observatory follow-up
DATE: 19/04/26 16:57:05 GMT
FROM: Jaime Alvarez-Muniz at Pierre Auger Observatory
<jaime.alvarezmuniz@gmail.com>

J. Alvarez-Muniz, F. Pedreira, E. Zas (Univ.  Santiago de Compostela, Spain),
K. H. Kampert & M. Schimp (Bergische Universitat, Wuppertal, Germany)
on behalf of the Pierre Auger Collaboration.
```

```
In response to:
LIGO/Virgo GW trigger S190425z
T0=2019-04-25 08:18:05 UTC

We searched for Ultra-High-Energy (UHE) neutrinos with energies above ∼ 1e17 eV
in data collected with the Surface Detector (SD) of the Pierre Auger
Observatory in a [-500,500] second interval about the LIGO-Virgo trigger
S1902425z as well as 1 day after it.

The field of view (fov) where the SD of Auger is sensitive to UHE neutrinos
(corresponding to inclined directions with respect to the vertical relative to
the ground) was PARTIALLY COINCIDENT (35.5%) with the LIGO/Virgo 90%
localization region at the time T0 of the merger alert.

NO events survived the cuts applied to reject the background due to UHE Cosmic
Rays i.e.  NO neutrino candidates were detected.

-------
The Pierre Auger Observatory is an UHE Cosmic Ray detector located in the
Mendoza Province in Argentina.  It consists of an array of Water Cherenkov
detectors spread over a total surface of 3000 km^2 arranged in a triangular grid
of 1.5 km side as well as Fluorescence telescopes and other systems
(see 10.1016/j.nima.2015.06.058 for more information).
For neutrino searches from GW events with Auger, please refer to:
https://journals.aps.org/prd/pdf/10.1103/PhysRevD.94.122007
```

When the first GW events were alerted, the follow-up and search for UHE neutrinos had a large latency of 5 days since Auger data needed to be processed and transferred to a server in Lyon (France) before it was accessible. Since July 2019 the data unblinding is done automatically in the computers at the Auger site in Malargüe with the minimum possible latency which is currently less than 15 min. The production of the GCN response still requires human intervention, in particular to obtain the fraction of the 90% localization contour of the GW event in the field of view of the ES and DG channels (see Sections 4.4.1 and 4.4.2).

During the LIGO and Virgo runs O1, O2 and O3, 62 GW triggers were sent and information about their sky localization distributed for follow-up observations through GCN. Most of the triggers were compatible with binary black-hole mergers (BBH), but there are also several candidate binary neutron-star mergers (BNS), neutron-star and black-hole mergers (NSBH) and a few MassGap events. The classification of the gravitational waves depends on the masses of the two celestial bodies that merge (see Fig. 4.2). The MassGap events are mergers in which at least one of the celestial bodies has an intermedium mass,

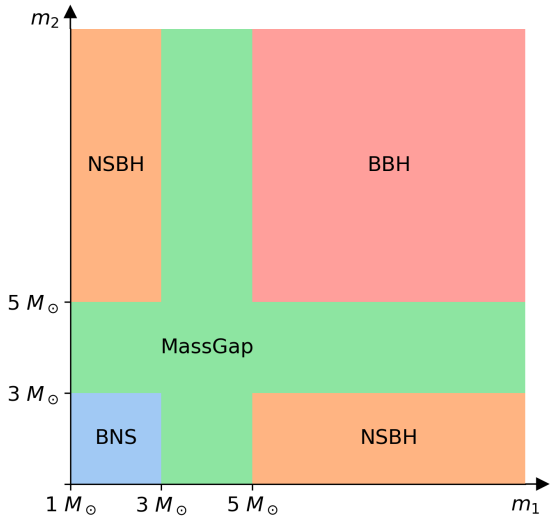

Figure 4.2: Source classification of the gravitational-wave events depending on the masses (m_1 and m_2 in units of solar masses $M_\odot$) of the two celestial bodies that merge.

that means that the mass is too large to be a neutron star ($m > 3$ $M_\odot$) but too small to be a black hole ($m < 5$ $M_\odot$). The existence of these bodies would imply a review of the stellar evolution as we know nowadays.

In Fig. 4.3 we represent all the GW triggers alerted by LIGO/Virgo (as given in [120]) and followed up in UHE neutrinos with the SD of the Pierre Auger Observatory. We distinguish between runs O1, O2 and O3 (different background colors: cyan, yellow and grey, respectively) and between types of sources (different dot colors).

4.3.1 Upper limits to the UHEν flux from GW events

No neutrino candidates were found in coincidence with any of the gravitational-wave events, so an upper limit to the UHE neutrino flux as a function of equatorial declination δ of the source can be established. The calculation of the limits involves obtaining the exposure of the SD of the Pierre Auger Observatory in the corresponding time window, as explained in Section 3.4.1.

The expected number of events for a neutrino flux $dN_\nu^{\rm GW}/dE_\nu$ from a pointlike source at declination δ is given by

$$N_{\rm expected}^{\rm GW} = \int_{E_\nu} \frac{dN_\nu^{\rm GW}}{dE_\nu}(E_\nu)\, \mathcal{E}_{\rm GW}(E_\nu, \delta)\, dE_\nu, \tag{4.1}$$

where $\mathcal{E}_{GW}(E_\nu, \delta)$ is the integral exposure to a pointlike flux of UHE neutrinos as a function of neutrino energy E_ν and declination (from Eq. 3.15).

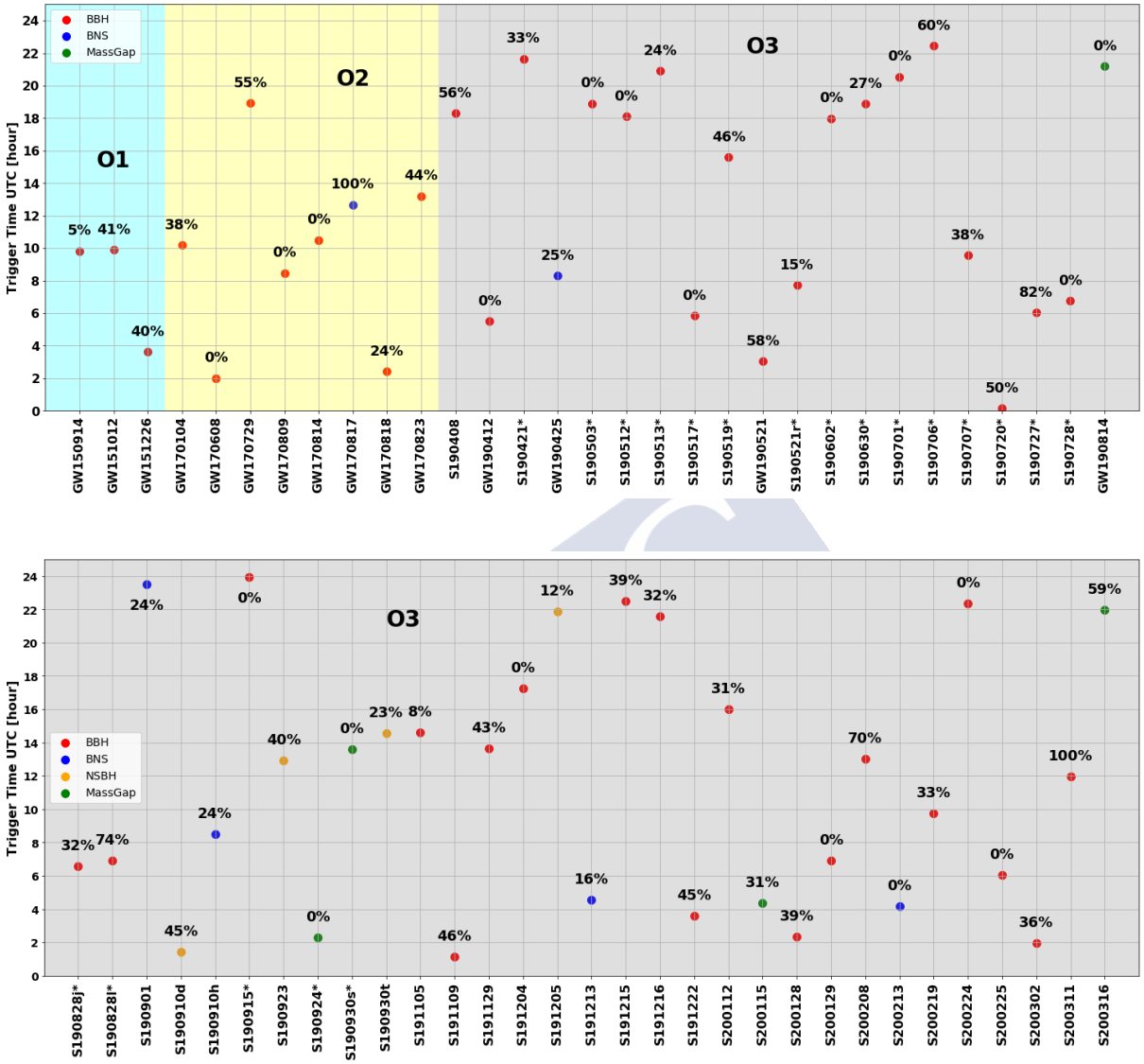

Figure 4.3: Representation of all the GW trigger alerts by LIGO/Virgo which were followed-up in UHEν with the SD of the Pierre Auger Observatory. The background color indicate the LIGO/Virgo run (blue: O1 (12 September 2015 - 19 January 2016), yellow: O2 (30 November 2016 - 25 August 2017) and grey: O3 (1 April 2019 - 27 March 2020)) and the different color of the points indicate the source clasification (red: BBH, blue: BNS, yellow: NSBH and green: MassGap, see Fig. 4.2). In the x-axis we represent the eventID while in the y-axis we give the UTC hour in the day the GW event was detected. The candidate events that were promoted to GW in [121] have an asterisk at the end of the eventID in the x-axis. The number on top of each event indicates the fraction of the 90% C.L. contour localization of the source overlaping with the field of Auger in the ES and DGH zenith angles ranges at the trigger time of the GW.

For each channel, ES and DGH, we calculate the exposure to UHE neutrinos $\mathcal{E}^{\rm ES}(E_\nu, \delta)$ and $\mathcal{E}^{\rm DGH}(E_\nu, \delta)$, respectively, following the procedure explained in Section 3.4.1. The exposure is obtained by integrating over the search period $T_{\rm search}$, the SD aperture (area $\times$ solid angle) multiplied by the neutrino cross-section for each neutrino channel, and weighted by the selection and detection efficiency obtained from Monte Carlo simulations [22]. When integrating over the search period, only the fraction of time when the source is visible from the SD of Auger within the zenith angle range of the corresponding neutrino selection contributes to the exposure. For all the search periods considered, the performance of the SD array was very stable. This is illustrated with several examples in Section 4.4.1.

Assuming a E_ν^{-2} energy dependence for a constant UHE neutrino flux per flavor from the source of each GW, namely, $dN_\nu^{\rm GW}/dE_\nu = k^{\rm GW} E_\nu^{-2}$, a 90% C.L. upper limit on $k^{\rm GW}$ can be obtained as

$$k^{\rm GW}(\delta) = \frac{2.39}{\int_{E_\nu} E_\nu^{-2}\, \mathcal{E}_{\rm GW}(E_\nu, \delta)\, dE_\nu}. \tag{4.2}$$

We applied Eq. (4.2) to obtain upper limits to the normalization of the reference flux $k^{\rm GW}_{\rm ES}(\delta)$ and $k^{\rm GW}_{\rm DGH}(\delta)$ in each channel. The combined upper limit to the normalization $k^{\rm GW}(\delta)$ of the flux is obtained as $(k^{\rm GW})^{-1} = (k^{\rm GW}_{\rm ES})^{-1} + (k^{\rm GW}_{\rm DGH})^{-1}$. With the exception of a few cases, the position in the sky of the source of the GW events alerted by LIGO/Virgo is not accurately known and, instead, a 90% C.L. contour localization is given, corresponding to several possible declinations where the source could actually be located. For this reason the limits shown in Section 4.4.1 will be given as a function of δ. From the limits to the flux normalization, we also obtained upper limits to the UHE neutrino spectral fluence (energy per unit area) radiated per flavor in a similar fashion to those obtained in [122]:

$$E_\nu^2 \frac{dN_\nu}{dE_\nu} \times T_{\rm search} = k^{\rm GW}(\delta)\, T_{\rm search}. \tag{4.3}$$

Here it is assumed that the sources of GW events emit UHE neutrinos continuously during the search period. The constraints on spectral fluence are strongly dependent on the source direction, this happens due to the different fractions of time a source at declination δ is within the field of view of the ES and DGH analyses (see Fig. 3.13b). The upper limit to the fluence is dominated by the intrinsically larger sensitivity of the ES analysis to UHE neutrinos at energies above 100 PeV.

Finally, it is straightforward to obtain constraints on the total energy radiated in neutrinos $E_{\nu,tot}(\delta)$ assuming the source is located at a luminosity distance D_s given by LIGO/Virgo observations:

$$E_{\nu,\rm tot}(\delta) = \mathcal{F}_\nu(\delta) \times 4\pi D_s^2. \tag{4.4}$$

The limits are naturally strongly dependent on the source visibility in the inclined directions during the search period. The UHEν flux cannot be constrained if the source is not visible in the ES or DG angular range during the search period. On the contrary, the

limit will be more restrictive the larger the time the source is visible in the ES channel, the most sensitive one.

In particular for the search period $T_{\text{search}} = 1$ day after the merger, the most restrictive upper limits on the total energy emitted per flavor in UHE neutrino are achieved at declinations $\delta \sim -53°$ and $\delta \sim 55°$ because at these declinations the source spends more time in the field of view of the ES channel. In the rest of this chapter we show several examples of the follow-up of different classes of GW events: The 3 BBH events in the O1 run, the 6 candidate BNS mergers detected so far, the 4 NSBH candidate mergers and the 5 MassGap candidate mergers.

4.4 Follow-up of GW events with the Pierre Auger Observatory

4.4.1 Binary Black Hole (BBH) mergers

In this section we show as an example the results of the follow-up of the three first BBH events detected during Ligo/Virgo O1 run, namely: GW150914, GW151012 and GW151226. In all cases we show:

- The performace of the SD array of the Pierre Auger Observatory during the search period (-500 s, $+1$ day) around the UTC time of the merger.
- The sky map in equatorial coordinates showing the 90% C.L. localization of the GW event and the field of view of the SD of Auger in the zenith angle range of ES and DGH at the UTC time of the merger.
- The fraction of the 90% C.L. GW localization overlapping with the field of view of Auger in the ES and DGH zenith angle ranges.
- The data collected at the SD of Auger during the search periods $T_{\text{search}} = \pm 500$ s around and $+1$ day after the merger.
- Upper limits to the UHEν fluence and energy emitted in UHEν from the absence of neutrino candidates in Auger data.

GW150914

GW150914 was detected on September 14, 2015 at UTC 09:50:45 by LIGO Hanford and Livingston. It was classified as a BBH merger with estimated masses $m_1 \simeq 36^{+5}_{-4}$ $M_\odot$ and $m_2 \simeq 29^{+4}_{-4}$ $M_\odot$. The event released $\simeq 3.1^{+0.4}_{-0.4}$ $M_\odot$ in the form of GW. The source was estimated to be at a luminosity distance $D_s = 410^{+160}_{-180}$ Mpc. This was the first GW event ever detected [4].

In Fig. 4.4 we show the stability of the SD array during the search periods ±500 s and +1 day around the trigger time of GW150914. Except for a few very short intervals the number of active stations is always above 1600. In Fig. 4.5a we show the sky localization of the event, extending over $\simeq$ 601 square degrees at 90% C.L. Only a small fraction of the 90% C.L. GW localization is in the fov of Auger in the inclined directions at the time of the merger. The overlap is also shown in Fig. 4.5b as a function of time for the period $T_{\text{search}} = (-500\text{s}, +1 \text{ day})$.

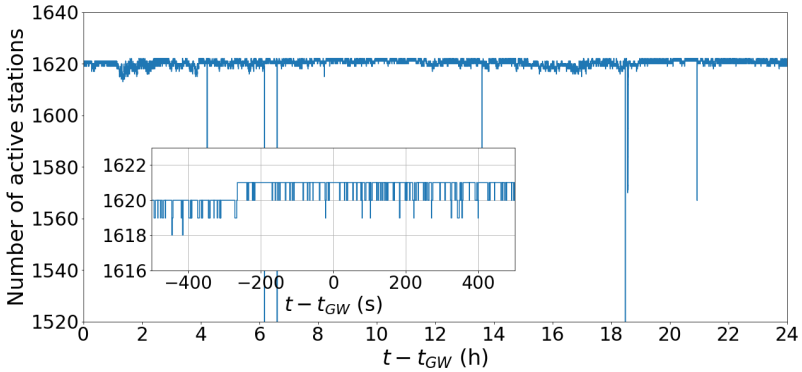

Figure 4.4: Number of active stations in the SD of the Pierre Auger Observatory vs time since the trigger time of GW150914. The larger panel is for the 1 day window, while the inset displays the details for the ±500 s window.

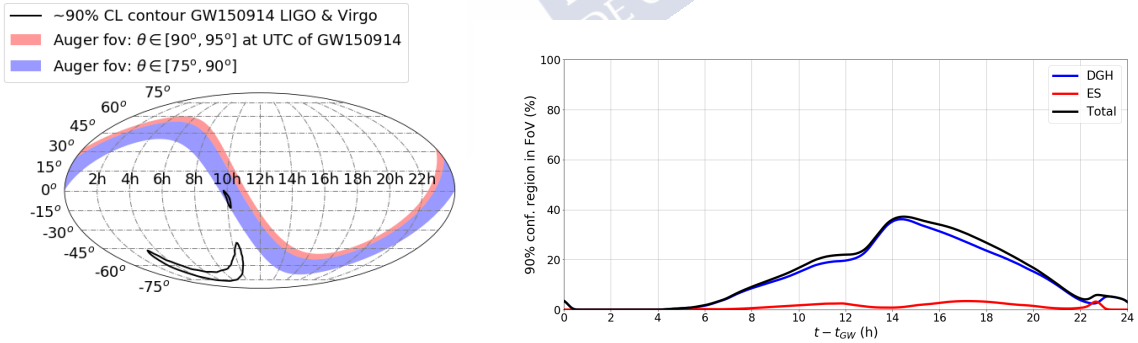

(a) FoV at the moment of GW150914.

(b) Fraction of 90% C.L. in FoV.

Figure 4.5: (a) Instantaneous field of view (FoV) of the Pierre Auger Observatory in the ES (red) and DGH (blue) zenith angle ranges at the moment of the GW150914 detection. The contour of the 90% confidence level of the direction of the detected gravitational wave is also plotted (black line). (b) Fraction of the 90% confidence level contour in the FoV of Auger during the day after the GW detection. We show both the ES fraction in blue and DGH fraction in red as well as the total (ES+DGH) in black.

In Fig. 4.6 we show the distributions of the neutrino identification observables (see Sect. 2.2) for the inclined events collected during the search period $T_{\rm search}$ = (−500 s, +1 day) around the merger, and compare them to those collected in 1 month worth of data at about the same time. There are no neutrino candidates in both the ES and DGH channels and in fact the events found in the period (−500 s, +1 day) fall inside the distribution of data collected in 1 month. There is one event of the monthly distribution that stands out to the right the others, it is an event close to the neutrino cut in both the ES and DGH channels classified as a background event compatible with being produced by a conventional cosmic-ray shower. The fact that an inclined event appears in both channels can occur for very inclined events that are picked up from data by both selections. It is a very inclined event with θ close to 90°. In Fig. 4.6 we show the values of the discriminating observables of the individual events as a function of time with respect to the time of the merger.

Finally in Figs. 4.7 we show the upper limits to the neutrino fluence and total energy radiated in the form of UHEν for the case of GW150914 assuming the energy is radiated isotropically. Using Eq. (4.4) we obtain that the most restrictive upper limit on the total energy emitted per flavor in UHEν is achieved at declination $\delta \sim -53°$,

$$E_{\nu,\rm tot}(\delta = -53°) < 7.7 \times 10^{53} \rm erg. \tag{4.5}$$

We should clarify that this is not the limit for this event. This is the best limit that we could establish if the source was in the most favorable position in the sky inside its 90% C.L. contour. So if the source actually is located in any other declination inside the 90% C.L. of the direction of the detected GW the limit would be worse.

The constraint on total energy can be also expressed as fractions f_ν of energy in UHEν $E_{\nu,\rm tot}$ relative to the energy radiated in gravitational waves $E_{\rm GW}$. The most stringent upper limit on the fraction f_ν of energy radiated in UHEν relative to the energy emitted in GW150914 is

$$f_\nu(\delta = -53°) < 14.3\%, \tag{4.6}$$

assuming the source is located at the central value of the 90% C.L. interval of distances D_s = 410 Mpc. This fraction changes from $\sim$ 4.5% to $\sim$ 27.6% as the source distance changes between the lower and upper limits of the 90% C.L. interval D_s = (230, 570) Mpc.

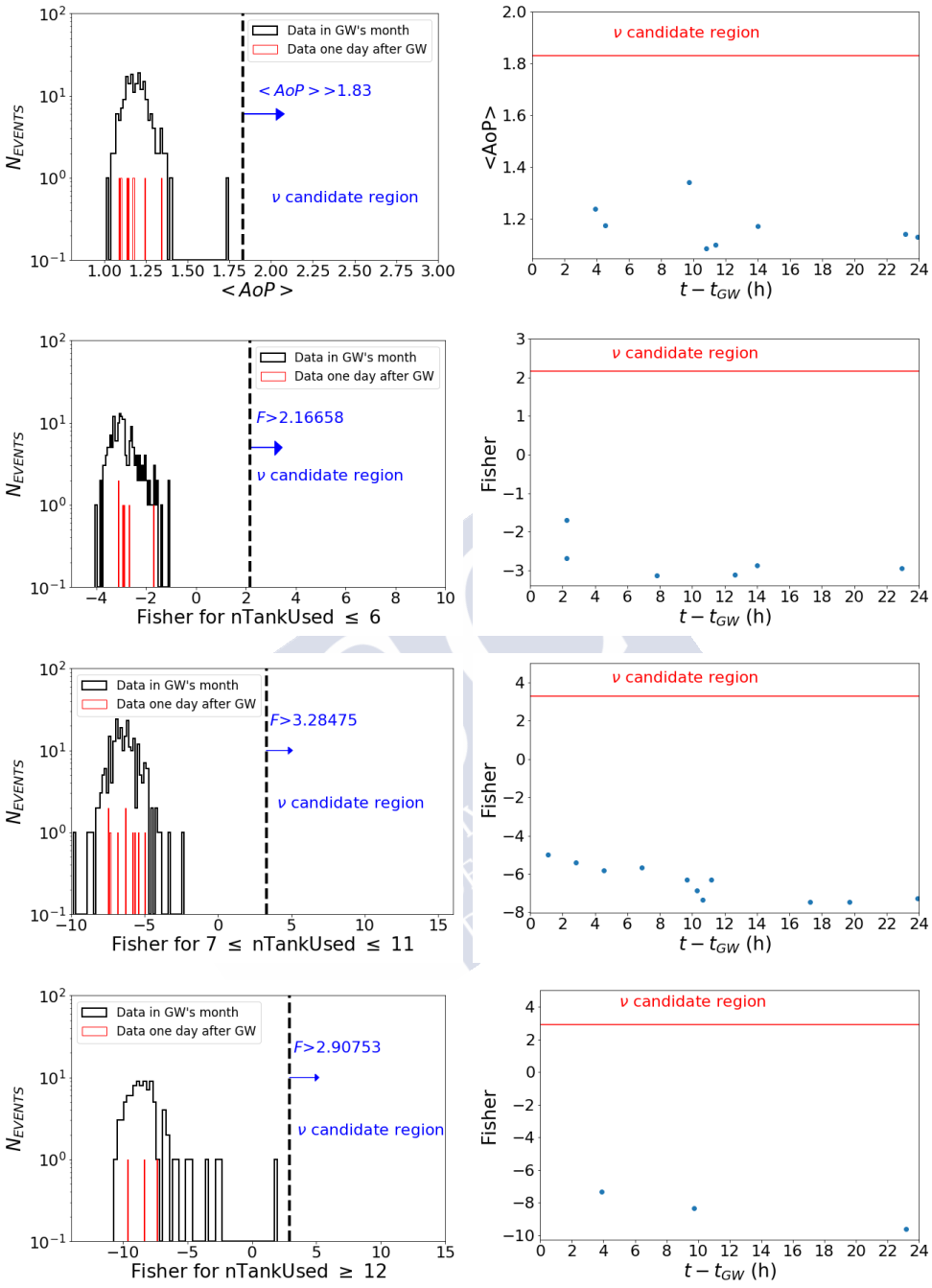

Figure 4.6: From top to bottom: ES, DGH low, DGH medium and DGH high. Left side: Histogram of the ⟨AoP⟩ (for ES) or Fisher value (for DGH) for the inclined events in the −500 s, +1 day window time around/after the merger time of GW150914. The black histogram represents the distribution for the whole month, showing that the events are under the bulk of the distribution. Right side: Values of the ⟨AoP⟩ or Fisher distribution as a function of time for the inclined events collected in the 1 day window time. The horizontal lines represent the neutrino cut and the symbols the inclined events in the 1-day time window. See Sect. 2.2.3 for details on the cuts.

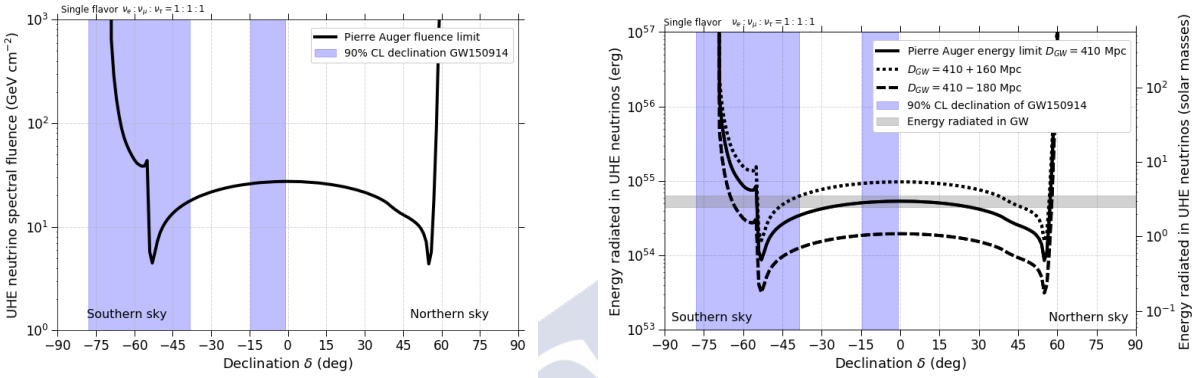

(a) Upper limits from GW150914.

(b) Constraints on $E_{\nu,\mathrm{tot}}$ from GW150914.

Figure 4.7: Left panel: Upper limits to the UHE neutrino spectral fluence per flavor (see Eq. 4.3) from the source of GW150914 as a function of equatorial declination δ. Fluences above the black solid line are excluded at 90% C.L. from the non-observation of UHE neutrino events in Auger. Right panel: Constraints on the energy radiated $E_{\nu,\mathrm{tot}}$ in UHE neutrinos (per flavor) from the source of GW150914 as a function of equatorial declination δ. Assuming the luminosity distance to the source is $D_s = 410$ Mpc, energies above the black solid line are excluded at the 90% C.L. from the nonobservation of UHE neutrinos in Auger. The long-dashed line illustrates the constraints if the source is farther away at $D_s = 410 + 160$ Mpc, and the short-dashed line if the source is closer to Earth at $D_s = 410 - 180$ Mpc corresponding to the 90% C.L. interval of possible distances to the source. For reference the gray horizontal rectangle represents $E_{GW} \simeq 5.4 \times 10^{54}$ erg, the inferred energy radiated in gravitational waves from GW150914 [4, 117]. The 90% C.L. declination bands of the GW150914 are indicated in the plot by the shaded blue rectangles.

GW151012

GW151012 was detected on October 12, 2015 at UTC 09:54:43 by LIGO Hanford and Livingston. It was classified as a BBH merger with estimated masses $m_1 \simeq 23.2^{+14.9}_{-5.5}$ $M_\odot$ and $m_2 \simeq 13.6^{+4.1}_{-4.8}$ $M_\odot$. The event released $\simeq 1.6$ $M_\odot$ in the form of GW. The source was estimated to be at a luminosity distance $D_s = 1080^{+550}_{-490}$ Mpc [123].

In Fig. 4.8 we show the stability of the SD array during the search periods. In the first 3.5 hours the number of active stations falls around 1260, but after that this number rises up to 1500, and keeps going up until it reaches 1600 about 2 hours later. After this, the number of active stations is always close and above 1600 except for a few very short intervals. In Fig. 4.9a we show the sky localization of the event, spanning over $\simeq 1800$ square degrees. Only a fraction of the 90% C.L. localization is in the fov of Auger in the inclined directions at the time of the merger. The overlap is also shown in Fig. 4.9b as a function of time for the period $T_{\rm search} = (-500\ {\rm s}, +1\ {\rm day})$.

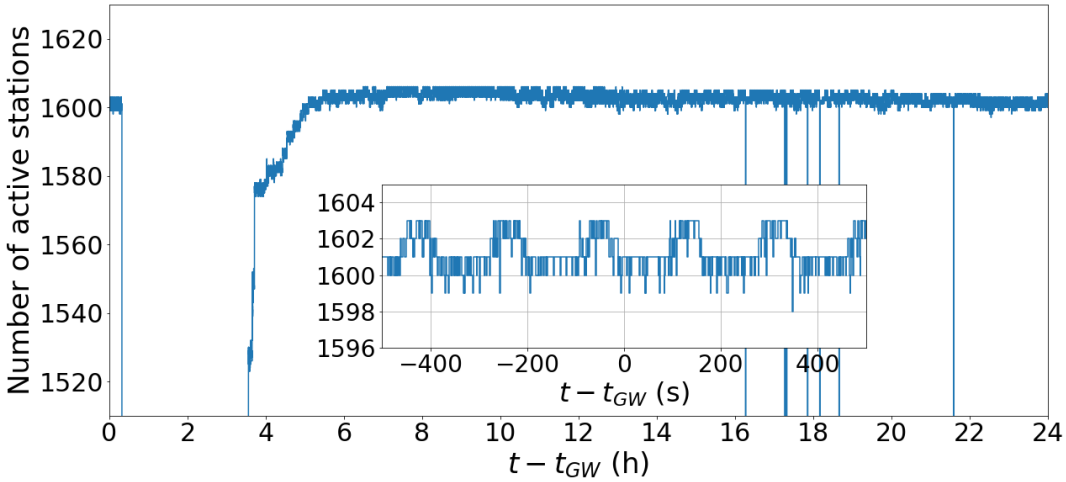

Figure 4.8: Number of active stations in the SD of the Pierre Auger Observatory vs time since the trigger time of GW151012. The larger panel is for the 1 day window, while the inset is for the ±500 s window.

In Fig. 4.10 we show the distributions of the neutrino identification observables (see Sect. 2.2) for the inclined events collected during the search period $T_{\rm search} = (-500$ s, +1 day) around the merger, and compare them to those collected in 1 month worth of data at about the same time. There are no neutrino candidates in both the ES and DGH channels and in fact the events found in the period $(-500\ {\rm s}, +1$ day) fall inside the distribution of data collected in 1 month. In Fig. 4.10 we also show the values of the discriminating observables of the individual events as a function of time with respect to the time of the merger.

Finally in Figs. 4.11 we show the upper limits to the neutrino fluence and total

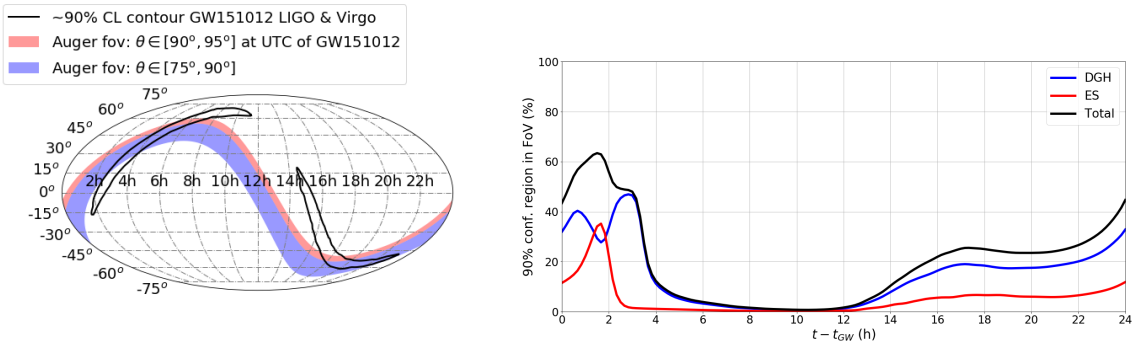

(a) FoV at the moment of GW151012. (b) Fraction of 90% C.L. in FoV.

Figure 4.9: (a) Instantaneous FoV of the Pierre Auger Observatory in the ES and DGH zenith angle ranges at the moment of the GW151012 detection and the contour of the 90% C.L. of the direction of the detected GW. (b) Fraction of the 90% C.L. contour in the FoV of Auger during the day after the GW detection. More details in Fig. 4.5 caption.

energy radiated in the form of UHEν for GW151012. Using equation 4.4 we obtain that the most restrictive upper limit on the total energy emitted per flavor in UHEν is achieved at declination $\delta \sim 55°$,

$$E_{\nu,tot}(\delta = 55°) < 5.5 \times 10^{54}\text{erg}. \tag{4.7}$$

In cases like this, when the 90% C.L. direction of the detected GW spreads over almost all declinations, the best limit would be located at $\delta = 55°$. The constraint on total energy can be also expressed as fractions f_ν of energy in UHEν $E_{\nu,tot}$ relative to the energy radiated in gravitational waves E_{GW}. The most stringent upper limit on the fraction f_ν of energy radiated in UHEν relative to the energy emitted in GW151012 is

$$f_\nu(\delta = 55°) < 192\%, \tag{4.8}$$

assuming the source is located at the central value of the 90% C.L. interval of distances $D_s = 1080$ Mpc. This fraction changes from $\sim 57.4\%$ to $\sim 438\%$ as the source distance changes between the lower and upper limits of the 90% C.L. interval $D_s = (590, 1630)$ Mpc. The results greater than 100% implies that our final limit is larger than the energy emitted in GW151012 in the form of gravitational waves, but this is not a problem in itself because the total energy lost in the merger can be much higher.

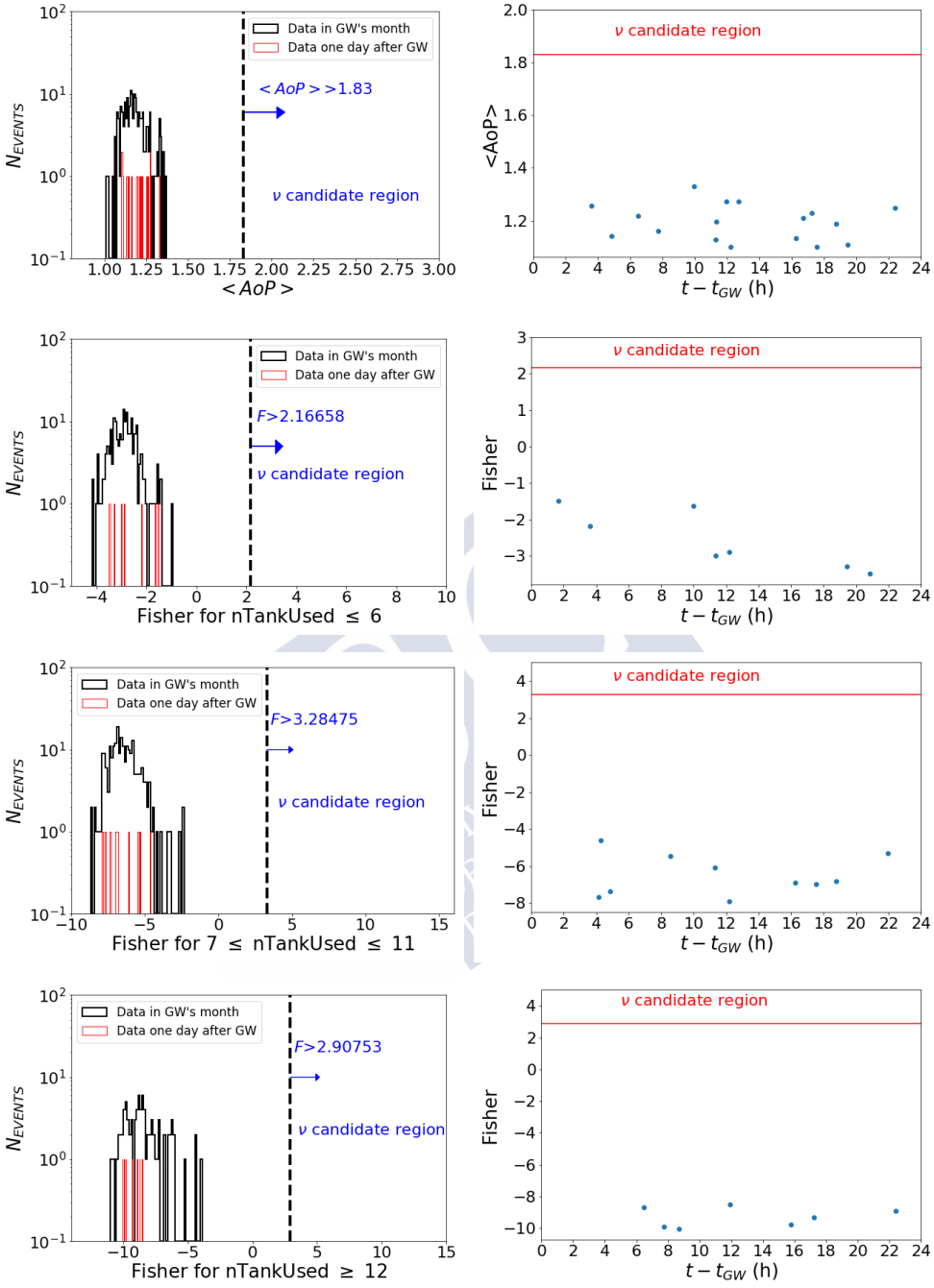

Figure 4.10: From top to bottom: ES, DGH low, DGH medium and DGH high. Left side: Histogram of the ⟨AoP⟩ or Fisher value for the inclined events in the −500 s, +1 day window time around/after the merger time of GW151012. Right side: Values of the ⟨AoP⟩ or Fisher distribution as a function of time for the inclined events collected in the 1 day window time after the merger time of GW151012. More details in Fig. 4.6 caption.

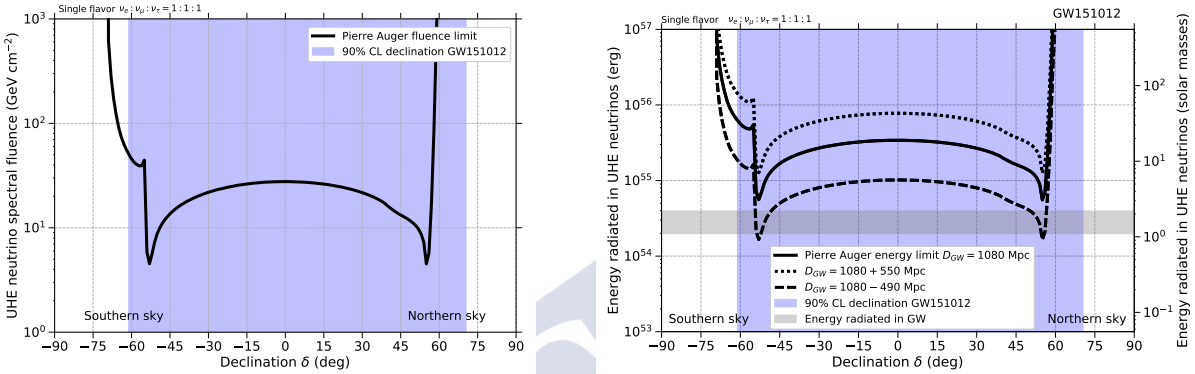

(a) Upper limits from GW151012.

(b) Constraints on $E_{\nu,\mathrm{tot}}$ from GW151012.

Figure 4.11: Left panel: Upper limits to the UHE neutrino spectral fluence per flavor (see Eq. 4.3) from the source of GW151012 as a function of equatorial declination δ. Fluences above the black solid line are excluded at 90% C.L. from the non-observation of UHE neutrino events in Auger. Right panel: Constraints on the energy radiated $E_{\nu,\mathrm{tot}}$ in UHE neutrinos (per flavor) from the source of GW151012 as a function of equatorial declination δ. Assuming the luminosity distance to the source is $D_s = 1080$ Mpc, energies above the black solid line are excluded at the 90% C.L. from the nonobservation of UHE neutrinos in Auger. The long-dashed line represents the constraints if the source is farther away at $D_s = 1080 + 550$ Mpc, and the short-dashed line if the source is closer to Earth at $D_s = 1080 - 490$ Mpc corresponding to the 90% C.L. interval of possible distances to the source. For reference the gray horizontal rectangle represents $E_{GW} \simeq 2.8 \times 10^{54}$ erg, the inferred energy radiated in gravitational waves from GW151012 [123]. The 90% C.L. declination bands of the GW151012 are indicated in the plot by the shaded blue rectangle.

GW151226

GW151226 was detected on December 26, 2015 at UTC 03:38:53 by LIGO Hanford and Livingston. It was classified as a BBH merger with estimated masses $m_1 \simeq 13.7^{+8.8}_{-3.2}$ $M_\odot$ and $m_2 \simeq 7.7^{+2.2}_{-2.5}$ $M_\odot$. The event released $\simeq 1.0^{+0.1}_{-0.1}$ $M_\odot$ in the form of GW. The source was estimated to be at a luminosity distance $D_s = 440^{+180}_{-190}$ Mpc [27].

In Fig. 4.12 we show the stability of the SD array during the search periods. Except for a few very short intervals, the number of active stations is always above 1600. In Fig. 4.13a we show the sky localization of the event, extending over $\simeq 1238$ square degrees at 90% C.L.. Only a fraction of the 90% C.L. GW localization is in the fov of Auger in the inclined directions at the time of the merger. The overlap is also shown in Fig. 4.13b as a function of time for the period $T_{\rm search} = (-500{\rm s}, +1$ day).

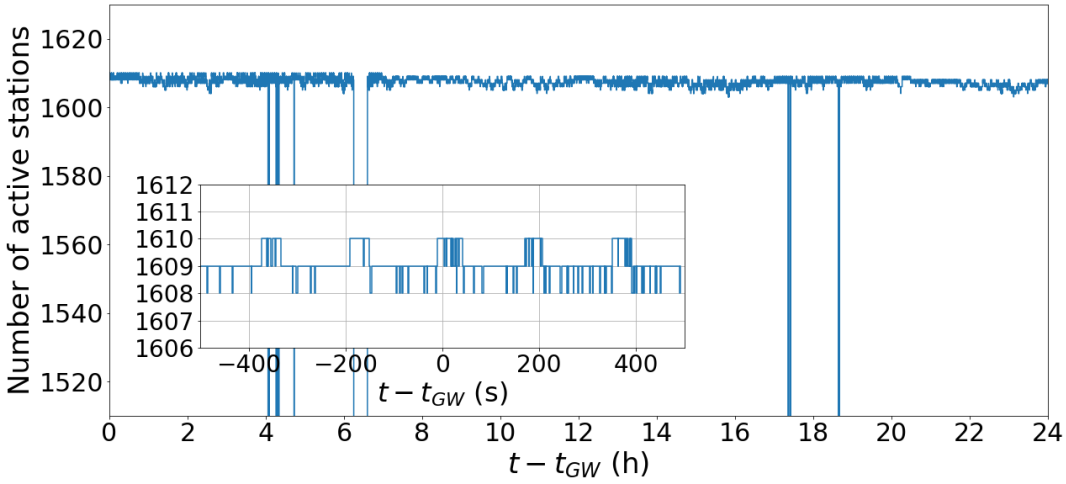

Figure 4.12: Number of active stations in the SD of the Pierre Auger Observatory vs time since the trigger time of GW151226. The larger panel is for the 1 day window, while the inset is for the ±500 s window.

In Fig. 4.14 we show the distributions of the neutrino identification observables (see Sect. 2.2) for the inclined events collected during the search period $T_{\rm search} = (-500$ s, +1 day) around the merger, and compare them to those collected in 1 month worth of data at about the same time. There are no neutrino candidates in both the ES and DGH channels and in fact the events found in the period $(-500$ s, +1 day) fall inside the distribution of data collected in 1 month. In Fig. 4.14 we also show the values of the discriminating observables of the individual events as a function of time with respect to the time of the merger.

Finally in Figs. 4.15 we show the upper limits to the neutrino fluence and total energy radiated in the form of UHEν for the case of GW151226. Using Eq. (4.4) we obtain that the most restrictive upper limit on the total energy emitted per flavor in UHEν is achieved

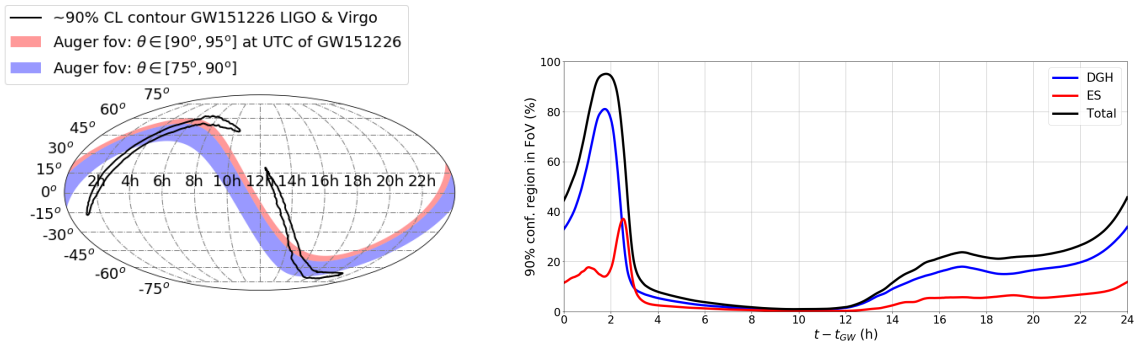

(a) FoV at the moment of GW151226. (b) Fraction of 90% C.L. in FoV.

Figure 4.13: (a) Instantaneous FoV of the Pierre Auger Observatory in the ES and DGH zenith angle ranges at the moment of the GW151226 detection and the contour of the 90% C.L. of the direction of the detected GW. (b) Fraction of the 90% C.L. contour in the FoV of Auger during the day after the GW detection. More details in Fig. 4.5 caption.

again at declination $\delta \sim 55°$,

$$E_{\nu,\mathrm{tot}}(\delta = 55°) < 7.9 \times 10^{53}\mathrm{erg}. \tag{4.9}$$

The constraint on total energy can be also expressed as fractions f_ν of energy in UHEν $E_{\nu,\mathrm{tot}}$ relative to the energy radiated in gravitational waves E_{GW}. The most stringent upper limit on the fraction f_ν of energy radiated in UHEν relative to the energy emitted in GW151226 is

$$f_\nu(\delta = 55°) < 44.1\%, \tag{4.10}$$

assuming the source is located at the central value of the 90% C.L. interval of distances $D_s = 440$ Mpc. This fraction changes from $\sim 14.2\%$ to $\sim 87.6\%$ as the source distance changes between the lower and upper limits of the 90% C.L. interval $D_s = (250, 620)$ Mpc.

In summary, the limits obtained here represent the first upper limits to UHE neutrino emission from an identified source of gravitational wave, being our most stringent upper limit to the total energy in the form of UHE neutrinos for the GW150914 event $\simeq 7.7 \times 10^{53}$ erg per flavor at $\delta_0 = -53°$ in the energy range [100 PeV, 25 EeV] [27].

Implications of the upper limits for UHEν production in BBH mergers

In [124] it was argued that black-hole mergers would have enough luminosity to power the acceleration of cosmic rays up to 100 EeV. Considering a efficiency $\lesssim 0.03$ per GW event per unit of gravitational-wave energy release radiated in the form of UHECRs and given the inferred rate of black-hole mergers [125], a source population of this type could achieve the energy budget needed to explain the observed UHECRs [124]. The most

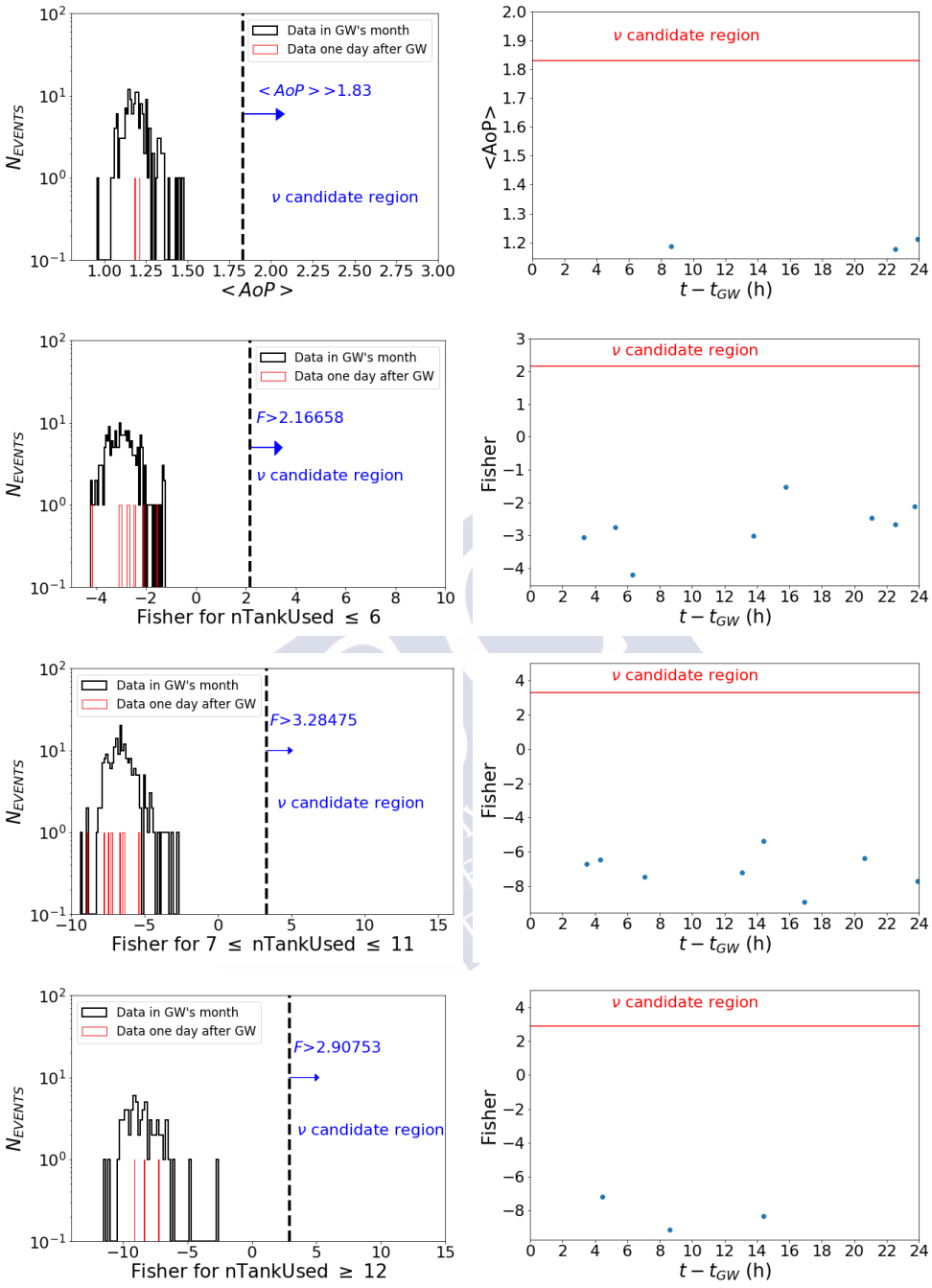

Figure 4.14: From top to bottom: ES, DGH low, DGH medium and DGH high. Left side: Histogram of the ⟨AoP⟩ or Fisher value for the inclined events in the −500 s, +1 day window time around/after the merger time of GW151226. Right side: Values of the ⟨AoP⟩ or Fisher distribution as a function of time for the inclined events collected in the 1 day window time after the merger time of GW151226. More details in Fig. 4.6 caption.

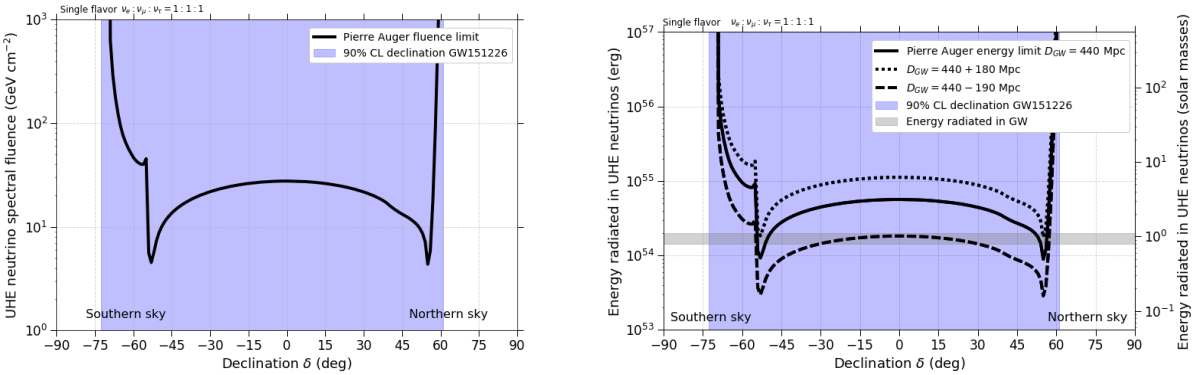

(a) Upper limits from GW151226.

(b) Constraints on $E_{\nu,\mathrm{tot}}$ from GW151226.

Figure 4.15: Left panel: Upper limits to the UHE neutrino spectral fluence per flavor (see Eq. 4.3) from the source of GW151226 as a function of equatorial declination δ. Fluences above the black solid line are excluded at 90% C.L. from the non-observation of UHE neutrino events in Auger. Right panel: Constraints on the energy radiated $E_{\nu,\mathrm{tot}}$ in UHE neutrinos (per flavor) from the source of GW151226 as a function of equatorial declination δ. Assuming the luminosity distance to the source is $D_s = 440$ Mpc, energies above the black solid line are excluded at the 90% C.L. from the nonobservation of UHE neutrinos in Auger. The long-dashed line represents the constraints if the source is farther away at $D_s = 440 + 180$ Mpc, and the short-dashed line if the source is closer to Earth at $D_s = 440 - 190$ Mpc corresponding to the 90% C.L. interval of possible distances to the source. For reference the gray horizontal rectangle represents $E_{GW} \simeq 1.8 \times 10^{54}$ erg, the inferred energy radiated in gravitational waves from GW151226 [27]. The 90% C.L. declination bands of the GW151226 are indicated in the plot by the shaded blue rectangles.

stringent upper limit on the fraction of GW energy channeled into neutrinos obtained for GW150914 was 14% (Eq. 4.6). If only 3% of the energy of the gravitational wave is channeled into UHECRs [124], and the same energy goes into UHE neutrinos, then we would expect at most on the order of 0.5 events in Auger in coincidence with GW150914 if its source was located at $\delta = -53°$.

An upper bound to the diffuse single-flavor neutrino flux integrated over a source population of this type was estimated also in [124],

$$E_\nu^2 \left.\frac{dN_\nu}{dE_\nu}\right|_{\mathrm{diffuse}}^{\mathrm{theory}} \lesssim (1.5 - 6.9) \times 10^{-8}\ \mathrm{GeV\,cm^{-2}s^{-1}sr^{-1}}, \tag{4.11}$$

depending on the evolution with redshift of the sources and assuming an optical depth $\tau = 1$ to neutrino production in the debris surrounding the black-hole mergers. This upper bound is a factor between ~ 3.5 and 15 above the limit to the diffuse flux of UHE

neutrinos obtained with Auger data up to August, 2018 (Eq. 3.7), namely,

$$E_\nu^2 \frac{dN_\nu}{dE_\nu}\bigg|_{\text{diffuse}}^{\text{Auger}} < 4.4 \times 10^{-9}\ \text{GeV}\,\text{cm}^{-2}\text{s}^{-1}\text{sr}^{-1}. \tag{4.12}$$

It is possible that there are no significant fluxes of UHE neutrinos associated with the coalescence of black holes; more phenomenological work in this area is needed. In the case that cosmic rays are indeed accelerated as suggested in [124], our constraints on the diffuse flux of UHE neutrinos would imply one or a combination of some of the three following possibilities:

- The optical depth to neutrino production τ is significantly smaller than 1 as expected in GRB models.
- Only a very small fraction of the luminosity that can be extracted from the black hole can be invested in UHECR acceleration.
- Only a very small fraction of the energy of the protons interact to produce charged pions (that are the parents of the neutrinos).

The recent detection of many more BBH mergers by LIGO allows us combine all them to obtain an upper limit on the isotropic UHE neutrino luminosity from BBH as a function of time after the merger. This stacking analysis is being pursued in Auger, see [126].

4.4.2 Binary Neutron Star (BNS) mergers

In this section we present the follow-up of the two BNS confirmed by LIGO and Virgo: GW170817 and GW190425, as well as all the BNS candidates publicly alerted by LIGO and Virgo with a probability of BNS $\geq 50\%$: S190901ap, S190910h, S191213g and S200213t. Special attention will be given to GW170817, the first BNS event detected by LIGO, which was also the first and only astrophysical event detected simultaneously with GW and electromagnetic radiation, and the most relevant multimessenger event so far [6].

GW170817

GW170817 was detected on August 17, 2017 at UTC 12:41:04 by LIGO Hanford and Livingston, with no detection in Virgo [6]. The event was classified as a BNS. Less than 2 s later the *Fermi* Gamma-Ray Burst Monitor detected a short GRB (GRB 170817A) with localization compatible with the position of GW170817 reported by LIGO. This GRB was also detected by the *International Gamma-Ray Astrophysics Laboratory* (*INTEGRAL*).

Responding to the *Fermi* and LIGO detections a large number of teams started to search across the electromagnetic spectrum, especially in the region of the sky where the GW was localized. As a consequence, a bright optical transient was discovered in NGC

4993 (at a distance of ~ 40 Mpc) by several telescopes, being the first one the One-Meter, Two-Hemisphere (1M2H) team using the 1 m Swope telescope in Chile, which announced the detection less than 11 hours after the merger.

Moreover, this multimessenger event was also detected in ultraviolet wavelengths, where early observations revealed a blue transient that disappeared in 48 hours. On the other hand, X-ray and radio were not detected in the first days, but ~ 9 and ~ 16 days, respectively, after the merger. Regarding ultra-high-energy ($E > 10^{18}$ eV) gamma rays, no candidates were found consistent with the source.

Searches for high-energy neutrinos (10^9 eV $< E_\nu < 10^{18}$ eV) in coincidence with GW170817 were performed by the three most sensitive high-energy neutrino observatories: ANTARES, IceCube and the Pierre Auger Observatory and reported in [26]. The different fields of view at the moment of the detection of GW170817 for the three experiments are shown in Fig. 4.17.

Remarkably, the position of the transient in NGC 4993 was just between 0.3° and 3.2° below the horizon at the Auger site in the ±500 s search window, corresponding to the zenith angle range of the ES channel, the most efficient for ν identification with Auger. The status of the SD array in this time interval is shown in Fig. 4.16 with the number of active tanks very close to 1600 at all times except for a very small number of periods lasting only a few seconds.

No inclined showers passing the neutrino selection were found in the time window ±500 s around the trigger time of GW170817 nor 1 day after it (Fig. 4.18) in both the ES or DGH channels. The absence of candidates in the ±500 s time window allows us to constrain the fluence in UHE neutrinos from GW170817, assuming they are emitted steadily in this interval and with an E^{-2} spectrum using the procedure explained in Section 4.3.1. Single-flavor differential limits to the spectral fluence are shown in the top panel of Fig. 4.20, in bins of one decade in energy. The sensitivity of the observatory is largest in the energy bin around 10^{18} eV. The single-flavor upper limit to the spectral fluence is $F(E) = 0.77(E/\text{GeV})^{-2}$ GeV^{-1} cm^{-2} in the energy range from 10^{17} eV to 2.5×10^{19} eV.

In the case of GW170817 and to cover predictions of longer-lived emission processes that could produce high-energy neutrinos [127, 128] a search for neutrinos was also performed in a 14-day time window following the detection of GW170817.

In the 14-day search period, as the Earth rotates, the position of NGC 4993 transits through the field of view of the Earth-skimming and downward-going channels. As seen from the Pierre Auger Observatory, the zenith angle of the optical counterpart oscillates daily between $\theta \sim 11°$ and $\theta \sim 121°$, and the source is visible in the ES channel for $\sim 4\%$ of the day and in the downward-going high channel for $\sim 11.1\%$ in the zenith angle range $75° < \theta < 90°$ (see Fig. 3.13b). No neutrino candidates were identified in the two-week search period (see Figs. 4.19). Single-flavor differential limits to the spectral fluence are shown in the bottom plot of Fig. 4.20. The corresponding upper limit to the spectral fluence is $F(E) = 25(E/\text{GeV})^{-2}\text{GeV}^{-1}\text{cm}^{-2}$ over the energy interval (10^{17}, 2.5×10^{19}) eV, where the less constraining limit in this case is due to the long periods of time in 2

weeks (approximately 96% of that time) when the source of GW170817 is not visible in the inclined directions at Auger [122].

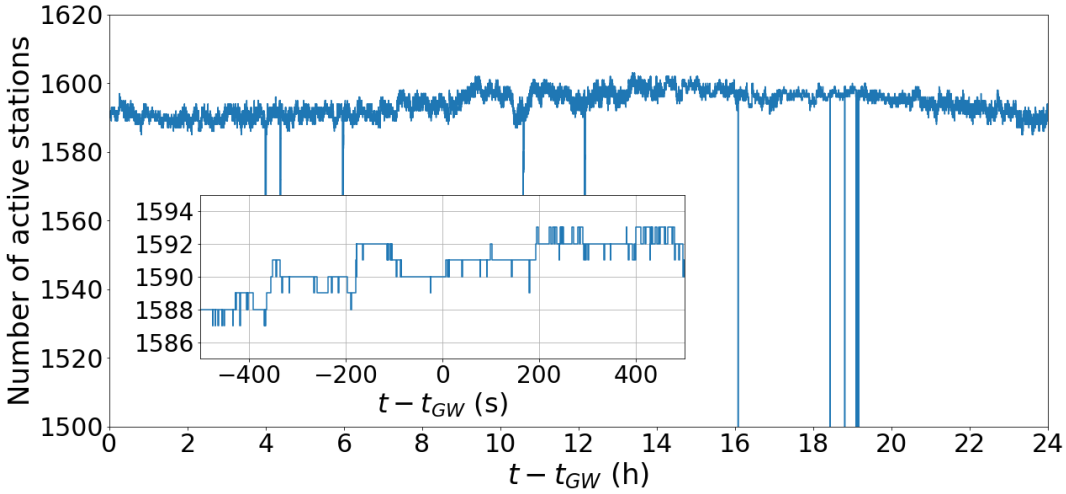

Figure 4.16: Number of active stations in the SD of the Pierre Auger Observatory vs time since the trigger time of GW170817. The larger panel is for the 1 day window, while the inset is for the ±500 s window.

Implications of the non-observation of neutrinos from GW170817

The origin of high-energy emission from the binary merger and its aftermath is not clear. The analysis of the electromagnetic information and in particular the very faint gamma-ray emission from GRB 170817A is consistent with a typical short GRB viewed off-axis, i.e. the viewing angle $\theta_{\rm obs} \gtrsim 20^\circ$ between the jet axis and the line of sight is greater than the GRB jet opening half-angle $\theta_j \approx 3^\circ - 10^\circ$. Assumming this off-axis scenario, the expected high-energy neutrino emission from a typical short GRB observed at different viewing angles was considered in [26].

The light curves of short GRBs consist of a prompt (early) emission followed by several (late) components. The prompt emission is attributed to the so-called internal shocks. These are produced by layers of material traveling outwards with different and large Lorentz factors ($\Gamma \sim 10^3$) that catch up and collide with each other and where particle acceleration (electrons and hadrons) can take place. Electrons can produce gamma rays through synchrotron and inverse Compton scattering on ambient photons (leptonic channel). Hadrons, if accelerated in the shocks, interact with matter and ambient photons producing neutral and charged mesons that subsequently decay producing gamma rays and neutrinos (hadronic channel) [129].

Late extended emission is caused by shocks produced in the collisions of ejecta with the circumburst medium. Particle acceleration in these shocks can produce gamma rays

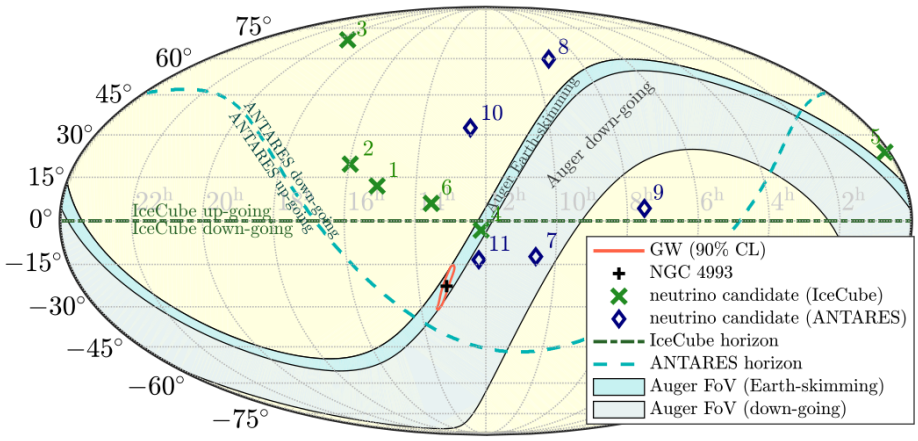

Figure 4.17: Localizations and sensitive sky areas at the time of the GW event in equatorial coordinates: GW 90% credible-level localization (red contour), direction of NGC 4993 (black plus symbol), directions of IceCube and ANTARES neutrino candidates (not correlated with the position of NGC 4993 and likely due to the atmospheric neutrino background) within 500 s of the merger (green crosses and blue diamonds, respectively), ANTARES horizon separating down-going (north of horizon) and up-going (south of horizon) neutrino directions (dashed blue line), and Pierre Auger fields of view for Earth-skimming $\theta \in [90°, 95°]$ (darker blue) and down-going $\theta \in [60°, 90°]$ (lighter blue) directions. IceCube up-going and down-going directions are on the northern and southern hemispheres, respectively (dashed-dotted green line). The zenith angle of the source at the detection time of the merger was 91°.9 for Auger, in the ES field of view [26].

through the leptonic and hadronic channels while neutrino emission is only expected to be efficiently produced in the hadronic channel [129].

The most promising neutrino-production mechanism from short GRBs is related to the so-called extended gamma-ray emission. Due to its relatively low Lorentz factor $\Gamma \sim 10 - 30$ the source expands relatively slowly compared with prompt emission, the photon density is high resulting in high pion production efficiency [130]. In Figure 4.20, we compare IceCube, ANTARES and Pierre Auger observational constraints with the expected neutrino fluence from the GRB's extended emission (EE). The prompt emission phase is less favorable for neutrino emission than the extended emission as shown in Fig. 4.20 due to the larger Lorentz factors involved and the resultant lower pion production efficiency.

We compared our neutrino constraints to neutrino emission expected for typical GRB parameters. For the prompt and extended emissions, we used the results of [130] and compared these to our constraints for the relevant ±500 s time window in the upper panel of Fig. 4.20. For extended emission we considered source parameters corresponding to both optimistic and moderate scenarios in Table 1 of [130]. IceCube limits would constrain the optimistic (lowest Lorentz factor assumed) extended-emission scenario for

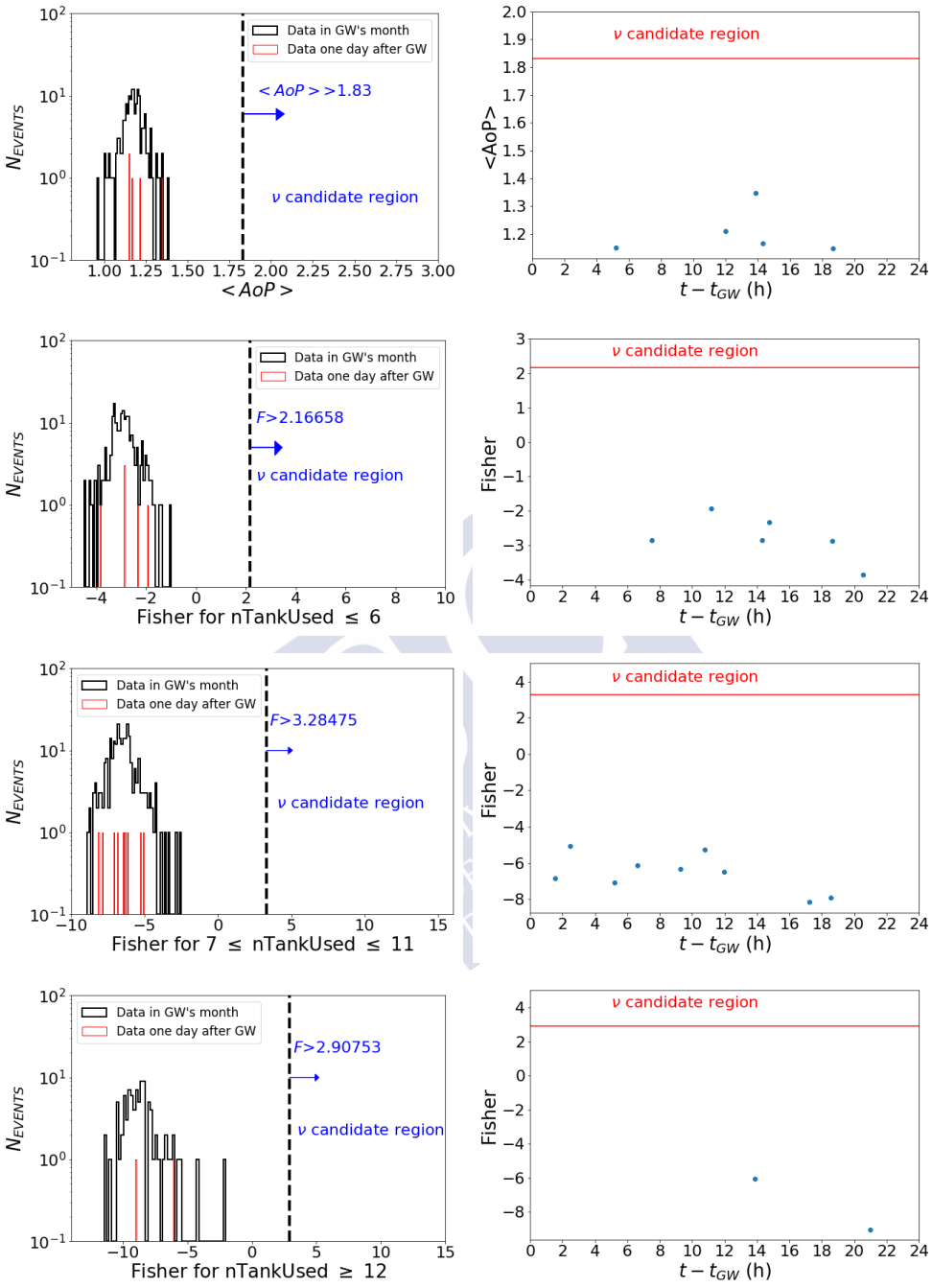

Figure 4.18: From top to bottom: ES, DGH low, DGH medium and DGH high. Left side: Histogram of the ⟨AoP⟩ or Fisher value for the inclined events in the −500 s, +1 day window time around/after the merger time of GW170817. Right side: Values of the ⟨AoP⟩ or Fisher distribution as a function of time for the inclined events collected in the 1 day window time after the merger time of GW170817. More details in Fig. 4.6 caption.

a typical GRB at $\sim$ 40 Mpc, viewed at zero viewing angle $\theta_{\rm obs}$. The Auger limit is consistent with the lower neutrino fluence expected at $\sim$ EeV energies in the extended emission model of [130]. The magnetic fields in the GRB are so strong that energy losses of charged pions due to synchrotron emission before they decay prevent the production of high-energy neutrinos (see [130] for details).

Another proposed explanation alternative to the GRB view off-axis, is the interaction of the GRB jet with ejecta material from the merger [131]. Energy deposition by the jet into the neutron star ejecta can form a cocoon that expands outwards at mildly relativistic speeds over a wide opening angle. High-energy neutrino production in this scenario may significantly exceed the observed gamma-ray emission as neutrinos can escape through the ejecta even before it becomes transparent to gamma rays [129].

We considered an additional neutrino-production mechanism related to ejecta material from the merger. If a rapidly rotating neutron star forms in the merger and does not immediately collapse into a black hole, it can power a relativistic wind with its rotational energy, which may be responsible for the sometimes observed extended emission [132]. Optically thick ejecta from the merger can attenuate the gamma-ray flux, while allowing the escape of high-energy neutrinos. Additionally, it may trap some of the wind energy until it expands and becomes transparent. This process can convert some of the wind energy to high-energy particles, producing a long-term neutrino radiation that can last for days [127, 128, 133]. The properties of ejecta material around the merger can be characterized from its kilonova/macronova emission.

We compared our constraints for the 14-day time window with the relevant results of [128], namely, emission from approximately 0.3 to 3 days and from 3 to 30 days following the merger. Auger limits are still far from constraining these type of models as shown in Fig. 4.20 in part due to the 4% fraction of time the source of GW170817 is visible in the FoV of the ES channel in Auger.

In summary, the lack of observation of UHE neutrino in coincidence with GW170817 is consistent with the low neutrino fluence expected from a short GRB that is viewed off-axis.

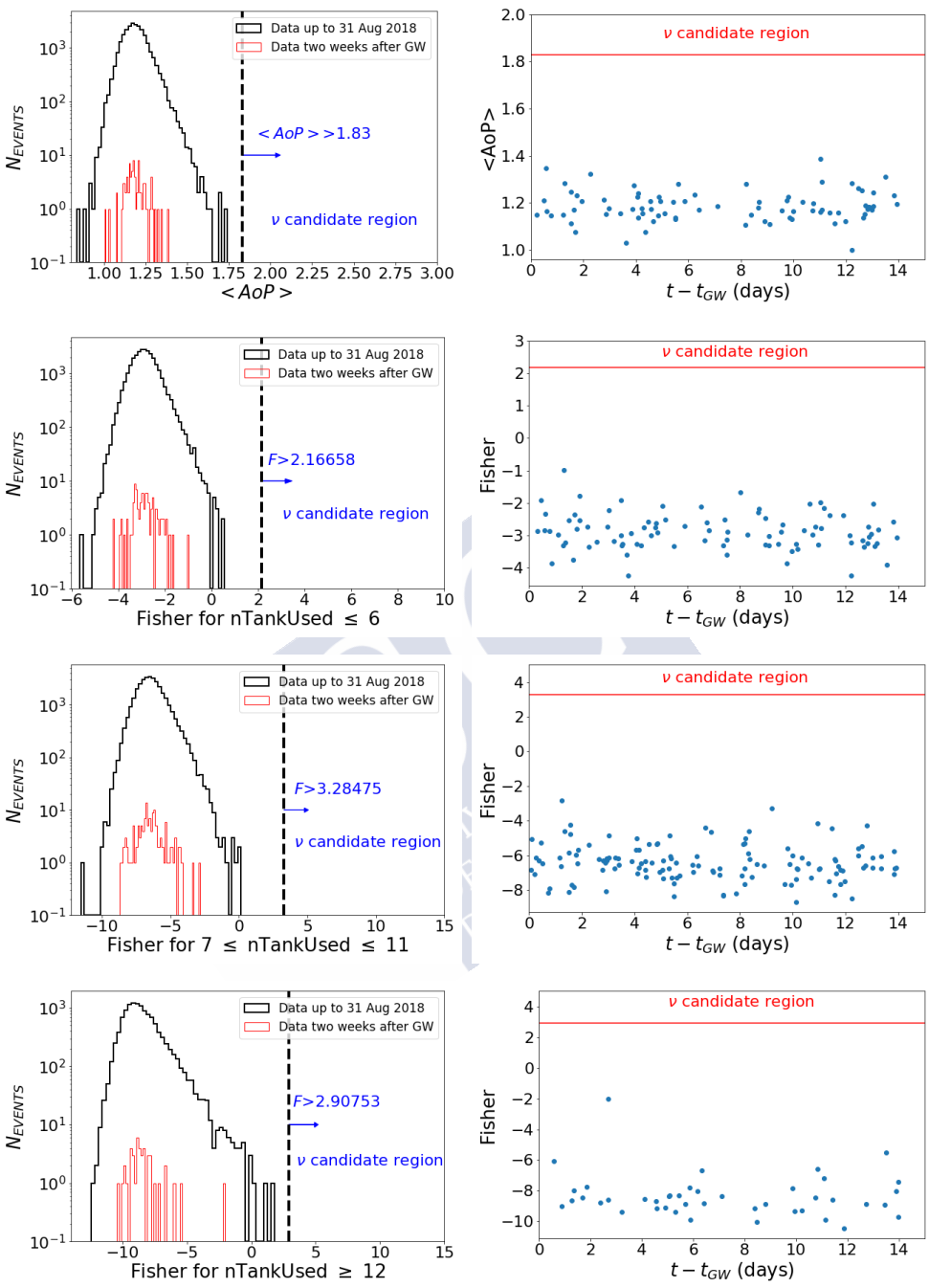

Figure 4.19: From top to bottom: ES, DGH low, DGH medium and DGH high. Left side: Histogram of the ⟨AoP⟩ or Fisher value for the inclined events in the −500 s, +14 day window time around/after the merger time of GW170817. The black histogram represents in this case the distribution for the full data from 1 January 2004 to 31 August 2018, showing that the events are under the bulk of the distribution. Right side: Values of the ⟨AoP⟩ or Fisher distribution as a function of time for the inclined events collected in the 14 day window time after the merger time of GW170817. More details in Fig. 4.6 caption.

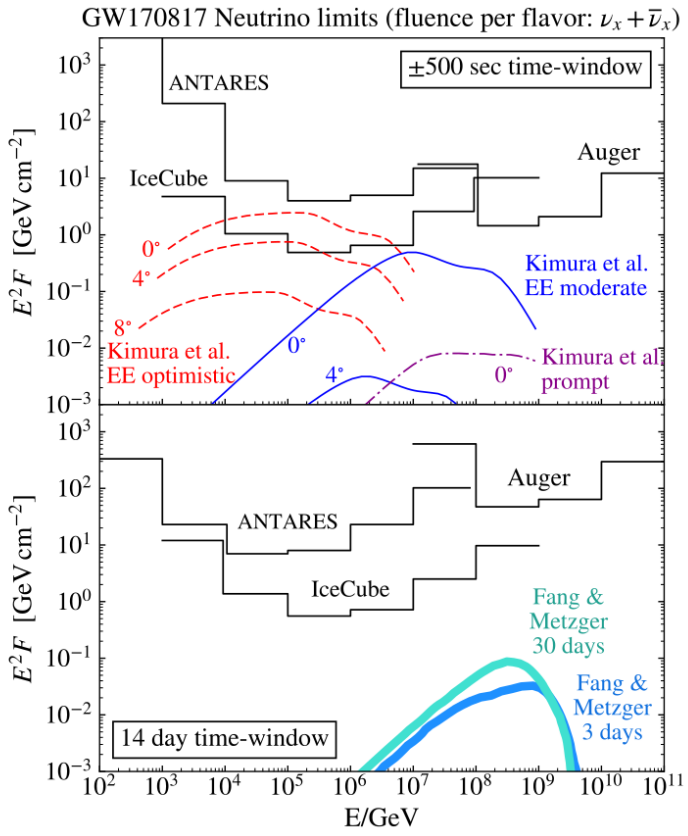

Figure 4.20: Upper limits (at 90% confidence level) on the neutrino spectral fluence from GW170817 during a ±500 s window centered on the GW trigger time (top panel), and a 14-day window following the GW trigger (bottom panel) from ANTARES, IceCube and the Pierre Auger Observatory [26]. Limits for each experiment are calculated separately for each energy decade, assuming a spectral fluence $F(E) = F_{up} \times [E/GeV]^{-2}$ in that decade only. Also shown are different predictions by neutrino emission models. In the upper plot, models from [130] for both extended emission (EE) and prompt emission scaled to a distance of 40 Mpc and shown for the case of the on-axis viewing angle ($\theta_{obs} \lesssim \theta_j$ with θ_j the jet opening half-angle that for short GRB is $\theta_j \sim 3° - 10°$) and selected off-axis angles measured in excess of θ_j to indicate the dependence on this parameter. GW data and the redshift of the host galaxy constrain the viewing angle to $\theta_{obs} \in [0°, 36°]$. In the lower plot, longer time emission models from [128] scaled to a distance of 40 Mpc. All fluences are shown as the per flavor sum of neutrino and antineutrino fluence, assuming equal fluence in all flavors, as expected for standard neutrino oscillation parameters.

GW190425

GW190425 was detected on April 25, 2019 at UTC 08:18:05 by LIGO Livingston. It was classified as a BNS merger ($> 99\%$) with estimated masses in the range 1.12 to 2.52 $M_\odot$. The status of the SD array in the ± 500 s and 1-day search window is shown in Fig. 4.21 with the number of active tanks staying very stable around 1636, being all the time in the interval (1632, 1637). The 90% C.L. localization region (plot in Fig. 4.22a) in this case is very large ($\simeq$ 8284 deg^2) because at the moment of the

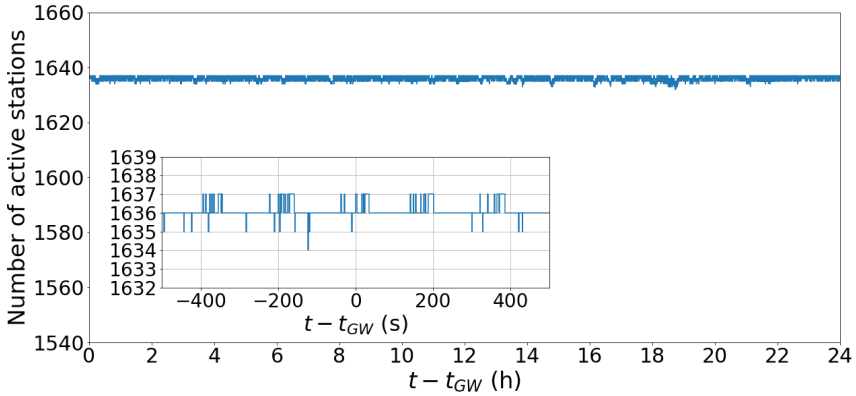

Figure 4.21: Number of active stations in the SD of the Pierre Auger Observatory vs time since the trigger time of GW190425. The larger panel is for the 1 day window, while the inset is for the ± 500 s window.

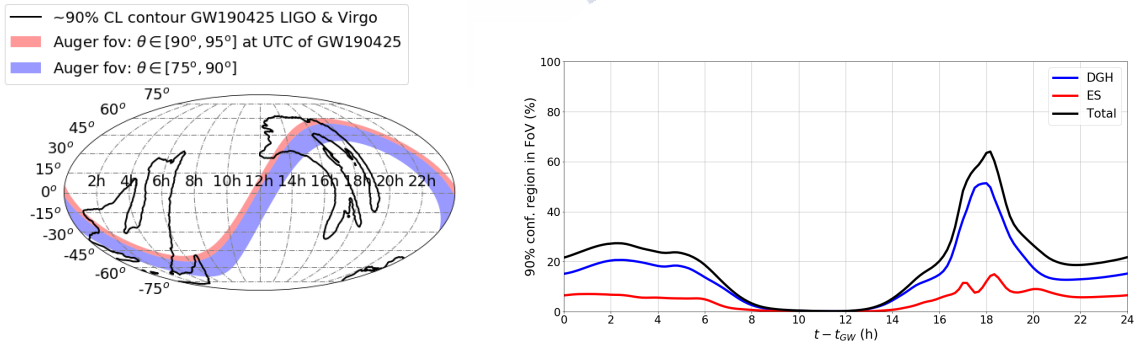

(a) FoV at the moment of GW190425.

(b) Fraction of 90% C.L. in FoV.

Figure 4.22: (a) Instantaneous FoV of the Pierre Auger Observatory in the ES and DGH zenith angle ranges at the moment of the GW190425 detection and the contour of the 90% C.L. of the direction of the detected GW. (b) Fraction of the 90% C.L. contour in the FoV of Auger during the day after the GW detection. More details in Fig. 4.5 caption.

GW merger LIGO Hanford was offline so only LIGO Livingston and Virgo were used to localize the merger [134]. This broad localization region did not allow the identification of an electromagnetic counterpart. Only a $\simeq 21\%$ of the 90% C.L. localization region is in the FoV of Auger in the inclined directions at the time of emission. This overlap is also shown in Fig. 4.22b as a function of time for the period $T_{\text{search}} = (-500\text{ s}, +1\text{ day})$.

In Fig. 4.23 we show the distributions of the neutrino identification observables (see Sect. 2.2) for the inclined events collected during the search period $T_{\text{search}} = (-500$ s, +14 days) around the merger, and compare them to those collected in 1 month worth of data at about the same time. There are no neutrino candidates in both the ES and DGH channels and in fact the distribution of events in the period -500 s, +14 day is compatible with that obtained with data collected in 1 month.

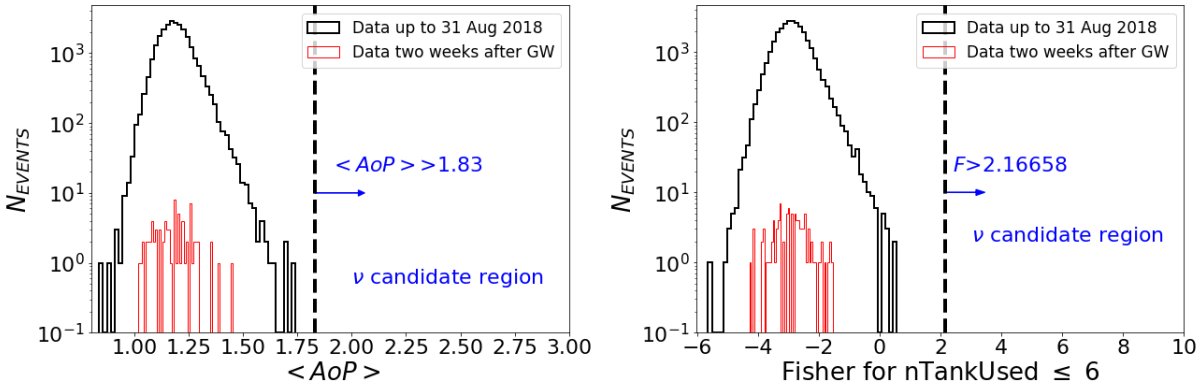

(a) ES (b) DGH low

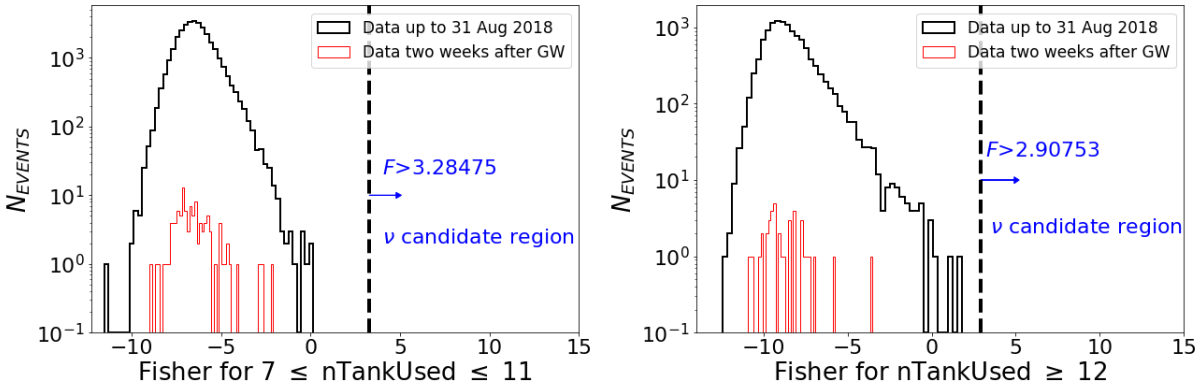

(c) DGH medium (d) DGH high

Figure 4.23: Histogram of the $\langle$AoP$\rangle$ or Fisher value for the inclined events in the -500 s, +14 day window time around/after the merger time of GW190425. More details in Fig. 4.19 caption.

S190901ap, S190910h, S191213g and S200213t

We report now the follow-up in UHE neutrinos of the four candidate BNS: S190901ap (86%), S190910h (61%), S191213g (77%) and S200213t (63%), where the numbers in parenthesis indicate the probability of being BNS mergers. These events are still under study by the LIGO Collaboration and at the time of writing of this thesis none of them had been promoted to GW. All of them were detected in the O3 run of LIGO/Virgo. Data collected with the SD of Auger were unblinded in the search for neutrinos in time windows of ±500 s around and 1 day after their detection with no neutrino candidates being found. In all cases the SD was stable and with almost 100% of the stations active except for S191213g for which for a period of half a day the fraction of active stations was only ∼ 80% (see Fig. 4.24).

In Fig. 4.25 we show the skymaps with the 90% C.L. localization of these GW candidates which covers a rather large fraction of the sky in all cases. The Figures also display the FoV of Auger in the ES and DGH channels at the instant of each merger. The bad 90% C.L. contours are probably caused because at the moment of the detection one of the detectors was not working correctly, so the triangulation cannot be done properly to obtain the origin. In Fig. 4.25 we also show the overlap of the FoV of Auger and the 90% C.L. localization of each GW candidate as a function of time in the day after each merger.

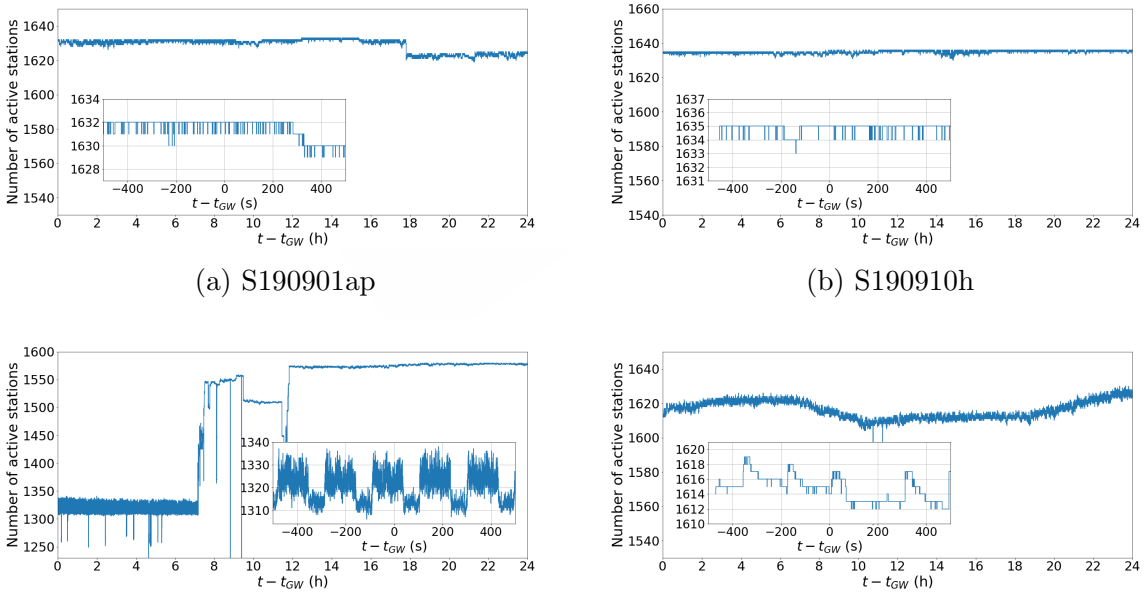

(a) S190901ap

(b) S190910h

(c) S191213g

(d) S200213t

Figure 4.24: Number of active stations in the SD of the Pierre Auger Observatory vs time since the trigger time for BNS candidates. The larger panel is for the 1 day window, while the inset is for the ±500 s window.

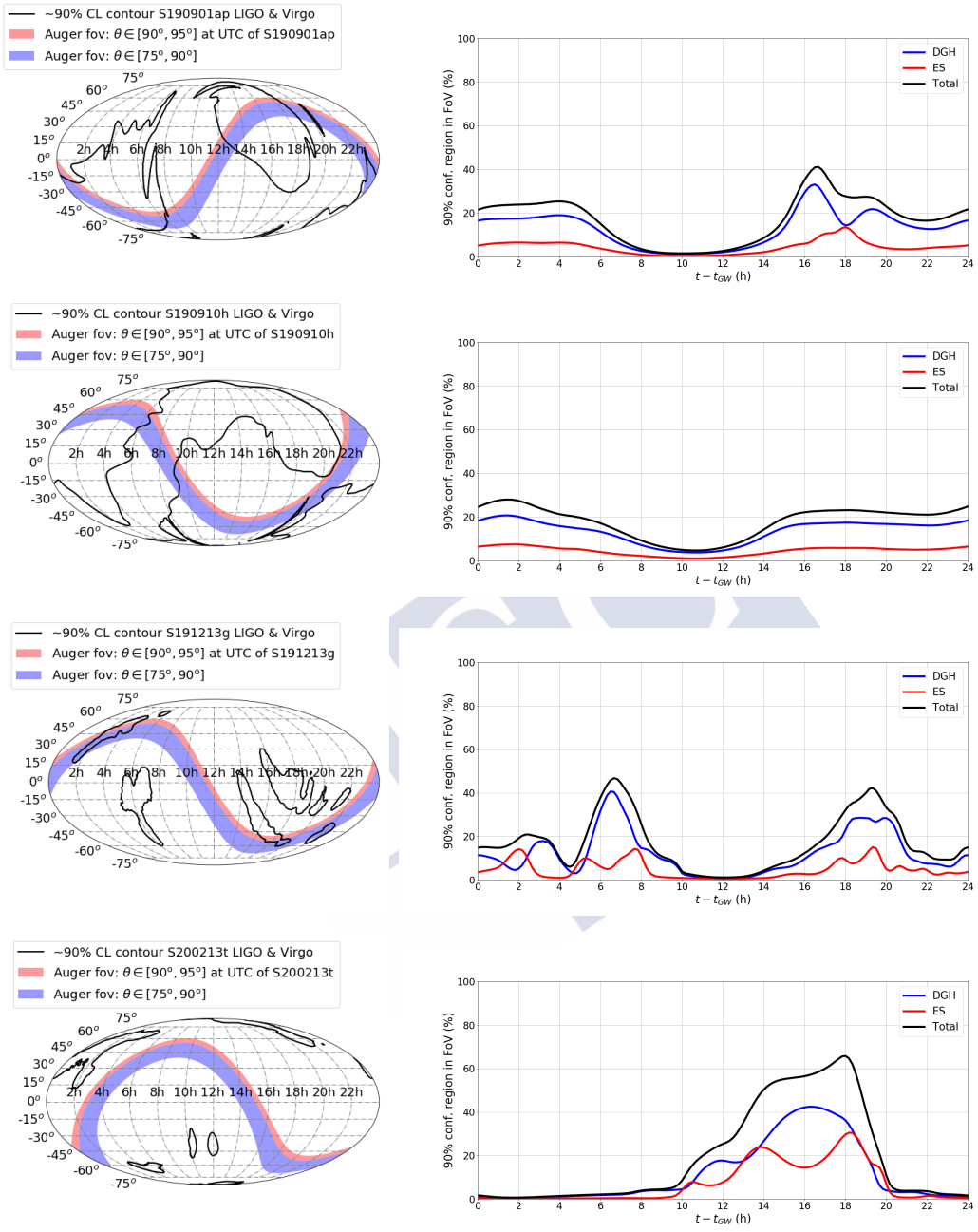

Figure 4.25: From top to bottom: S190901ap, S190910h, S191213g and S200213t. Left panels: Instantaneous FoV of the Pierre Auger Observatory in the ES and DGH zenith angle ranges at the moment of the BNS candidates detection and the contour of the 90% C.L. of the direction of the GW candidate. Right panels: Fraction of the 90% C.L. contour in the FoV of Auger during the day after the GW candidate detection. More details in Fig. 4.5 caption.

4.4.3 Neutron Star-Black Hole (NSBH) merger candidates

In this section we report on the follow-up in UHE neutrinos of the four NSBH candidates publicly alerted by LIGO/Virgo with a probability of them being NSBH $\geq 50\%$: S190910d (98%), S190923y (68%), S190930t (74%) and S191205ah (93%), where the numbers in parenthesis indicate the probability. These events are still under study by the LIGO Collaboration and at the time of writing of this thesis none of them had been promoted to GW. All of them were detected in the O3 run of LIGO/Virgo. Data collected with the SD of Auger was unblinded in the search for neutrinos in time windows of ± 500 s around and 1 day after their detection with no candidates found. In all cases the SD was stable and with almost 100% of the stations active except for a few very short intervals of a few seconds (see Fig. 4.26).

In Fig. 4.27 we show the skymap with the 90% C.L. localization of these GW candidates which covers a rather large fraction of the sky in all cases, and the FoV of Auger in the ES and DGH channels at the instant of each merger. In Fig. 4.27 we also show the overlap of the FoV of Auger and the 90% C.L. localization of each GW candidate as a function of time in the day after each merger.

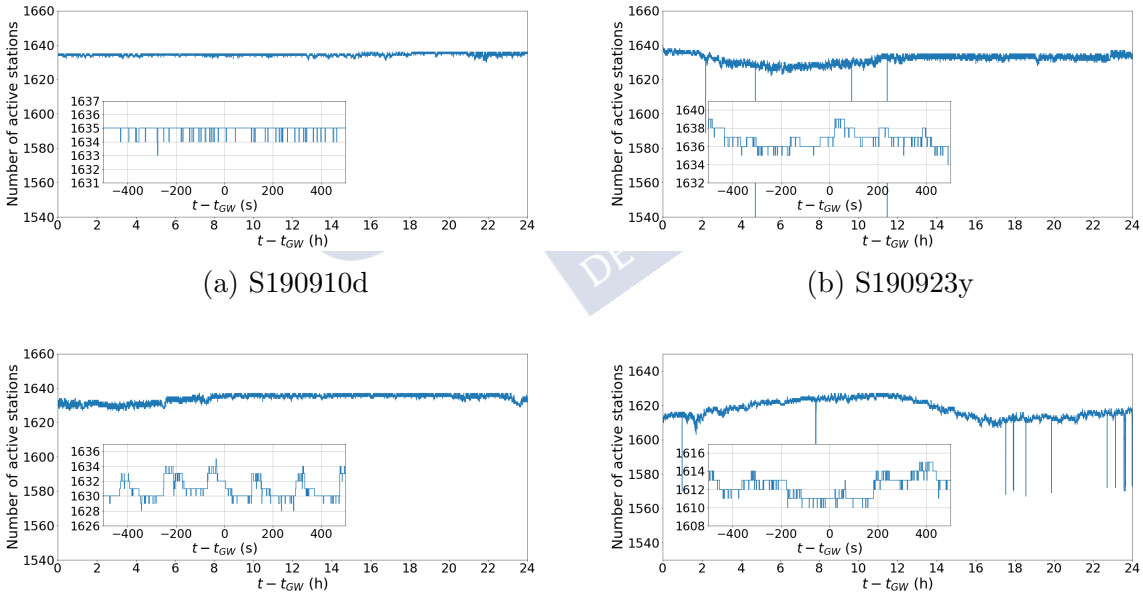

(a) S190910d (b) S190923y

(c) S190930t (d) S191205ah

Figure 4.26: Number of active stations in the SD of the Pierre Auger Observatory vs time since the trigger time for NSBH candidates. The larger panel is for the 1 day window, while the inset is for the ± 500 s window.

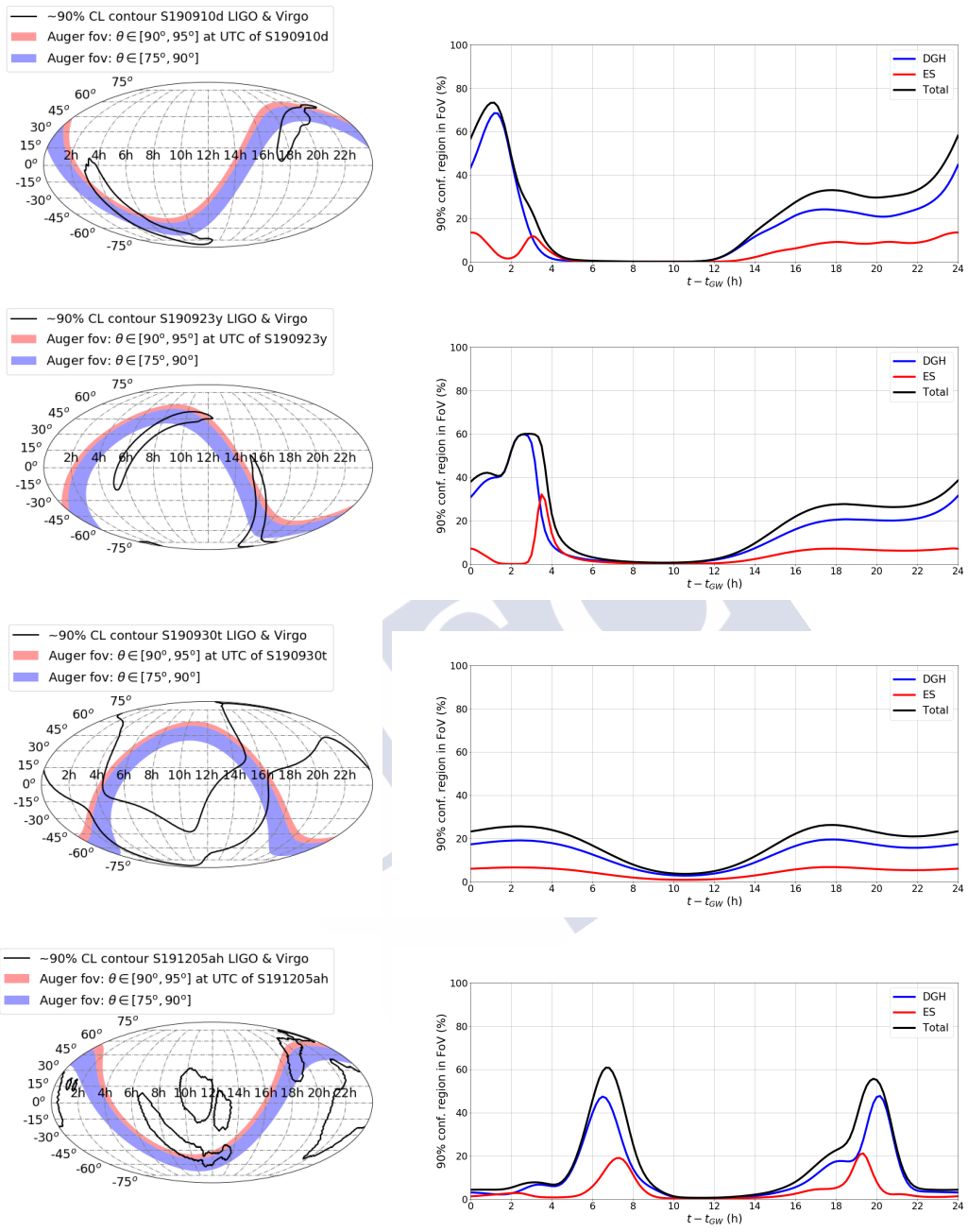

Figure 4.27: From top to bottom: S190910d, S190923y, S190930t and S191205ah. Left panels: Instantaneous FoV of the Pierre Auger Observatory in the ES and DGH zenith angle ranges at the moment of the NSBH candidates detection and the contour of the 90% C.L. of the direction of the GW candidate. Right panels: Fraction of the 90% C.L. contour in the FoV of Auger during the day after the GW candidate detection. More details in Fig. 4.5 caption.

4.4.4 MassGap mergers

A GW event is classified as a MassGap if at least one of the estimated masses of the two components is between 2 $M_\odot$ (too large for a NS) and 5 $M_\odot$ (too small for a stellar BH). In this section we report on the follow-up in UHE neutrinos of the only MassGap confirmed by LIGO/Virgo: GW190814, as well as all the MassGap candidates publicly alerted by LIGO/Virgo with a probability of MassGap $\geq$ 50%: S190924h, S190930s, S200115j and S200316bj. Special attention will be given to GW190814 [135].

GW190814

GW190814 was detected on August 14, 2019 at UTC 21:10:39 by LIGO Hanford and Livingston and Virgo. It was classified as a MassGap merger, being one of the objects a BH with mass $m_1 = 23.2^{+1.1}_{-1.0}$ $M_\odot$ and the second one a compact object with mass $m_2 = 2.59^{+0.08}_{-0.09}$ $M_\odot$. The status of the SD array in the $\pm$500 s and 1-day search window is shown in Fig. 4.28 with the number of active tanks being around 1620 except for very short time intervals. In Fig. 4.29a we show the skymap with the 90% C.L. localization of GW190814 which cover a very small fraction of the sky ($\simeq$ 18.5 deg^2) and the FoV of Auger in the ES and DGH channels at the instant of each merger. The fraction of the 90% C.L. localization region in the FoV of Auger in the inclined directions is shown in Fig. 4.29b as a function of time for the period $T_{\text{search}} = (-500\text{ s}, +1\text{ day})$.

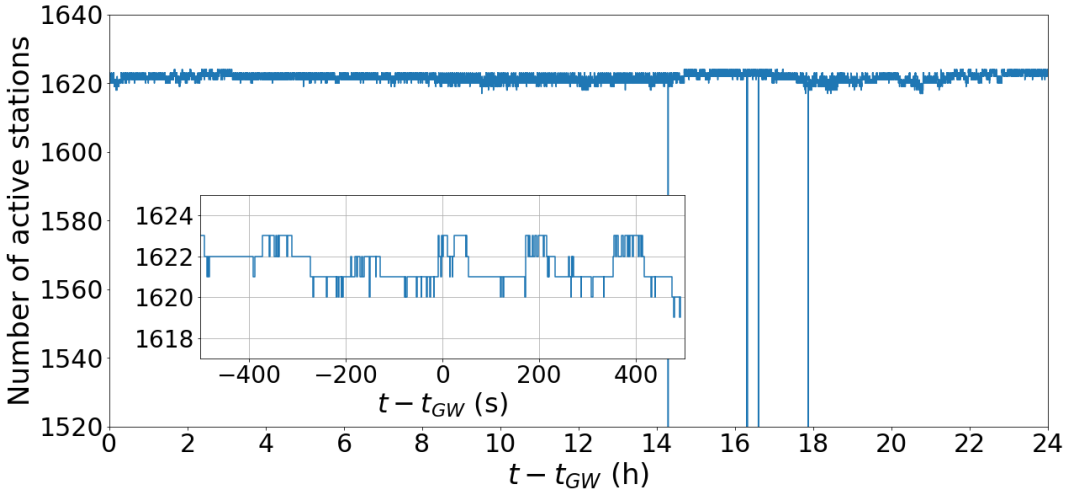

Figure 4.28: Number of active stations in the SD of the Pierre Auger Observatory vs time since the trigger time of GW190814. The larger panel is for the 1 day window, while the inset is for the $\pm$500 s window.

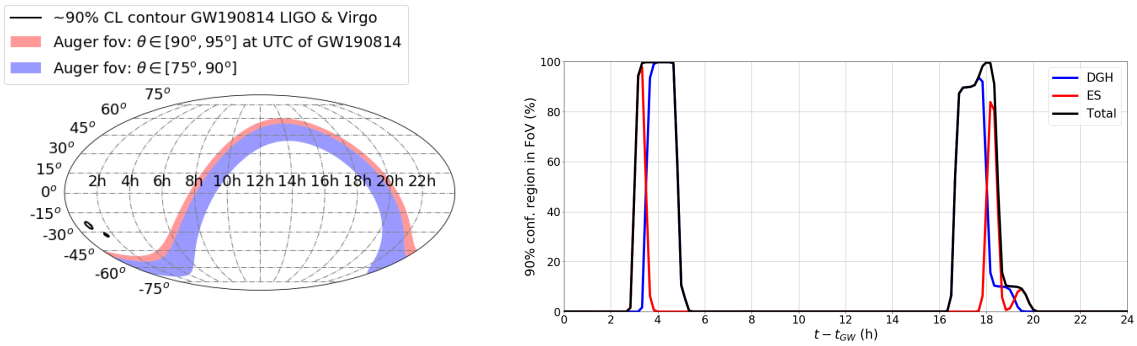

(a) FoV at the moment of GW190814.

(b) Fraction of 90% C.L. in FoV.

Figure 4.29: (a) Instantaneous FoV of the Pierre Auger Observatory in the ES and DGH zenith angle ranges at the moment of the GW190814 detection and the contour of the 90% C.L. of the direction of the detected GW. (b) Fraction of the 90% C.L. contour in the FoV of Auger during the day after the GW detection. More details in Fig. 4.5 caption.

S190924h, S190930s, S200115j and S200316bj

We give now the information on the follow-up of the candidate MassGap S190924h ($> 99\%$), S190930s (95%), S200115j ($> 99\%$) and S200316bj ($> 99\%$), where the numbers in parenthesis indicate the probability of the events being MassGap mergers. These events are still under study by the LIGO Collaboration and at the time of writing of this thesis none of them had been promoted to GW. All of them were detected in the O3 run of LIGO/Virgo. Data collected with the SD of Auger were unblinded to search for neutrinos in time windows of ± 500 s around and 1 day after their detection and no candidates were found. In all cases the SD was stable and with a high percent of the stations active except for S200316bj for which for a period of half an hour the fraction of active stations fell to 0 (see Fig. 4.30).

In Fig. 4.31 we show the skymap with the 90% C.L. localization of these GW candidates and the FoV of Auger in the ES and DGH channels at the instant of each merger. In Fig. 4.31 we show the overlap of the FoV of Auger and the 90% C.L. localization of each GW candidate as a function of time in the day after each merger. S190930s in an example of GW candidate with a very north 90% C.L. contour, so a large fraction of the 90% C.L. localization would be never in the FoV of Auger.

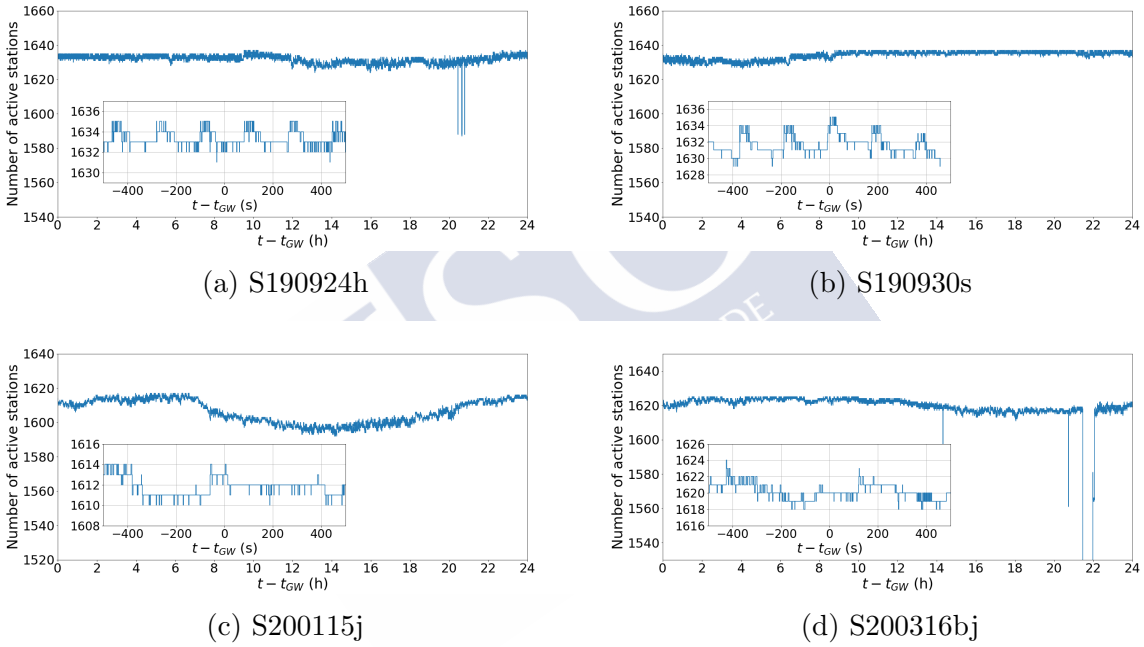

(a) S190924h (b) S190930s

(c) S200115j (d) S200316bj

Figure 4.30: Number of active stations in the SD of the Pierre Auger Observatory vs time since the trigger time for MassGap candidates. The larger panel is for the 1 day window, while the inset is for the ±500 s window.

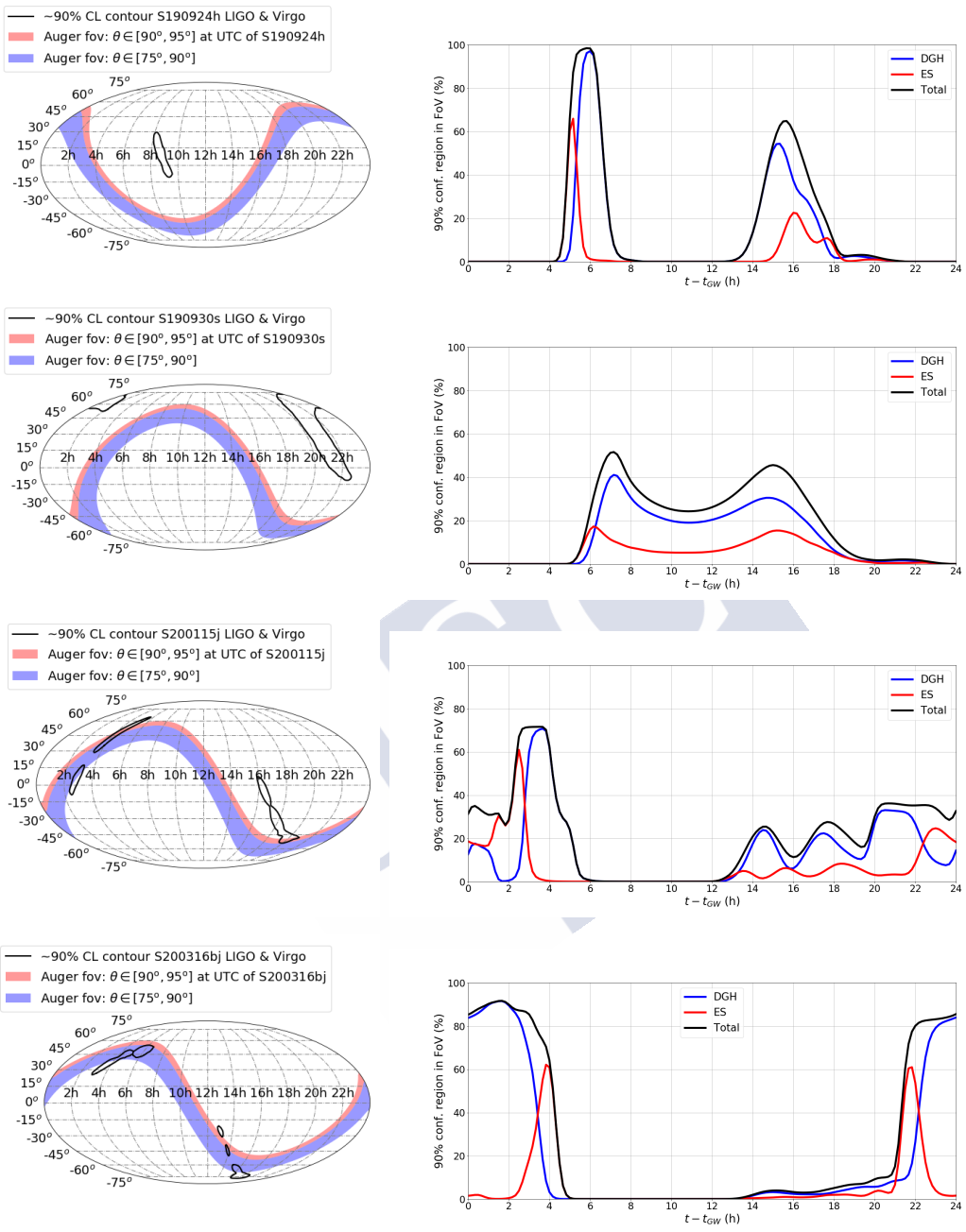

Figure 4.31: From top to bottom: S190924h, S190930s, S200115j and S200316bj. Left panels: Instantaneous FoV of the Pierre Auger Observatory in the ES and DGH zenith angle ranges at the moment of the MassGap candidates detection and the contour of the 90% C.L. of the direction of the GW candidate. Right panels: Fraction of the 90% C.L. contour in the FoV of Auger during the day after the GW candidate detection. More details in Fig. 4.5 caption.

5

Conclusions

In this thesis we described the search for UHE neutrinos with the Surface Detector of Pierre Auger Observatory. Besides the detailed procedure for searching neutrinos and a characterization of neutrino showers explained in Chapter 2, the main results are obtained in Chapters 3 and 4. In Chapter 3 we obtained limits to diffuse and point-like neutrino fluxes, constraining many models of UHE neutrino production in interactions with the CMB as well as models of UHEν in astrophysical sources that are candidates for UHECR origin. Chapter 4 was devoted to the search for UHE neutrinos in coincidence with gravitational-wave events detected in runs O1, O2 and O3 by the LIGO/Virgo GW interferometers.

There are two kinds of conclusions in this thesis: technical and physical conclusions. On the one hand, the technical conclusions are:

1. Neutrino selection criteria and unblinding procedure is now fully detailed, step by step, both Earth-skimming and downward-going high analyses.

2. Previous simulations were analyzed in detail, and despite the neutrino selection efficiency over inclined showers is really high, maybe the efficiency of inclined events selection could be improved after a detailed study. This improvement in the efficiency could make possible that the Pierre Auger Observatory overtakes IceCube at energies larger than $\sim 10^{18}$ eV.

3. The signal of neutrino-induced showers in the Surface Detector was studied and represented graphically, giving a clear visual difference between neutrinos and background events.

4. The detector exposure for diffuse sources and the effective area for point-like sources of UHE neutrinos were characterized for the main neutrino channels in terms of neutrino flavors and interactions, source position, time and duration of the neutrino flux.

5. The procedure for the UHE neutrino follow-up of big astrophysical events was developed, being automated since July 2019.

On the other hand, the physical conclusions are:

1. No neutrino candidates have been identified in Auger data from 1 Jan 2004 until 31 Aug 2018 in any of the channels explored, namely, Earth-skimming and downward-going.

2. Upper limits to the diffuse flux of UHE neutrino were obtained. They are competitive with limits placed by dedicated UHEν experiments such as IceCube at energies around 10^{18} eV.

3. Strong constraints on the potential sources of UHECR and their nature were derived from the non-observation of UHEν. Sources accelerating only protons at UHE and with an evolution with redshift z stronger than Star Formation Rate are disfavoured by Auger data, while UHEν fluxes in models predicting a mixed composition are generally out of reach of the current Auger sensitivity.

4. Upper limits to UHE neutrino fluxes from steady point-like sources were also placed. These limits complement those of other neutrino experiments at sub-EeV energies such as ANTARES and IceCube. With the SD of Auger we can monitor a large region of the sky from almost the Southern Celestial Pole to declinations $\delta \simeq 60^\circ$ with peak sensitivities at $\delta \sim -53^\circ$ and $\delta \sim 55^\circ$.

5. The Surface Detector of the Pierre Auger Observatory has an unmatched sensitivity to potential sources of EeV neutrinos in the Northern terrestrial hemisphere. This complements perfectly with other experiments like IceCube, which cannot search for neutrinos in the EeV energy range over this region in the sky due to the opacity of the Earth to neutrinos in those directions when seen from the South Pole.

6. The sensitivity of the Pierre Auger Observatory to transient sources of UHEν is highly dependent on the efficiency of the detection during the time interval of the transient. Depending on the inclination of the event, the sensitivity can exceed by far that of other dedicated neutrino detectors. This was clearly shown in the case of the GW170817 event, the first binary neutron star merger detected in GW. The source of GW170817 was just at the perfect place in the exact moment, slightly below the horizon, where the sensitivity of the SD of Auger is highest due to the Earth-skimming ν channel. The results for the short interval time was even better than the limit obtained by neutrino experiments.

7. A follow-up search for UHEν from confirmed and candidate GW events alerted by LIGO/Virgo in runs O1, O2 and O3 was performed. This is the first time sources of GW events were followed up in UHEν.

8. No neutrino candidates were found in coincidence with Binary Black Hole mergers in the time window (-500 s, $+1$ day) around the trigger time of the GW events. Strong constraints on the energy emitted in UHEν by BBH mergers, $\lesssim$ few solar masses, were established.

9. No neutrino candidates were found in coincidence with Binary Neutron Star mergers. In the particular case of GW170817, for which the source (a short and extremely weak GRB) was identified, the absence of neutrinos was shown to be consistent with the observation of the short GRB at large $\sim 20^\circ$ off-axis angle.

Finally, during the development of this thesis a new era of multimessenger astronomy (MMA) has started. The Pierre Auger Observatory is a key experiment in MMA at UHE with its capabilities and sensitivity to search for neutrinos in the EeV range in correlation with the detection of high-energy gamma ray and TeV-PeV neutrino sources and/or sources of gravitational waves.

USC
UNIVERSIDADE
DE SANTIAGO
DE COMPOSTELA

A

Top-Down Selection

In the following we explain the Top-Down Selection algorithm that we introduced in Chapter 2, Section 2.2.3:

1. We perform a simple reconstruction of the zenigh angle of the event, θ_{rec}. Firstly, we calculate the barycenter:

$$\overrightarrow{r_b} = \frac{\sum_i \overrightarrow{r_i} S_i}{\sum_i S_i}, \tag{A.1}$$

where $\overrightarrow{r_i}$ and S_i are the ground position and the integrated signal of each station. In the following, $\overrightarrow{r_i}$ denotes the station coordinates relative to the barycenter. We can fit a plane shower front model moving with the speed of light and an arrival time to the barycenter, t_0, and to each station, t_i, while neglecting the individual altitude z_i of each station with respect to the ground plane:

$$c\ (t_i - t_0) = -\overrightarrow{a} \cdot \overrightarrow{r_i} \Longleftrightarrow \langle t_i \rangle = t_0 - \frac{1}{c}(u\ x_i + v\ y_i), \tag{A.2}$$

where $\overrightarrow{a} = (u, v, w)^T$ is the shower incoming direction. Free parameters of the model are u, v and t_0, so a unique solution can be obtained from the linear least squares method. Finally, the shower front fit is improved by approximately taking into account the altitude of the station:

$$\langle t_i \rangle = t_0 - \frac{1}{c}(u\ x_i + v\ y_i + w_0\ z_i) \tag{A.3}$$

where $w_0 = \max(0, 1 - u_0^2 - v_0^2)$ is the fixed vertical component of the normalised shower direction from the first fit. The linear least squares method can still be applied because w_0 is not considered as a free parameter.

2. We evaluate the temporal compatibility for each individual station and for the whole event:

   - $\Delta t_i < (N-2) \cdot 250 \text{ ns} \cdot \max(\cos\theta_{rec}, 0.2)$
   - $\frac{\sum_i \Delta t_i^2}{N-3} < [(N-2) \cdot 200 \text{ ns} \cdot \max(\cos\theta_{rec}, 0.2)]^2$

   being Δt_i the difference between the actual trigger time of the station and the time predicted by the plane fit.

   These cuts depend on the reconstructed zenith angle and on the multiplicity N. The dependence on N arises due to the curvature of the front, the most distant stations from the axis of the shower present a larger time difference with the reconstructed plane fit (see Fig. A.1). This effect is more relevant for larger N. On the other hand, the dependence on the zenith angle appears because inclined showers go through more matter before reaching the surface. The zenith angle is related to the shower front radius ($R \propto \sec\theta$ [136]), so at high zenith angle the shower front presents a small curvature. If $\cos\theta < 0.2$ ($\theta > 80°$) it is assumed that the shower front reaches its minimum curvature. This is the reason why Δt reaches a minimum $(N-2)\cdot 50$ ns.

3. We also require that the event is spatially compact. All the stations projected on the shower plane need to be contained in a circle of radius

$$r_{max} = \sqrt{1300^2 \cdot (N-2)} \text{ m}.$$

4. After this station selection the T3 conditions are again evaluated.

5. If any of the previous conditions is not satisfied, the algorithm is applied to subsets of $N-1, N-2, \ldots$, stations successively until a configuration is found satisfying all the conditions. The first station removed is the one with lowest signal, if it did not work, we remove the second one with lowest signal, and so on. After trying with all the $N-1$ subsets, if all the combinations fails, we start with the $N-2$ subsets, and so on.

If all stations in an event are aligned it is not posible to perform the reconstruction ($\sim 60\%$ of the events in the MC simulations of ES UHEν are aligned). The alternative is to calculate the apparent velocity of the signal V_{ij} between all pair of stations (i, j) with a T2 trigger:

$$V_{ij} = \frac{d_{ij}}{\Delta t_{ij}}, \tag{A.4}$$

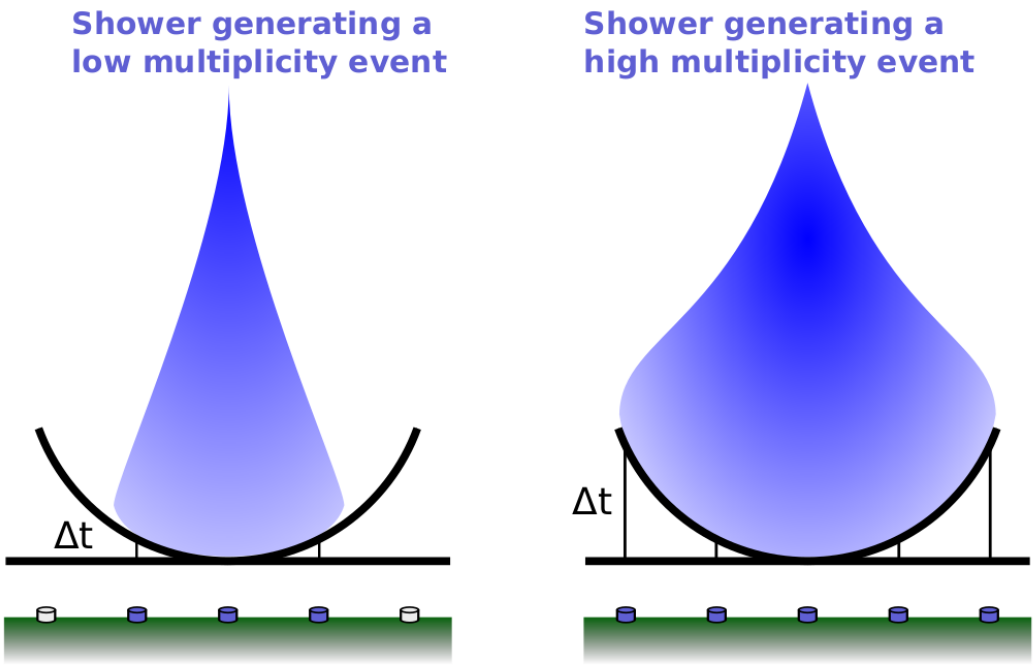

Figure A.1: Sketch of the arrival time difference between in a small (left panel) and a large (right panel) multiplicity event. In showers with small number of triggered stations (left panel) the time difference between the actual trigger time and the time obtained in the plane fit tends to be shorter than in large multiplicity events (right panel), especially for stations far from the shower core.

where d_{ij} is the distance between the stations i and j and Δt_{ij} their time difference. Using the values of V_{ij} it is possible to calculate the average velocity $\langle V \rangle$ and the timing compatibility is checked with the following condition between all pair of stations:

$$\frac{V_{ij} - \langle V \rangle}{\langle V \rangle} < 0.1. \tag{A.5}$$

USC
UNIVERSIDADE
DE SANTIAGO
DE COMPOSTELA

B

Calculation of the exposure

The calculation of the exposure consists on several steps: the first one is the selection of the representative configuration (see Sect. 3.1.1); in the second step we throw the simulated showers on the representative configuration selected for every 3-days period; the third one consists on combining the ES and DGH selections to avoid double counting of showers fulfilling both selections simultaneously; after that we calculate the effective areas (see Sect. 3.1.2) for each 3-days period for all the depths, angles and energies, and finally, we integrate this area to obtain the exposure.

B.1 Selection of the representative SD configuration

In this first step we use the t2Files (where information on the stations active at each moment is saved) and the Bad Periods to obtain the configuration representative for each of the 3-days periods (details of how this configuration is obtained in Sect. 3.1.1). The output gives us the time of the configuration selected, the number of stations active at that time and the dead time (including the time while the number of active stations is smaller than the active stations in the repesentative configuration) during the 3 days.

B.2 Shower simulation on the representative configuration

This second step is the key one, here we use the $\overline{\text{Off}}\underline{\text{line}}$ software to throw the previously simulated neutrinos on the representative configuration obtained in the first step. This software is a framework which provides various modules to perform the simulation and reconstruction of the Pierre Auger Observatory SD events. These modules have to be configured and run in a certain sequence:

- **RealAperture:** This module takes the information of the simulated neutrinos on the ideal SD, and takes into account the actual number and positions of the active stations in the representative configuration and the dead time eliminated in the corresponding period to calculate the real aperture depending on the 3-days period considered.
- **TankGPSSimulatorOG:** This is an auxiliary module, employed to find out if the signal from a certain station fulfills the local T2 trigger criteria.
- **CentralTriggerSimulatorXb:** This module emulates the T3 trigger condition performed by CDAS to select events.
- **CentralTriggerEventBuilderOG:** This module is an "event builder" used after central trigger, that copies the information from the simulation and stores the data in a file to be used for the reconstruction.
- **BadTriggerRejectorUBA:** This module rejects the stations that give an error in the trigger.
- **SdEventSelectorUBA:** This module removes events that take place during the Bad Periods, from the 3-days period.
- **TopDownSelectorUBA:** This module implements the top-down station selection algorithm (it also works for aligned events), to determine which stations actually participate in the event. It basically removes accidental tanks that do not belong to the event.
- **simpleRec:** This module reconstructs and calculates the necessary variables for each event to use for the inclined selection and the neutrino identification analyses, namely L, W, $\langle V \rangle$, $RMS(V)$, $\langle AoP \rangle$, etc. See Sect. 2.2.2 for more details.

The procedure defined by the sequence above is applied in both ES and DGH analyses for all neutrino simulations (ES, DGH CC, DGH NC and DGH τ). For each analysis two output files, the RealAperture (that has the relevant information to calculate the effective area asociated to each energy, angle and depth simulation) and the DumpFile (that includes the relevant information used for the selection and neutrino identification).

B.3 Combination of DGH and ES selections

To enhance the fraction of selected events we applied the two channel analysis to each sample of simulated showers (ES and DGH) regardless of channel. Doing this, the fraction of identified MonteCarlo events is increased, for example, an ES simulated shower induced by a τ might not fulfill the requirements of the ES selection, but might still pass the DGH criteria, and contribute to the fraction of identified events [22].

In the last step we process the same simulated events with both the ES and the DGH algorithms. Several events can trigger both the ES and DGH reconstructions, so we have to take this in account to avoid double counting of events. In this code we compare the ID of the simulation and we count the total number of simulated events that trigger what avoids the double counting.

B.4 Calculation of the effective area of the SD

In this fourth step we multiply the number of events passing the selection criteria in the real array by the surface areas of the representative configurations obtained in the second step. Doing this we calculate the effective Area seen by the neutrinos of different energies, angles and depths. This Area is plotted in Figs. 3.4-3.6.

B.5 Calculation of the exposure of the SD

The final step consists in integrating the Area obtained in the fourth step to obtain the exposure using Eqs. (3.1), (3.2) and (3.12).

REFERENCES

[1] M. Spurio, *Probes of Multimessenger Astrophysics*, Astronomy and Astrophysical Library (2018). (Cited on page 2.)

[2] M. G. Aartsen *et al.* [IceCube Collaboration], *First observation of PeV-energy neutrinos with icecube*, Phys. Rev. Lett. **111** (2013) 021103. (Cited on page 2.)

[3] M. Unger on behalf of the Pierre Auger Collaboration, *Highlights from the Pierre Auger Observatory*, PoS(ICRC2017)1102. (Cited on page 2.)

[4] B. P. Abbott *et al.* [LIGO Scientific and Virgo Collaborations], *Observation of Gravitational Waves from a Binary Black Hole Merger*, Phys. Rev. Lett. **116** (2016) 061102. (Cited on pages 2, 91, 100, and 104.)

[5] https://gcn.gsfc.nasa.gov/ (Cited on pages 3 and 92.)

[6] B. P. Abbott *et al.* [LIGO & Virgo *et al.* Collaborations] *Multi-messenger Observations of a Binary Neutron Star Merger*, Astrophys. J. Lett. **848** (2017) L12. (Cited on pages 3, 4, and 113.)

[7] M. G. Aartsen *et al.* [IceCube *et al.* Collaborations], *Multimessenger observations of a flaring blazar coincident with high-energy neutrino IceCube-170922A*, Science **361** (2018) eaat1378, and "research article summary" (2018) 146. (Cited on page 5.)

[8] A. Aab *et al.* [Pierre Auger Collaboration], *A search for ultra high energy neutrinos from TXS 0506+056 using the Pierre Auger Observatory*, Astrophys. J. **902** (2020) 105. (Cited on pages 5 and 7.)

[9] F. Acero, *et al.*, *FERMI LAT Third Source Catalog*, Astrophys. J. Suppl. **218** (2015) 23. (Cited on page 5.)

[10] K.-H. Kampert, M. A. Mostafa, E. Zas, and The Pierre Auger Collaboration, *Multi-Messenger Physics with the Pierre Auger Observatory*, Frontiers in Astronomy and Space Sciences **6** (2019) 24. (Cited on page 6.)

[11] V. S. Berezinskii, and A. Yu. Smirnov, *Cosmic neutrinos of ultra-high energies and detection possibility*, Astrophysics and Space Science **32** (1975) 461. (Cited on page 6.)

[12] K.S. Capelle, J.W. Cronin, G. Parente, and E. Zas, *On the detection of ultra high energy neutrinos with the Auger observatory*, Astropart. Phys. **8** (1998) 321. (Cited on pages 6 and 23.)

[13] X. Bertou, P. Billoir, O. Deligny, C. Lachaud, and A. Letessier-Selvon, *Tau neutrinos in the Auger Observatory: A new window to UHECR sources*, Astropart. Phys. **17** (2002) 183. (Cited on pages 6, 80, and 81.)

[14] J. Abraham *et al.* [Pierre Auger Collaboration], *Upper Limit on the Diffuse Flux of Ultrahigh Energy Tau Neutrinos from the Pierre Auger Observatory*, Phys. Rev. Lett. **100** (2008) 211101. (Cited on pages 6, 25, and 71.)

[15] J. Abraham *et al.* [Pierre Auger Collaboration], *Limit on the diffuse flux of ultrahigh energy tau neutrinos with the surface detector of the Pierre Auger Observatory*, Phys. Rev. D **79** (2009) 102001. (Cited on pages 6, 25, 62, and 71.)

[16] J. S. Tiffenberg, PhD Thesis, Univ. Buenos Aires, Argentina (2011). Available at: https://digital.bl.fcen.uba.ar/download/tesis/tesis_n4901_Tiffenberg.pdf (Cited on pages 6, 24, 34, 35, and 57.)

[17] J. L. Navarro, PhD Thesis, Univ. Granada, Spain (2012). Available at: http://digibug.ugr.es/handle/10481/26377 (Cited on pages 6, 23, and 78.)

[18] Y. Guardincerri, PhD Thesis, Univ. Buenos Aires, Argentina (2013). Available at: https://bibliotecadigital.exactas.uba.ar/download/tesis/tesis_n5405_Guardincerri.pdf (Cited on pages 6, 33, 34, and 35.)

[19] P. Pieroni, PhD Thesis, Univ. Buenos Aires, Argentina (2016). Available at: https://bibliotecadigital.exactas.uba.ar/download/tesis/tesis_n5927_Pieroni.pdf (Cited on pages 6, 33, 34, and 35.)

[20] J. Abraham *et al.* [Pierre Auger Collaboration], *Search for ultrahigh energy neutrinos in highly inclined events at the Pierre Auger Observatory*, Phys. Rev. D **84** (2011) 122005. (Cited on pages 6, 25, 35, 57, 61, 62, and 78.)

[21] P. Abreu *et al.* [Pierre Auger Collaboration], *Search for Point-Like Sources of Ultra-High Energy Neutrinos at the Pierre Auger Observatory and Improved Limit on the Diffuse Flux of Tau Neutrinos*, Astrophys. J. Lett. **755** (2012) L4 (Cited on page 6.)

[22] A. Aab *et al.* [Pierre Auger Collaboration], *Improved limit to the diffuse flux of UHE neutrinos with the Pierre Auger Observatory*, Phys. Rev. D **91** (2015) 092008. (Cited on pages 6, 25, 32, 34, 35, 55, 57, 61, 62, 70, 74, 86, 99, and 141.)

[23] A. Aab *et al.* [Pierre Auger Collaboration], *Probing the origin of ultra-high-energy cosmic rays with neutrinos in the EeV energy range using the Pierre Auger Observatory*, JCAP **10** (2019) 022. (Cited on pages 7, 11, 23, 69, 71, 76, and 86.)

[24] A. Aab *et al.* [Pierre Auger Collaboration], *Limits on point-like sources of ultra-high-energy neutrinos with the Pierre Auger Observatory* , JCAP **11** (2019) 004. (Cited on pages 7, 78, 82, 85, 87, and 88.)

[25] F. Pedreira on behalf of the Pierre Auger Collaboration, *Bounds on diffuse and point source fluxes of ultra-high energy neutrinos with the Pierre Auger Observatory*, PoS(ICRC2019)979. (Cited on page 7.)

[26] A. Albert *et al.* [ANTARES, IceCube, Pierre Auger and LIGO/Virgo Collaborations], *Search for high-energy neutrinos from binary neutron star merger GW170817 with ANTARES, IceCube and the Pierre Auger Observatory*, Astrophys. J. Lett. **850** (2017) L35. (Cited on pages 7, 82, 85, 114, 115, 116, and 120.)

[27] A. Aab *et al.* [Pierre Auger Collaboration], *Ultrahigh-energy neutrino follow-up of gravitational wave events GW150914 and GW151226 with the Pierre Auger Observatory*, Phys. Rev. D **94** (2016) 122007. (Cited on pages 7, 109, 110, and 112.)

[28] D. Caprioli, *Cosmic-ray Acceleration and Propagation*, PoS(ICRC2015)008. (Cited on page 7.)

[29] K. Greisen, *End to the Cosmic-Ray Spectrum?*, Phys. Rev. Lett. **16** (1966) 748. (Cited on page 7.)

[30] G.T. Zatsepin, and V.A. Kuzmin, *Upper Limit of the Spectrum of Cosmic Rays*, JETP Lett. **4** (1966) 78. (Cited on page 7.)

[31] A. Aab *et al.* [Pierre Auger Collaboration], *Measurement of the cosmic-ray energy spectrum of cosmic rays above* 2.5×10^{18} *eV using the Pierre Auger Observatory*, Phys. Rev. D **102** (2020) 062005. (Cited on pages 8 and 74.)

[32] A. Aab *et al.* [Pierre Auger Collaboration], *Features of the energy spectrum of cosmic rays above* 2.5×10^{18} *eV using the Pierre Auger Observatory*, Phys. Rev. Lett. **125** (2020) 121106. (Cited on pages 8 and 74.)

[33] M. Gerbino, *Neutrino properties from cosmology*, Proceedings Prospects in Neutrino Physics (NuPhys2017-Gerbino) (2018). (Cited on page 9.)

[34] M. Trini, PhD Thesis, Univ. Nova Gorica, Slovenia (2019). Auger internal note GAP-2019-072 (2019). (Cited on page 9.)

[35] A. Cooper-Sarkar, P. Mertsch, and S. Sarkar, *The high energy neutrino cross-section in the Standard Model and its uncertainty*, JHEP **1108** (2011) 042. (Cited on pages 10, 15, and 62.)

[36] H. Athar, M. Jezabek, and O. Yasuda, *Effects of neutrino mixing on high-energy cosmic neutrino flux*, Phys. Rev. D **62** (2000) 103007. (Cited on pages 10, 23, and 69.)

[37] M. Ave, N. Busca, A. V. Olinto, A. A. Watson, and T. Yamamoto, *Cosmogenic neutrinos from ultra-high energy nuclei*, Astropart. Phys. **23** (2005) 19. (Cited on pages 10 and 74.)

[38] D. Hooper *et al.*, *The impact of heavy nuclei on the cosmogenic neutrino flux*, Astropart. Phys. **23** (2005) 11. (Cited on pages 10 and 74.)

[39] M. Settimo for the Pierre Auger Collaboration, *Measurement of the mass composition of ultra-high energy cosmic rays with the Pierre Auger Observatory*, Journal of Physics: Conference Series, **718** (2016) 052037. (Cited on page 11.)

[40] M. G. Aartsen *et al.* [IceCube Collaboration], *Differential limit on the EHE cosmic neutrino flux in the presence of astrophysical background from nine years of IceCube data*, Phys. Rev. D **98** (2018) 062003. (Cited on pages 11, 72, and 73.)

[41] A. Aab *et al.* [Pierre Auger Collaboration], *Inferences on mass composition and tests of hadronic interactions from 0.3 to 100 EeV using the water-Cherenkov detectors of the Pierre Auger Observatory*, Phys. Rev. D **96** (2017) 122003. (Cited on pages 11 and 74.)

[42] D. Hopkins, and J. F. Beacom, *On the normalisation of the cosmic star formation history*, Astrophys. J. **651** (2006) 142. (Cited on page 11.)

[43] H. Yüksel *et al.*, *Revealing the High-Redshift Star Formation Rate with Gamma-Ray Bursts*, Astrophys. J. **683** (2008) L5. (Cited on pages 11 and 12.)

[44] J. V. Wall *et al.*, *The Parkes quarter-Jansky flat-spectrum sample*, Astronomy and Astrophysics **434** (2005) 133. (Cited on page 11.)

[45] D. Allard *et al.*, *Cosmogenic neutrinos from the propagation of ultrahigh energy nuclei*, JCAP **09** (2006) 005. (Cited on page 12.)

[46] P. A. Ade *et al.*, *Planck 2015 results-XIII. Cosmological parameters*, Astronomy and Astrophysics **594** (2016) A13. (Cited on page 12.)

[47] R. Engel *et al.*, *Neutrinos from propagation of ultrahigh energy protons*, Phys. Rev. D **64** (2001) 093010. (Cited on page 12.)

[48] K. Kotera, D. Allard, and A. V. Olinto, *Cosmogenic neutrinos: parameter space and detectability from PeV to ZeV*, JCAP **10** (2010) 013. (Cited on pages 12, 72, 74, and 77.)

[49] F. W. Stecker *et al.*, *High-energy neutrinos from active galactic nuclei*, Phys. Rev. Lett. **66** (1991) 2697. (Cited on page 13.)

[50] C. M. Urry, and P. Padovani, *Unified schemes for radio-loud active galactic nuclei*, Publ. Astron. Soc. Pac. **107** (1995) 803. (Cited on page 13.)

[51] P. Mészáros *et al.*, *Multi-messenger astrophysics*, Nature Reviews Physics **1** (2019) 585. (Cited on page 13.)

[52] P. Kumarand, and B. Zhang, *The physics of gamma-ray bursts and relativistic jets*, Physics Reports **561** (2014) 1. (Cited on page 13.)

[53] J. Matthews, *A Heitler model of extensive air showers*, Astropart. Phys. **22** (2005) 387. (Cited on page 13.)

[54] W. Heitler, *The Quantum Theory of Radiation*, Dover Books on Physics and Chemistry (1954). (Cited on page 14.)

[55] A. Cooper-Sarkar, and S. Sarkar, *Predictions for high energy neutrino cross-sections from the ZEUS global PDF fits*, JHEP **0801** (2008) 075. (Cited on page 14.)

[56] N. Armesto *et al.*, *Charged current neutrino cross section and tau energy loss at ultrahigh energies*, Phys. Rev. D **77** (2008) 013001. (Cited on page 15.)

[57] A. Aab *et al.* [Pierre Auger Collaboration], *The Pierre Auger Cosmic Ray Observatory*, Nucl. Instrum. Meth. A **798** (2015) 172. (Cited on pages 17, 19, and 83.)

[58] J. Abraham *et al.* [Pierre Auger Collaboration], *Trigger and aperture of the surface detector array of the Pierre Auger Observatory*, Nucl. Instrum. Meth. A **613** (2010) 29. (Cited on pages 20, 21, and 55.)

[59] D. Fargion, *Discovering Ultra High Energy Neutrinos by Horizontal and Upward tau Air-Showers: Evidences in Terrestrial Gamma Flashes?*, Astrophys. J. **570** (2002) 909 (Cited on page 23.)

[60] A. Letessier-Selvon, *Establishing the GZK cutoff with ultrahigh-energy tau neutrinos*, AIP Conf. Proc. **566** (2001) 157. (Cited on page 23.)

[61] J. G. Learned, and S. Pakvasa, *Detecting tau-neutrino oscillations at PeV energies*, Astropart. Phys. **3** (1995) 267. (Cited on pages 23 and 69.)

[62] L. A. Anchordoqui *et al.*, *Cosmic neutrino pevatrons: A brand new pathway to astronomy, astrophysics, and particle physics*, JHEAp, **1** (2014) 1. (Cited on page 23.)

[63] M. Schimp, PhD Thesis in preparation. (Cited on page 23.)

[64] A. Aab *et al.* [Pierre Auger Collaboration], *Reconstruction of inclined air showers detected with the Pierre Auger Observatory*, JCAP **08** (2014) 019. (Cited on page 24.)

[65] I. Lhenry-Yvon, and P. L. Ghia, *Implementation of PMTs Quality Cuts in Auger Sd Data*, Auger internal note GAP-2009-080 (2009). (Cited on page 27.)

[66] P. Lipari, *TeV Muons in Hadronic Showers*, Astropart. Phys. **1** (1993) 399. (Cited on page 29.)

[67] J. Blumer, *On the influence of accidental muons on air shower detection*, Auger internal note GAP-2008-110 (2008). (Cited on page 30.)

[68] P. Billoir, *FADC trace cleaning in Surface Detector through a segmentation procedure*, Auger internal note GAP-2005-074 (2005). (Cited on page 30.)

[69] P. Billoir, *Top-down Selection of Events and Stations in Surface Detector Triggers*, Auger internal note GAP-2006-072 (2006). (Cited on page 31.)

[70] R. Fisher, *The use of multiple measurements in taxonomic problems*, Ann. Eugenics **7** (1936) 179. (Cited on page 35.)

[71] P. Abreu *et al.* [Pierre Auger Collaboration], *The Exposure of the Hybrid Detector of the Pierre Auger Observatory*, Astropart. Phys. **34.6** (2011) 368. (Cited on page 54.)

[72] O. Blanch Bigas, O. Deligny, K. Payet, and V. Van Elewyck, *Ultrahigh energy tau neutrino flux regeneration while skimming the Earth*, Phys. Rev. D **78** (2008) 063002. (Cited on pages 62, 80, and 81.)

[73] J. Alvarez-Muñiz, W. R. Carvalho Jr., K. Payet, A. Romero-Wolf, H. Schoorlemmer, and E. Zas, *Comprehensive approach to tau-lepton production by high-energy tau neutrinos propagating through the Earth*, Phys. Rev. D **97** (2018) 023021; Erratum: Phys. Rev. D **99** (2019) 069902. (Cited on pages 62, 80, and 81.)

[74] J. Alvarez-Muñiz *et al.*, *A limit on the diffuse flux of UHE neutrinos with down-going showers from the Pierre Auger Observatory*, Auger internal note GAP-2008-054 (2008). (Cited on page 63.)

[75] S. Iyer Dutta, M. H. Reno, I. Sarcevic, and D. Seckel, *Propagation of muons and taus at high energies*, Phys. Rev. D **63** (2001) 094020. (Cited on page 69.)

[76] G. J. Feldman, and R. D. Cousins, *A Unified approach to the classical statistical analysis of small signals*, Phys. Rev. D **57** (1998) 3873. (Cited on pages 70, 71, and 86.)

[77] J. Conrad, O. Botner, A. Hallgren, and C. Pérez de los Heros, *Including systematic uncertainties in confidence interval construction for Poisson statistics*, Phys. Rev. D **67** (2003) 012002. (Cited on pages 70 and 71.)

[78] P. W. Gorham *et al.* [ANITA Collaboration], *Constraints on the diffuse high-energy neutrino flux from the third flight of ANITA*, Phys. Rev. D **98** (2018) 022001. (Cited on pages 72 and 73.)

[79] M. Ahlers, L. A. Anchordoqui, M. C. Gonzalez-Garcia, F. Halzen, and S. Sarkar, *GZK Neutrinos after the Fermi-LAT Diffuse Photon Flux Measurement*, Astropart. Phys. **34** (2010) 106. (Cited on pages 72, 75, and 77.)

[80] K.-H. Kampert, and M. Unger, *Measurements of the Cosmic Ray Composition with Air Shower Experiments*, Astropart. Phys. **35** (2012) 660. (Cited on pages 72, 74, 75, and 77.)

[81] R. Aloisio, D. Boncioli, A. di Matteo, A. F. Grillo, S. Petrera, and F. Salamida, *Cosmogenic neutrinos and ultra-high energy cosmic ray models*, JCAP **10** (2015) 006. (Cited on pages 72 and 77.)

[82] E. Waxman, and J. Bahcall, *High energy neutrinos from astrophysical sources: An upper bound*, Phys. Rev. D **59** (1999) 023002. (Cited on page 73.)

[83] R. U. Abbasi *et al.* [HiRes Collaboration], *First Observation of the Greisen-Zatsepin-Kuzmin Suppression*, Phys. Rev. Lett. **100** (2008) 101101. (Cited on page 74.)

[84] P. Abreu *et al.* [Pierre Auger Collaboration], *Measurement of the Depth of Maximum of Extensive Air Showers above* 10^{18} *eV*, Phys. Rev. Lett. **104** (2010) 091101. (Cited on page 74.)

[85] A. Aab *et al.* [Pierre Auger Collaboration], *Depth of maximum of air-shower profiles at the Pierre Auger Observatory. I. Measurements at energies above* $10^{17.8}$ *eV*, Phys. Rev. D **90** (2014) 122005. (Cited on page 74.)

[86] J. Bellido for the Pierre Auger Collaboration, *Depth of maximum of air-shower profiles at the Pierre Auger Observatory: Measurements above* $10^{17.2}$ *eV and Composition Implications*, PoS (ICRC2017) 506. (Cited on pages 74 and 75.)

[87] A. Aab *et al.* [Pierre Auger Collaboration], *Evidence for a mixed mass composition at the ankle in the cosmic-ray spectrum*, Phys. Lett. B **762** (2016) 288. (Cited on page 74.)

[88] A. Aab *et al.* [Pierre Auger Collaboration], *Combined fit of spectrum and composition data as measured by the Pierre Auger Observatory*, JCAP **04** (2017) 038. (Cited on page 74.)

[89] A. Aab *et al.* [Pierre Auger Collaboration], *Anisotropy and chemical composition of ultra-high energy cosmic rays using arrival directions measured by the Pierre Auger Observatory*, JCAP **06** (2011) 022. (Cited on page 74.)

[90] J. Heinze, A. Fedynitch, D. Boncioli, and W. Winter, *A new view on Auger data and cosmogenic neutrinos in light of different nuclear disintegration and air-shower models*, Astrophys. J. **873** (2019) 88. (Cited on page 74.)

[91] R. Alves Batista, R. M. de Almeida, B. Lago, and K. Kotera, *Cosmogenic photon and neutrino fluxes in the Auger era*, JCAP **01** (2019) 002. (Cited on page 74.)

[92] D. Wittkowski, and K.-H. Kampert, *On the flux of high-energy cosmogenic neutrinos and the influence of the extragalactic magnetic field*, Monthly Notices of the Royal Astronomical Society **488-1** (2019) L119. (Cited on page 74.)

[93] A. A. Abdo et al., [Fermi-LAT Collaboration], *Spectrum of the Isotropic Diffuse Gamma-Ray Emission Derived from First-Year Fermi Large Area Telescope Data*, Phys. Rev. Lett. **104** (2010) 101101. (Cited on page 75.)

[94] R. Alves Batista *et al.*, *CRPropa 3 - a Public Astrophysical Simulation Framework for Propagating Extraterrestrial Ultra-High Energy Particles*, JCAP **05** (2016) 038. (Cited on pages 75 and 76.)

[95] A. van Vliet, R. Alves Batista, and J. R. Hörandel, *Determining the fraction of cosmic-ray protons at ultra-high energies with cosmogenic neutrinos*, Phys. Rev. D **100** (2019) 021302. (Cited on page 75.)

[96] M. S. Muzio, M. Unger, and G. Farrar, *Progress towards characterizing ultrahigh energy cosmic ray sources*, Phys. Rev. D **100** (2019) 103008. (Cited on page 75.)

[97] K. Murase, Y. Inoue, and C. D. Dermer, *Diffuse neutrino intensity from the inner jets of active galactic nuclei: Impacts of external photon fields and the blazar sequence*, Phys. Rev. D **90** (2014) 023007. (Cited on pages 76 and 77.)

[98] K. Fang, K. Kotera, K. Murase, and A. V. Olinto, *Testing the Newborn Pulsar Origin of Ultrahigh Energy Cosmic Rays with EeV Neutrinos*, Phys. Rev. D **90**, 103005 (2014); Erratum: Phys. Rev. D **92** (2014) 129901. (Cited on pages 76 and 77.)

[99] L. Lu for the IceCube Collaboration, talk given at the Ultra High Energy Cosmic Rays 2018, 8 - 12 October 2018, Paris (France). (Cited on page 77.)

[100] F. Halzen, review talk given at the 36$^{\text{th}}$ International Cosmic Ray Conference, 24 July - 1 August, Madison, Wisconsin (USA) PoS(ICRC2019)021. (Cited on page 77.)

[101] M. G. Aartsen *et al.* [IceCube Collaboration], *All-sky Search for Time-integrated Neutrino Emission from Astrophysical Sources with 7 yr of IceCube Data*, Astrophys. J. **835** (2017) 151. (Cited on pages 79, 80, 86, 87, and 88.)

[102] https://www.auger.org/index.php/science/data (Cited on page 79.)

[103] E. Zas, *Neutrino detection with inclined air showers*, New J. Phys. **7** (2005) 130. (Cited on pages 80 and 81.)

[104] http://tevcat.uchicago.edu/?mode=1;id=324 (Cited on page 82.)

[105] A. Aab *et al.* [Pierre Auger Collaboration], *Observation of a large-scale anisotropy in the arrival directions of cosmic rays above* 8×10^{18} *eV*, Science **357** (2017) 1266. (Cited on page 86.)

[106] A. Albert *et al.* [ANTARES Collaboration], *First all-flavour neutrino pointlike source search with the ANTARES neutrino telescope*, Phys. Rev. D **96**, 082001 (2017). (Cited on pages 86, 87, and 88.)

[107] A. Cuoco, and S. Hannestad, *Ultrahigh energy neutrinos from Centaurus A and the Auger hot spot*, Phys. Rev. D **78** (2008) 023007. (Cited on pages 86 and 88.)

[108] M. Kachelriess, S. Ostapchenko, and R. Tomas, *High energy radiation from Centaurus A*, New J. Phys. **11** (2009) 065017. (Cited on pages 86 and 88.)

[109] P. Billoir *et al.*, *A study of trigger rates for ToTd and MoPS*, Auger internal note GAP2015-019 (2015). (Cited on page 88.)

[110] A. Coleman, *The New Trigger Settings*, Auger internal note GAP2018-001 (2018). (Cited on page 88.)

[111] M. Schimp, *Neutrino follow up, benefits from new triggers*, Contribution 131 of Auger Collaboration Meeting June 2018. (Cited on page 89.)

[112] A. Aab *et al.* [Pierre Auger Collaboration], *The Pierre Auger Observatory Upgrade - Preliminary Design Report*, arXiv:1604.03637. (Cited on page 89.)

[113] B. Pont for the Pierre Auger Collaboration, *A large radio detector at the Pierre Auger Observatory - measuring the properties of cosmic rays up to the highest energies*, PoS(ICRC2019)395. (Cited on page 89.)

[114] A. Castellina for the Pierre Auger Collaboration, *AugerPrime: the Pierre Auger Observatory Upgrade*, EPJ Web of Conferences **210** (2019) 06002. (Cited on page 89.)

[115] J. Alvarez-Muñiz, *Ultra-high energy neutrinos: status and prospects*, PoS(ICRC2017)1111. (Cited on page 89.)

[116] https://www.ligo.caltech.edu (Cited on pages 91 and 92.)

[117] B. P. Abbott *et al.* [LIGO Scientific and Virgo Collaborations], *Properties of the Binary Black Hole Merger GW150914*, Phys. Rev. Lett. **116** (2016) 241102. (Cited on pages 93, 94, and 104.)

[118] https://emfollow.docs.ligo.org/userguide/index.html (Cited on page 95.)

[119] B. Baret *et al.*, *Bounding the time delay between high-energy neutrinos and gravitational-wave transients from gamma-ray bursts*, Astropart. Phys. **35** (2011) 1. (Cited on page 95.)

[120] https://gracedb.ligo.org/ (Cited on page 97.)

[121] B. P. Abbott *et al.* [LIGO Scientific and Virgo Collaborations], *GWTC-2: Compact Binary Coalescences Observed by LIGO and Virgo During the First Half of the Third Observing Run*, arXiv:2010.14527v1 (2020). (Cited on page 98.)

[122] S. Adrián-Martínez *et al.* [LIGO & Virgo, IceCube, and ANTARES Collaborations], *High-energy neutrino follow-up search of gravitational wave event GW150914 with ANTARES and IceCube*, Phys. Rev. D **93** (2016) 122010. (Cited on pages 99 and 115.)

[123] B. P. Abbott *et al.* [LIGO Scientific and Virgo Collaborations], *GWTC-1: A Gravitational-Wave Transient Catalog of Compact Binary Mergers Observed by LIGO and Virgo during the First and Second Observing Runs*, Phys. Rev. X **9** (2019) 031040. (Cited on pages 105 and 108.)

[124] K. Kotera, and J. Silk, *Ultrahigh-Energy Cosmic Rays and Black Hole mergers*, Astrophys. J. Lett. **823** (2016) L29. (Cited on pages 110, 112, and 113.)

[125] B. P. Abbott *et al.* [LIGO Scientific and Virgo Collaborations], *Binary Black Hole Mergers in the First Advanced LIGO Observing Run*, Phys. Rev. X **6** (2016) 041015. (Cited on page 110.)

[126] M. Schimp on behalf of the Pierre Auger Collaboration, *Follow-up searches for ultra-high energy neutrinos from transient astrophysical sources with the Pierre Auger Observatory*, PoS(ICRC2019)415. (Cited on page 113.)

[127] H. Gao, B. Zhang, X.-F. Wu, and Z.-G Dani, *Possible high-energy neutrino and photon signals from gravitational wave bursts due to double neutron star mergers*, Phys. Rev. D **88** (2013) 043010. (Cited on pages 114 and 118.)

[128] K. Fang, and B. D. Metzger, *High-energy Neutrinos from Millisecond Magnetars Formed from the Mergerof Binary Neutron Stars*, Astrophys. J. **849** (2017) 153. (Cited on pages 114, 118, and 120.)

[129] P. Mészáros, and E. Waxman, *TeV Neutrinos from Successful and Choked Gamma-Ray Bursts*, Phys. Rev. Lett. **87** (2001) 171102. (Cited on pages 115, 116, and 118.)

[130] S. S. Kimura, K. Murase, P. Mészáros, and K. Kiuchi, *High-energy Neutrino Emission from Short Gamma-Ray Bursts: Prospects for Coincident Detection with Gravitational Waves*, Astrophys. J. Lett. **848** (2017) L4. (Cited on pages 116, 118, and 120.)

[131] O. Gottlieb, E. Nakar, T. Piran, and K. Hotokezaka, *A cocoon shock breakout as the origin of the γ-ray emission in GW170817*, Monthly Notices of the Royal Astronomical Society **479-1** (2018) 588. (Cited on page 118.)

[132] B. D. Metzger, E. Quataert, and T. A. Thompson, *Short-duration gamma-ray bursts with extended emission from protomagnetar spin-down*, Monthly Notices of the Royal Astronomical Society **385-3** (2008) 1455. (Cited on page 118.)

[133] K. Murase, P. Mészáros, and B. Zhang, *Probing the birth of fast rotating magnetars through high-energy neutrinos*, Phys. Rev. D **79** (2009) 103001. (Cited on page 118.)

[134] B. P. Abbott *et al.* [LIGO Scientific and Virgo Collaborations], *GW190425: Observation of a Compact Binary Coalescence with Total Mass* $\sim 3.4 M_{\odot}$, Astrophys. J. Lett. **892**, (2020) L3. (Cited on page 122.)

[135] B. P. Abbott *et al.* [LIGO Scientific and Virgo Collaborations], *GW190814: Gravitational Waves from the Coalescence of a 23 Solar Mass Black Hole with a 2.6 Solar Mass Compact Object*, Astrophys. J. Lett. **896**, (2020) L44. (Cited on page 127.)

[136] P. Billoir, *Reconstruction of first year EA events from the Surface Detector*, Auger internal note GAP-2002-044 (2002). (Cited on page 136.)